

Alma Mater Studiorum – Università di Bologna

DOTTORATO DI RICERCA IN  
INGEGNERIA CIVILE, CHIMICA, AMBIENTALE E DEI  
MATERIALI

Ciclo XXXIII

**Settore Concorsuale: 08/B2**

**Settore Scientifico Disciplinare: ICAR/08 Scienza delle costruzioni**

MODE-I FRACTURE PARAMETERS OF QUASI-BRITTLE  
MATERIALS: DIRECT EVALUATION USING DIC AND  
RELATIONSHIP WITH MODE-II INTERFACIAL PARAMETERS

**Presentata da:** Giulia Baietti

**Coordinatore Dottorato**

Prof. Luca Vittuari

**Supervisore**

Prof. Christian Carloni

**Esame finale anno 2021**



# Contents

|   |    |
|---|----|
| List of Figures.....  | 6  |
| List of Tables.....   | 11 |
| Abstract .....  | 12 |
| 1 Chapter 1 – Introduction.....   | 13 |
| 1.1 Fracture mechanics: a general overview.....                               | 15 |
| 1.1.1 Linear elastic fracture mechanics (LEFM).....                           | 16 |
| 1.1.2 Nonlinear fracture mechanics.....                                       | 16 |
| 1.1.3 Cohesive crack model.....   | 17 |
| 1.1.4 Softening curve.....  | 19 |
| 1.1.4.1 Determination of the softening curve and fracture parameters.....     | 20 |
| 1.1.5 Background on the size effect .....                                     | 21 |
| 1.2 Bond characteristics between composites and quasi-brittle substrates..... | 23 |
| 1.2.1 Experimental investigation of debonding.....                            | 24 |
| 1.2.2 Single-lap direct shear test.....                                       | 24 |
| 1.2.3 Failure modes .....   | 25 |
| 1.2.4 Anchorage system.....   | 26 |
| 2 Chapter 2 – Materials .....   | 28 |
| 2.1 Concrete.....   | 28 |
| 2.2 Alkali-activated mortars .....  | 30 |
| 2.2.1 Physical and mechanical characterization .....                          | 33 |
| 2.3 Masonry.....  | 35 |
| 2.3.1 <i>Vivo</i> bricks .....  | 35 |
| 2.3.2 Natural stones and fired-clay bricks .....                              | 36 |
| 2.4 <i>Tharros</i> stone.....   | 38 |
| 2.5 Composite materials .....   | 41 |
| 2.5.1 Steel fibers .....  | 42 |
| 2.5.2 SRG mortar matrices .....   | 43 |
| 2.5.3 Mortar for injection .....  | 44 |

|          |   |     |
|----------|---|-----|
| 3        | Chapter 3 – Mode-I fracture properties of quasi-brittle materials .....   | 45  |
| 3.1      | Specimens .....   | 48  |
| 3.1.1    | Concrete specimens .....  | 49  |
| 3.1.2    | Alkali-activated mortars .....  | 50  |
| 3.2      | Test set-up .....   | 51  |
| 3.3      | Discussion of results .....   | 54  |
| 3.3.1    | Load responses .....  | 54  |
| 3.3.1.1  | Concrete specimens .....  | 54  |
| 3.3.1.2  | Alkali-activated mortars .....  | 56  |
| 3.3.2    | Other quasi-brittle materials: fired-clay bricks, natural stones and steel reinforced grout (SRG) matrices..... | 60  |
| 3.3.3    | Comparison between LVDTs and DIC.....   | 64  |
| 3.3.3.1  | Concrete specimens .....  | 64  |
| 3.3.3.2  | Alkali-activated mortars .....  | 66  |
| 3.3.4    | Failure modes .....   | 68  |
| 3.3.4.1  | Concrete specimens .....  | 68  |
| 3.3.4.2  | Alkali-activated mortars .....  | 69  |
| 3.3.5    | Evaluation of fracture energy .....   | 71  |
| 3.3.5.1  | Concrete specimens .....  | 73  |
| 3.3.5.2  | Alkali-activated mortars .....  | 75  |
| 3.3.6    | Comparison between fracture energies of quasi-brittle materials .....   | 79  |
| 3.3.7    | Evaluation of the Elastic modulus from DIC .....  | 80  |
| 3.3.8    | Strain profiles, contour plots and crack opening from DIC analysis.....   | 86  |
| 3.3.8.1  | Alkali-activated mortars .....  | 86  |
| 3.3.8.2  | Concrete specimens .....  | 95  |
| 3.3.9    | Size and width effect .....   | 100 |
| 3.3.9.1  | Concrete specimens .....  | 100 |
| 3.3.9.2  | Alkali-activated mortars .....  | 103 |
| 3.3.10   | A new method to determine the critical crack opening .....  | 104 |
| 3.3.10.1 | Concrete specimens .....  | 104 |

|         |   |     |
|---------|---|-----|
| 4       | Chapter 4 – Bond behavior between SRG composites and quasi-brittle substrate..... | 108 |
| 4.1     | Preparation of masonry specimens .....  | 108 |
| 4.1.1   | Masonry blocks without anchorage.....   | 108 |
| 4.1.2   | Masonry blocks with anchorage .....   | 110 |
| 4.1.3   | Concrete prisms with anchorage.....   | 114 |
| 4.2     | Test set-up and procedure.....  | 115 |
| 4.3     | Discussion of results.....  | 117 |
| 4.3.1   | Failure modes .....   | 117 |
| 4.3.2   | Load responses .....  | 119 |
| 4.3.2.1 | Influence of SRG matrix width.....  | 120 |
| 4.3.2.2 | Influence of the type of matrix .....   | 122 |
| 4.3.2.3 | Influence of the test rate .....  | 123 |
| 4.3.2.4 | Influence of the substrate.....   | 124 |
| 4.3.2.5 | Influence of the anchorage .....  | 126 |
| 4.3.2.6 | Concrete prisms with anchorage.....   | 127 |
| 4.4     | Pull-out test.....  | 129 |
| 4.4.1   | Preparation of specimens.....   | 129 |
| 4.4.2   | Test set-up .....   | 130 |
| 4.4.3   | Discussion of results and failure modes .....                                     | 131 |
| 5       | Chapter 5 – Indirect calibration of the cohesive material law .....               | 133 |
| 5.1.1   | Definition of the analytical expression of the CML .....                          | 134 |
| 5.1.2   | Construction of the analytical load-global slip response.....                     | 134 |
| 5.1.3   | Implementation of the indirect method and modelling of the anchorage .....        | 137 |
|         | Conclusions .....   | 140 |
|         | References .....  | 144 |

## List of Figures

|   |    |
|---|----|
| Figure 1 Fracture modes [10] .....  | 16 |
| Figure 2 Uniaxial tension test: (a) test set-up, (b) load-elongation response [3].....  | 17 |
| Figure 3 Tensile behavior of concrete: (a) stress-deformation curve for the whole volume; (b) stress-opening curve for the damage zone [3] .....      | 18 |
| Figure 4 Tensile behavior of concrete [14] .....  | 18 |
| Figure 5 (a) Stress-opening curves for 4 types of concrete; (b) $\sigma_t/f_t$ as a function of $w/w_c$ [7] .....                                     | 20 |
| Figure 6 Possible shapes for the softening curve [7].....   | 20 |
| Figure 7 Comparison between maximum tensile stress for small and large specimen predicted by the Strength of Materials (courtesy of Dr. Carloni)..... | 21 |
| Figure 8 Logarithmic plot of $\sigma_N$ versus D [18] .....   | 22 |
| Figure 9 Bond tests: (a) single-lap and (b) double-lap direct shear test set-up [42].....   | 24 |
| Figure 10 Sketches of failure modes in shear bond test [53].....  | 25 |
| Figure 11 Examples of anchorages: (a) 90° and (b) 180° anchor spike; c) transverse wrapping anchorage [58].....                                       | 27 |
| Figure 12 (a) Concrete columns; (b) prisms; (c) vibration of concrete; (d) flattening the surface and (d) sandblasting procedure .....                | 29 |
| Figure 13 Compressive (a) and tensile (b) strength as a function of time .....  | 30 |
| Figure 14 Optical microscope images of the aggregates used in this work a) fine sand; b) coarse sand; and c) expanded perlite. ....                   | 31 |
| Figure 15 Particle size distribution of the three aggregates used in this study. ....   | 32 |
| Figure 16 Specimens in prismatic molds of different sizes .....   | 32 |
| Figure 17 Vivo solid clay brick .....   | 35 |
| Figure 18 Tests set-up (a) splitting tensile strength test; (b) compression test and (c) compression test failure mode .....                          | 35 |
| Figure 19 Example of a) tuff blocks and b) fired-clay bricks collected from demolished structures .....   | 36 |
| Figure 20 (a) Example of specimen cored from tuff block; (b) compressive strength test and (c) splitting tensile strength test .....                  | 37 |
| Figure 21 Archeological site top view.....  | 38 |
| Figure 22 (a) The archeological site of Tharros; (b) example of a tomb and (c) example of a collected block.....                                      | 39 |
| Figure 23 (a) Coring the specimens (b) Group of specimens after the coring operations .....   | 39 |
| Figure 24 Set-up for (a) compression test and (b) splitting tensile strength test .....   | 40 |
| Figure 25 (a) Steel fibers layout; (b) low (LD ) and (c) medium (MD) density fiber sheet .....  | 42 |
| Figure 26 Test set-up: (a) flexural test and (b) compression test .....   | 43 |
| Figure 27 Mortar prisms for flexural test .....   | 44 |

|  |    |
|--|----|
| Figure 28 Specimen dimensions [158] .....  | 48 |
| Figure 29 Photo of a representative concrete specimen with a blow-up on the V-shaped tip .....   | 49 |
| Figure 30 Concrete prisms with different cross-sections: (a) 70 mm-depth specimens and (b) 150 mm-depth specimens .....  | 49 |
| Figure 31 AAMs beams.....  | 50 |
| Figure 32 Experimental set-up for fracture mechanics tests (a) sketch of the TPB set-up; (b) concrete specimen .....   | 51 |
| Figure 33 (a) Example of specimens prepared for fracture mechanics test; (b) Clip-on-gauge ....  | 52 |
| Figure 34 Preparation of specimen for DIC: (a) application of white paint; (b) creation of a speckle pattern with black paint; c) finished specimen .....  | 53 |
| Figure 35 Digital image correlation set-up.....  | 54 |
| Figure 36 P/B versus $\delta$ response for specimens cured in the lime-saturated bath with D=70 mm (a) and D=150 mm (c), and comparison among specimens cured in the lime-saturated bath, DRY specimens, W-DRY specimen with D=150 mm (e). P/B versus CMOD response for specimens cured in the lime-saturated bath with D=70 mm (b) and D=150 mm (d), and comparison among specimens cured in the lime-saturated bath, DRY specimens, W-DRY specimen with D=150 mm (f). [16] ..... | 55 |
| Figure 37 P – $\delta$ response for: (a) FS; (c) CS; and (e) EP specimens. P – CMOD response for: (b) FS; (d) CS; and (f) EP specimens.[159] .....   | 57 |
| Figure 38 P – $\delta$ response for: (a) CS_2; P – CMOD response for: (b) CS; (c) FS; and (d) EP specimens. ....   | 58 |
| Figure 39 Examples of a) fired-clay bricks and b) tuff brick .....   | 61 |
| Figure 40 (a) Representative tuff bricks prepared for fracture tests; (b) TPB test set-up.....   | 61 |
| Figure 41 (a) Failure mode; (b) P- $\delta$ and (c) P-CMOD response of Tharros notched beams.....  | 63 |
| Figure 42 (a) P- $\delta$ response and (b) P-CMOD response of lime-based mortar; (c) P- $\delta$ response and (d) P-CMOD response of cement-based mortar matrix [162] .....  | 64 |
| Figure 43 Comparison between the P- $\delta$ response obtained from LVDTs (solid line) and the P- $\delta$ response obtained from DIC (dotted line) for specimen FM_150_70_300_G6_1 (a) and specimen FM_150_70_300_G7_3 (b).....   | 65 |
| Figure 44 . Comparison between P – $\delta$ response from DIC and LVDTs for specimens: (a) 70_70_300_FS_1 subset 41 and step = 10); and (b) 70_70_300_CS_2. (green squares are the squares used to average the displacements of the supports).....   | 67 |
| Figure 45 Comparison between P – $\delta$ response from DIC and LVDTs for specimen FM_35_35_200_CS_2 .....   | 68 |
| Figure 46 Specimen FM_150_150_600_G7_5 at failure: side view (a) and fracture surfaces (b).69  |    |
| Figure 47 Failure mode of two representative specimens (a) FM_70_70_300_EP_2; and (b) FM_70_70_300_CS_2 and (c) FM_70_70_300_FS_1 .....  | 70 |

|   |     |
|---|-----|
| Figure 48 Photos of fractured cross-sections of representative TPB specimens at 300 days (after testing).....   | 70  |
| Figure 49 Load-deflection curve from a three-point bending test and the corresponding curve when the weight of the beam is taken into account to evaluate $G_F$ .....   | 73  |
| Figure 50 Average fracture energy for different cross-sections .....  | 74  |
| Figure 51 SEM micrographs of representative specimens: (a) FS, (b) CS and (c) EP. ....  | 78  |
| Figure 52 Definition of the interval of $x$ and rectangular areas used to average the strain and displacement values.....   | 86  |
| Figure 53 $\epsilon_{xx}$ versus $y/(D-a_0)$ of FM_70_70_300_CS_2 specimen for $d=10$ mm: (a) subset=31 and step=10; and (b) subset=41 and step=10. ....  | 88  |
| Figure 54 Specimen FM_70_70_300_EP_2: (a) $P - \delta$ response; (b) $\epsilon_{xx}$ versus $y/(D-a_0)$ for $d = 10$ mm, subset=41, and step=10. ....   | 89  |
| Figure 55. $\Delta u$ versus $y/(D-a_0)$ for subset=41, step=10 and $d = 10$ mm: (a) FM_70_70_300_CS_2 specimen; and (b) FM_70_70_300_EP_2 specimen .....   | 91  |
| Figure 56 Contour plots of strain component $\epsilon_{xx}$ for specimen FM_70_70_300_CS_2, points: (a) C; (b) D; (c) E; and (d) F.....   | 93  |
| Figure 57 Strain (a) and $\Delta u$ (b) profiles along the crack ligament for specimen FM_35_35_200_CS_2 for different points of the load response .....  | 94  |
| Figure 58 Contour plots of strain component $\epsilon_{xx}$ for specimen FM_35_35_200_CS_2, for points B (a), C (b), D (c) and E (d) of the load response .....   | 95  |
| Figure 59. Contour plot of $\epsilon_{xx}$ at different points of the load response (Figure 60b) for specimen FM_150_150_600_G4_2: Point C (a), Point D (b), Point E (c). Square areas for the evaluation of $w$ (d). ....  | 97  |
| Figure 60. $\epsilon_{xx}$ profile along the crack ligament for different values of the load for specimen FM_150_150_600_G4_2 (a). Load-displacement response obtained from LVDT readings for specimen FM_150_150_600_G4_2 (b). $\epsilon_{xx}$ profile along the crack ligament for different values of the load for specimen FM_70_70_300_G8_1 (c). Load-displacement response obtained from LVDT readings for specimen FM_70_70_300_G8_1 (d). $\epsilon_{xx} - x$ plot for specimen FM_150_150_600_G4_2 at point C (e), point D (f), and point E (g). .... | 99  |
| Figure 61 Logarithmic plots of $\sigma_N$ versus $D$ to investigate size and width effects: average $\sigma_N$ for each width and depth (a); average of $\sigma_N$ for each width and depth without specimen FM_150_70_300_4 (b); and $P/B$ versus $\delta$ response for specimens with a cross-section equal to $150 \text{ mm} \times 70 \text{ mm}$ (c).....   | 101 |
| Figure 62 Comparison of the nominal stress vs. CMOD for families with the same geometries (i.e. $70 \times 70 \times 300$ and $150 \times 150 \times 600$ ) or the same depth ( $D=150 \text{ mm}$ ) and two widths ( $B=70 \text{ mm}$ , $B=150\text{mm}$ ) (a) and specimens with rectangular cross-section (i.e. $35 \times 70 \times 300$ and $70 \times 150 \times 600$ ) or the same width ( $B=70 \text{ mm}$ ) and two depths ( $D=70\text{mm}$ and $D=150\text{mm}$ ) (b).....   | 102 |

|   |     |
|---|-----|
| Figure 63 Size effect study in terms of nominal stress vs. CMOD for 35 mm wide specimens (a), 70 mm wide specimens (b), and 150 mm wide specimens (c) .....   | 103 |
| Figure 64 Logarithmic plot of $\sigma_N$ versus D for the three AAMs .....  | 103 |
| Figure 65 Time versus strain for specimen (a) 70_70_300_G8_1; (c) 70_70_300_G8_2; Cropped graph for specimen time versus strain graph for (b) 70_70_300_G8_1 and (d) 70_70_300_G8_2 .....   | 105 |
| Figure 66 $\Delta\varepsilon/\Delta t$ versus time for (a) FM_70_70_300_G8_1; (b) FM_70_70_300_G8_2 .....   | 106 |
| Figure 67 $\Delta u$ plot for (a) 70_70_300_G8_1; (b) 70_70_300_G8_2 .....  | 106 |
| Figure 68 Preparation of specimen prior to the application of the SRG composite: (a) masonry blocks left soak in the water (b) wet specimen removed from the bucket.....  | 109 |
| Figure 69 Phases of application of SRG reinforcement (a) delimitation of the bonded area; (b) application of the first layer of mortar matrix; (c) application of steel fiber sheet; (d) application of the second layer of mortar matrix.....  | 109 |
| Figure 70 Construction phases of masonry block: (a) first layer of bricks; (b) mortar joints; (c) second layer of brick; (d) finished specimen and (d) masonry block covered with wet cloths...   | 111 |
| Figure 71 Types of anchorage: (a) extension of the fibers of the SRG strip inserted into the masonry block at the free end; (b) separate spike at the loaded end (second top layer of bricks); and (c) separate spike at the free end (second bottom layer of bricks).....  | 111 |
| Figure 72 Preparation of A1 specimens: (a) masonry block with of the hole; (b) Insertion of steel fibers into the hole; (c) application of the first layer of mortar (d) finished masonry block with SRG strip .....  | 112 |
| Figure 73 Preparation of the spike: (a) bending fibers; (b) bundled anchor spike .....  | 113 |
| Figure 74 Preparation of A3 specimens: (a) realization of the hole; (b) fibers covered with mortar; (c) anchor spike open radially in the front face; (d) spike fibers interweaved with the longitudinal fibers of the SRG strip (e) application of first layer of mortar .....   | 114 |
| Figure 75 (a) Concrete prisms configuration; (b) prims with the hole .....  | 115 |
| Figure 76 (a) Steel fibers inserted into the hole filled with fluid mortar; (c) application of the second layer of SRG mortar matrix .....  | 115 |
| Figure 77 Single-lap direct shear test set-up: (a) sketch of the test set-up, front view and (b) top view; photo of (c) masonry and (d) concrete set-up .....   | 116 |
| Figure 78 Test set-up for A2 specimens .....  | 117 |
| Figure 79 Failure modes of representative specimens: (a) interlaminar failure with debonding at the interface between the internal layer of mortar and steel fibers (MF); (b) partial interlaminar failure at the interface between the internal layer of mortar and steel fibers (MF*); (c) rupture of fibers (FR); (d) detachment of the SRG strip from the substrate with a thin layer of masonry attached to it (SF)..... | 118 |
| Figure 80 Example of failure modes for a) A1 b) A2 and c) A3 specimens .....  | 119 |

|   |     |
|---|-----|
| Figure 81 Definition of $g_1$ and $g_2$ , $P_{crit}$ and $P^*$ .....  | 121 |
| Figure 82 Load responses of SRG-masonry joints with matrix width equal to (a) 50 mm [162]; (b) 70 mm; and (c) 90 mm .....   | 122 |
| Figure 83 Comparison of load responses of SRG-masonry joints strengthened with two types of matrix.....   | 123 |
| Figure 84 Comparison of load response of SRG-masonry joints tested with two test rates.....   | 124 |
| Figure 85 (a) Photo of failure mode due to the rupture of steel fibers and (b) Load response of SRG-concrete joints [162] .....   | 125 |
| Figure 86 Load responses of (a) A1 (b) A2 and (c) A3 specimens .....  | 126 |
| Figure 87 Concrete prism with anchorage: (a) failure mode and (b) load-slip responses .....   | 128 |
| Figure 88 Concrete prism without anchorage: (a) failure mode and (b) load-slip responses [162] .....  | 129 |
| Figure 89 (a) Sketch of pull-out specimen; (b) masonry blocks with fiber sheets cut along the principal direction; (c) 7-mm epoxy tab .....   | 130 |
| Figure 90 (a) Pull-out test set-up; (b) application of torque and (c) position of LVDTs.....  | 130 |
| Figure 91 (a) Failure mode; (b) load responses .....  | 132 |
| Figure 92 (a) Example of a typical CML for FRCM composites; (b) load-slip response associated to the typical CML [182].....   | 135 |
| Figure 93 Experimental P-g responses with the average P-g curve for (a) A1 masonry blocks; (b) A3 masonry blocks and (c) A4 concrete prisms .....   | 137 |
| Figure 94 (a) Comparison between CMLs obtained from the calibration method of load-responses of A1 and A3 masonry blocks; (b) comparison between experimental and analytical P-g response ..... | 138 |
| Figure 95 (a) average curve of pull out tes; (b) comparison between experimental and analytical curves.....   | 139 |

## List of Tables

|  |     |
|--|-----|
| Table 1 Casting groups and casting time.....   | 28  |
| Table 2 Chemical composition of the fly ash.....   | 31  |
| Table 3 Mix design.....  | 33  |
| Table 4 Physical and mechanical properties at 28 days (flexural strength is the average of 2 measurements, thus CoV is not reported).....  | 34  |
| Table 5 Physical and mechanical properties at 300 days (flexural strength is the average of 2 measurements, thus CoV is not reported)..... | 34  |
| Table 6 Mechanical properties of bricks .....  | 36  |
| Table 7 Mechanical properties of fired-clay bricks and tuff units.....   | 37  |
| Table 8 Results of compression tests in terms of maximum load $W$ and compressive strength $C$   | 40  |
| Table 9 Results of splitting tensile tests in terms of maximum load $P$ , splitting tensile strength $\sigma_t$ .....                      | 41  |
| Table 10 Elastic modulus .....   | 41  |
| Table 11 Physical and mechanical properties of steel fibers (provided by the manufacturer [91])  | 43  |
| Table 12 Mechanical properties of Matrix 1 and Matrix 2.....   | 44  |
| Table 13 Specimen dimensions (depth, width, length, notch and CoV), weight and peak load ...   | 58  |
| Table 14 Specimen dimensions (depth, width, length and CoV), span, weight, notch length and peak load [147] [146] .....                    | 62  |
| Table 15 Comparison between fracture energy of concrete beams evaluated obtained from LVDTs and DIC .....                                  | 74  |
| Table 16 Comparison between fracture energy of alkali activated mortars obtained from LVDTs and DIC .....                                  | 76  |
| Table 17 Comparison of $G_F$ values of quasi-brittle materials.....  | 80  |
| Table 18 Indirect determination of the elastic modulus from the $P - \delta$ and $P - \text{CMOD}$ responses .....                         | 83  |
| Table 19 Evaluation of $\beta$ coefficients.....   | 107 |
| Table 20 Experimental results in terms of $g_1$ and $g_2$ , $P_{\text{crit}}$ , $P^*$ , and failure mode .....                             | 119 |
| Table 21 Test results of SRG-concrete joints [148] .....   | 125 |
| Table 22 Single-lap direct shear test results for concrete prisms .....  | 128 |
| Table 23 Pull-out test results .....   | 131 |
| Table 24 Fracture parameters obtained from the indirect calibration method.....  | 138 |

## Abstract

The objective of this thesis is the investigation of the Mode-I fracture mechanics parameters of quasi-brittle materials to shed light onto the influence of the width and size of the specimen on the fracture response of notched beams. To further the knowledge on the fracture process, 3D digital image correlation (DIC) was employed. A new method is proposed to determine experimentally the critical value of the crack opening, which is then used to determine the size of the fracture process zone (FPZ). In addition, the Mode-I fracture mechanics parameters are compared with the Mode-II interfacial properties of composites materials that feature as matrices the quasi-brittle materials studied in Mode-I conditions. To investigate the Mode II fracture parameters, single-lap direct shear tests are performed. Notched concrete beams with six cross-sections has been tested using a three-point bending (TPB) test set-up (Mode-I fracture mechanics). Two depths and three widths of the beam are considered. In addition to concrete beams, alkali-activated mortar beams (AAMs) that differ by the type and size of the aggregates have been tested using the same TPB set-up. Two dimensions of AAMs are considered. The load-deflection response obtained from DIC is compared with the load-deflection response obtained from the readings of two linear variable displacement transformers (LVDT). Load responses, peak loads, strain profiles along the ligament from DIC, fracture energy and failure modes of TPB tests are discussed. The Mode-II problem is investigated by testing steel reinforced grout (SRG) composites bonded to masonry and concrete elements under single-lap direct shear tests. Two types of anchorage systems are proposed for SRG reinforced masonry and concrete element to study their effectiveness. An indirect method is proposed to find the interfacial properties, compare them with the Mode-I fracture properties of the matrix and to model the effect of the anchorage.

# 1 Chapter 1 – Introduction

Fracture of concrete is an important topic for the design and durability of concrete structures. There are several studies in literature that focus on the fracture process in concrete. Various methods were presented to study concrete fracture process, such as acoustic emissions (AE), scanning electron microscopy, dye penetration, moiré interferometry, and several parameters were investigated, such as fracture toughness ( $K_{IC}$ ) to express the material's resistance to brittle fracture when the crack is present, fracture energy ( $G_F$ ), usually determined with the concept of work of fracture, size of the fracture process zone (FPZ) and crack opening ( $w_c$ ) [1] [2] [3].

More recently, fracture parameters were investigated using digital image correlation technique (DIC). DIC is an optical technique that compares the images taken with a chosen frequency during the test with a reference image taken prior to starting the test. The tracking of the pixels between an image and the reference allows to obtain the displacement field on the surface. If two cameras are used, the out of plane displacement can be measured as well.

One of the main advantages using DIC is the possibility to monitor the whole fracture process. Some authors used DIC to determine qualitatively the displacement field and the strain on the specimen's surface [4]. Shah et al performed three-point bending tests and monitored the fracture process using digital image analysis [5]. The authors plotted the displacement perpendicular to the crack ligament and defined the crack tip by looking at the jump in the displacement along the ligament. Wu et al [6] determined the crack opening along the ligament to determine the FPZ, and used the critical value of the opening  $w_c$  from Petersson [7] to identify the size of the FPZ. They assumed that if the crack tip opening was equal to  $w_c$ , then the entire portion of the ligament where DIC measured a jump in the horizontal displacement, corresponded to the FPZ. Graziani et al. [8] used DIC to identify the crack location, the crack length and to determine the stress intensity factor and draw the  $R$ -curve of clay bricks. The work of Graziani et al. confirmed the potential of this technique to identify fracture parameters of cohesive materials.

In addition, some authors combined DIC with other techniques: Alam et al. investigated the growth of the fracture zone combining DIC and acoustic emissions (AE), to record in real time the damage evolution during the test [1]. With both techniques, the author obtained continuous real time data acquisition, to identify fracture parameters and the fracture process zone. AE technique was employed to locate microcracks. This technique was already employed to determine the influence of fracture parameters such as porosity, aggregates, load type and specimen's geometry on the fracture process zone based on statistical analysis. On the other hand, digital image analysis was employed to measure the displacement field on the surface of the specimen. With these two methods, the author monitored the fracture growth in concrete specimens during three-point bending tests. Even if the authors were able to capture useful information combining the two

methods, they observed that DIC was more helpful to measure the crack length, while they faced a loss of information with the criterion used for AE.

Even though many studies focused on this topic, the development of the FPZ and the critical value of the crack opening ( $w_c$ ) in quasi-brittle materials is still an open issue. All the aforementioned methods were employed to study the fracture process zone but it is still difficult to detect whether the fracture process zone was fully developed or not.

One important aspect to consider when using DIC and that it is not usually taken into account, is the importance of considering a suitable combination of subset and step, while post processing DIC data. In this work, different combinations of subset and step were considered to understand the most appropriate to be used for the analysis. In fact, using a non-appropriate combination of subset and step, means losing useful information during the analysis, thus obtaining non-accurate solutions.

The majority of studies focused on fracture behavior of concrete, being concrete the most used building material worldwide whose consumption is constantly increasing due to its increasing request from developing countries. Conversely, fracture mechanics of AAMs is not extensively studied yet. Investigating the suitability of AAMs for civil engineering applications also means investigating their fracture properties, since as ordinary portland cement (OPC) materials, AAMs are quasi-brittle in nature. In the present work, the same approach employed for concrete and presented in the next chapters was applied to alkali-activated mortars (AAMs). AAMs can be considered an emerging technology, alternative to OPC that have some advantages as lower CO<sub>2</sub> emissions, resistance to chemical attack by chloride, various acids, alkali and sulphate, resistance to high temperatures with no spalling phenomena. Thus, understanding the fracture properties of AAMs is a topic of great interest, and is not extensively studied yet in the literature.

In this work, three-point bending tests were performed to study the fracture process of quasi-brittle materials. A new method was proposed to determine experimentally the critical value of the crack opening  $w_c$  using DIC, which was then used to determine the size of the fracture process zone. Without the expedient of digital analysis, values of  $w_c$  for Mode I fracture are available in the literature but they cannot be directly confirmed for a specific type of material.

In addition to Mode I fracture parameters, Mode II fracture parameters were investigated. Although DIC is needed to evaluate the critical value of the crack opening of Mode I, the same technique cannot be employed to evaluate the slip at the free end of Mode II. The reason why DIC was not used when fiber reinforced cementitious matrix (FRCM) composites were bonded to structural elements, is because the slip typically occurred inside the matrix of the composite, and therefore DIC was not able to acquire useful data to evaluate fracture parameters. In this work, steel reinforced grout (SRG) composites, made of steel fibers embedded in a mortar matrix, were bonded to concrete and masonry elements and tested using single-lap direct shear test. The load versus loaded slip, called global slip, was obtained. The interfacial parameters were determined from the

load response by applying an indirect calibration method. Results of single-lap direct shear tests on masonry blocks strengthened with SRGs were discussed to analyze the bond behavior between the composite material and the substrate. Several parameters were considered: the change in the width of the SRG mortar matrix while keeping the width of the fiber sheet fixed, the type of mortar used for the SRG, the influence of the test rate and the type of substrate (i.e. concrete vs masonry). Since one of the most observed failure mode when SRGs were bonded to masonry and concrete elements was premature debonding, the present work gives a hint on the study of a possible solution with an anchorage system. Two types of anchorage were considered when SRGs are bonded to masonry substrate: an extension of the SRG fibers into the masonry block obtained by bending the fibers and inserting them into a hole filled with a mortar, and a separate anchor spike that interacts with the bonded strip. In addition to masonry blocks, concrete prisms strengthened with the same SRG system with the extension of the SRG fibers inclined  $45^\circ$  into the concrete prism, were tested for comparison, using the same test set-up.

## **1.1 Fracture mechanics: a general overview**

The tensile strength is an important property of concrete that allows to distinguish concrete from other materials, for example sand. Without the tensile strength, the possibility of using concrete beams, slabs, columns and other elements for structural purposes would vanish. The tensile strength is not the only essential property of concrete, in fact, tensile fracture behavior and in particular the fracture toughness play an important role. If concrete were a perfectly brittle material, when a small crack or flaw occurs in a region with tensile stresses, then a running crack would form, which could lead to a catastrophic failure [3]. In many cases, the safety of a structure depends on the toughness of concrete, even though it has never been considered in the design, due to the lack of knowledge and methods. In relatively recent years, researchers [3] [7] have found some methods to evaluate the influence of the fracture toughness on the fracture behavior of concrete. One way to determine the fracture toughness is by means of the fracture energy, which is the total amount of energy absorbed in a tensile test to failure. For many materials, such as concrete, metals and rocks, the failure is linked to the growth of a crack. The science that studies this phenomenon is known as fracture mechanics. Fracture mechanics is mainly based on linear elastic principles however, some techniques take into account for the energy absorption, plasticity and other phenomena that occur near the tip of a crack. There are still some issues that need to be clarified: the size of the fracture process zone is not small with respect to the size of the structure, the stresses within the fracture process zone are assumed to remain constant or increase, conventional fracture mechanics only deals with the behavior of the element with an existing crack. Therefore, conventional fracture mechanics is not suitable to analyze the influence of the fracture toughness on the fracture behavior of concrete.

### 1.1.1 Linear elastic fracture mechanics (LEFM)

The fundamental basis of the modern fracture theory comes from Griffith [9]. Over the last 80 years, many studies were conducted on fracture mechanics and the work of Griffith has been expanded for new applications and a wide variety of problems. Two main approaches were used: the strain energy release rate, from the global energy balance of Griffith, and the stress intensity factor. The main assumption considered is the linear elastic behavior of material, and therefore describing the material behavior as linear elastic fracture mechanics (LEFM). In LEFM it is assumed that the fracture process happens near the crack tip. Three fracture modes can be distinguished [10] (Figure 1):

- Opening mode (Mode I);
- Planar shear mode (Mode II);
- Antiplane shear mode (Mode III).

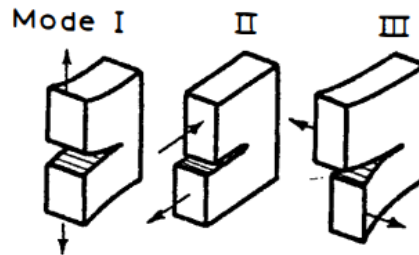


Figure 1 Fracture modes [10]

The first two modes are planar symmetric and antisymmetric, while Mode III is a three-dimension mode. In general, fracture is a linear combination of the three modes [10], but it is possible to study them separately.

However, for the majority of structural materials, the basic assumption of LEFM that states that all the available strain energy is needed to propagate the crack, is not appropriate. In fact, there are many microstructural complex mechanisms, which are presented in the following paragraphs that can dissipate strain energy. These mechanisms, known as toughening mechanisms, can affect the measure of the fracture energy. When their effects are small, LEFM can be still considered, but if they are large, nonlinearities have to be considered in the model.

### 1.1.2 Nonlinear fracture mechanics

LEFM theory assumed a sharp tip, and the elastic solution predict infinite stresses at the crack tip. In reality, damage prevent this to occur. The concept of a damage zone, known as fracture process zone (FPZ), was introduced to overcome the problem of inapplicability of LEFM to quasi-brittle materials. The FPZ can be seen as a bridging zone between the cracked and uncracked regions, where softening occurs. The FPZ depends on the material and it is usually coincident with the size

of the region of nonlinearities [11]. As long as the dimension of the damage zone is small, LEFM can be applied. As mentioned above, when this region is large, nonlinear model has to be considered. Therefore, it is important to evaluate the size of the damage zone to understand which model has to be considered for the evaluation of fracture parameters.

### 1.1.3 Cohesive crack model

Two models can be used to describe the FPZ: in the first model, the FPZ is considered smeared over a band located in front of the notch tip of the crack. The second model, introduced by Barenblatt in 1962 [12], is characterized in the form of stress-displacement law with softening, and it considers the FPZ as lumped into the crack line. The latter is called cohesive or fictitious crack model: a fictitious crack is considered that is able to transfer stresses from one face of the crack to the other. A similar approach was used by Hillerborg et al. in 1976 to model the effects of the fracture process zone in concrete [13]. In fact, in order to account for microcracking and bridging, a fictitious crack is proposed, which means that the real crack is replaced by an equivalent crack that contains stresses at the tip.

Hillerborg started from a uniaxial tension test (Figure 2) and described the tensile behavior as follows: the load increases almost linearly up to the peak, with an increase in the deformation. A single crack is expected to form, where the maximum principal stress reaches the tensile strength of concrete, and it is assumed almost perpendicular to the specimen's axis, due to the heterogeneity of concrete. Then, the load decreases, while the deformation continues to increase. It should be noted that the permanent deformation in the bulk of the specimen is small at failure and it is assumed that the increase in the deformation will concentrate in the crack after the peak. The bulk is assumed to behave as isotropic linear elastic materials. Another comment should be made on the evolution of crack.

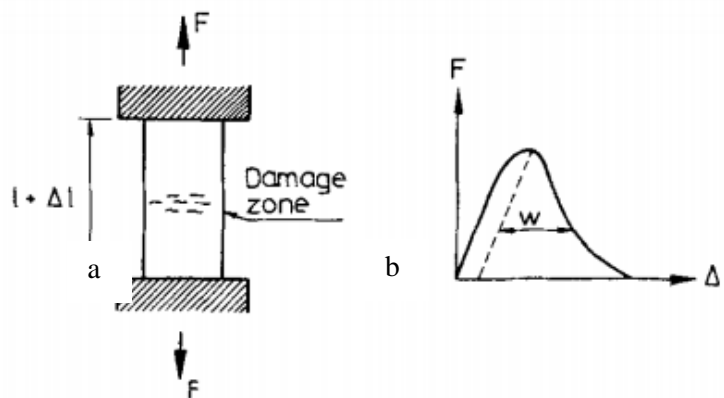


Figure 2 Uniaxial tension test: (a) test set-up, (b) load-elongation response [3]

Tensile tests showed that after the peak, the response exhibits a post peak region. Experimental results from Heilmann, Hilsdorf and Finestervalder in 1969 showed that near the peak, the strain

measured by strain gauges that were far from the crack rapidly decreased, while the strain measured by the gauges placed near the crack that was about to open increased.

Therefore, Hillerborg described the stress-deformation properties of concrete using two curves: up to the peak, the load increases and the strain is distributed over the entire specimen. At the peak, a cohesive crack forms and after the peak it opens by an amount  $w$ . Therefore, the first curve is the stress-deformation for the whole volume (Figure 3a), and the second curve is the stress-opening for the deformation within the damage zone (Figure 3b).

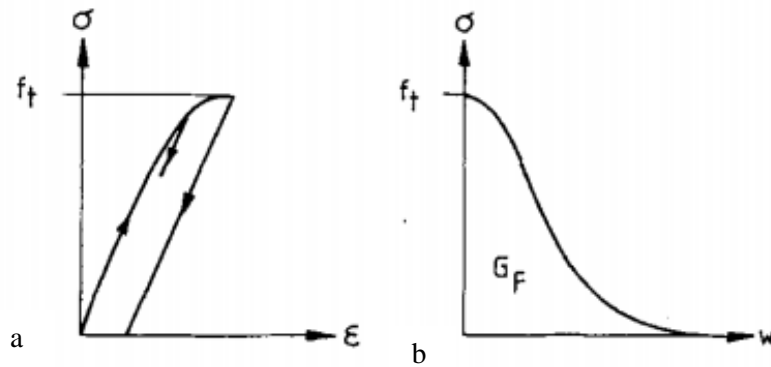


Figure 3 Tensile behavior of concrete: (a) stress-deformation curve for the whole volume; (b) stress-opening curve for the damage zone [3]

The model proposed by Hillerborg, can be represented as follows (considering the inelastic behavior of material):

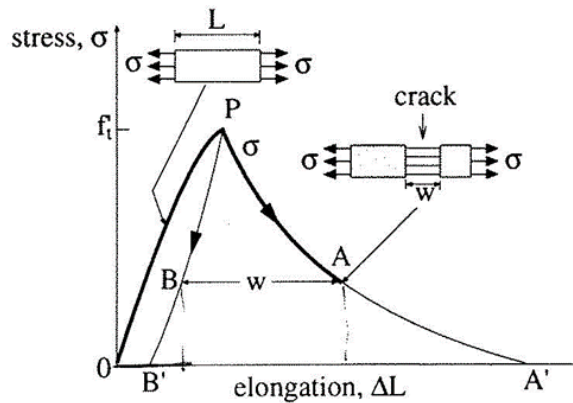


Figure 4 Tensile behavior of concrete [14]

The total elongation at point A is:

$$\Delta L = L\epsilon_b + w \quad (1)$$

Where  $\epsilon_b$  is the deformation of the portion of specimen that does not contain the crack.

Once the crack has formed, the stress is transferred through the faces of the cohesive crack, and it can be evaluated as a function of  $w$ :

$$\sigma = f(w) \quad (2)$$

Where  $f$  is the softening function, and it is a material property. When  $w = 0, f = f'_t$ , where  $f'_t$  is the tensile strength of concrete.

In nearly all materials, there are microstructural mechanisms around the crack tip that are responsible for the fracture process, and those mechanisms are capable of dissipating energy:

- Microcracking: in concrete it is usually caused by the presence of weak interfaces between the cement matrix and the aggregate. Microcracks have random orientation and they tend to be near the tip of the existing crack;
- Bridging: it occurs with the presence of a grain or aggregate. When the crack advances beyond an aggregate, it continues to transmit stresses until it ruptures or it is pulled out;
- Inclusions: it occurs when a crack tip hits an inclusion (a grain in metals or rock, or an aggregate in concrete) and the crack tends to deflect around the object;
- Interlocking: if the path of crack is tortuous, the crack surfaces might be in contact, and this cause energy dissipation through friction;
- Presence of voids: the tip of a crack can terminate by internal voids, and therefore additional energy is required to propagate the crack with a new tip;
- Crack branching: due to heterogeneity of concrete, the crack may propagate through several branches, which require more energy.

All these mechanisms can affect fracture behavior to varying degree. If the effects are small, LFM can be usually applied, while when they are large, nonlinearities must be taken into account.

#### **1.1.4 Softening curve**

The softening curve  $\sigma = f(w)$  is the main constituent of the cohesive crack model. It is a characteristic of material, and therefore it is not possible to describe a unique curve, since it might depend on the mix design. Petersson in 1981 [7] showed that curves are similar for ordinary concrete, even if the mix design is different (Figure 5). The actual softening curve might be difficult to use for computational aims. Therefore, there are several shape of the softening curve used in literature, and the simplest form is the rectangular one (Figure 6). However, the rectangular shape might overestimate the prediction of the strength in a normal-sized specimen. The second simple curve is the linear one, and it was proposed by Hillerborg in 1976, but predictions made with this

curve were not realistic.

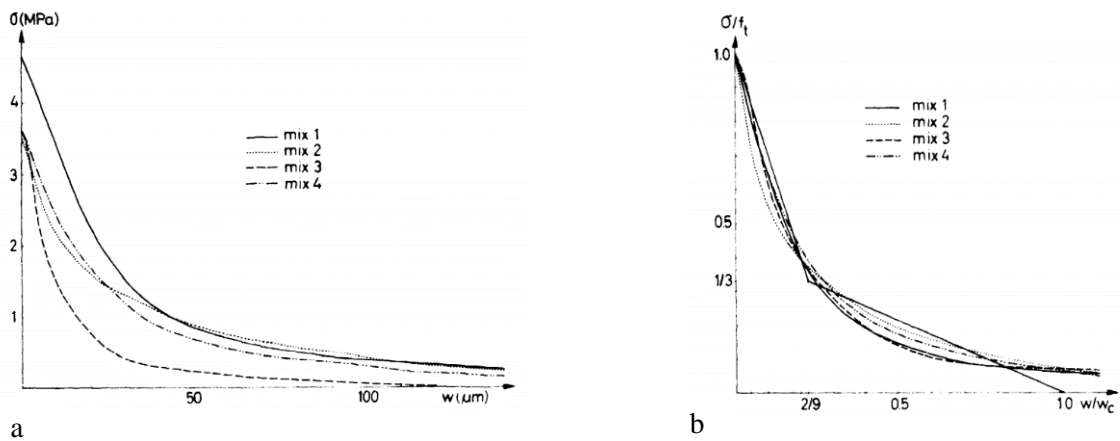


Figure 5 (a) Stress-opening curves for 4 types of concrete; (b)  $\sigma_i/f_t$  as a function of  $w/w_c$  [7]

The most popular shape for concrete, which can fairly describes the softening behavior of concrete, is the bilinear curve proposed by Petersson in 1981 [7] (Figure 6), even if there is no agreement on the kink point.

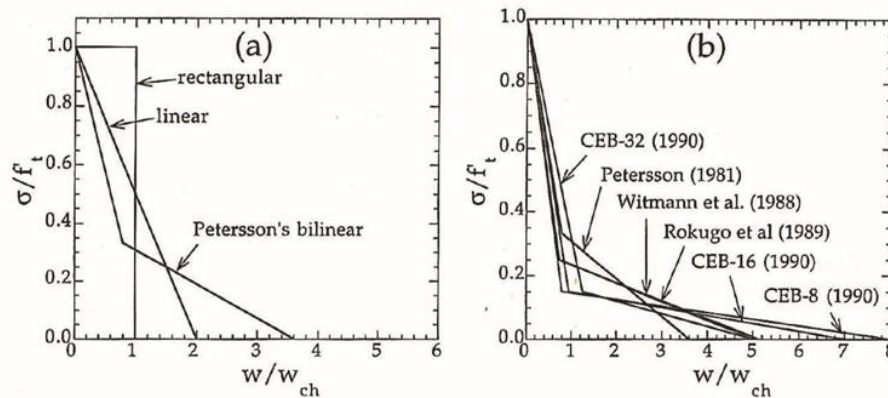


Figure 6 Possible shapes for the softening curve [7]

It was observed that in some cases the softening curve showed a long tail, and a curve that captured this behavior was proposed by Planas in 1992 [15] .

#### 1.1.4.1 Determination of the softening curve and fracture parameters

Notched beams have been used to determine experimentally the parameters of the softening curve. This expedient was adopted to overcome the problems related to the tensile test, such as the difficulty to grip and test a concrete tensile test specimen, the randomness location of the crack and the presence of more than one crack. Therefore, three-point bending (TPB) tests on notched beams are performed. With three-point bending test, it is also possible to determine the fracture energy  $G_F$ , which is the energy absorbed within the damage zone. The fracture energy is determined using the work of fracture introduced by Hillerborg [3], and it will be described later. This method provide

results that are size and width dependent [16]. Some researchers argue that some aspects of the experimental procedure are not correct [17]. Even after careful examination of the procedure, it was observed that the fracture energy is not a material property, since it is not constant when different sizes are considered. The concept of  $G_F$  can be used to evaluate the fracture toughness of materials. In order to evaluate the fracture energy, some considerations can be made: the test has to run in quasi-static condition, and some spurious work contributions or dissipations have to be taken into account (friction, self-weight, hysteretic behavior of the loading system, crushing at the support, energy dissipation in the bulk of the specimen near the crack).

### 1.1.5 Background on the size effect

One of the most argued topic of fracture mechanics is the size effect. The size effect states that if different sizes of specimens but geometrically similar are considered, then the specimens failed at different levels. In this scenario, the maximum stress level at failure decreases if the size of the specimen increases. On the other hand, the classic approach based on the strength of materials, states that if the size of the beam doubles, then the applied load to failure doubles (Figure 7).

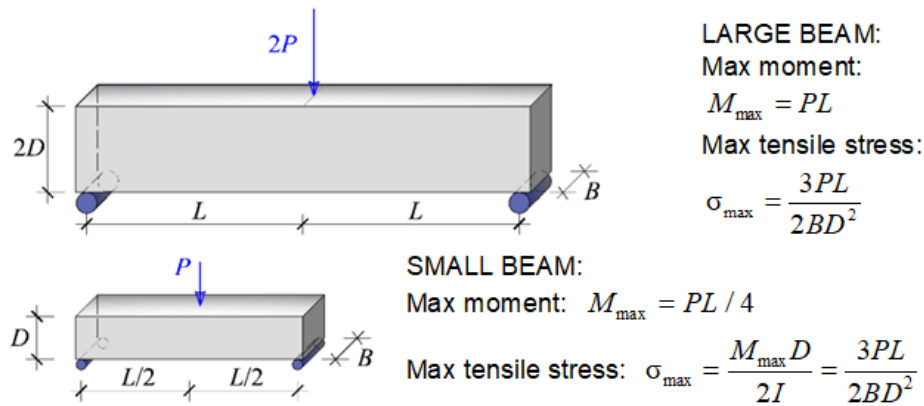


Figure 7 Comparison between maximum tensile stress for small and large specimen predicted by the Strength of Materials (courtesy of Dr. Carloni)

The size effect can be studied by means of fracture mechanics. Figure 8 explains the size effect through a logarithmic plot of the depth of the specimens versus the nominal strength  $\sigma_N$  (i.e. the nominal stress at maximum load) calculated as follows:

$$\sigma_N = \frac{P}{BD} \quad (3)$$

Where  $P$  is the applied load,  $B$  is the specimen width and  $D$  is the depth of the specimen.

When LEFM is applied, the size effect is predicted to follow the trend identified with the dashed line of slope  $-1/2$  [10], as shown in Figure 8.

To prove this, the stress intensity factor (SIF) can be used.

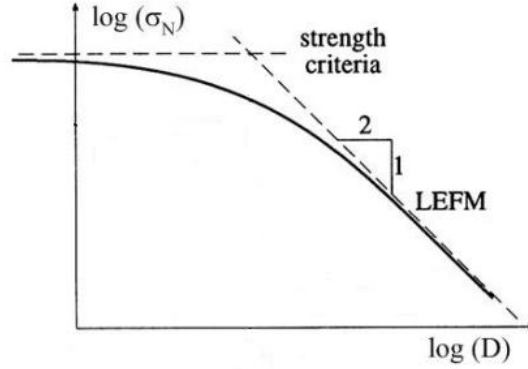


Figure 8 Logarithmic plot of  $\sigma_N$  versus  $D$  [18]

Focusing on Mode I fracture mechanics, the SIF can be written as:

$$K_I = \sigma_N \sqrt{D} k(\alpha) \quad (4)$$

Where  $K_I$  is the SIF,  $\sigma_N$  is defined in equation 3,  $\alpha = a/D$  with  $a$  the notch length,  $k(\alpha)$  depends on the geometry of the specimen. If two sizes are considered, with a depth equal to  $D_1$  and  $D_2$ , respectively, then the ratio of the two stresses failure is related through the following formula:

$$\frac{\sigma_{Nu,1}}{\sigma_{Nu,2}} = \frac{K_{Ic}}{\sqrt{D_1} k(\alpha)} \frac{\sqrt{D_2} k(\alpha)}{K_{Ic}} = \frac{\sqrt{D_2}}{\sqrt{D_1}} \quad (5)$$

Assuming that  $k(\alpha)$  does not vary with the size of the specimen, and  $K_{Ic}$  is the fracture toughness and it is a material property (if  $K_I$  is equal to  $K_{Ic}$  the crack propagation occurs), and the crack length does not change, then the size effect is proportional to  $D^{-1/2}$ .

The key point is that the strength of a member is not linearly proportional to its size and therefore, it should be very careful when the strength approach is used for design of structures because it can be inappropriate.

The size of a structural element could be relatively large, the nature of the material could be brittle (as concrete and masonry) and there is no a specific study for this concept. Several approaches can be found in literature, although it is not easy to adapt them to the specific case and some of them are contradicting each other. Some questions remain open:

- Is the size effect a general phenomenon or it is observed only for some cases?
- When size effect is observed, is the trend similar for large sizes?
- Is the size effect mitigated by the reinforcement?
- Is the size effect dependent on how similarities between specimens is defined?
- Is it possible to find a mechanics-based approach for the size effect?
- Is the type of curing of specimens important for the size effect?

To answer those questions, it is important to consider the region around the tip of the crack, known as FPZ, in which softening occurs. For quasi-brittle materials, such as concrete, masonry, ceramics, rocks and composites, the FPZ is not negligible and it is well predicted by the Bažant's size effect law [18]. The main idea is that when the FPZ is large compared to the size of the specimen, LEFM might not be appropriate. Therefore, in smaller specimen, the influence of the FPZ is greater, and they have relatively high toughness. If the size of the element increases, the FPZ tends to become smaller compared to the size, and thus larger specimens exhibit a behavior closer to that predicted by LEFM.

## **1.2 Bond characteristics between composites and quasi-brittle substrates**

The use of composite materials for strengthening existing masonry structures is a topic of great interest among civil engineers. Fiber-reinforced polymer (FRP) systems, which belong to the family of composite materials, comprise fibers of different kinds, such as glass, steel, aramid, and carbon impregnated with a polymeric matrix (typically epoxy resin). When FRPs are applied to the tension side of a beam, the composite increase the internal moment capacity of the section [19], and when FRPs are applied to a region subjected to high shear, it contributes to the shear capacity of this section. One of the main reason of the inefficiency of the FRPs applied to quasi-brittle substrates is the debonding of the composite. In fact, being a brittle phenomenon, the debonding can occur without any visible warning.

Although FRPs have been widely used and studied over the past decades to strengthen concrete and masonry structures [20] [21] [22], there are some disadvantages, mainly associated with the use of epoxy matrices, such as poor performance at high temperatures and poor vapor permeability, high costs, inapplicability on wet surfaces, hazardous fumes for workers, and incompatibility with the substrate. Therefore, a new type of composite with the same type of fibers organized in an open-mesh textile embedded in an inorganic matrix, instead of a polymeric matrix, has been recently employed. Due to their advantages, such as compatibility with different types of substrate and high vapor permeability, these new materials, usually referred to as fiber-reinforced cementitious matrix (FRCM) composites [23], are considered an effective system to strengthen historical masonry structures [5]. When a unidirectional textile made of high strength steel fibers is employed, FRCMs are named steel-reinforced grout (SRG). Numerous experimental campaigns were conducted in the last 15 years to investigate the contribution of externally bonded FRCMs and SRGs to the load-carrying capacity of concrete and masonry members. These studies showed an increase in the bending [24] [25] [26], shear [27] [28], and axial capacity [29] of FRCM/SRG-strengthened reinforced concrete (RC) members that are comparable with the counterparts strengthened with FRPs. Analogously, FRCMs and SRGs were proven to be effective to increase the in-plane and

out-of-plane strength of masonry walls [30] [31] [32], axial strength of masonry columns [33] [34], and the load-carrying capacity of masonry arches [35] [36].

The crucial point in strengthening and designing structural elements is the bond behavior between the composite and the substrate [37]. In fact, the bond behavior could compromise the effectiveness of the composite system, since the bond is a mechanism to transfer stresses from the structural element to the composite. There are guidelines that contain sections regarding the strengthening of masonry structures, analyzing the bond behavior between FRPs and masonry [38], and then evaluating the bond strength. Although some considerations made for FRPs are applied to SRGs, it would be better to recalibrate the parameters used in the formulations by means of experimental tests.

### 1.2.1 Experimental investigation of debonding

Shear bond test is widely used to characterize the bond behavior between externally bonded composite and the substrate. The optimal test to investigate the bond behavior between FRP and concrete substrate are the beam tests [11] [39] [40]. However, this set-up is complex, its cost is high and the crack pattern is difficult to predict. Therefore, starting from mid 90s, researchers started to look for another solution to study the stress transfer mechanisms between concrete substrate and FRPs, to understand what happens during the crack propagation and to determine the effective anchor length, which is the bond length beyond which any increase in the length does not increase the load carrying capacity or anchorage strength.

Among different types of set-up [19] [41] [42], the most common are the single-lap and double-lap direct shear set-ups (Figure 9). Chajes et al., Talijssten and Neal et al. are among the first researchers who used single-lap shear test to study the stress transfer mechanisms between FRP and concrete [43] [44] [45].

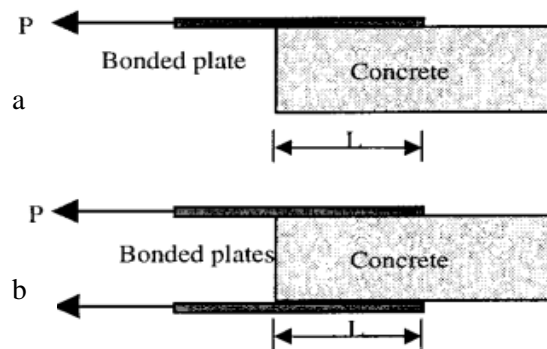


Figure 9 Bond tests: (a) single-lap and (b) double-lap direct shear test set-up [42]

### 1.2.2 Single-lap direct shear test

Single-lap direct shear test that was used to evaluate the bond behavior between FRPs and concrete substrates was adopted also for FRCM composite bonded to masonry and concrete elements. The

classical pull-push configuration was used [46] [47]. The specimen was centered to have the composite strip perfectly aligned with the wedges of the testing machine. The substrate was then blocked against movements at the top and at the bottom by two steel plates, while fibers were pulled out from the free end. The two plates were connected by four steel bars through bolts. The unbonded fibers were left dry, i.e. they were not impregnated with mortar. The free end of fibers was reinforced with metal plates [47] to avoid any premature rupture of fibers inside the gripping area. The load  $P$  was recorded by the load cell, and the relative displacement was recorded by linear variable displacement transformers (LVDTs). One end of the LVDTs was fixed to the substrate, while the other one reacted off of a thin metal plate, which was mounted out of the bonded area, to the bare fibers. Photos of single-lap direct shear test set-up used in this thesis will be shown in section 4.2.

### 1.2.3 Failure modes

When FRPs are bonded to masonry elements, the most frequent failure mode is associated to the debonding of the FRP strip from the substrate, with a thin layer of masonry attached to it [22] [48] [49] [50]. In this scenario, experimental results showed that the fracture process at the FRP-masonry interface depends on the materials and the geometry of the masonry.

When FRCM composites are applied to concrete or masonry elements, failure is usually associated with the debonding, which can occur at different interfaces [51], due to the heterogeneity of inorganic matrices, and therefore several failure modes are observed (Figure 10).

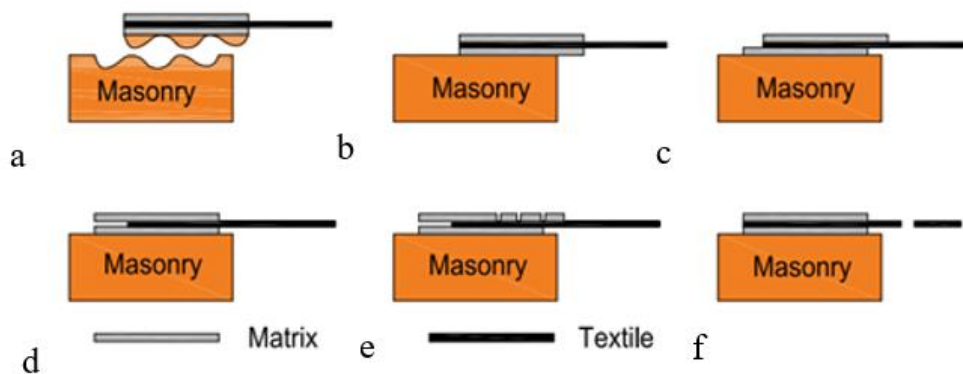


Figure 10 Sketches of failure modes in shear bond test [53]

From single-lap direct shear tests presented in literature, the following modes of failure were observed [46] [47] [52] [53] [54]:

- a) Debonding of the composite strip with cohesive failure of the substrate;
- b) Interlaminar failure at the matrix-substrate interface;
- c) Interlaminar failure at the matrix-fiber interface;

- d) Sliding of fibers within the matrix layers without cracking of the external layer of matrix;
- e) Sliding of fibers within the matrix layers with cracking of the external layer of matrix;
- f) Rupture of fibers outside the bonded region.

#### **1.2.4 Anchorage system**

The introduction of the anchorage system for structures reinforced with composite materials is a recent topic, and it is limited to FRP composite. Even if FRP systems were proved to be very effective for strengthening and repair concrete structures [20] [45], there are still many challenges that could compromise the efficiency of the system. Among these challenges there is the brittle failure of FRP strengthened RC structures, deterioration of FRP mechanical properties in adverse environmental conditions, strength reduction due to the FRP installation process, premature debonding caused by the lack of the bonded length or a proper anchorage system [43] [55] [56] [57] [58]. Therefore, recently, new methods that make use of anchorage systems are proposed.

One of the main function of the anchorage applied to FRP reinforced structural elements is to prevent or delay the process of debonding, which occurs when externally bonded FRP system detaches from RC substrate [59]. In some cases, anchorages are used to avoid a sudden failure, thus providing a ductile failure and to transfer the load in correspondence to the critical locations of the structural members [58]. Some researchers studied and proposed different types of anchorage system for FRP externally bonded to concrete elements [58] [59] [60] [61] [62]. One critical aspect when dealing with anchorages is to properly design them without compromising the efficiency of FRPs: in fact, failure modes associated to local stress concentrations due to the presence of the anchorage can cause the brittle failure of the FRP system.

Studies demonstrated that when a certain length of the FRP system is reached, which is referred in literature as effective bonded length, the majority of the bond stress is transferred to the concrete element. Increasing the bonded length beyond the effective length, does not increase the load transferred between the FRP system and the substrate or it does not prevent a premature debonding [41] [42] [63]. Therefore, to delay or prevent the debonding of FRP from the substrate with greater transferred load, other methods should be proposed, and when premature debonding occurred, it is believed that the addition of a proper anchorage system can be effective.

Several anchorage systems for FRPs bonded to concrete structures have been proposed in literature, and among them the most common are FRP U-jackets, FRP anchors (Figure 11a and b), patch anchors, transverse wrapping (Figure 11c), nailed metal plates, mechanical fastening and mechanical substrate strengthening [62] [64] [65] [66] [67] [68]. Anchor spikes are fibers bundled and then inserted into the concrete substrate with the other end embedded in the mortar matrix. One advantage of the anchor spikes is that the same FRP material used to strengthen the element can be used for the anchor system, and therefore avoiding problems of materials compatibility. Anchor

spikes can be installed orthogonal to ( $90^\circ$  anchors) or in plane with ( $180^\circ$  anchors) the FRP (Figure 11 a and b) [58] [64] [65].

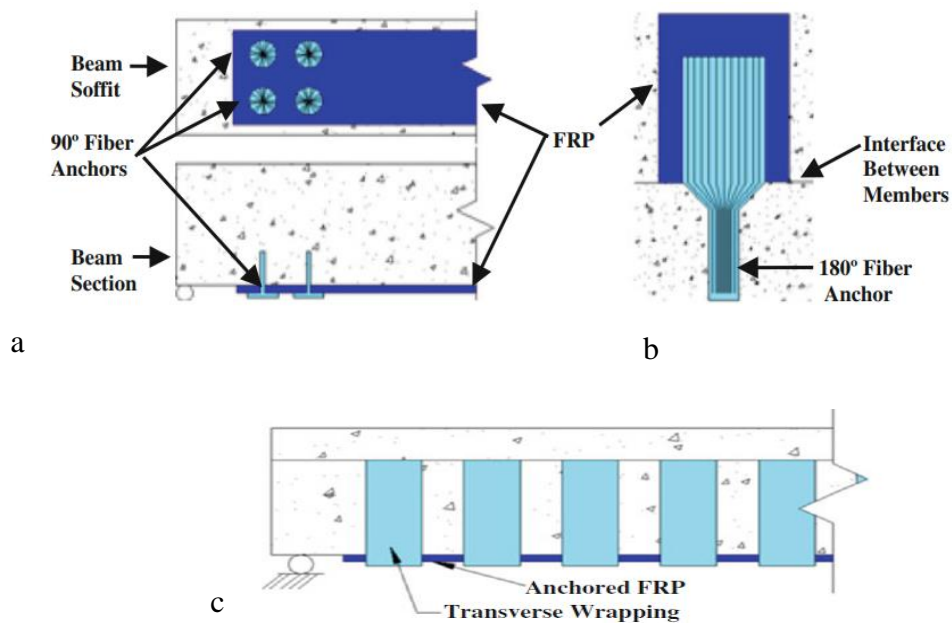


Figure 11 Examples of anchorages: (a)  $90^\circ$  and (b)  $180^\circ$  anchor spike; (c) transverse wrapping anchorage [58]

Results obtained from the experimental tests on anchorages applied to FRP systems demonstrated an increase in the ductility, deformability and strength of the structural element, preventing or delaying the debonding of FRPs from the substrate [58] [62]. However, these solutions were limited to concrete members and to a limited number of FRP-to concrete cases.

There are still a few published guidelines for the design of FRP anchorage system [58] [69]. In ACI 440.2R [69], the performance of FRPs with the addition of transverse wrapping anchorage (Figure 11c) is described, however the other types of anchorage are not taken into account. Therefore, there are not yet specific procedures or suggestions to know which anchorage system is more appropriate for a specific use. While FRP anchorage methods have been studied in the past few years, anchorage behavior of FRCM is not widely understood due to a lack of experimental tests, models and published data.

## 2 Chapter 2 – Materials

This chapter shows, describes and characterizes all the materials that were employed in the present experimental campaign. Several materials were used: two types of concrete (Type 1 and 2), fired-clay masonry bricks, natural stones (tuff and sandstone), alkali-activated mortars, and steel reinforced grout (SRG) composite materials. The methods used to evaluate the mechanical properties of materials are described. For some materials, such as alkali-activated mortars, chemical and physical properties were also evaluated.

### 2.1 Concrete

Two types of concrete were employed, which will be named in the rest of this research, Concrete Type 1 and Concrete Type 2. For Concrete Type 1, one batch was used to cast all the specimens (Figure 12). The mixture proportions by weight of the constituents used were: cement (1.00): water (0.43): coarse aggregate (3.00): fine aggregate (3.00). The maximum aggregate size  $d_{max}$  was 15 mm. Within the same batch of concrete, specimens were cast at different times. Time 0:00 corresponds to the beginning of the casting process (Table 1). Specimens were divided into eight groups based on the time of casting, which means that specimens of the same group were cast at approximately the same time interval. Time of casting is important and therefore reported because the casting protocol might affect the behavior and properties of the specimens. For example, between the beginning and end of a long period of casting, the amount of water might vary, and therefore the properties of fresh concrete could be different. In addition, there could be a difference in the distribution of aggregates if concrete is not properly mixed during casting. Concrete specimens were covered with plastic bags to keep the concrete moist and cured for 28 days.

*Table 1 Casting groups and casting time.*

| Group of casting | Time interval [hours:minutes] |
|------------------|-------------------------------|
| G1               | 0:00 – 0:15                   |
| G2               | 0:15 – 0:30                   |
| G3               | 0:30 – 0:45                   |
| G4               | 0:45 – 1:00                   |
| G5               | 1:00 – 1:15                   |
| G6               | 1:15 – 1:30                   |
| G7               | 1:30 – 1:45                   |
| G8               | 1:45 – 2:00                   |

The compressive strength of concrete was determined according to EN 12390-3 [70] on 150 mm side cubes tested at different ages (7, 14, 21, 28, 56, 84, 112, 117, 150, and 232 days after casting). The average value of density, compressive strength and the corresponding coefficient of variation (CoV) of three cubes is reported in Figure 13 as a function of time.



*Figure 12 (a) Concrete columns; (b) prisms; (c) vibration of concrete; (d) flattening the surface and (e) sandblasting procedure*

Compressive tests were performed also on three 150 mm (diameter)  $\times$  300 mm (length) cylinders at 28 days according to [70], obtaining an average compressive strength,  $f_{cm}$ , equal to 19.8 MPa (CoV 0.003). Two cylinders, instrumented with four 30 mm gauge length strain gauges, were used to determine the elastic modulus of concrete,  $E_c$ , that resulted equal to 19.4 GPa [71]. The tensile splitting strength of concrete,  $f_t$ , was determined according to EN 12390-6 [72] employing 150 mm (diameter)  $\times$  300 mm (length) cylinders at different ages (7, 14, 21, 28, and 232 days after casting). The average value of splitting tensile strength, the corresponding coefficient of variation (CoV) and density of three cylinders for each day of testing is shown in Figure 13b.

It should be noted that the cubes and cylinders used to determine the compressive and tensile splitting strengths at different ages were selected from all the eight groups and included for each age cubes cured under wet cloths and in the lime-saturated bath.

It is interesting to note that no difference was observed among the cubes and cylinders. In addition, even the density of the cubes and cylinders, as reported in Figure 13, appears to be consistent among the groups and the different curing conditions.

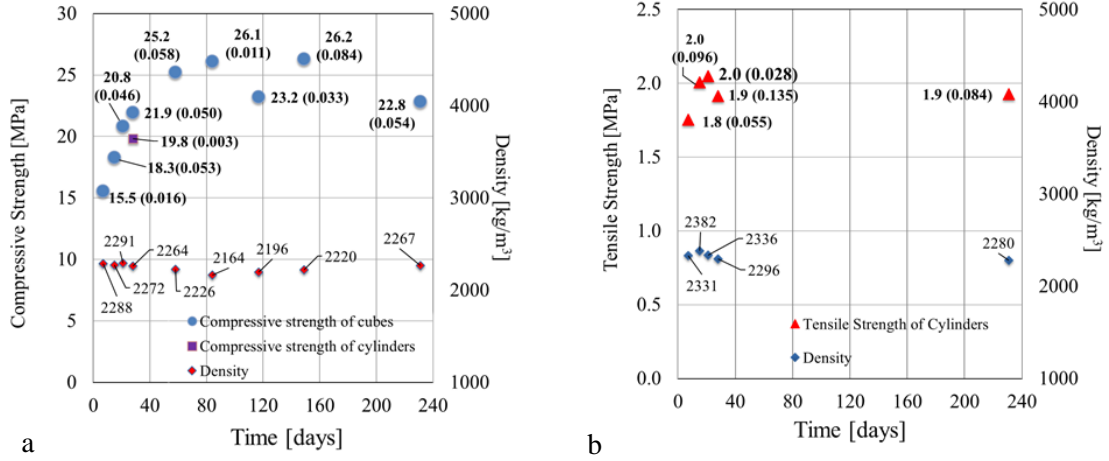


Figure 13 Compressive (a) and tensile (b) strength as a function of time

The behavior of the cubic compressive strength at different ages was fitted using the formula proposed in [73]:

$$R_{cm}(t) = \exp \left\{ s \left[ 1 - \left( \frac{28}{t} \right)^{1/2} \right] \right\} R_{cm} \quad (6)$$

where  $R_{cm}=21.9$  MPa is the mean cubic compressive strength at 28 days obtained from experimental tests, while  $s$  is a parameter defined through a non-linear regression. The coefficient  $s$  was determined to be equal to 0.23, which is slightly lower than the prescriptions suggested in [73].

For the second type of concrete (Concrete Type 2), eight batches were used with the same mixture proportions: cement (1.00): water (0.55): coarse aggregate (2.50): fine aggregate (3.00). The maximum aggregate size was 10 mm. The compressive strength of concrete was determined according to [70] on 150 mm side cubes tested at 28 days from the casting, and the average value resulted equal to 23.7 MPa (CoV=0.073).

## 2.2 Alkali-activated mortars

Coal fly ash (FA), sourced from the Italian coal-fired power station of Torrevadalliga Nord (Rome), was used as precursor for the synthesis. FA was characterized by a low content of calcium and iron oxides, while nearly 80 wt% was constituted of silicon and aluminum oxides (Table 2).

As alkaline activators, 8 M sodium hydroxide (NaOH, supplied by Sigma-Aldrich) and sodium silicate (SiO<sub>2</sub>/Na<sub>2</sub>O ratio = 2.07, supplied by Ingessil Srl, Verona, Italy) solutions were used.

*Table 2 Chemical composition of the fly ash*

| Oxide | SiO <sub>2</sub> | Al <sub>2</sub> O <sub>3</sub> | Fe <sub>2</sub> O <sub>3</sub> | CaO  | TiO <sub>2</sub> | MgO  | K <sub>2</sub> O | SO <sub>3</sub> | Na <sub>2</sub> O | BaO  | Cr <sub>2</sub> O <sub>3</sub> | LOI <sup>1</sup> | IR   |
|-------|------------------|--------------------------------|--------------------------------|------|------------------|------|------------------|-----------------|-------------------|------|--------------------------------|------------------|------|
| (wt%) | 49.37            | 29.23                          | 2.71                           | 6.63 | 1.59             | 1.05 | 0.60             | 0.33            | 0.05              | 0.07 | 0.02                           | 3.28             | 5.07 |

<sup>1</sup>LOI: loss on ignition

<sup>2</sup>IR: insoluble residue

The compositional parameters of the binder, i.e. SiO<sub>2</sub>/Al<sub>2</sub>O<sub>3</sub> and Na<sub>2</sub>O/SiO<sub>2</sub> molar ratios, were kept constant for all mixtures and equal to 3.52 and 0.12, respectively, while the amount and the type of the aggregate were changed. Three different types of aggregates were used (Figure 14):

- fine silica sand (FS) with a fixed grain size distribution according to [74] (maximum aggregate size  $d_{max} = 2$  mm and density  $\rho = 2.64$  g/cm<sup>3</sup>);
- coarse silica sand (CS) ( $d_{max} = 6.0$  mm and  $\rho = 2.68$  g/cm<sup>3</sup>);
- expanded perlite (EP) ( $d_{max} = 2.8$  mm and  $\rho = 0.95$  g/cm<sup>3</sup>).

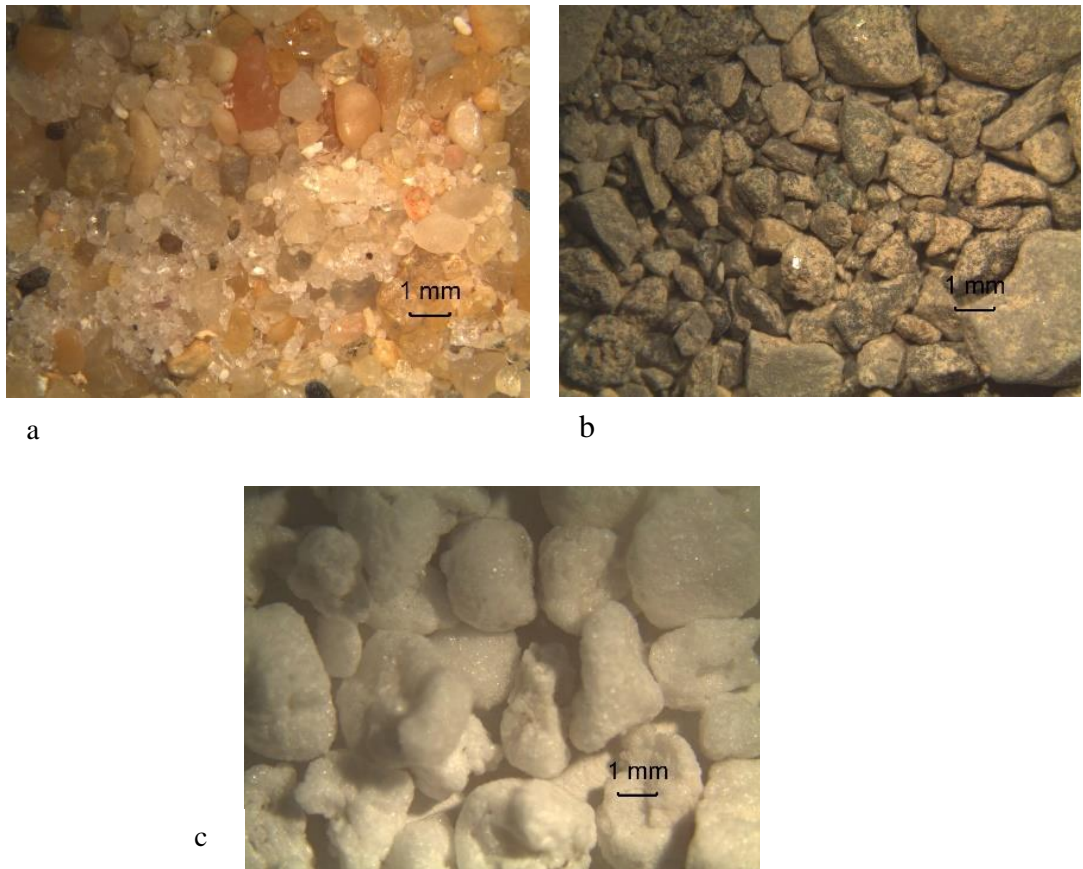


*Figure 14 Optical microscope images of the aggregates used in this work a) fine sand; b) coarse sand; and c) expanded perlite.*

The three aggregates were used in saturated surface dry condition. The particle size distribution of the aggregates is reported in Figure 15.

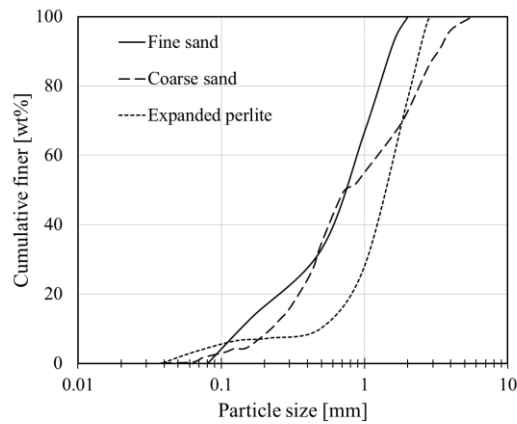


Figure 15 Particle size distribution of the three aggregates used in this study.

Fly ash and the selected aggregate were manually pre-mixed in dry conditions and then poured in the Hobart mixer (capacity: 10 L), where alkaline solutions were added. After mixing for 60 s, water was gradually added and mixed for additional 4 min. The mixer was paused for 60 s and re-started for an additional minute. The slurry was poured into prismatic molds of different sizes (Figure 16) in two layers with approximately the same height (each layer was vibrated on a shaker for 60 s).



Figure 16 Specimens in prismatic molds of different sizes

All molds were sealed in plastic bags and cured at  $T = 21 \pm 2$  °C for 24 h. Specimens were demolded after 24 h and cured in plastic bags (i.e. sealed conditions) at  $T = 21 \pm 2$  °C until testing. The physical–mechanical characterizations were performed at 28 and 300 days, whereas fracture testing of the three mortars was conducted at 300 days. The water content was also adjusted as a function of the aggregate to obtain a workable mixture.

Table 3 presents the formulations of the mortars investigated in this study and the liquid/fly ash (L/FA) weight ratio, where the liquid is calculated as the sum of the alkaline solutions and the water.

*Table 3 Mix design*

| Sample name | Mix design (wt%) |                  |                          |                  |           |             |                  | L/FA |
|-------------|------------------|------------------|--------------------------|------------------|-----------|-------------|------------------|------|
|             | FA               | 8M NaOH solution | Sodium silicate solution | Expanded Perlite | Fine sand | Coarse sand | H <sub>2</sub> O |      |
| FS          | 23.7             | 1.8              | 8.9                      | -                | 64        | -           | 1.1              | 0.52 |
| CS          | 23.7             | 1.8              | 8.9                      | -                | -         | 64          | 1.1              | 0.52 |
| EP          | 52.0             | 4.0              | 19.5                     | 13.0             | -         | -           | 11.2             | 0.67 |

### 2.2.1 Physical and mechanical characterization

Bulk density ( $\rho_{bulk}$ ) was obtained as the dry mass divided by the geometrical volume, whereas water absorption (WA) was calculated as the difference of wet mass and dry mass divided by the dry mass. Both were measured on 40 mm × 40 mm × 20 mm prisms.

Dynamic modulus of elasticity ( $E_d$ ), elastic modulus ( $E$ ), three-point flexural strength ( $R_f$ ), and compressive strength ( $R_c$ ) were determined on 40 mm × 40 mm × 160 mm prisms.  $E_d$  was determined according to [75], using a commercial ultrasonic testing instrument comprised of a pulse generator and two transducers (55 kHz) that were positioned at the two ends of the 160 mm-long prisms. The elastic modulus was calculated according to [71]. Dynamic modulus of elasticity was calculated according to [75]. Flexural and compressive strengths were determined according to [74] by means of a 100 kN Amsler Wolpert testing machine. Flexural and compressive strengths herein reported are the average of two and five measurements, respectively.

The properties of the three mortars after 28 and 300 days of curing in sealed conditions at room temperature are reported in Table 4 and Table 5, respectively.

Among the three mortars, FS exhibited the greatest mechanical properties at 28 days in terms of compressive strength ( $R_c=65.3$  MPa) and elastic modulus ( $E_d=26.7$  MPa and  $E=19.7$  MPa). The increase in the dimension of the aggregate (i.e. CS vs. FS) lead to a decrease of  $R_c$  and  $E$  as well as to a slight increase in WA, which can be correlated to the increase in open porosity of the material. The use of expanded perlite as aggregate allowed for obtaining a lightweight mortar characterized by very low density and high porosity (i.e. WA=30.47% at 28 days). As a result, the EP mortar resulted weaker in terms of mechanical properties when compared with the FS and CS mortars. A significant reduction of the elastic modulus was observed for the EP mortar.

The influence of the curing time on the properties of the mortar can be observed by comparing Table 4 and Table 5.

In all three mortars, an increase in  $\rho_{\text{bulk}}$  was observed, which is consistent with the decrease in WA. An increase of mechanical properties associated with an increase of the curing time was observed for all mortars. Interestingly, curing time resulted beneficial mainly for the CS mortar that increased its compressive strength by 34% while the FS and EP mortars exhibited an increase in compressive strength by 10 and 14%, respectively. The FS mortar resulted the most performing mortar, although the differences between the FS and CS mortars were reduced after 300 days. The elastic modulus computed above at 300 days will be compared with the elastic modulus obtained indirectly from the load – displacement curves in the following Sections.

*Table 4 Physical and mechanical properties at 28 days (flexural strength is the average of 2 measurements, thus CoV is not reported)*

| Mortar | $\rho_{\text{bulk}}$<br>[g/cm <sup>3</sup> ]<br>(CoV) | WA<br>[%]<br>(CoV) | $R_f$<br>[MPa] | $R_c$<br>[MPa]<br>(CoV) | $E_d$<br>[GPa]<br>(CoV) | $E$<br>[GPa]<br>(CoV) |
|--------|---|--------------------|----------------|-------------------------|-------------------------|-----------------------|
| FS     | 2.02<br>(0.005)                                       | 6.55<br>(0.020)    | 10.0           | 65.3<br>(0.018)         | 26.7<br>(0.015)         | 19.7<br>(0.041)       |
| CS     | 2.00<br>(0.005)                                       | 8.05<br>(0.006)    | 9.4            | 47.6<br>(0.059)         | 20.5<br>(0.005)         | 17.8<br>(0.056)       |
| EP     | 1.11<br>(0.036)                                       | 30.47<br>(0.011)   | 3.6            | 14.7<br>(0.034)         | 3.5<br>(0.086)          | 1.2<br>(0.083)        |

*Table 5 Physical and mechanical properties at 300 days (flexural strength is the average of 2 measurements, thus CoV is not reported)*

| Mortar | $\rho_{\text{bulk}}$<br>[g/cm <sup>3</sup> ]<br>(CoV) | WA<br>[%]<br>(CoV) | $R_f$<br>[MPa] | $R_c$<br>[MPa]<br>(CoV) | $E_d$<br>[GPa]<br>(CoV) | $E$<br>[GPa]<br>(CoV) |
|--------|---|--------------------|----------------|-------------------------|-------------------------|-----------------------|
| FS     | 2.11<br>(0.005)                                       | 5.89<br>(0.010)    | 12.3           | 71.7<br>(0.036)         | 25.7<br>(0.012)         | 22.9<br>(0.014)       |
| CS     | 2.11<br>(0.005)                                       | 7.55<br>(0.011)    | 12.1           | 63.7<br>(0.011)         | 26.3<br>(0.010)         | 20.5<br>(0.025)       |
| EP     | 1.26<br>(0.008)                                       | 25.84<br>(0.001)   | 4.2            | 16.6<br>(0.024)         | 5.2<br>(0.025)          | 4.7<br>(0.094)        |

It should be noted that the three-point bending specimens were weighted prior to testing and their weights used to determine the density. The weight is reported in Table 13. The densities are consistent with the values of  $\rho_{\text{bulk}}$  reported in Table 5, which tend to be lower because obtained from dry mass whereas the densities were determined without drying the specimens in the oven.

## 2.3 Masonry

The first type of masonry brick that will be described was provided by a factory in the north of Italy, while the other types of bricks were collected from demolished structures. Two types of tuff, collected from demolished structures are also presented.

### 2.3.1 *Vivo* bricks

The first family of masonry bricks includes commercially available bricks. *Vivo* solid clay bricks were provided by San Marco – Terreal Italia [76], and they are the first exposed bricks with a finish without sand on the surface that is able to reflect light in incomparable way (Figure 17). This is due to the production process, which allows to obtain the single brick from the mold without using sand. Bricks have nominal dimensions of 120 mm (depth)  $\times$  55 mm (height)  $\times$  250 mm (length).



Figure 17 *Vivo* solid clay brick

The compressive strength of the bricks  $f_b$ , determined as the average of thirteen specimens tested in accordance with [77], was 20.3 MPa (CoV= 0.17). Among the thirteen specimens tested in compression, five were used to evaluate the elastic modulus  $E_b$ : specimens were instrumented with two strain gauges, placed 180° apart (Figure 18). The average strain calculated from the measurements of the strain gauges as the slope of the stress-strain curve between 5% and 30% of the peak stress, was used to evaluate  $E_b$ . The average value resulted equal to 7.3 GPa (CoV= 0.29).

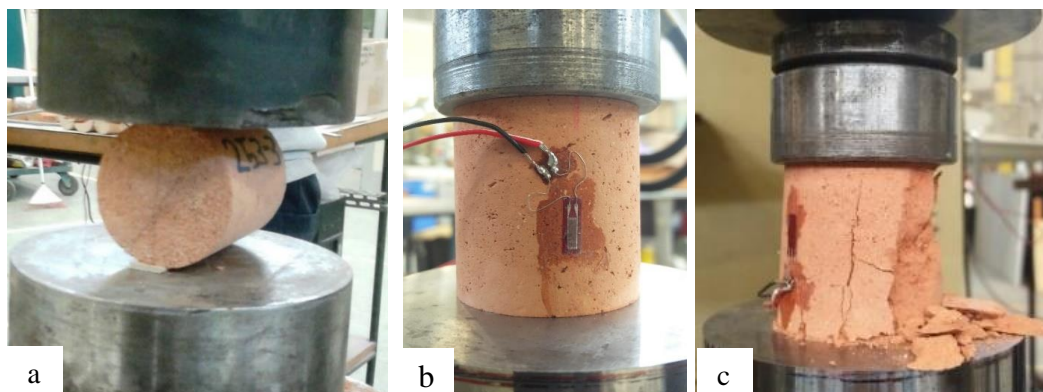


Figure 18 Tests set-up (a) splitting tensile strength test; (b) compression test and (c) compression test failure mode

Tensile strength of bricks was evaluated as the average of seven 50 mm (diameter) × 50 mm (length) cylinders through splitting tensile strength test, according to [72]. The average splitting tensile strength  $f_{bt}$  resulted equal to 3.12 MPa (CoV= 0.12). Mechanical properties are summarized in Table 6:

*Table 6 Mechanical properties of bricks*

| Specimen          | $f_b$<br>(CoV)<br>[MPa] | $f_{bt}$<br>(CoV)<br>[MPa] | $E_b$<br>(CoV)<br>[GPa] |
|-------------------|-------------------------|----------------------------|-------------------------|
| <i>Vivo</i> Brick | 20.3<br>(0.170)         | 3.12<br>(0.120)            | 7.3<br>(0.290)          |

### 2.3.2 Natural stones and fired-clay bricks

The second family of bricks comprised fired-clay bricks and natural stones (Figure 19).

The natural stone consisted of tuff, which is a magmatic rock of pyroclastic origin, i.e. it formed during explosive eruptions by the accumulation of volcanic fragments that were projected onto the earth's surface.

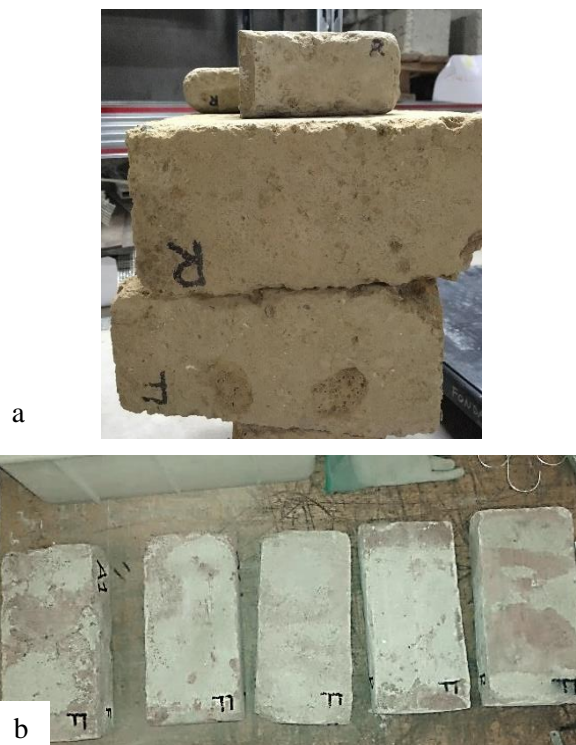


*Figure 19 Example of a) tuff blocks and b) fired-clay bricks collected from demolished structures*

The deposition environment determines the composition, color, microstructure and texture of tuff. In general, these materials are characterized by voids, clasts and other intrusive materials. It is common to find tuff deposits in Italy, in particular in the Alpine regions and in the central-south

regions. Due to its advantages such as its availability, lightweight and workability, tuff was employed for centuries by ancient romans as a construction material. Two typologies of tuff were employed both collected from demolished structures in Rome and Naples (Italy). Fired-clay bricks were collected from demolished structures in Asti, Modena and Pesaro.

Chemical and physical properties of fired-clay bricks and tuff were evaluated for another experimental campaign [78] [79]. Mechanical properties such as the compressive strength  $f_b$ , splitting tensile strength  $f_{bt}$ , and elastic modulus  $E$  of fired-clay bricks and tuff were evaluated (Figure 20).

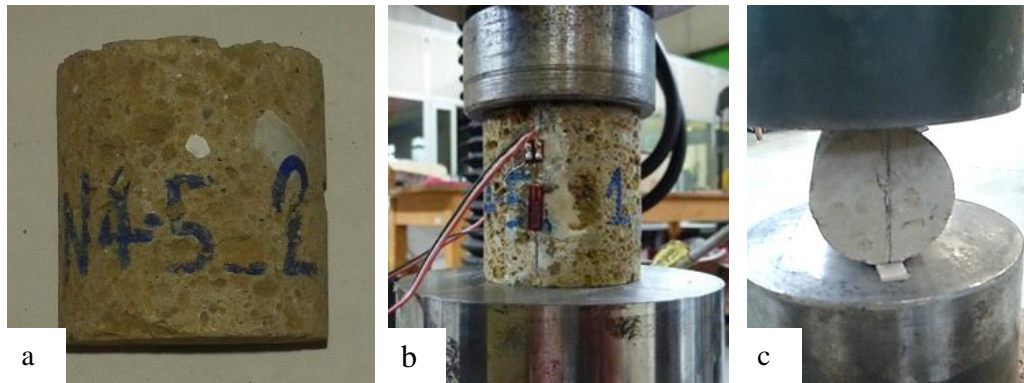


Figure 20 (a) Example of specimen cored from tuff block; (b) compressive strength test and (c) splitting tensile strength test

Four 50 mm (length) × 50 mm (diameter) cylinders cored from bricks and four cylinders cored from tuff blocks were employed to determine the compressive strength according to [80].

Table 7 Mechanical properties of fired-clay bricks and tuff units

| Bricks origin | $f_b$           | $f_{bt}$       | $E$            |
|---------------|-----------------|----------------|----------------|
|               | (CoV)<br>[MPa]  | (CoV)<br>[MPa] | (CoV)<br>[MPa] |
| Asti          | 18.7<br>(0.191) | 3.4<br>(0.118) | 7.4            |
| Modena        | 23.5<br>(0.038) | 3.1<br>(0.116) | 7.1            |
| Pesaro        | 25.7<br>(0.132) | 3.2<br>(0.126) | 6.9            |
| Rome          | 6.3<br>(0.063)  | 1.1<br>(0.158) | 4.3            |
| Naples        | 4.3<br>(0.126)  | 0.7<br>(0.100) | 3.4            |

In addition, three cylinders for each type of brick and tuff were used to determine the splitting tensile strength according to [72]. Four additional cylinders (two cored from bricks and two from tuff) were instrumented with two strain gauges placed at mid-height 180° apart to determine the elastic modulus [77]. Results are summarized in Table 7.

## 2.4 *Tharros* stone

The archeological site in the city of *Tharros* is located in the southernmost of the Sinis peninsula, in the city of Cabras (OR), Sardinia. It was probably founded at the end of the 8<sup>th</sup> century B.C. by Phoenicians. Many tourists visit the site every year. The object of the present research is the Punic necropolis, which corresponds to the blue area in Figure 21.



*Figure 21 Archeological site top view*

Surveys started in 2017. The aim of the project was to evaluate the properties of the materials that constitute the necropolis. Some blocks that were left after the 2017 surveys were brought to the laboratory to evaluate chemical-physical characteristics and mechanical properties.



Figure 22 (a) The archeological site of Tharros; (b) example of a tomb and (c) example of a collected block

The stones collected from the archeological site of *Tharros*, derived from the excavations carried out on the eastern side of the Phoenician-Punic necropolis, in 2017. Five blocks were collected from different parts of the necropolis and named A, B, C, D and E.

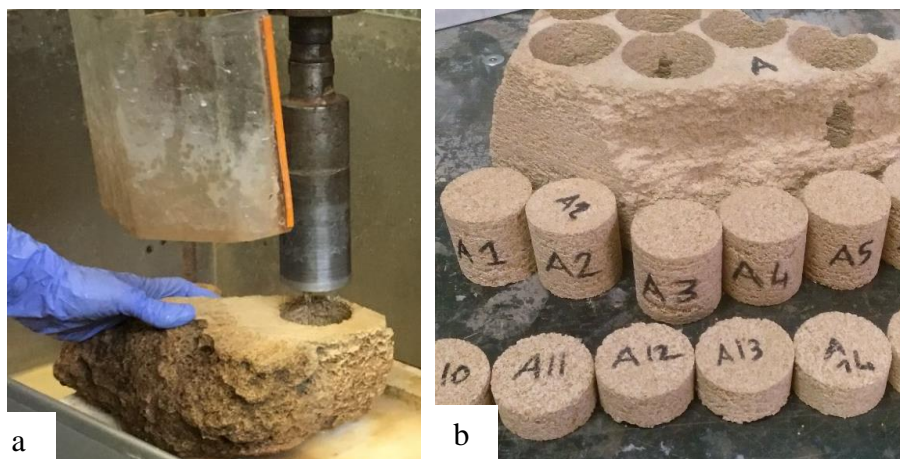


Figure 23 (a) Coring the specimens (b) Group of specimens after the coring operations

From a chemical analysis [81], it was possible to evaluate the composition of the stone, which was mainly made by Calcite ( $\text{CaCO}_3 \approx 85\%$ ) and quartz.

Uniaxial compression tests, splitting tensile strength tests and fracture mechanics tests were performed.

Twelve cylinders of dimensions 50 mm (diameter)  $\times$  50 mm (height) that belonged to different blocks were tested in compression [82] (Figure 24). Splitting tensile strength tests were performed according to [83] on 50 mm (diameter)  $\times$  25 mm (height) cylinders (Figure 24).

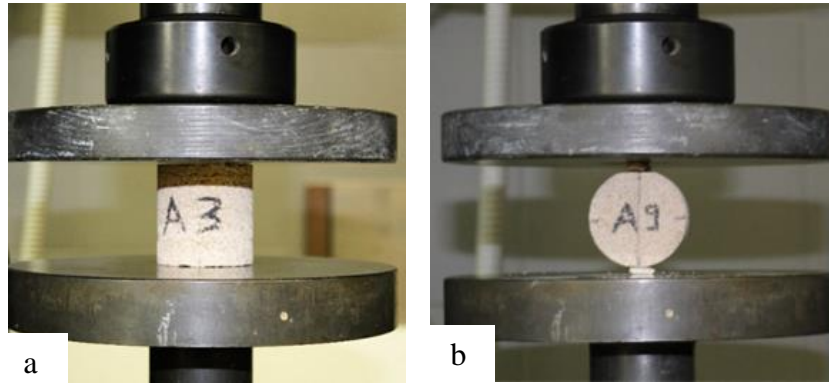


Figure 24 Set-up for (a) compression test and (b) splitting tensile strength test

Elastic modulus  $E_b$  was determined considering five cylinders that were tested under cyclic compression loading, according to [84].

Table 8 Results of compression tests in terms of maximum load  $W$  and compressive strength  $C$

| Specimen | $W$<br>[kN] | $C$<br>[MPa] |
|----------|-------------|--------------|
| A3       | 11.2        | 5.7          |
| A6       | 8.4         | 4.3          |
| B3       | 9.3         | 4.8          |
| B4       | 10.6        | 5.3          |
| B7       | 9.7         | 4.9          |
| C1       | 9.8         | 5.0          |
| C2       | 16.6        | 8.4          |
| C3       | 18.0        | 9.1          |
| D1       | 8.8         | 4.5          |
| D2       | 6.8         | 3.4          |
| E1       | 4.7         | 2.4          |
| E2       | 5.5         | 2.8          |

Two strain gauges were placed on the opposite sides of each cylinder, 180° apart, and then the average value of the strain was considered to evaluate  $E_b$ . Results are reported in Table 10.

Table 9 Results of splitting tensile tests in terms of maximum load  $P$ , splitting tensile strength  $\sigma_t$

| Specimen | $P$<br>[kN] | $\sigma_t$<br>[MPa] |
|----------|-------------|---------------------|
| A9       | 12.1        | 5.7                 |
| A10      | 4.1         | 2.0                 |
| A11      | 2.9         | 1.5                 |
| A12      | 4.0         | 2.0                 |
| B16      | 2.1         | 1.0                 |
| B17      | 3.1         | 1.5                 |
| B18      | 2.1         | 1.1                 |
| C4       | 1.0         | 0.5                 |
| C5       | 2.5         | 1.2                 |
| C6       | 1.9         | 0.9                 |

Table 10 Elastic modulus

| Specimen | $E_b$<br>[GPa] | $\overline{E}_b$<br>(CoV)<br>[GPa] |
|----------|----------------|------------------------------------|
| A4       | 4.82           |                                    |
| A5       | 8.41           | 9.8                                |
| A7       | 8.64           | (0.73)                             |
| B1       | 22.35          |                                    |
| B2       | 4.99           |                                    |

## 2.5 Composite materials

Due to inherent aging of existing structures, there is a significant need for strengthening reinforced concrete and masonry structures. In the past, methods for providing external confinement included the application of concrete jackets or external steel elements. External confinement of concrete elements by means of fiber-reinforced polymer (FRP) materials has been proven to be an effective strengthening solution if compared to conventional techniques [85] [86] [87] [88]. Some of the advantages of FRPs are limited invasiveness, high strength-to-weight ratio, and limited time required for the application [89] [90]. During the last two decades, innovative composite system namely, fiber-reinforced mortar (FRM), textile reinforced mortar (TRM), and fiber-reinforced cementitious matrix (FRCM) composites that combine high-strength fibers in the form of textiles or fabrics with inorganic matrixes have been studied. Research has shown that using a grout-based confining system is a very promising alternative to FRP retrofitting solutions [91] [92]. In the last decade, two additional systems namely, steel-reinforced polymer (SRP) and steel-reinforced grout (SRG) composites have been added to the toolbox [33] [93] [94] [95]. They consist of high-strength

steel fibers embedded in an epoxy resin or cementitious (inorganic) matrix, respectively. Compared to organic matrices, inorganic matrices have better resistance to high temperatures and fire, good vapor permeability, and they can be applied onto wet surfaces and at low temperatures [96]. Although the research on the use of SRG strengthening systems is still in its infancy, SRG has been shown to increase the flexural and shear capacity of concrete beams [97] [98], the flexural and shear capacity of masonry panels [99] [100] [30], the load carrying capacity of masonry columns, vaults, and domes, and the seismic capacity of masonry structures [35] [101] [102] [103] [104] [105].

This section describes the composite materials that were used to reinforce concrete and masonry elements. The two constituents are:

1. Mortar matrix;
2. Steel fibers.

The system employed have recently obtained the European certification and it has been approved as reinforcing system from the international code council.

### 2.5.1 Steel fibers

Steel fibers were in the form of a unidirectional sheet of high strength galvanized twisted steel micro-cords on a glass fiber micro-mesh (Figure 25) to facilitate the installation.

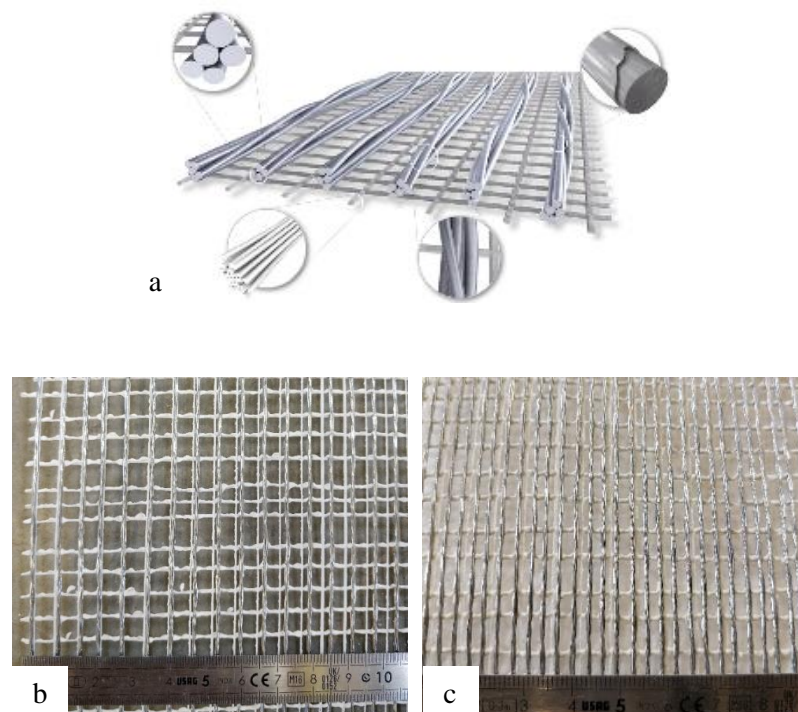


Figure 25 (a) Steel fibers layout; (b) low (LD ) and (c) medium (MD) density fiber sheet

The micro-cords are comprised of five filaments, three of which are straight, and the remaining two filaments are wrapped around the other three with a high torque angle. The steel cords have a cross-

sectional area of  $0.538 \text{ mm}^2$ . Fiber sheets with two different area weights, achieved by different spacing of the microcords, were employed (Figure 25). The two area weights considered were  $670 \text{ g/m}^2$  (LD) and  $1200 \text{ g/m}^2$  (MD).

The physical and mechanical properties of the steel fibers reported by the manufacturer [106] are summarized in Table 11.

*Table 11 Physical and mechanical properties of steel fibers (provided by the manufacturer [106])*

|                                    | LD   | MD  |
|------------------------------------|--|---|
| Properties                         |  |  |
| Wire characteristic tensile stress | > 3000 MPa   | > 3000 MPa  |
| Wire Elastic Modulus               | > 190 GPa  | > 190 GPa   |
| Sheet break deformation            | > 1.5%   | > 1.5%  |
| n° of strands/cm                   | 1.57 strands/cm  | 3.19 strands/cm   |
| Mass (including heat-sealing)      | $\approx 670 \text{ g/m}^2$  | $\approx 1200 \text{ g/m}^2$  |

### 2.5.2 SRG mortar matrices

Two mortar matrices were employed. The first matrix that will be named Matrix 1 in the rest of this thesis, is a natural hydraulic lime (NHL) mortar with fine particle size developed for concrete and masonry applications and intended for highly breathable historical masonry restoration. The second matrix, which will be named Matrix 2, is an inorganic cementitious mortar matrix. It is mainly used for restoration, structural rehabilitation and protection of concrete structures.

The flexural strength of each mortar matrix was determined using three  $40 \text{ mm}$  (width)  $\times$   $160 \text{ mm}$  (length)  $\times$   $40 \text{ mm}$  (height) prisms from each batch (Figure 26), tested in accordance with [107].

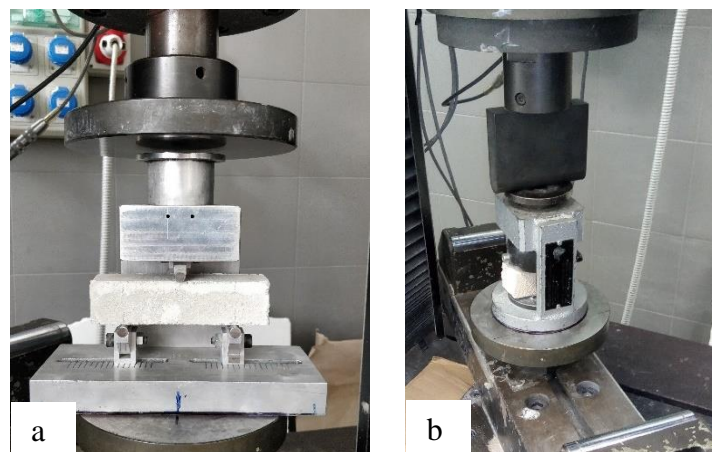


*Figure 26 Test set-up: (a) flexural test and (b) compression test*

The average flexural strength resulted equal to 1.8 MPa (CoV=0.113) and 11.2 MPa (CoV=0.155), for Matrix 1 and 2, respectively. The average value of the compressive strength determined on the two halves that resulted from the flexural strength, was equal to 12.5 MPa (CoV=0.090) and 69.5 MPa (CoV=0.110). Results are summarized in Table 12.

*Table 12 Mechanical properties of Matrix 1 and Matrix 2*

| Properties                       | Matrix 1        | Matrix 2        |
|----------------------------------|-----------------|-----------------|
| Flexural strength (CoV) [MPa]    | 1.8<br>(0.113)  | 11.2<br>(0.155) |
| Compressive strength (CoV) [MPa] | 12.5<br>(0.090) | 69.5<br>(0.110) |

### 2.5.3 Mortar for injection

This is a certified pure natural lime (NHL) fluid mortar. It is usually combined with steel fibers to realize connections for structural reinforcement and seismic retrofitting.

Mechanical properties, such as flexural and compressive strength, were evaluated. The flexural strength was determined on three prisms per batch (Figure 27) with nominal dimensions of 40 mm (width) × 160 mm (length) × 40 mm (height), in accordance with [107].



*Figure 27 Mortar prisms for flexural test*

The average value of flexural strength resulted equal to 6.35 MPa (CoV=0.229). The two halves that were obtained from the flexural strength test were tested under compression according to [107]. The average value of the compressive strength resulted equal to 22.7 MPa (CoV=0.029).

### 3 Chapter 3 – Mode-I fracture properties of quasi-brittle materials

Since the early 70s [12] [13] [108] [109], it is well-known that linear elastic fracture mechanics (LEFM) does not fully capture the fracture phenomenon in concrete elements. As explained in section 1.1.3, a new impetus in the study of fracture of concrete came from Hillerborg et al. [13], who introduced the cohesive crack model for concrete. The concept of the cohesive crack model builds on the original works by Bareblatt [12] [110] and Dugdale [111], and it allows to model the presence of a non-linear softening zone at the crack tip, known as fracture process zone (FPZ). Conversely, LEFM assumes that the FPZ reduces to one mathematical point and cannot be applied. Hillerborg et al. [7] [13] assumed that the crack is a zero-width line (fictitious crack model) that opens by an amount  $w$  (known as separation or opening displacement) while still transferring stresses  $\sigma$ .

The relationship between  $w$  and the stress transferred between the faces of the crack is called softening curve since the stress decreases from the tensile strength to zero while  $w$  increases from zero to the critical value  $w_f$ , which corresponds to the physical complete separation of the crack faces at a certain location. The portion of the ligament between the tip of the notch and where the stress is equal to tensile strength is called fracture process zone (FPZ). The adjective quasi-brittle indicates the presence of a softening behavior after the tensile strength is reached. The region where nonlinear softening occurs is the FPZ.

Therefore, the softening function  $\sigma = f(w)$  is the main ingredient to characterize the fracture process of the material. The area under the curve is the fracture energy  $G_F$ , which can be obtained from tests by employing the concept of work of fracture [3] [17] [112] [113]. It should be pointed out that an alternative model to the one proposed by Hillerborg et al. [13], but to some extent equivalent, was proposed by Bažant [14] [114]. In addition, the cohesive crack model applies to other materials [115] [116] and interfaces between materials [11] [117] [118] [57]. Because of its behavior, concrete is typically defined as a quasi-brittle material [18]. Many researchers have contributed to the development of the cohesive crack model and therefore to the study of concrete as a quasi-brittle material. In this brief introduction, only few key contributions are reported for the sake of brevity [3] [7] [9] [17] [119] [120] [121] [122] [123] [124] [125] [126] [127] [128].

One interesting aspect of the behavior of concrete is how the size effect deviates from what it is observed in LEFM. Size effect itself is a quite intriguing phenomenon. As explained in section 1.1.5, it simply states that, contradicting what predicted by strength of materials, structural members of different sizes would fail at different stress levels. Pioneering results by Walsh [129] indicated that if notched beams of different sizes are tested, the plot of the nominal stress  $\sigma_N$  deviates from

the straight line of slope  $-1/2$  in a double logarithmic plot. This is one proof that LEFM does not apply for concrete, at least for a vast set of sizes, as it is easily proven that, if LEFM holds, similar notched beams of different sizes exhibit a variation of the nominal stress  $\sigma_N$  that depends on the inverse of the square root of one of the dimensions  $D$  of the beams [18].

As mentioned above, LEFM is able to predict the size effect. However, if a material like concrete has a large FPZ with respect to the dimensions of the structural element, LEFM does not apply. A first analytical attempt to investigate the size effect in concrete is reported in [130]. Bažant also proposed a simple size effect formula [116] [131] that allows also to determine the material fracture properties as the peak loads of specimens of different sizes are available. Bažant's size effect law (SEL) is derived from equivalent LEFM concepts. If a constant finite FPZ size is assumed, then Bažant's SEL allows to simulate the deviation of the experimental size effect data from the LEFM prediction.

The experimental evidence of the size effect is fundamental to develop an analytical approach. Typically, notched beams of different sizes are tested and the peak load is used to represent the size effect in terms of nominal stress versus one of the dimensions of the beam. The peak load has been proven to be associated with the first portion of the softening curve [132] if the size of the element is within certain limits and the softening curve itself has a certain shape. However, recent works have shown that as the size increases or the initial slope of the softening curve is low the assumption would not be correct [131][133]. As testing different sizes could become cumbersome, most researchers have agreed over the years that while the depth  $D$  should be scaled with the length  $L$  of notched beam, the width  $B$  of the specimens could be kept constant. The width effect is partially studied in the literature and certain phenomena, such as the wall effect, hydration, shrinkage, are known to contribute to the width effect. Nevertheless, to the best of the authors' knowledge, a robust study of the width effect is not present in the literature [134]. The present research investigates the width effect as a possible coupled problem with the size effect. Notched beams with different depths and different widths were tested using a three-point bending (TPB) test set-up.

As pointed out in [112] [135] [136], particular care was paid to obtain a series of specimens that were carefully cast from the same batch, cured under the same conditions, and tested at the same age under the same environmental conditions. Few specimens (named DRY specimens), left to cure outside the lime-saturated bath until testing, showed the importance of the curing regimen adopted. The peak load was used to plot in a double logarithmic scale the nominal stress versus the depth. In addition, from the experimental point of view, it was noted how the measurement devices used to obtain the load–displacement curves could influence the calculation of the fracture energy. The presence of friction, even though expedients were put in place to reduce its effect, could be relevant for larger (and wider) specimens, and thus should be carefully considered. Finally, three

dimensional digital image correlation (3D-DIC) measurements were used to discuss the shape and length of the FPZ.

In addition, the same considerations that were made for concrete specimens, were made for other quasi-brittle materials. Concrete consumption is constantly increasing due to its increasing request from developing countries. To satisfy this demand, cement shall also be produced, being one of the fundamental constituents of concrete. Production of cement has an impacts on the environment: it can be estimated that nowadays, the cement industry accounts for approximately 8% of global anthropogenic CO<sub>2</sub> emissions considering that the production of 1 ton of cement implies the release of about 0.73–0.99 ton of carbon dioxide in the atmosphere. Furthermore, it is estimated that in a business-as-usual scenario, CO<sub>2</sub> emissions from cement production are expected to increase 260% between 1990 and 2050 [137] [138].

In this alarming scenario, a new class of cement-free materials known as alkali-activated materials (AAMs) has raised some interest. AAMs have been successfully investigated as an emerging technology, which is alternative to ordinary portland cement (OPC)-based mortars and concrete [139]. This technology is based on the reaction between a solid aluminosilicate source and an alkali activator to obtain an amorphous 3D network of aluminosilicates with binding properties. One of the main advantages of AAMs is the possibility of using waste powders as amorphous aluminosilicate source that react in sodium and/or potassium hydroxide and silicate solutions [140]. This aspect makes AAMs particularly interesting for obtaining sustainable materials and for pursuing a circular economy approach.

Research conducted in the last two decades has already demonstrated the suitability and potential use of AAMs as building material in terms of mechanical properties and durability [140] [141] [142] [143]. In particular, AAMs resulted excellent in terms of resistance to chemical attack by chloride, various acids, alkali, and sulphate [144] [145]. Furthermore, because of their intrinsically thermal resistant ceramic-like structure [146] [147], AAMs showed interesting advantages when compared with OPC-based materials in applications requiring resistance to high temperatures [148] [149]. In fact, when alkali-activated concrete (AAC) was exposed to fire, high residual strength and no presence of spalling phenomena were found [150] [151], which is in contrast to what generally occurs for OPC-concrete structures. However, in order to obtain high performance materials, a strict control on the choice of the activators according to the chemistry of the aluminosilicate source is required. Furthermore, attention must be paid to the curing method and to the water/binder ratio, which must be as low as possible [143]. In this research, three different mortars are investigated. They are obtained using the same binding system but two maximum sizes of the same type of aggregate (silica sand) and a different type of aggregate (expanded perlite).

Investigating the suitability of AAMs for civil engineering applications also means investigating their fracture properties. As OPC-based materials, AAMs are quasi-brittle in nature.

Understanding the fracture properties of these materials is a topic of great interest, and is not extensively studied yet in the literature. Actually, only a limited number of papers deal with the evaluation of the fracture properties for plain AAMs and alkali-activated concrete [152] [153] [154] [155] [156]. Some authors [154] [155] [156] have used linear elastic fracture mechanics (LEFM) to determine the fracture toughness of AAMs, which seems inappropriate given the load response of the AAMs considered in those studies. In addition, Xie et al. [154] is one of the few (if not the only) studies in which DIC was used to determine the fracture properties of AAMs. However, in their study the authors were not able to fully measure the fracture process zone (FPZ). In this research, DIC is used to investigate the size of the fracture process zone (FPZ) and argue on the reliability of the values of the fracture energy. To some extent, the DIC analysis herein presented could be considered a modern version of Moiré interferometry to study the fracture process, which was used in the pioneering work conducted in [157].

The main focus of the first part of the research is on concrete specimens and alkali-activated mortars, while the other quasi-brittle materials (fired-clay bricks, natural stone and composite matrix) are tested under the same TPB set-up and used for comparison.

### 3.1 Specimens

Fracture mechanics tests were conducted using a TPB set-up, according to ACI/ASCE 446 Technical Committee report [158]. Specimen dimensions were in accordance with the dimensions defined in the standard. At least three prismatic specimens were built for each material with a beam depth ( $D$ ) and width ( $B$ ) that were at least equal to or greater than 4 times the maximum aggregate size  $d_a$ , except for those beams whose width was equal to 35 mm. The loading span ( $S$ ) was 3 times  $D$ , and the total beam length ( $L$ ) should be at least 50 mm longer than 3 times  $D$ . The relations between the dimensions are reported in Figure 28.

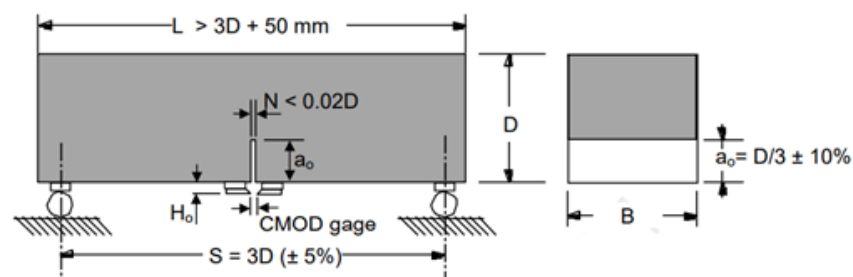


Figure 28 Specimen dimensions [158]

All prisms had a central notch with a V-shaped tip (Figure 29), that was created by using a diamond saw with water cooling. The notch front was perpendicular to the screeded face of each specimen. Thus, the notched beam was placed in the testing ring so that the screeded face became one of the side faces. The nominal notch depth  $a_0$  was equal to  $D/3$ , and the width  $N$  was 3 mm. The tip of the

notch was cut sharp by means of a special blade. This is an important detail in fracture testing, as a rectangular notch tip might trigger anomalous fracture paths [155], which in turn may invalidate the use of the work of fracture method [18] [119]. It should be noted that the notch was not pre-cast. This procedure is not recommended, as the properties of the material would change near the mould surface [156].

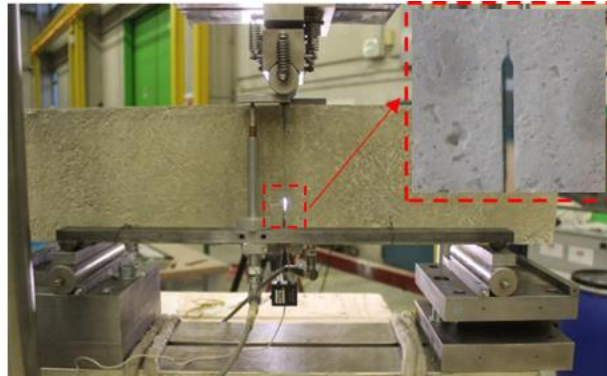


Figure 29 Photo of a representative concrete specimen with a blow-up on the V-shaped tip

### 3.1.1 Concrete specimens

In total, thirty-eight concrete prisms were tested using a TPB set-up. Type 1 concrete was used to cast all the prisms. Concrete prisms with six different cross-sections were cast. Two specimen depths were investigated, i.e. 70 mm and 150 mm. Specimens with a depth equal to 70 mm had a length equal to 300 mm, while specimens with a depth equal to 150 mm had a length equal to 600 mm. For each depth, three different widths were investigated, nominally 35 mm, 70 mm, and 150 mm (Figure 30).

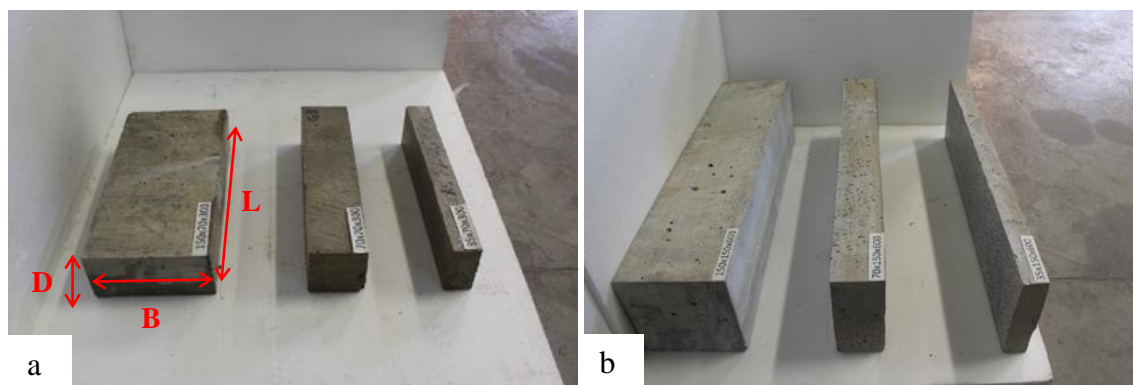


Figure 30 Concrete prisms with different cross-sections: (a) 70 mm-depth specimens and (b) 150 mm-depth specimens

All concrete prisms had a central notch with a V-shaped tip. The notch length ( $a_0$ ) was equal to one third of the prism depth. The width of the notch was equal to 3 mm for all specimens. For each specimen, six measures of the width ( $B$ ), six measures of the depth ( $D$ ), eight measures of the length

( $L$ ) and three measures of the initial notch ( $a_0$ ) were taken and the average values are reported in Table 13 for each specimen together with their CoV. The majority of specimens were left in the lime-saturated bath until the day of testing and water was sprayed on the surface of each specimen during the application of the steel plates employed for the fracture mechanics set-up and during testing. Fracture mechanics tests were performed approximately 230 days after prisms were cast.

### 3.1.2 Alkali-activated mortars

In total, twenty-one alkali-activated mortar prisms were cast and then tested using a TPB set-up to evaluate the fracture properties of the mortars and investigate the size of the fracture process zone (FPZ). Two different sizes of the notched beams were tested. The nominal dimensions were either 70 mm (width)  $\times$  70 mm (depth)  $\times$  300 mm (length) or 35 mm (width)  $\times$  35 mm (depth)  $\times$  200 mm (length). After demolding, all specimens were left in the plastic bags and cured at  $T = 21 \pm 2^\circ\text{C}$  until testing. It should be noted that specimens were removed from the plastic bags few hours prior to testing. The notch was cut after the specimens were stored in laboratory condition for at least 100 days. As for concrete specimens, a special blade was used to obtain a sharp tip in order to force the crack propagation along the axis of the notch and limit the variability of the results, which appears to be hardly achieved with a non-sharp tip [3] [148] [151] [150]. The notch length  $a_0$  was equal to  $D/3$  and its width  $N$  was 3 mm. The net span  $S$  was equal to  $3D$  [158]. The actual measurements of the  $B$  and  $D$  were taken at six different locations, while eight measurements of the length ( $L$ ) of the specimens were taken and three measures of the initial notch were taken and the average values are reported in Table 13 for each specimen together with their CoV. The length of the notch was measured at the end of the test at three locations across the width.

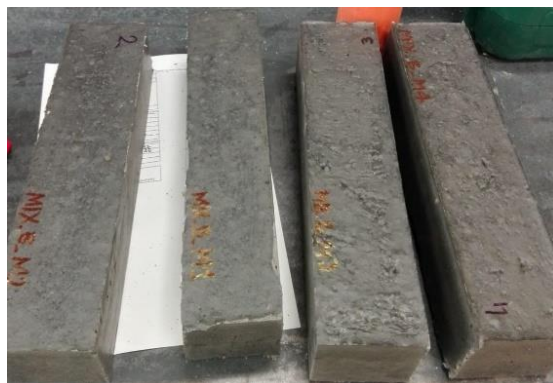


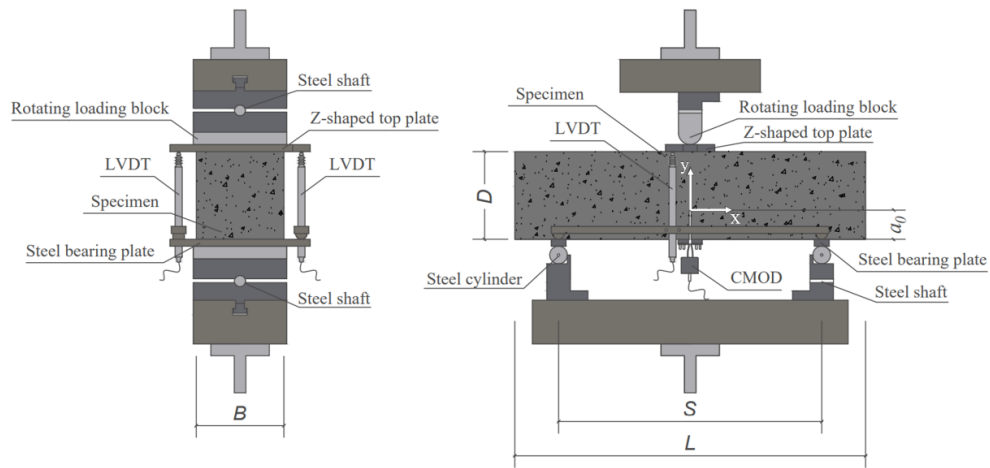
*Figure 31 AAMs beams*

AAMs prisms were sprayed with water while the fixtures for the clip-on gauge knives and the bearing blocks were attached to the specimens themselves. This expedient was necessary to test all specimens in moist conditions as difference in humidity content in the specimens could alter the fracture properties. Fracture testing of the three mortars was conducted at 300 days.

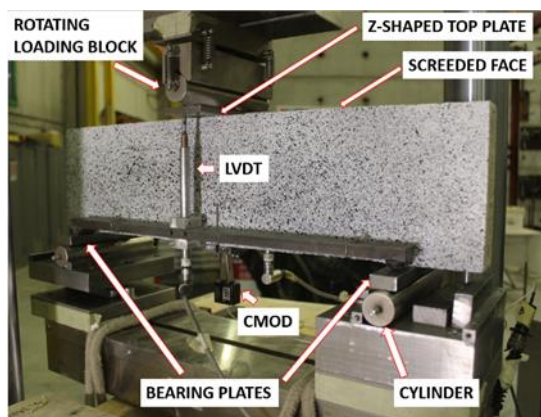
Dimensions of specimens, weight, peak load, average peak load and the respective coefficients of variation (CoV) are reported in Table 13.

### 3.2 Test set-up

The set-up herein presented is based on the draft of ACI/ASCE 446 Technical Committee report on fracture testing [158]. The notched beam was placed in the testing rig so that the screeded face became one of the side faces. The loading apparatus consisted of two steel cylinders placed at a distance  $S$  and used as supports for the notched beam. The net span ( $S$ ) was equal to three times the depth  $D$  of the specimens. The steel cylinders were free to rotate on steel blocks mounted on the base.



a



b

Figure 32 Experimental set-up for fracture mechanics tests (a) sketch of the TPB set-up; (b) concrete specimen

A steel cylinder (loading block) centered with respect to its span was used to apply the load at the midspan. The cylinder should be able to rotate minimizing the torsion of the specimen. The radius of the cylinders  $R$  has to respect the following conditions:  $0.1 D \leq R \leq 0.2 D$ , and its length  $L \geq B$ .

Therefore, the radius of the cylinders was  $0.2 D$  for the 70 mm deep beams and  $0.10 D$  for the 150 mm deep beams. Two steel bearing plates were glued to the bottom face of the specimen and placed on top of the supporting cylinders to eliminate friction. The width of the plates was no larger than  $0.25 D$ , and the depth no less than  $0.42$  the width of the plate. Prior to testing, the cylindrical rollers and the plates were cleaned of any dust. The rollers can be clamped during the preparation of the test set-up but they have to be unclamped before the beginning of the test. A “Z-shaped” steel plate was placed on the top face of the specimen. The plate had a central V-shaped section to assure that the loading cylinder rested firmly on the plate itself. Both the top and the bottom bearing plates had a length exceeding the prism width. On both sides of the concrete prism, a steel bar, with a semi-spherical and a cylindrical support rested on the bottom bearing plates.

Two linear variable displacement transformers (LVDTs) measured the vertical displacement  $\delta$  (i.e. load point displacement) of the prism where the load was applied. Each LVDT was fastened to a steel element and reacted off of the “Z-shaped” top plate. The two LVDTs were placed at a distance  $s$  from the side-face of the specimen equal to 10 mm.

Two small steel plates were glued to the bottom face of the prism near each edge of the central notch. Two screws were welded on each small plate in order to mount the knives used to hold a clip-on-gage (Figure 33). The clip-on-gage (Figure 33b) measured the crack mouth opening displacement (CMOD) and it was used to control the test. The test rate (CMOD control) was chosen to reach the peak load between 150 and 210 s from the beginning of the test [158].

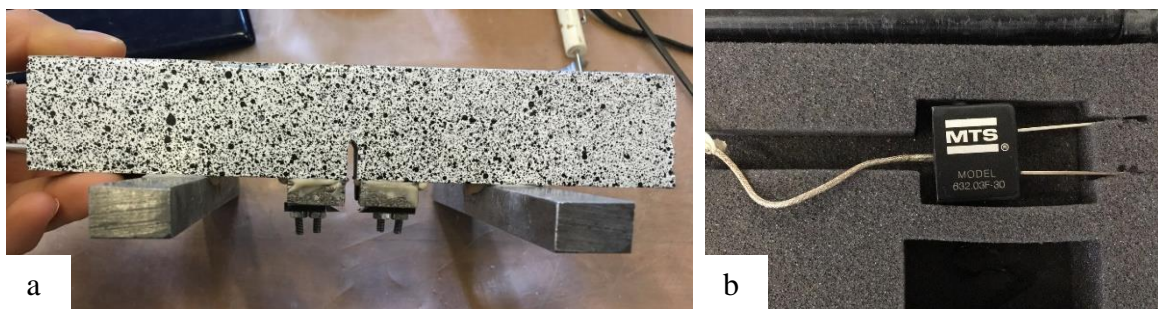


Figure 33 (a) Example of specimens prepared for fracture mechanics test; (b) Clip-on-gauge

Therefore, to respect the aforementioned condition, the initial test rate varied depending on the type of specimen tested.

For AAM specimens and *Tharros* specimens, the initial test rate  $v_1$  was equal to 0.0001 mm/s. When the load reached 80% of the peak load in the descending branch of the response, the test rate  $v_2$  was increased to 0.0003 mm/s. Finally, when the load reached 35% of the peak load in the descending branch, the test rate  $v_3$  was increased to 0.0005 mm/s until the end of the test. The increase of the rate was adopted to take into account that as the crack propagates the strain rate at the tip of the crack would change if the CMOD rate were kept constant.

For concrete prisms with  $D = 150$  mm,  $v_1$  was equal to 0.0002 mm/s, while for specimens with  $D = 70$  mm, the initial test rate was equal to 0.00015 mm/s. The loading rate was increased once in the softening branch of the load response of 150 mm-depth specimens, while the loading rate was varied twice in the softening branch of the load response of 70 mm-depth specimens. For specimens with  $D = 150$  mm, the test rate was increased to 0.0005 mm/s when the load reached 80% of the peak in the softening branch of the response. For specimens with  $D = 70$  mm, the test rate was first increased to 0.0005 mm/s after the applied load reached 80% of the peak load in the softening branch of the response and then to 0.001 mm/s when the load was equal to 35% of the peak load in the softening branch.

For concrete prisms and AAM specimens, three-dimensional (3-D) digital image correlation (DIC) was used to measure the displacement field and derive the strain field on the formed (opposite to the screeded face) side-face of each specimen. This technique requires the preparation of the investigated side-surface of each specimen by spraying uniformly with white paint and then create a speckle pattern with black paint (Figure 34).

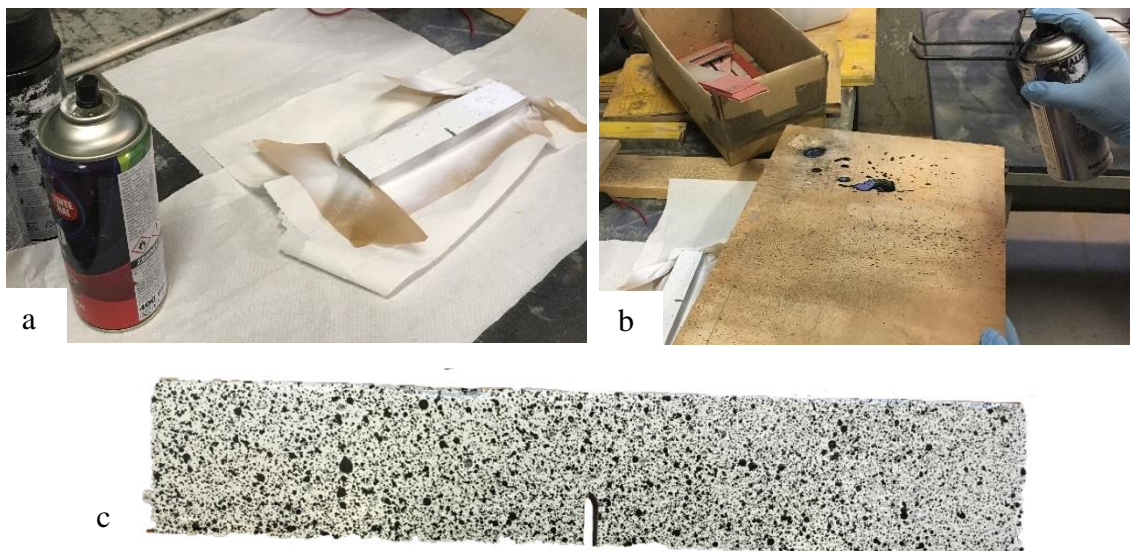


*Figure 34 Preparation of specimen for DIC: (a) application of white paint; (b) creation of a speckle pattern with black paint; c) finished specimen*

Two DIC digital cameras (Figure 35) were placed at a distance of approximately 1.5 m from the surface of the specimen. Resolution of the DIC images was  $2452 \times 2056$  pixel. The resolution of images was such that there were 7 pixel/mm. Images were processed using VIC3D (from CorrelatedSolutions), considering the origin of the Cartesian reference system at the tip of the notch of each specimen (Figure 32a).



Figure 35 Digital image correlation set-up

### 3.3 Discussion of results

In the following paragraphs, results of three-point bending tests are presented and discussed. Fracture behavior of specimens is analyzed in terms of applied load ( $P$ ) versus displacement ( $\delta u$ ), and  $P$  versus CMOD. In addition, results obtained from the LVDTs are compared with those obtained with DIC. Some further considerations are made to evaluate the fracture energy of specimens using the work of fracture, and DIC analysis was employed to evaluate the elastic modulus, the strain profile, the crack opening with a particular attention to the investigation of the fracture process zone (FPZ).

#### 3.3.1 Load responses

##### 3.3.1.1 Concrete specimens

This section presents the results of the fracture tests performed on 38-notched concrete beams. Two depths and three widths were considered. Concrete specimens were named following the notation FM\_X\_Y\_W\_G\_C\_Z, where X indicates the specimen width ( $B$ ) in mm, Y represents the specimen depth ( $D$ ) in mm, W indicates the specimen length ( $L$ ) in mm, G denotes the specimen group related to the casting time, C if present indicates how the specimen was cured (W-DRY=W-DRY specimen, DRY=DRY specimen), and Z=specimen number. For 18 concrete specimens (i.e. 2 specimens per type of mortar), DIC was used to measure the displacement field and derive the strain field on the formed (opposite to the screeded face) side-face of each specimen. Two graphs are plotted for each specimen, except for the W-DRY specimens (i.e. FM\_70\_150\_600\_W-DRY\_1, FM\_35\_70\_300\_W-DRY\_1, FM\_70\_70\_300\_W-DRY\_1, FM\_150\_70\_300\_W-DRY\_1), that features the load per unit width,  $P/B$ , on the vertical axis, and the load point displacement  $\delta$  or the CMOD on the horizontal axis. Figure 36 shows the responses for 70 mm-depth specimens and 150 mm-depth specimens, respectively. Figure 36a-c-e shows the load per unit width  $P/B$  versus  $\delta$  response while Figure 36b-d-f shows the  $P/B$  versus CMOD response. The trend is similar for all the specimens: the first linear branch is followed by a nonlinear behavior up to the peak load  $P_{max}$ .

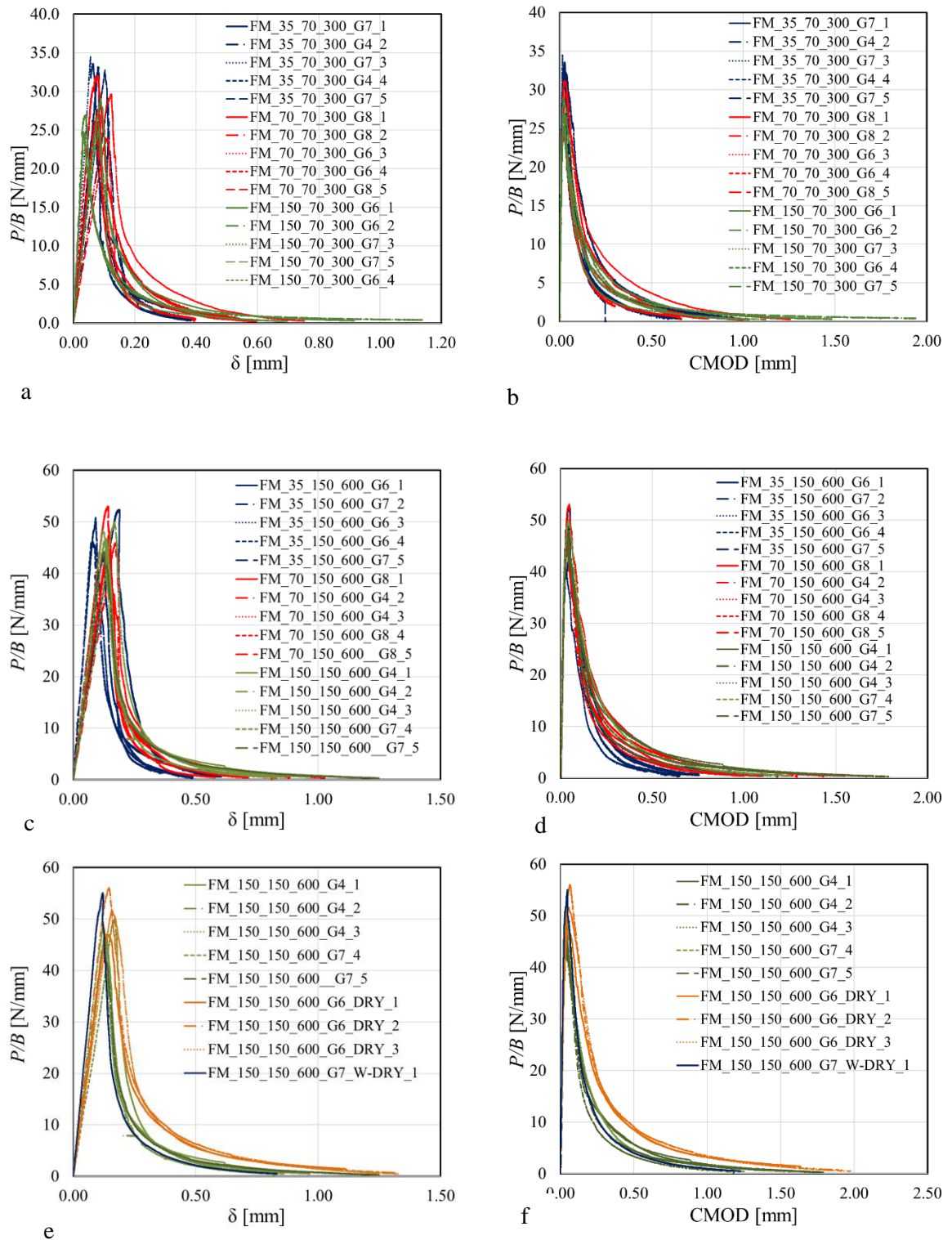


Figure 36  $P/B$  versus  $\delta$  response for specimens cured in the lime-saturated bath with  $D=70$  mm (a) and  $D=150$  mm (c), and comparison among specimens cured in the lime-saturated bath, DRY specimens, W-DRY specimen with  $D=150$  mm (e).  $P/B$  versus CMOD response for specimens cured in the lime-saturated bath with  $D=70$  mm (b) and  $D=150$  mm (d), and comparison among specimens cured in the lime-saturated bath, DRY specimens, W-DRY specimen with  $D=150$  mm (f). [16]

The post peak behavior is characterized by a descending branch that features a long tail. Figure 36a–c indicates that each set of specimens with the same depth shows a slightly different initial

slope. This fact will be further investigated. Figure 36e–f shows the comparison between the load responses of the  $150 \times 150 \times 600$  specimens cured in the lime-saturated bath and three specimens named DRY specimens, which were left at room temperature ( $20\text{ }^{\circ}\text{C}$ ) and humidity equal to 60% after they were cured for 28 days under wet cloths, until testing. In addition, specimen FM\_150\_150\_600\_G7\_W-DRY\_1, which was removed from the lime-saturated bath 24 h prior to testing, is plotted in the same figure for comparison. It can be noted that the average peak load of DRY specimens and peak load of FM\_150\_150\_600\_G7\_W-DRY\_1 increase by 13% and 18%, respectively, with respect to the remaining  $150 \times 150 \times 600$  specimens.

### 3.3.1.2 Alkali-activated mortars

This paragraph presents the results obtained from the TPB tests of 21 alkali-activated mortars. Two different sizes of the notched beams were tested. The nominal dimensions were either 70 mm (width  $B$ )  $\times$  70 mm (depth  $D$ )  $\times$  300 mm (length  $L$ ) or 35 mm (width  $B$ )  $\times$  35 mm (depth  $D$ )  $\times$  200 mm (length  $L$ ). AAM beams employed to determine the fracture properties were named FM\_X\_Y\_W\_I\_Z, where X indicates the specimen width ( $B$ ) in mm, Y represents the specimen depth ( $D$ ) in mm, W indicates the specimen length ( $L$ ) in mm, I denotes the specimen group related to the type of aggregate (FS= fine silica, CS= coarse silica and EP= expanded perlite), and Z=specimen number.

For 12 (i.e. 2 specimens per type of mortar) AAM specimens, DIC was used to measure the displacement field and derive the strain field on the formed (opposite to the screeded face) side-face of each specimen.

The results are plotted in terms of applied load ( $P$ ) versus CMOD and applied load versus load point displacement ( $\delta$ ), and are shown in Figure 37. The  $P$  – CMOD responses are consistent among specimens of the same family, while the  $P$ - $\delta$  curves exhibit a slightly different slope of the linear branch among specimens of the same family. However, the trend of the  $P$  –  $\delta$  curves is similar for all specimens, and it can be described as follows. A short nonlinear branch that leads to the peak load  $P_{max}$  follows the first linear ascending branch. After the peak, a steep (almost vertical) descending branch is observed that transitions into a long tail in between 20% and 30% of the peak load. For some specimens (i.e. FS\_1, FS\_2, CS\_2, CS\_4), it was possible to observe the full long tail until the test was stopped at 1% of  $P_{max}$ . The  $P$  –  $\delta$  responses of the EP specimens and remaining FS and CS specimens (i.e. FS\_3, FS\_4, CS\_1, and CS\_3) exhibit a limited tail as premature failure occurred.

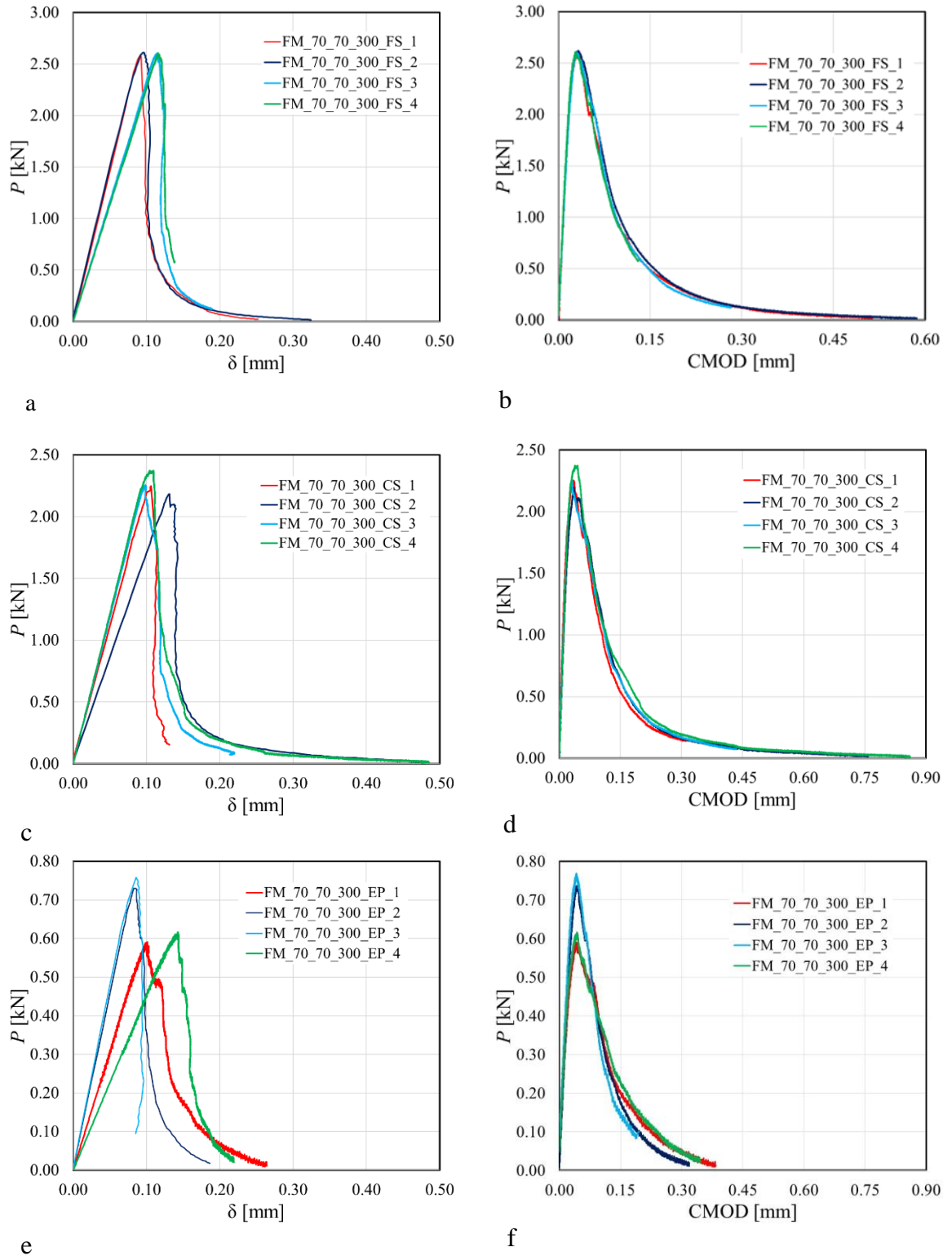


Figure 37  $P - \delta$  response for: (a) FS; (c) CS; and (e) EP specimens.  $P - \text{CMOD}$  response for: (b) FS; (d) CS; and (f) EP specimens.[159]

It should be noted that for all  $35 \times 35 \times 200$  specimens, only one LVDT was used in order to have a full field DIC image of the specimen. This expedient was adopted in order to compute an additional

value of  $\delta$  from DIC, which corresponds to placing the support squares near the supports themselves rather than at their centroid.

Only the  $P$ - $\delta$  response of a 35\_35\_200\_CS\_2 is plotted (Figure 38a) because since only one LVDT was employed, there was no control on a possible rotation of the specimen out-of-plane, which would translate in different readings of the two LVDTs, and therefore results are not reliable.

Therefore, only  $P$ -CMOD response of all  $35 \times 35 \times 200$  specimens is shown (Figure 38b-d).

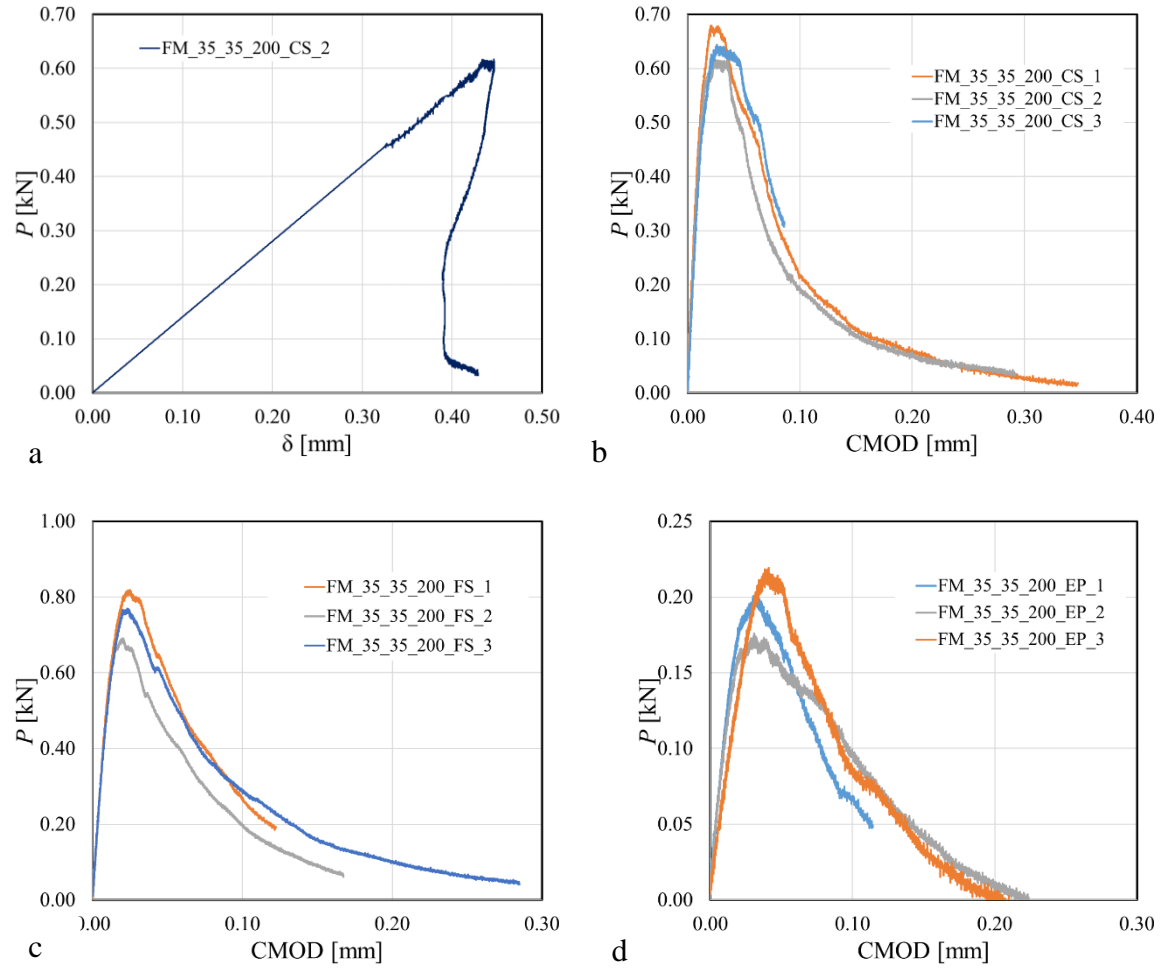


Figure 38  $P$  –  $\delta$  response for: (a) CS<sub>2</sub>;  $P$  – CMOD response for: (b) CS; (c) FS; and (d) EP specimens.

Table 13 Specimen dimensions (depth, width, length, notch and CoV), weight and peak load

| Specimen          | $D$<br>(CoV)<br>[mm] | $B$<br>(CoV)<br>[mm] | $L$<br>[mm]      | $S$<br>[mm] | Weight<br>[kg] | $a_0$<br>(CoV)<br>[mm] | $P_{max}$<br>[kN] | $\bar{P}_{max}$<br>(CoV)<br>[kN] |
|-------------------|----------------------|----------------------|------------------|-------------|----------------|------------------------|-------------------|----------------------------------|
| FM_35_70_300_G7_1 | 71.1<br>(0.002)      | 35.7<br>(0.012)      | 300.5<br>(0.001) | 210.0       | 1.7            | 22.7<br>(0.037)        | 1.18              |                                  |
| FM_35_70_300_G4_2 | 70.5<br>(0.004)      | 35.2<br>(0.010)      | 300.5<br>(0.001) | 210.0       | 1.7            | 22.9<br>(0.030)        | 1.03              | 1.15<br>(0.068)                  |
| FM_35_70_300_G7_3 | 71.7<br>(0.008)      | 36.0<br>(0.022)      | 299.6<br>(0.000) | 210.0       | 1.8            | 23.4<br>(0.020)        | 1.24              |                                  |

|                          |                  |                  |                   |       |      |                 |      |         |
|--------------------------|------------------|------------------|-------------------|-------|------|-----------------|------|---------|
| FM_35_70_300_G4_4        | 71.3<br>(0.008)  | 35.3<br>(0.011)  | 299.9<br>(0.001)  | 210.0 | 1.7  | 22.7<br>(0.007) | 1.13 |         |
| FM_35_70_300_G7_5        | 71.9<br>(0.007)  | 35.0<br>(0.016)  | 301.0<br>(0.001)  | 210.0 | 1.8  | 23.1<br>(0.003) | 1.15 |         |
| FM_70_70_300_G8_1        | 69.8<br>(0.013)  | 70.1<br>(0.010)  | 301.0<br>(0.001)  | 210.0 | 3.4  | 22.7<br>(0.061) | 1.94 |         |
| FM_70_70_300_G8_2        | 70.5<br>(0.005)  | 70.4<br>(0.011)  | 300.7<br>(0.001)  | 210.0 | 3.4  | 23.1<br>(0.004) | 1.84 | 1.94    |
| FM_70_70_300_G6_3        | 70.1<br>(0.009)  | 69.8<br>(0.015)  | 300.9<br>(0.001)  | 210.0 | 3.3  | 22.2<br>(0.004) | 2.07 | (0.101) |
| FM_70_70_300_G6_4        | 70.6<br>(0.004)  | 69.7<br>(0.014)  | 300.8<br>(0.001)  | 210.0 | 3.4  | 22.3<br>(0.004) | 2.17 |         |
| FM_70_70_300_G8_5        | 70.2<br>(0.003)  | 69.5<br>(0.012)  | 301.0<br>(0.000)  | 210.0 | 3.4  | 23.0<br>(0.025) | 1.67 |         |
| FM_150_70_300_G6_1       | 69.8<br>(0.008)  | 150.3<br>(0.003) | 299.8<br>(0.003)  | 210.0 | 7.2  | 22.0<br>(0.039) | 3.73 |         |
| FM_150_70_300_G6_2       | 70.2<br>(0.007)  | 150.7<br>(0.004) | 299.5<br>(0.002)  | 210.0 | 7.2  | 22.5<br>(0.009) | 4.06 | 4.11    |
| FM_150_70_300_G7_3       | 70.4<br>(0.006)  | 150.8<br>(0.002) | 299.6<br>(0.002)  | 210.0 | 7.2  | 22.8<br>(0.013) | 3.82 | (0.087) |
| FM_150_70_300_G6_4       | 70.1<br>(0.012)  | 150.1<br>(0.002) | 299.4<br>(0.002)  | 210.0 | 7.2  | 22.0<br>(0.005) | 4.36 |         |
| FM_150_70_300_G7_5       | 69.7<br>(0.007)  | 149.4<br>(0.005) | 299.3<br>(0.003)  | 210.0 | 7.1  | 22.3<br>(0.005) | 4.00 |         |
| FM_35_70_300_G4_W-DRY_1  | 70.9<br>(0.007)  | 35.9<br>(0.019)  | 299.3<br>(0.002)  | 210.0 | 1.7  | 22.7<br>(0.011) | 1.16 |         |
| FM_70_70_300_G6_W-DRY_1  | 70.3<br>(0.005)  | 69.3<br>(0.012)  | 299.76<br>(0.000) | 210.0 | 3.4  | 22.0<br>(0.000) | 2.15 |         |
| FM_150_70_300_G7_W-DRY_1 | 69.5<br>(0.009)  | 150.1<br>(0.003) | 299.5<br>(0.003)  | 210.0 | 7.1  | 22.0<br>(0.007) | 4.58 |         |
| FM_35_150_600_G6_1       | 150.5<br>(0.003) | 36.4<br>(0.012)  | 601.1<br>(0.002)  | 450.0 | 7.3  | 50.0<br>(0.003) | 1.91 |         |
| FM_35_150_600_G7_2       | 150.0<br>(0.008) | 36.7<br>(0.026)  | 600.8<br>(0.002)  | 450.0 | 7.4  | 48.9<br>(0.003) | 1.69 | 1.67    |
| FM_35_150_600_G6_3       | 149.7<br>(0.009) | 35.6<br>(0.022)  | 600.0<br>(0.001)  | 450.0 | 7.1  | 49.7<br>(0.006) | 1.41 | (0.113) |
| FM_35_150_600_G6_4       | 150.2<br>(0.003) | 34.8<br>(0.010)  | 600.9<br>(0.000)  | 450.0 | 7.3  | 49.8<br>(0.006) | 1.77 |         |
| FM_35_150_600_G7_5       | 149.2<br>(0.008) | 36.3<br>(0.018)  | 600.9<br>(0.000)  | 450.0 | 7.4  | 49.1<br>(0.013) | 1.57 |         |
| FM_70_150_600_G8_1       | 150.6<br>(0.001) | 71.1<br>(0.006)  | 599.9<br>(0.000)  | 450.0 | 14.7 | 49.4<br>(0.003) | 3.34 |         |
| FM_70_150_600_G4_2       | 150.3<br>(0.001) | 71.0<br>(0.008)  | 599.9<br>(0.000)  | 450.0 | 14.5 | 48.8<br>(0.020) | 3.27 |         |
| FM_70_150_600_G4_3       | 150.8<br>(0.003) | 70.6<br>(0.020)  | 600.9<br>(0.001)  | 450.0 | 14.5 | 50.9<br>(0.011) | 3.13 | 3.34    |
| FM_70_150_600_G8_4       | 150.4<br>(0.001) | 68.5<br>(0.019)  | 599.9<br>(0.001)  | 450.0 | 14.3 | 49.3<br>(0.003) | 3.25 | (0.068) |
| FM_70_150_600_G8_5       | 150.6<br>(0.001) | 70.2<br>(0.007)  | 599.8<br>(0.000)  | 450.0 | 14.6 | 49.7<br>(0.012) | 3.73 |         |
| FM_150_150_600_G4_1      | 151.0<br>(0.005) | 150.4<br>(0.008) | 601.0<br>(0.000)  | 450.0 | /    | 50.8<br>(0.017) | 7.03 |         |
| FM_150_150_600_G4_2      | 150.3<br>(0.003) | 150.4<br>(0.009) | 601.5<br>(0.000)  | 450.0 | 31.0 | 49.5<br>(0.017) | 6.95 | 7.09    |
| FM_150_150_600_G4_3      | 151.0<br>(0.003) | 151.1<br>(0.010) | 601.5<br>(0.000)  | 450.0 | 31.2 | 50.9<br>(0.008) | 7.30 | (0.048) |
| FM_150_150_600_G7_4      | 150.8<br>(0.003) | 150.7<br>(0.005) | 600.6<br>(0.001)  | 450.0 | 30.9 | 51.2<br>(0.008) | 7.53 |         |
| FM_150_150_600_G7_5      | 150.7<br>(0.002) | 150.2<br>(0.005) | 600.4<br>(0.001)  | 450.0 | 30.9 | 50.4<br>(0.011) | 6.64 |         |

|                               |                   |                   |                  |       |      |                  |      |                 |
|-------------------------------|-------------------|-------------------|------------------|-------|------|------------------|------|-----------------|
| FM_150_150_600_G6_D<br>RY_1   | 150.26<br>(0.001) | 154.11<br>(0.013) | 600.5<br>(0.001) | 450.0 | 30.6 | 49.9<br>(0.001)  | 7.24 |                 |
| FM_150_150_600_G6_D<br>RY_2   | 150.35<br>(0.001) | 155.74<br>(0.015) | 600.1<br>(0.002) | 450.0 | 30.4 | 49.7<br>(0.008)  | 8.73 | 8.02<br>(0.093) |
| FM_150_150_600_G6_D<br>RY_3   | 150.3<br>(0.001)  | 156.2<br>(0.006)  | 601.0<br>(0.001) | 450.0 | 30.7 | 49.3<br>(0.003)  | 8.08 |                 |
| FM_70_150_600_G4_W-<br>DRY_1  | 150.5<br>(0.001)  | 71.1<br>(0.015)   | 599.3<br>(0.001) | 450.0 | 14.8 | 49.9<br>(0.007)  | 3.07 |                 |
| FM_150_150_600_G7_<br>W-DRY_1 | 150.6<br>(0.002)  | 151.4<br>(0.004)  | 600.6<br>(0.001) | 450.0 | 30.8 | 49.0<br>(0.008)  | 8.34 |                 |
| FM_70_70_300_FS_1             | 72.3<br>(0.013)   | 72.2<br>(0.017)   | 299.8<br>(0.001) | 210.0 | 2.1  | 24.7<br>(0.030)  | 2.59 |                 |
| FM_70_70_300_FS_2             | 70.9<br>(0.006)   | 73.2<br>(0.006)   | 301.2<br>(0.002) | 210.0 | 2.1  | 23.2<br>(0.028)  | 2.62 | 2.60            |
| FM_70_70_300_FS_3             | 70.6<br>(0.004)   | 71.1<br>(0.006)   | 281.5<br>(0.002) | 210.0 | 2.1  | 22.6<br>(0.019)  | 2.60 | (0.005)         |
| FM_70_70_300_FS_4             | 69.1<br>(0.015)   | 70.1<br>(0.003)   | 299.9<br>(0.001) | 210.0 | 2.1  | 21.6<br>(0.019)  | 2.61 |                 |
| FM_70_70_300_CS_1             | 68.5<br>(0.012)   | 69.4<br>(0.021)   | 299.9<br>(0.001) | 210.0 | 2.1  | 21.3<br>(0.054)  | 2.25 |                 |
| FM_70_70_300_CS_2             | 71.2<br>(0.019)   | 68.8<br>(0.009)   | 265.7<br>(0.360) | 210.0 | 2.4  | 25.1<br>(0.044)  | 2.20 | 2.27            |
| FM_70_70_300_CS_3             | 72.2<br>(0.013)   | 70.9<br>(0.013)   | 288.3<br>(0.001) | 210.0 | 2.0  | 24.4<br>(0.047)  | 2.26 | (0.032)         |
| FM_70_70_300_CS_4             | 70.7<br>(0.019)   | 70.0<br>(0.008)   | 299.4<br>(0.001) | 210.0 | 2.1  | 25.4<br>(0.012)  | 2.37 |                 |
| FM_70_70_300_EP_1             | 70.2<br>(0.004)   | 67.9<br>(0.003)   | 299.8<br>(0.002) | 210.0 | 1.3  | 23.4<br>(0.005)  | 0.59 |                 |
| FM_70_70_300_EP_2             | 70.8<br>(0.003)   | 71.8<br>(0.016)   | 300.5<br>(0.003) | 210.0 | 1.3  | 23.4<br>(0.030)  | 0.74 | 0.68            |
| FM_70_70_300_EP_3             | 70.9<br>(0.007)   | 72.1<br>(0.007)   | 299.6<br>(0.001) | 210.0 | 1.3  | 23.3<br>(0.014)  | 0.77 | (0.129)         |
| FM_70_70_300_EP_4             | 60.1<br>(0.433)   | 70.7<br>(0.010)   | 300.1<br>(0.001) | 210.0 | 1.5  | 22.9<br>(0.018)  | 0.62 |                 |
| FM_35_35_200_FS_1             | 35.8<br>(0.013)   | 35.8<br>(0.018)   | 198.1<br>(0.003) | 105.0 | 2.1  | 11.3<br>(0.010)  | 0.82 | 0.76            |
| FM_35_35_200_FS_2             | 35.5<br>(0.003)   | 36.1<br>(0.007)   | 196.8<br>(0.005) | 105.0 | 2.1  | 11.3<br>(0.016)  | 0.69 | (0.086)         |
| FM_35_35_200_FS_3             | 35.7<br>(0.004)   | 35.2<br>(0.006)   | 198.3<br>(0.003) | 105.0 | 2.1  | 11.5<br>(0.024)  | 0.77 |                 |
| FM_35_35_200_CS_1             | 35.8<br>(0.006)   | 35.6<br>(0.025)   | 198.0<br>(0.004) | 105.0 | 2.1  | 12.3<br>(0.041)  | 0.68 | 0.65            |
| FM_35_35_200_CS_3             | 36.5<br>(0.009)   | 34.67(0<br>.046)  | 199.9<br>(0.005) | 105.0 | 2.1  | 12.1<br>(0.041)  | 0.62 | (0.047)         |
| FM_35_35_200_CS_4             | 35.7<br>(0.013)   | 35.5<br>(0.013)   | 199.3<br>(0.004) | 105.0 | 2.0  | 11.67<br>(0.034) | 0.64 |                 |
| FM_35_35_200_EP_1             | 35.7<br>(0.009)   | 34.7<br>(0.012)   | 198.1<br>(0.006) | 105.0 | 1.3  | 11.9<br>(0.023)  | 0.20 | 0.20            |
| FM_35_35_200_EP_2             | 35.7<br>(0.001)   | 36.4<br>(0.013)   | 197.2<br>(0.004) | 105.0 | 1.3  | 10.6<br>(0.015)  | 0.18 | (0.100)         |
| FM_35_35_200_EP_3             | 36.2<br>(0.021)   | 35.3<br>(0.015)   | 199.3<br>(0.003) | 105.0 | 1.3  | 11.9<br>(0.010)  | 0.22 |                 |

### 3.3.2 Other quasi-brittle materials: fired-clay bricks, natural stones and steel reinforced grout (SRG) matrices

The other quasi-brittle materials were tested using the same TPB set-up described in section 3.2. When possible, the dimensions of specimens respected the requirements of the fracture mechanics

report [158]. For *Tharros* stone (named TH) and SRGs matrices (called Matrix1 and Matrix 2) [160] the relation between the dimensions were respected. However, bricks that were collected from existing structures (Figure 39), such as fired-clay bricks and tuff did not have constant dimensions.



Figure 39 Examples of a) fired-clay bricks and b) tuff brick

Therefore, it was decided not to cut the specimens to have the desirable span-to-depth ratio equal to 3 as recommended in fracture mechanics report [158]. Tuff bricks were only rectified to correct their irregularities, while fired-clay bricks were left in their original configuration, to avoid the break of the brick itself. A special blade was used to have a notch with a sharp edge, with a width of 3 mm and a length  $a_0$  reported in Table 14 for each specimens, which was measured at the end of each test. Specimens were named following the notation AZ where A refers to the type of brick and the region/city it came from (N = tuff from Naples, R = tuff from Rome, M = fired-clay brick from Modena, S = *Vivo* bricks, P = fired-clay bricks from Asti), and Z is the number of the specimen. Two LVDTs measured the load-point displacement  $\delta$ , while the test rate was controlled by the CMOD, and it was set to reach the peak between 60 and 120 s from the beginning of the test, as per [158].



Figure 40 (a) Representative tuff bricks prepared for fracture tests; (b) TPB test set-up

The same procedure explained for concrete specimens, was used to cut the V-shaped notch on fired-clay bricks and tuff. All the specimens had a central notch that was equal to 1/3 of the depth of the specimen.

Table 14 Specimen dimensions (depth, width, length and CoV), span, weight, notch length and peak load [161] [160]

| Specimen  | $D$<br>(CoV)<br>[mm] | $B$<br>(CoV) [mm] | $L$<br>(CoV)<br>[mm] | $S$<br>[mm] | Weight<br>[kg] | $a_0$<br>(CoV)<br>[mm] | $P_{max}$<br>[kN] | $\bar{P}_{max}$<br>(CoV)<br>[kN] |
|-----------|----------------------|-------------------|----------------------|-------------|----------------|------------------------|-------------------|----------------------------------|
| S1        | 115.9<br>(0.010)     | 53.6<br>(0.004)   | 246.9<br>(0.002)     | 210.0       | 2.6            | 40                     | 3.32              |                                  |
| S2        | 119.7<br>(0.007)     | 55.3<br>(0.015)   | 250.6<br>(0.001)     | 210.0       | 2.7            | 38                     | 3.69              | 3.52<br>(0.053)                  |
| S3        | 119.7<br>(0.013)     | 55.3<br>(0.014)   | 250.2<br>(0.001)     | 210.0       | 2.7            | 36                     | 3.56              |                                  |
| A1        | 123.1<br>(0.011)     | 64.8<br>(0.080)   | 253.8<br>(0.002)     | 210.0       | 2.9            | 38                     | 2.55              |                                  |
| A2        | 123.5<br>(0.005)     | 60.2<br>(0.040)   | 252.6<br>(0.011)     | 210.0       | 2.7            | 39                     | 3.21              | 2.76<br>(0.140)                  |
| A3        | 123.2<br>(0.009)     | 60.5<br>(0.022)   | 255.0<br>(0.006)     | 210.0       | 3.1            | 39                     | 2.53              |                                  |
| M1        | 129.1<br>(0.017)     | 60.4<br>(0.016)   | 269.5<br>(0.006)     | 210.0       | 3.5            | 45                     | 3.60              |                                  |
| M2        | 129.5<br>(0.012)     | 58.0<br>(0.018)   | 272.0<br>(0.006)     | 210.0       | 3.2            | 40                     | 4.11              | 3.71<br>(0.096)                  |
| M3        | 129.9<br>(0.018)     | 59.3<br>(0.025)   | 271.9<br>(0.011)     | 210.0       | 3.4            | 43                     | 3.42              |                                  |
| P1        | 143.1<br>(0.001)     | 59.5<br>(0.006)   | 311.2<br>(0.011)     | 210.0       | 4.3            | 32                     | 5.12              |                                  |
| P2        | 145.6<br>(0.001)     | 46.7<br>(0.011)   | 317.3<br>(0.005)     | 210.0       | 3.5            | 36                     | 4.50              | 4.56<br>(0.116)                  |
| P3        | 148.5<br>(0.002)     | 50.2<br>(0.002)   | 304.6<br>(0.009)     | 210.0       | 3.7            | 33                     | 4.07              |                                  |
| N1        | 111.0<br>(0.003)     | 55.8<br>(0.009)   | 245.7<br>(0.006)     | 210.0       | 2.0            | 35                     | 0.96              |                                  |
| N2        | 112.2<br>(0.004)     | 56.7<br>(0.012)   | 244.4<br>(0.002)     | 210.0       | 1.9            | 33                     | 0.98              | 1.0<br>(0.047)                   |
| N3        | 110.7<br>(0.004)     | 60.0<br>(0.020)   | 244.9<br>(0.001)     | 210.0       | 1.9            | 33                     | 1.05              |                                  |
| R1        | 108.5<br>(0.023)     | 61.7<br>(0.015)   | 250.6<br>(0.004)     | 210.0       | 1.95           | 32                     | 1.54              |                                  |
| R2        | 109.7<br>(0.011)     | 61.2<br>(0.013)   | 248.7<br>(0.003)     | 210.0       | 1.9            | 36                     | 1.51              | 1.49<br>(0.038)                  |
| R3        | 108.6<br>(0.017)     | 59.3<br>(0.046)   | 248.1<br>(0.003)     | 210.0       | 1.9            | 33                     | 1.43              |                                  |
| TH_1      | 71.8<br>(0.012)      | 68.4<br>(0.015)   | 289.3<br>(0.002)     | 210.0       | 2.33           | 23                     | 0.82              |                                  |
| TH_2      | 69.9<br>(0.012)      | 72.0<br>(0.032)   | 287.63<br>(0.002)    | 210.0       | 2.42           | 23                     | 0.74              | 0.81<br>(0.06)                   |
| TH_3*     | 70.0                 | 70.0              | 300.0                | 210.0       | 2.33           | 23                     | 0.83              |                                  |
| TH_4*     | 70.0                 | 70.0              | 300.0                | 210.0       | 2.42           | 23                     | 0.84              |                                  |
| Matrix1_1 | 79.6<br>(0.003)      | 70.3<br>(0.007)   | 300.7<br>(0.001)     | 210.0       | 2.7            | 24                     | 0.80              |                                  |
| Matrix1_2 | 70.3<br>(0.003)      | 74.0<br>(0.012)   | 300.7<br>(0.002)     | 210.0       | 2.8            | 24                     | 0.91              | 0.86<br>(0.07)                   |
| Matrix1_3 | 70.5<br>(0.001)      | 72.8<br>(0.025)   | 299.6<br>(0.001)     | 210.0       | 2.7            | 24                     | 0.88              |                                  |
| Matrix2_1 | 70.6<br>(0.002)      | 74.6<br>(0.007)   | 300.7<br>(0.001)     | 210.0       | 3.1            | 24                     | 1.77              |                                  |
| Matrix2_2 | 70.3<br>(0.002)      | 74.4<br>(0.015)   | 301.1<br>(0.002)     | 210.0       | 3.0            | 24                     | 1.66              | 1.61<br>(0.12)                   |
| Matrix2_3 | 70.6<br>(0.002)      | 74.1<br>(0.009)   | 301.0<br>(0.002)     | 210.0       | 3.0            | 24                     | 1.40              |                                  |

\*For specimens TH\_3 and TH\_4, only nominal dimensions are reported in the table because of the lack of measurements, thus the CoV is not reported.

Four beams of dimensions 70 mm × 70 mm × 290 mm were obtained from the blocks collected from *Tharros*. The beams were tested following the draft ASTM Test Procedure [158] requirements, using the three-point bending tests (Figure 41a). Results are plotted in terms of applied load ( $P$ ) versus CMOD and  $P$  versus load point displacement ( $\delta$ ). The trend is similar for all the specimens: the first branch is linear followed by a non-linear branch up to the peak load. Then, a descending branch was observed followed by a tail, until the complete separation of the beam in two halves. The length of the tail depends on whether the specimen's failure occurred prematurely or not. It should be noted that specimen TH\_3 was characterized by a long tail before failure, while specimen TH\_1 failed prematurely.

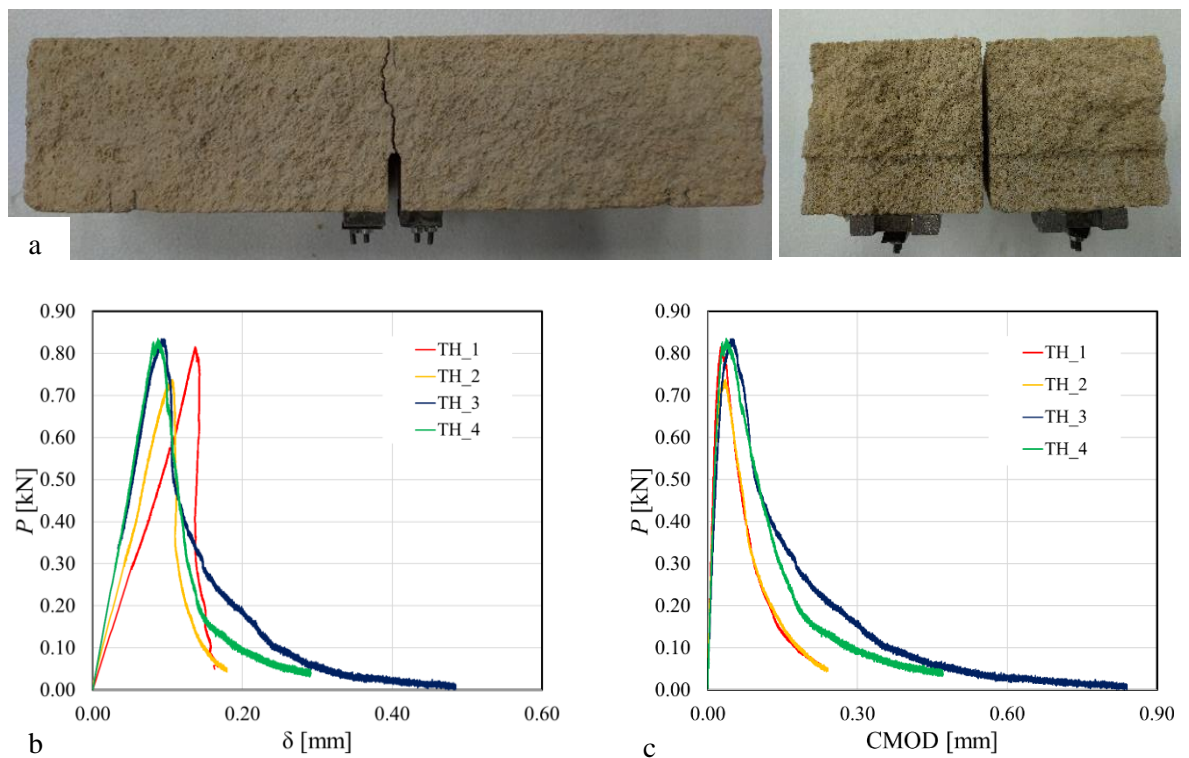


Figure 41 (a) Failure mode; (b)  $P$ - $\delta$  and (c)  $P$ -CMOD response of *Tharros* notched beams

The same three-point bending tests were performed on the two SRGs matrices, whose nominal dimensions were 70 mm ( $B$ ) × 70 mm ( $D$ ) × 300 mm ( $L$ ). The load-response in terms of  $P$ - $\delta$  and  $P$ -CMOD is shown in Figure 42. The trend is similar among all the specimens.

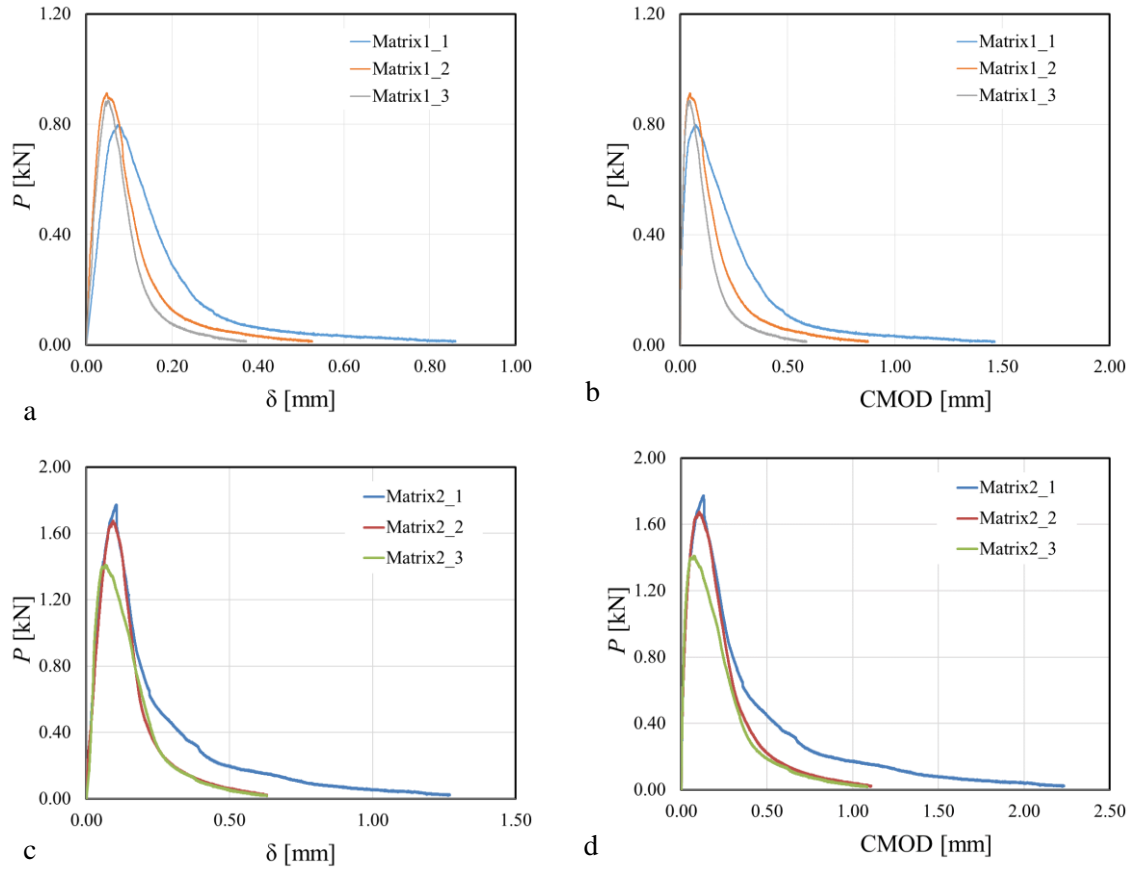


Figure 42 (a)  $P$ - $\delta$  response and (b)  $P$ -CMOD response of lime-based mortar; (c)  $P$ - $\delta$  response and (d)  $P$ -CMOD response of cement-based mortar matrix [162]

### 3.3.3 Comparison between LVDTs and DIC

#### 3.3.3.1 Concrete specimens

Digital image correlation (DIC) was employed for 18 concrete specimens out of 38, in order to evaluate the displacement field and, consequently, obtain the strain field on one of the side faces of each specimen [163]. In order to allow the DIC analysis, the surface of each specimen was painted with non-reflective white spray and hatched with non-reflective black points. A subset of 31 pixels (approximately 7.5 mm, i.e. half of  $d_a$ ) and a step of 10 pixel (approximately 2.5 mm) was chosen for the DIC analysis. For specimen FM\_70\_150\_600\_G8\_1 it was not possible to synchronize the DIC pictures with the experimental response and therefore the DIC analysis for this specimen is not presented. For 17 out of 18 specimens with DIC, the results of the DIC analysis are presented. The displacements measured by DIC were employed to obtain the load-displacement response for each specimen. The load point displacement  $\delta$  was obtained by subtracting the average vertical displacement of the supports from the vertical displacement of the point where the load was applied [164]. For all specimens with  $D = 150$  mm, it was not possible to evaluate the vertical displacement of the left support from the DIC measurements, since it was hidden by the left steel column of the testing machine. Therefore, for these specimens, the vertical displacement of the

supports was evaluated by considering only the vertical displacements at the right end. The vertical displacements of each support were computed as the average of the displacements in a 10 mm square area placed at the centroid of the cross-section corresponding to the support, i.e. where the ideal neutral axis was located. In order to be consistent with the 150 mm-depth specimens, also for the 70 mm-depth specimens, the vertical displacement of the supports was evaluated considering only a square area at the right support. It should be noted that the averages of the displacements at both supports were very small and consistent between supports. Thus, subtracting the displacement of one support rather than the average of both supports was not considered detrimental to obtain the load point displacement. In fact, for those specimens (with depth equal to 70 mm) for which both supports were captured by DIC, the load point displacement was also computed using the average of the squares at the supports and no difference was observed with the values of the load point displacement obtained from subtracting the displacements of one support. The load point was computed as the difference between the average of the displacements in a 10 mm square area, centered with respect to the top roller at 10 mm under the top Z-shaped steel plate (Figure 59) and the average of the displacements in a 10 mm square centered at the centroid of one support. It should be noted that a variation of the distance of the mid-span square, used to compute the displacement, from the Z-Shaped plate did not affect the calculation of the results.

The  $P$ - $\delta$  responses evaluated from the DIC analysis were then compared with the  $P$ - $\delta$  responses obtained from the average of the LVDTs, as it is shown in Figure 43a and b for specimens FM\_150\_70\_300\_G6\_1 and FM\_150\_70\_300\_G7\_3, respectively. Generally, a good agreement between the DIC-based load response and the LVDT-based load response can be observed (Figure 43a).

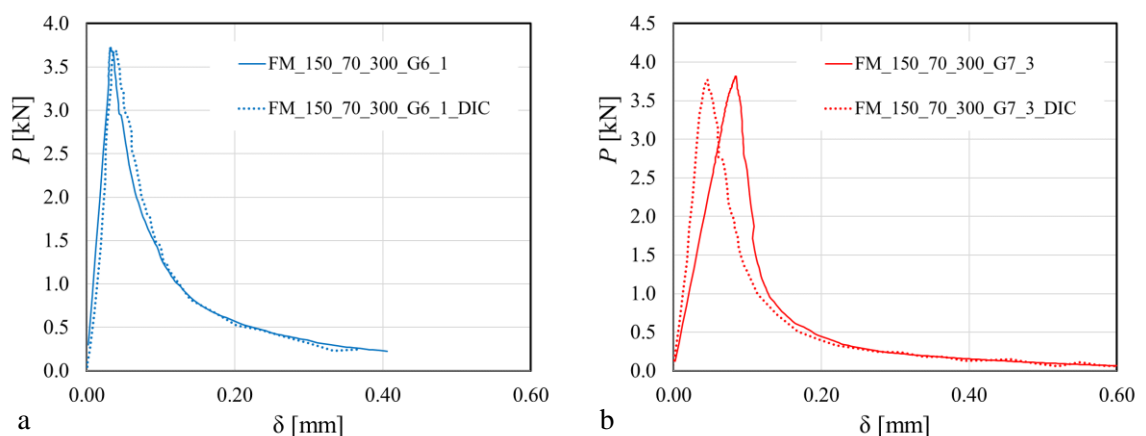


Figure 43 Comparison between the  $P$ - $\delta$  response obtained from LVDTs (solid line) and the  $P$ - $\delta$  response obtained from DIC (dotted line) for specimen FM\_150\_70\_300\_G6\_1 (a) and specimen FM\_150\_70\_300\_G7\_3 (b).

However, for all specimens (except specimen FM\_150\_70\_300\_G6\_1) the initial slope (elastic behavior) appeared to be greater for the  $P$ - $\delta$  responses obtained from the DIC analysis than the  $P$ -

$\delta$  responses obtained from LVDTs (Figure 43b). This fact can be partially explained by taking into account that small adjustments or rotations of the LVDT holders could affect the measure of the vertical displacement, which in turn might result in values of the load point displacement that are larger than the ones obtained from DIC. It should be pointed out that the readings of the two LVDTs were not always consistent and on the other hand, the DIC analysis was performed only on one side.

#### 3.3.3.2 Alkali-activated mortars

DIC was employed for 12 out of 21 AAMs specimens. As for concrete specimens, prior to testing, the side surface of AAMs was prepared for DIC. The DIC analysis was carried out using a 41 pixel subset (approximately 10.8 mm) and a step of 10 pixels (approximately 2.5 mm).

In addition to the LVDT readings, the load point displacement was also obtained from DIC measurements by considering the average of the vertical displacements evaluated over an 8 mm square area under the load point. In order to consider the effect of the supports, the average of the displacements computed over an 8 mm-square area centered at the centroid of the cross-section of each support was computed. Then, the average of the two averages of displacements of the squares corresponding to the supports was subtracted from the average of displacements of the 8 mm square under the load point to obtain  $\delta$ .  $P - \delta$  curves of 70\_70\_300 AAMs specimens obtained from DIC and LVDTs are compared in Figure 44. In Figure 44b the two  $P - \delta$  curves have two different initial slopes, while in Figure 44a there is a slightly better match between the two curves. Two specimens out of six, have a similar trend as FM\_7\_70\_300\_FS\_1 (Figure 44a). Whereas, for the remaining specimens, the linear response from DIC readings has a substantially higher slope than the response from the LVDT readings, as specimen FM\_7\_70\_300\_CS\_2 in Figure 44b. This fact was already pointed out for concrete specimens, and since the LVDTs are mounted on a steel bar, it is possible that some compliance of the system used to read the displacement is added, which in turn increases the displacement read by the LVDT with respect to the actual displacement. Some authors have argued that measuring the displacement where the load is applied will account for the damage of concrete due to stress concentration and therefore cannot be used to compute the work of fracture [17]. To address this concern, two different locations of the top square under the load point were considered and reported in Figure 44. The first location (red square in Figure 44) is just under the load point and the second location (blue square in Figure 44) is shifted vertically to avoid the area near the load point. It should be observed that the green squares in Figure 44 correspond to the areas used to compute the displacements of the two supports, which were averaged and subtracted from the displacement computed over the red or blue areas. The  $P - \delta$  curve corresponding to first location of the square area is plotted with diamond-shaped markers in Figure 44. The  $P - \delta$  curve corresponding to second location (i.e. shifted area) is plotted with a dashed line in Figure 44. It can be observed that there is no difference between the two  $P - \delta$  curves from DIC when the top square

is moved vertically. In addition, for CS\_2 (Figure 44b), three combinations of subset and step were considered when the center square was shifted vertically to avoid the potentially damaged concrete area below the load point. The three dashed lines corresponding to different subsets and steps and the same location of the midspan square overlap. It can be concluded that there is no difference between the three combinations, therefore only one combination of subset and step will be considered in the remainder of the work.

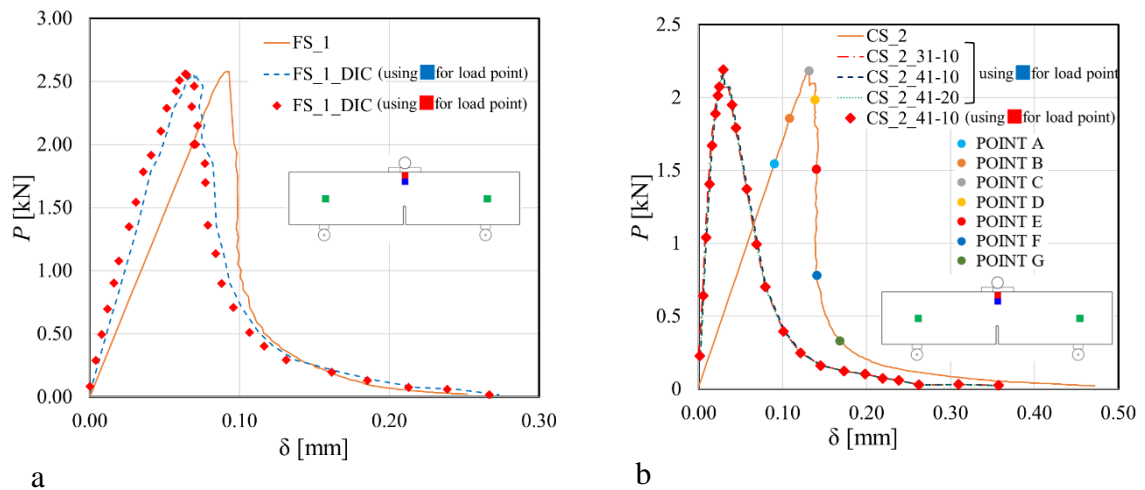


Figure 44 . Comparison between  $P - \delta$  response from DIC and LVDTs for specimens: (a) 70\_70\_300\_FS\_1 subset 41 and step = 10); and (b) 70\_70\_300\_CS\_2. (green squares are the squares used to average the displacements of the supports).

The same procedure was used for  $35 \times 35 \times 200$  AAMs specimens. The  $P - \delta$  curve, referred to the readings of the LVDT, is compared with the  $P - \delta$  curve of the same specimen obtained from DIC in Figure 45. The same procedure of  $70 \times 70 \times 300$  AAMs specimens to evaluate the displacement was adopted for  $35 \times 35 \times 200$  AAMs specimens. The  $P - \delta$  curve from DIC is plotted in Figure 45. The curve that corresponds to the square placed in correspondence to the actual load point is marked in red in Figure 45 and the corresponding curve is plotted with a red dashed line. It can be observed that the red curve and the curve that resulted from placing the square under to the load point (plotted with diamond-shaped markers) are basically coincident, which suggests that damage near the load point might be negligible. As the DIC curves are compared with the  $P - \delta$  curve obtained from LVDT readings, it can be noted that also for  $35 \times 35 \times 200$  mm specimens the initial stiffness is different, which suggests that the hypothesis made for concrete and  $70 \times 70 \times 300$  are acceptable. It should be noted that for all  $35 \times 35 \times 200$  mm specimens, only one LVDT was used in order to have a full field DIC image of the specimen. This expedient was adopted in order to compute an additional value of  $\delta$  from DIC, which corresponds to placing the support squares near the supports themselves rather than at their centroid. These squares are marked in green in Figure 45a. The corresponding  $P - \delta$  curve, which uses the top blue square and the green squares at the supports, is plotted with a dashed green line. It can be concluded that damage at either support is limited and

does not affect the measurements of  $\delta$ . The initial linear portion of the  $P$ - $\delta$  or  $P$ -CMOD curve can be used to determine the elastic modulus.

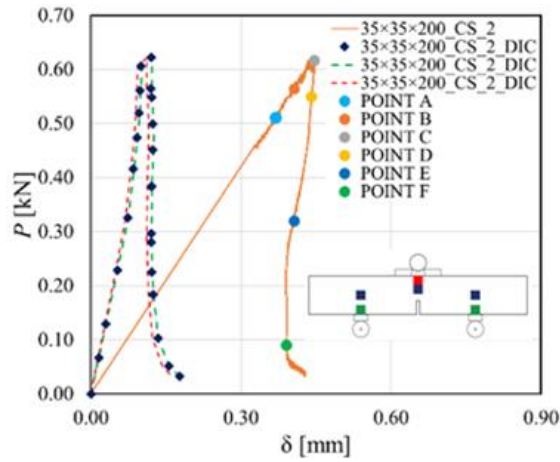


Figure 45 Comparison between  $P$  –  $\delta$  response from DIC and LVDTs for specimen  $FM_{35_35_200\_CS_2}$

### 3.3.4 Failure modes

#### 3.3.4.1 Concrete specimens

For all concrete specimens, crack formed before the peak although its propagation occurred after the peak, i.e. in the descending branch of the load response, which is characterized by a long tail. Specimens broke into two parts at a value of the load very close to zero. Specimen  $FM_{35_70_300\_G4_2}$  failed prematurely at a value of the load approximately equal to 10% of the peak load, therefore the tail of the response was incomplete. For this specimen, the fracture surface was similar to the other specimens that exhibited a long tail. It can be observed, from both the load versus CMOD response and from the load versus load point displacement response, that the length of the tail is longer as the width of the specimen increases. This observation can be related in part to the fact that wider specimens are more stable. A typical cohesive crack pattern of a specimen tested (Specimen  $FM_{150_150_600\_G7_5}$ ) and the relative crack surfaces are shown in Figure 46a and b, respectively. It should be observed how the crack surface right after the test is still wet.





Figure 46 Specimen FM\_150\_150\_600\_G7\_5 at failure: side view (a) and fracture surfaces (b).

#### 3.3.4.2 Alkali-activated mortars

For all AAMs specimens, crack propagation started after the peak load was reached and continued until complete separation of the specimen in two halves. As it will be discussed further, it should be pointed out that crack formation and initiation occurred before the peak load  $P_{max}$  was reached. Eight specimens out of 12 failed prematurely at a load that ranged between 5 and 20% of the peak load. Therefore, the load response of those specimens exhibited a short tail at the end, as shown in Figure 37. Figure 47 shows the failure of three representative specimens. As shown in Figure 47b and c, for specimens CS\_2 and FS\_2 there is a relatively even distribution of the coarse and fine aggregates in the paste. On the other hand, expanded perlite in EP specimens tended to accumulate towards the top (screeded) face of casting, leaving only the paste with almost no aggregates at the bottom of the specimen (Figure 47a). It should be pointed out that the face opposite to the screeded (or trowelled) face is the surface where DIC was employed. Photos in Figure 47 suggest that the crack surface was almost plane and within the width of the notch. This is an important aspect to consider. The use of a rectangular notch tip reported in the literature is associated with a tortuous crack path that make it questionable the use of the area of the ligament to determine the fracture energy [153]. In addition, Figure 47 shows that the surface of the crack was still moist and uneven evaporation of water did not occur.



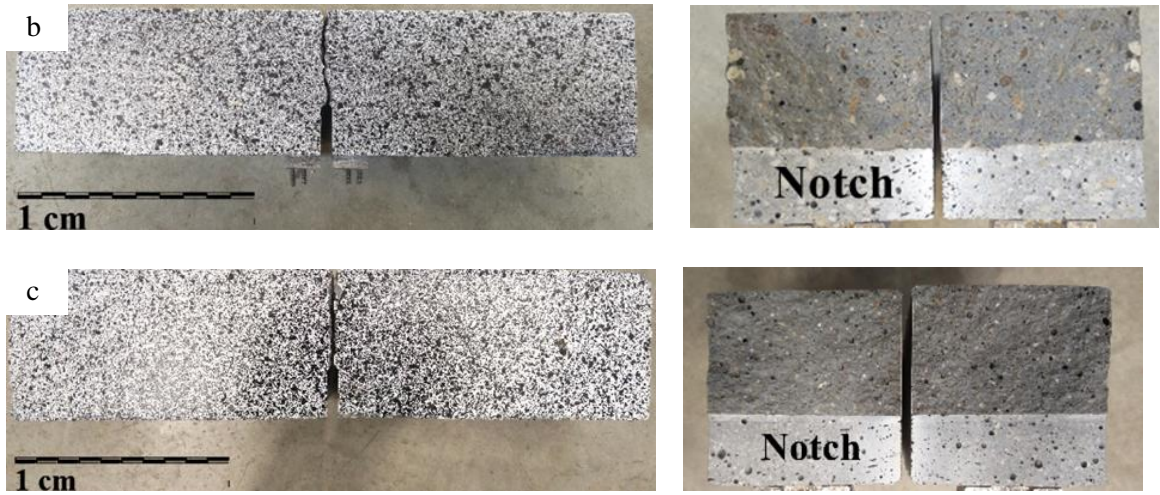


Figure 47 Failure mode of two representative specimens (a) FM\_70\_70\_300\_EP\_2; and (b) FM\_70\_70\_300\_CS\_2 and (c) FM\_70\_70\_300\_FS\_1

Figure 48 shows photos of the cross-section of AAMs representative TPB specimens after testing at 300 days. In all three mortars, the aggregate appeared to be well distributed in the binder. However, as already pointed out when failure modes were presented, for EP specimens an uneven redistribution of the aggregates towards the top (screeded) surface of casting was observed on the fracture surface. Such behavior is typical for lightweight aggregates as expanded perlite.

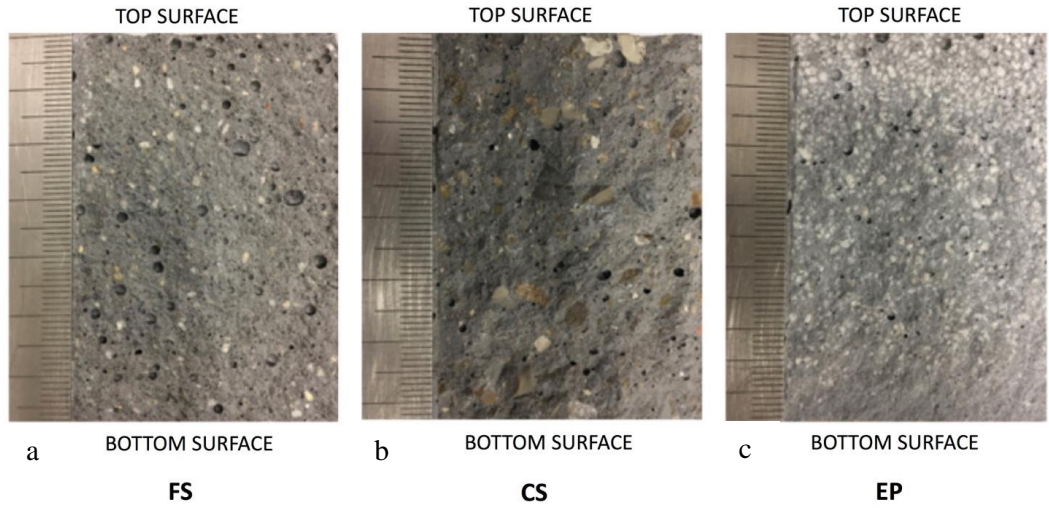


Figure 48 Photos of fractured cross-sections of representative TPB specimens at 300 days (after testing)

Some closed porosity was identified, especially in the FS mortar, and was ascribed to the air entrapped during specimen preparation.

The fracture mechanism at the macroscopic level is similar to cement-based mortars and OPC. Fracture initiated before the peak when the tensile strength at the tip of the notch was reached. As

the peak was reached, the fracture process zone developed. Crack propagated through the paste with fracture of some of the aggregates while the fracture process zone expanded in the post peak.

### 3.3.5 Evaluation of fracture energy

The most direct way to determine the Mode-I fracture energy  $G_F$  is by means of uniaxial tensile tests, where the stress-deformation curve is measured. Deformation has to increase in a stable way, which means that no sudden jumps can happen, and it has to increase slowly during the test [119]. However, it is not easy to perform a stable tensile test because some testing facilities are required. Therefore, to evaluate  $G_F$  bending tests on notched beams are performed. The most common and easy to perform is the three-point bending test on notched beams.

The general idea is to measure the energy ( $A$ ), which is the amount of energy absorbed when the specimen is broken into two halves. This area is then divided by the fracture area, which is the area projected on a plane perpendicular to the direction of the tensile stress, to get  $G_F$ .

Three-point bending tests are easy to perform, their reliability depends on the test specimen and on the procedure followed. There are some requirements for the three-point bending test [119]:

- Specimen should be easy to handle;
- The risk to break the specimen during handling should be limited;
- Some ratios between dimensions have to be followed to get a representative values of the test;
- The demand of the machine stiffness should be limited to simplify the test equipment.

It is important to understand that the possibility of using this type of test to measure the fracture energy depends on the materials: in fact, the compressive strength should be high compared to the tensile strength because during the tests, compressive stresses can occur. If these stresses lead to plastic deformations, the values of  $G_F$  is not reliable.

During the test, the notched beam is acting upon the load but also its weight. Therefore, the area under the load-deflection curve does not give the exact amount of energy absorbed, but some corrections are needed to take into account also for the weight.

Figure 49 shows in a full line the load-displacement response, while the dashed line represent the hypothetical complete  $P$ - $\delta$  curve. The additional load  $P_0$  gives the same bending moment as the weight of the beam. The total amount of the energy absorbed is:

$$A = A_1 + A_2 + A_3 + A_4 \quad (7)$$

Where

- $A_1$  is the area under the load-deflection curve;
- $A_2$  is  $P_0\delta_{P0}$  in which  $\delta_{P0}$  is the deflection when  $P=0$  and the beam breaks;
- $A_3$  is approximately equal to  $A_2$  [7];
- $A_4$  is the area of the triangle shown in the sketch of Figure 49.

The self-weight,  $P_0$ , is considered as a concentrated load [165], and is obtained comparing the bending moment due to a distributed load with the one due to a concentrated load:

$$\frac{mgLS}{4} - \frac{mgL^2}{8} = \frac{P_0S}{4} \rightarrow P_0 = Mg \left( 1 - \frac{L}{2S} \right) \quad (8)$$

where  $m$  is the mass of the specimen per unit length,  $M$  is the mass of the specimen, and  $g$  is the acceleration of gravity.

The displacement due to the self-weight  $\delta_{p_0}$  can be evaluated through the following formulas [18] that assume linear elastic behavior and approximate the sharp tip notch with a line crack as typically done in LEFM:

$$\delta_{p_0} = \frac{3}{2} \frac{P_0 S^2}{BD^2 E'_c} v(\alpha) \quad v(\alpha) = v_0 + v^c(\alpha) \quad v_0 = \delta_0 \frac{2}{3} \frac{BD^2 E'_c}{P_0 S^2} \quad v^c(\alpha) = 3 \int_0^\alpha k^2(\alpha') d\alpha' \quad (9)$$

$\delta_0$  is the elastic displacement of the unnotched beam,  $\alpha$  is equal to  $a_0/D$ ,  $E'_c$  is the elastic modulus for plane stress states ( $\nu$  is assumed equal to 0.2) and  $k$  is the shape factor obtained from the following equation:

$$k = \sqrt{\alpha} \frac{p_{S/D}(\alpha)}{(1+2\alpha)(1-\alpha)^{3/2}} \quad (10)$$

where  $p_{S/D}$  is a fourth degree polynomial function of  $\alpha$  obtained using the procedure described in [18].

Thus the total energy is:

$$A = A_1 + 2P_0 \delta_0 \quad (11)$$

And this energy is divided by the fracture area to get the fracture energy:

$$G_F = \frac{A}{B(D-a_0)} \quad (12)$$

Where  $D$  is the beam depth,  $a_0$  is the notch depth and  $B$  is the beam width.

It should be noted that the influence of  $P_0$  may amount for 40-60% [119], and it is possible to decrease or eliminate this influence using some expedients.

The bending moment due to the weight should be compensated by means of supports moments, but such expedient complicates the execution of the test. In fact, in such a test, the load-deflection curve would have a long tail, and the curve would asymptotically approaches the  $x$ -axis and make the measurement of the area difficult.

The general procedure to determine the fracture energy  $G_F$  is reported in many papers in literature [13] [16] [112] [113] [166]. It should be pointed out that the fracture energy and more in general the fracture properties of quasibrittle materials can be obtained using different approaches [36].

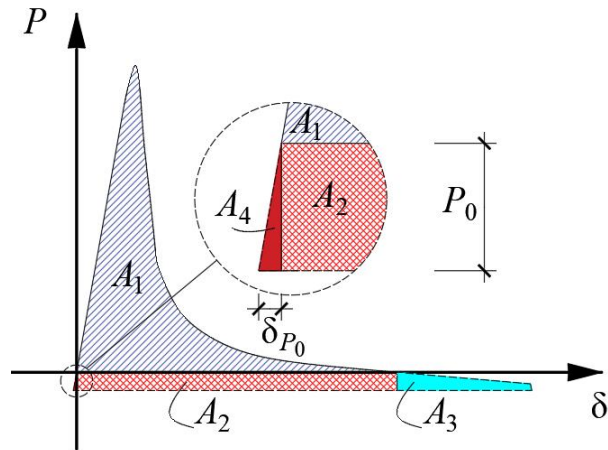


Figure 49 Load-deflection curve from a three-point bending test and the corresponding curve when the weight of the beam is taken into account to evaluate  $G_F$ .

Among other, the two-parameter model [167] and the size effect model [131] could be valid alternatives. In this thesis, only the method explained above, known as the concept of work of fracture, introduced by Hillerborg [17] [113] [119] will be used to evaluate the fracture energy.

### 3.3.5.1 Concrete specimens

Figure 50 shows the average fracture energy for each cross-section evaluated from the area under the load-displacement response obtained from the LVDT measurements. It can be observed that the average fracture energy for specimens with a cross-section equal to  $35 \times 150$  mm (65.4 N/m) is similar to the average fracture energy evaluated for specimens that have a depth equal to 70 mm, that ranges between 63.4 N/m and 68.1 N/m. In addition, considering specimens with a depth equal to 150 mm, it can be noted that the fracture energy seems to become greater as the width of the specimen becomes larger. This fact can be partially explained considering that specimens with a cross-section equal to  $70 \times 150$  mm and  $150 \times 150$  mm have a relevant weight with respect to other specimens. Due to the weight of these specimens, it is possible that the effect of friction between the steel bearing plates and the rollers is not negligible [121] [168] [15] and can affect the value of the fracture energy. Further investigation of this aspect is needed and the significance of the tail of the response, which accounts for a large contribution to the area, should be considered in future works. Considering specimens with a cross-section equal to  $150 \text{ mm} \times 150 \text{ mm}$  it can be observed that DRY specimens reached larger values of the fracture energy (average value equal to 128.1 N/m) than specimens that were cured in a lime-saturated bath until testing (average value equal to 91.3 N/m). In this regard, it is interesting to note how the descending branch of the DRY specimens is wider than the corresponding lime-saturated specimens. In addition, it should be pointed out that

the value of the fracture energy of the W-DRY specimen is within the standard deviation of the corresponding group of specimens that feature the same cross-section. For example, for specimen FM\_70\_70\_300\_G6\_ W-DRY\_1 the fracture energy is 62.1 N/m. The average fracture energy of 5 specimens with cross-section 70×150 mm and its CoV are 66.9 N/m and 0.625, respectively.

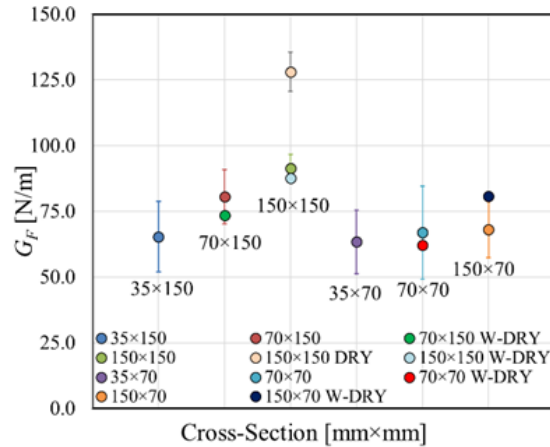


Figure 50 Average fracture energy for different cross-sections

An alternative value of the fracture energy has been determined from the work of fracture using the displacements measured from DIC. The corresponding fracture energy has been named  $G_F^{DIC}$ .  $G_F^{LVDT}$  and  $G_F^{DIC}$  are reported in Table 15 for all specimens together with the averages ( $\bar{G}_F^{LVDT}$  and  $\bar{G}_F^{DIC}$ , respectively) for each set of specimens with the same cross-section. It can be observed that there is a good agreement between the fracture energies computed either from the LVDT measurements or DIC, even though the DIC response appears to have often a higher initial stiffness. Results from Table 13 (peak load) and Table 15 (fracture energy) suggest that the different groups corresponding to different casting times are not related to a specific variation of the quantities analyzed.

Table 15 Comparison between fracture energy of concrete beams evaluated obtained from LVDTs and DIC

| Specimen                 | $G_F^{LVDT}$ | $\bar{G}_F^{LVDT}$ | $G_F^{DIC}$ | $\bar{G}_F^{DIC}$ |
|--------------------------|--------------|--------------------|-------------|-------------------|
|                          | (LVDT)       | (CoV)              | (DIC)       | (CoV)             |
|                          | [N/m]        | [N/m]              | [N/m]       | [N/m]             |
| FM_35_70_300_G7_1        | 49.4         |                    | 45.6        |                   |
| FM_35_70_300_G4_2        | 55.0         | 63.4               | 42.5        | 49.3              |
| FM_35_70_300_G7_3        | 66.0         | (0.191)            | 59.8        | (0.188)           |
| FM_35_70_300_G7_4        | 81.0         |                    | /           |                   |
| FM_35_70_300_G7_5        | 65.7         |                    | /           |                   |
| FM_35_70_300_G4_ W-DRY_1 | /            |                    | /           |                   |

|                           |       |         |      |         |
|---------------------------|-------|---------|------|---------|
| FM_70_70_300_G8_1         | 54.5  |         | 44.8 |         |
| FM_70_70_300_G8_2         | 65.1  | 66.9    | 57.3 | 62.3    |
| FM_70_70_300_G6_3         | 93.5  | (0.265) | 84.6 | (0.327) |
| FM_70_70_300_G6_4         | 73.4  |         | /    |         |
| FM_70_70_300_G8_5         | 48.2  |         | /    |         |
| FM_70_70_300_G6_W-DRY_1   | 62.1  |         | /    |         |
| FM_150_70_300_G6_1        | 60.0  |         | 64.7 |         |
| FM_150_70_300_G6_2        | 63.0  | 68.1    | 76.1 | 64.8    |
| FM_150_70_300_G7_3        | 59.4  | (0.156) | 53.7 | (0.173) |
| FM_150_70_300_G6_4        | 83.7  |         | /    |         |
| FM_150_70_300_G7_5        | 74.6  |         | /    |         |
| FM_35_150_600_G6_1        | 88.7  |         | 60.2 |         |
| FM_35_150_600_G7_2        | 60.7  | 65.4    | 48.9 | 47.1    |
| FM_35_150_600_G6_3        | 54.4  | (0.205) | 32.2 | (0.300) |
| FM_35_150_600_G6_4        | 62.3  |         | /    |         |
| FM_35_150_600_G7_5        | 60.9  |         | /    |         |
| FM_70_150_600_G8_1        | 78.0  |         | /    |         |
| FM_70_150_600_G4_2        | 73.5  | 80.6    | 70.3 | 77.1    |
| FM_70_150_600_G4_3        | 87.9  | (0.128) | 83.9 | (0.125) |
| FM_70_150_600_G8_4        | 69.3  |         | /    |         |
| FM_70_150_600_G8_5        | 94.5  |         | /    |         |
| FM_70_150_600_G4_W-DRY_1  | 73.5  |         | /    |         |
| FM_150_150_600_G4_1       | 92.9  |         | 94.3 |         |
| FM_150_150_600_G4_2       | 82.2  | 91.3    | 75.1 | 82.2    |
| FM_150_150_600_G4_3       | 92.9  | (0.059) | 77.1 | (0.128) |
| FM_150_150_600_G7_4       | 96.8  |         | /    |         |
| FM_150_150_600_G7_5       | 91.9  |         | /    |         |
| FM_150_150_600_G6_DRY_1   | 120.0 |         | /    |         |
| FM_150_150_600_G6_DRY_2   | 134.7 | 128.1   | /    | /       |
| FM_150_150_600_G6_DRY_3   | 129.6 | (0.059) | /    |         |
| FM_150_150_600_G7_W-DRY_1 | 87.6  | /       | /    | /       |

### 3.3.5.2 Alkali-activated mortars

In order to obtain the values of the fracture energy of alkali activated mortar notched beams from the work of fracture, both  $P - \delta$  curves obtained from the average of the LVDTs and DIC analysis were employed. There is a good agreement between the  $G_F$  values obtained from the LVDT  $P - \delta$  curves ( $G_F^{LVDT}$ ) and the DIC  $P - \delta$  curves ( $G_F^{DIC}$ ), even if the DIC responses often presented a higher initial stiffness. Table 16 provides the values of  $G_F$  for each specimen, obtained from DIC

and LVDT  $P - \delta$  curves. Additionally, the average values (an over bar is used to indicate the average) and the CoVs are reported (Table 16).

The highest values of  $G_F$  are found for CS specimens, i.e. specimens with coarse aggregate. The values of the fracture energy of CS specimens are lower than the values of the fracture energy of concrete specimens with the same dimensions and similar aggregate size (Table 15). The values of the fracture energy for FS specimens are similar to the one of CS specimens, which suggests that changing the maximum aggregate size from 2.8 mm to 6 mm does not influence the fracture properties. The lowest values of  $G_F$  are obtained for EP specimens.

The values of fracture energy determined in this work are lower than the values reported in [152] [153] [154] [155] [156]. However, it is important to note that in [154] [155] [156], geopolymers were cured at 60 °C for at least the first 24 hours, in [152] fly-ash and ground granulated blast furnace slag (GGBFS) were jointly used as geopolymer precursors, and in [153] the geopolymer based on 100% FA cured at room temperature was obtained with liquid/FA ratios lower than the ratio used in this research (L/FA in [153] was 0.40 and 0.35, on the other hand L/FA in this work is 0.52).

*Table 16 Comparison between fracture energy of alkali activated mortars obtained from LVDTs and DIC*

| Specimen           | $G_F^{LVDT}$<br>[N/m] | $\bar{G}_F^{LVDT}$<br>(CoV)<br>[N/m] | $G_F^{DIC}$<br>[N/m] | $\bar{G}_F^{DIC}$<br>(CoV)<br>[N/m] |
|--------------------|-----------------------|--------------------------------------|----------------------|-------------------------------------|
| FM_70×70×300_FS_1  | 50.0                  |                                      | 55.0                 |                                     |
| FM_70×70×300_FS_2  | 53.9                  | 56.0                                 | 49.2                 | 52.1                                |
| FM_70×70×300_FS_3  | 57.1                  | (0.098)                              | /                    | (0.079)                             |
| FM_70×70×300_FS_4  | 62.9                  |                                      | /                    |                                     |
| FM_70×70×300_CS_1  | 51.6                  |                                      | 64.6                 |                                     |
| FM_70×70×300_CS_2  | 66.3                  | 60.3                                 | 48.3                 | 56.4                                |
| FM_70×70×300_CS_3  | 54.4                  | (0.144)                              | /                    | (0.204)                             |
| FM_70×70×300_CS_4  | 69.1                  |                                      | /                    |                                     |
| FM_70×70×300_EP_1  | 17.6                  |                                      | /                    |                                     |
| FM_70×70×300_EP_2  | 15.3                  | 18.6                                 | 13.5                 | 11.4                                |
| FM_70×70×300_EP_3* | /                     | (0.206)                              | 9.2                  | (0.272)                             |
| FM_70×70×300_EP_4  | 22.8                  |                                      | /                    |                                     |
| FM_35_35_200_FS_1  | /                     | /                                    | 52.7                 | 61.7                                |
| FM_35_35_200_FS_2  | /                     | /                                    | 70.7                 | (0.206)                             |
| FM_35_35_200_FS_3  | /                     | /                                    | /                    |                                     |
| FM_35_35_200_CS_1  | /                     | /                                    | 74.4                 | 61.5                                |
| FM_35_35_200_CS_2  | /                     | /                                    | 48.6                 | (0.296)                             |
| FM_35_35_200_CS_3  | /                     | /                                    | /                    |                                     |

|                   |   |   |      |         |
|-------------------|---|---|------|---------|
| FM_35_35_200_EP_1 | / | / | 9.1  |         |
| FM_35_35_200_EP_2 | / | / | 19.1 | 14.1    |
| FM_35_35_200_EP_3 | / | / | /    | (0.503) |

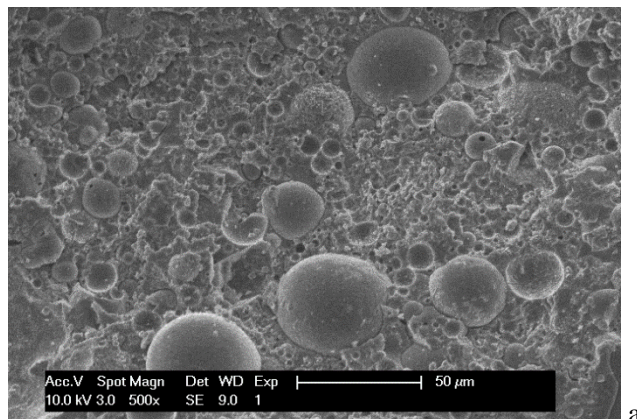
\*for EP\_3  $G_F$  was not computed due to the premature failure of the specimen.

It is well known that geopolymerization is strongly influenced by curing temperature and liquid/binder ratio [143]. Curing at high temperature (60-70 °C) and/or having a low liquid/binder ratio commonly lead to a high geopolymerization rate of the precursor, which entails for the geopolymers to be characterized by a very compact microstructure and improved mechanical properties.

Similarly to what happens for OPC concrete, fracture energy of geopolymers may be influenced by several parameters, but, as stated in [155], microstructure is the most relevant. Unreacted FA particles in geopolymers (typically present when curing is carried out at room temperature and/or in the case of only partial geopolymerization), thanks to their spherical shape, scarcely deviate crack propagation, thus leading to a lower amount of energy per unitary crack propagation.

Figure 51 reports SEM micrographs of representative specimens herein reported after TBP test were performed: unreacted FA are clearly visible for FS, CS and EP specimens. Moreover, EP specimens also exhibit an uneven distribution of expanded perlite (Figure 48 and Figure 51), which can be associated with a further decrease of the fracture energy as crack propagation is not forced to pass around or through the aggregates.

It is interesting to review the results herein reported in comparison with similar OPC specimens. In Sarker et al. [156], the fracture energy of the geopolymer concrete (max aggregate size 10 mm) was higher or similar to the corresponding OPC but the former was cured at 60 °C for 24 hours. Nath and Sarker [153] [156] cured the geopolymer concrete (max aggregate size 10 mm) in ambient temperature and the fracture energy of the geopolymer concrete was greater than that of the reference OPC.



a

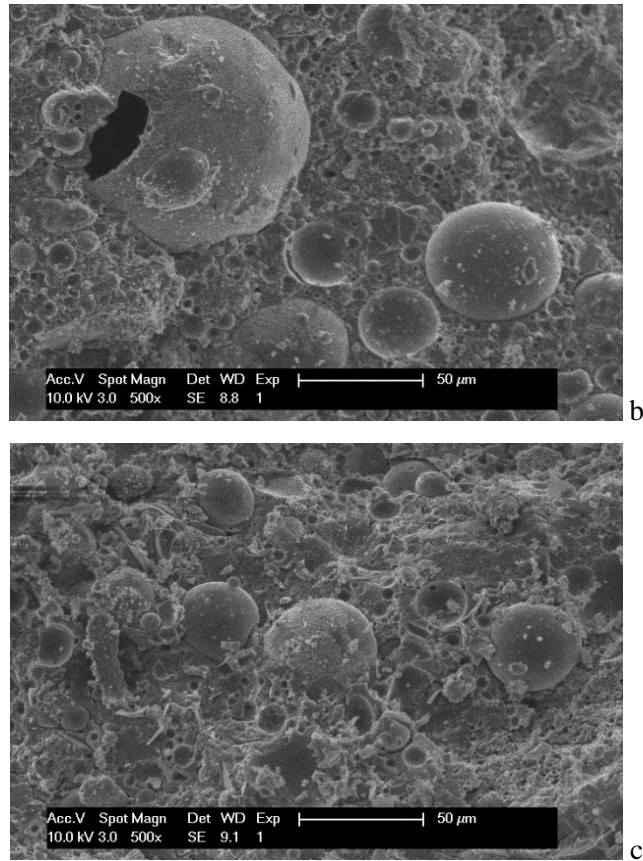


Figure 51 SEM micrographs of representative specimens: (a) FS, (b) CS and (c) EP.

However, the geopolymer concrete mix included fly ash and ground granulated blast furnace slag (GGBFS). The authors also tested the same geopolymer concrete mix without GGBFS and the corresponding fracture energy was lower than the reference OPC. Ding et al. [152] studied geopolymer concrete with GGBFS and FA and noted that fracture energy increases as the ratio GGBFS/FA increases. Interestingly, Pan et al. [155] considered both geopolymer paste (i.e. no aggregate was used) and geopolymer concrete (with maximum aggregate size equal to 14 mm). Both the paste and concrete mixes include only FA and were cured at 60 °C for 18 hours. Their fracture energy was lower than the corresponding paste and concrete made with cement. The compressive strength of the mixes was similar to the strength of the cement-based counterparts. These results suggest once again that unreacted FA (as the amount of unreacted FA might depend on the time cured at higher temperature) might be responsible for the low fracture energy in AAM. Even more importantly, this comparison indicate that while FA-based geopolymer concrete might have a compressive strength similar to OPC, the fracture properties might be different depending on the amount of unreacted FA and on the presence of GGBFS.

It should be mention that for 35 × 35 × 200 mm AAMs specimens, only the  $P$ - $\delta$  curves obtained from DIC were used to compute  $G_f$ . In fact, as the small specimens were equipped only with one LVDT, there was no control on a possible rotation of the specimen out-of-plane, which would translate in different readings of the two LVDTs. Table 16 provides the average fracture energy for

each family of specimens and its coefficient of variation. The values of the fracture energy from corresponding 70×70×300 and 35×35×200 specimens are consistent although slightly higher for smaller specimens, which in part might be due to the size effect [18] [156] that reflects in a higher peak load for smaller specimens.  $G_F$  does not vary significantly as the size of the maximum diameter of the silica sand changes from 2 mm to 6 mm. A substantial difference in the fracture energy can be observed if FS and CS specimens are compared with EP specimens.

### 3.3.6 Comparison between fracture energies of quasi-brittle materials

The fracture energy of the materials herein reported was evaluated through the procedure described in section 3.3.5. The average value of the fracture energy ( $\overline{G_F}$ ) was computed for each group of specimens and it is reported in Table 17. Some observations can be made: natural stones such as Rome, Naples tuff and *Tharros* stone, showed lower values of  $\overline{G_F}$  than concrete and alkali-activated mortars. A lower value of  $\overline{G_F}$  could be related to the presence of “weak points” inside the stones, such as inclusions, clasts and voids. In fact, results of chemical-physical analysis performed on *Tharros* samples, reported a high open porosity, on average equal to 30% [81], while tuff samples, due to their volcanic origin, presented clasts and inclusions. Conversely, fired-clay bricks (i.e. Asti, Modena and Pesaro bricks) showed higher values of  $\overline{G_F}$  than tuff and *Tharros* stones. Among them, Modena brick had the highest value of  $\overline{G_F}$ , which can be associated to the manufacturing process of the brick itself.

Instead of having a single value of  $\overline{G_F}$ , for concrete a range of values of  $\overline{G_F}$  is reported in Table 17, which could be related to different reasons. Some authors argued that during three-point bending tests, some sources of energy dissipation due to testing equipment and preparation of specimens influence the values of  $G_F$  [168]. However, in the present work, all the expedients that have to be adopted during three-point bending tests were accurately considered. Therefore, as already noted by some authors, different values of fracture energy are associated to the variation of the size, width and curing conditions [15][168].

Even for alkali-activated mortars, the fracture varied among the three mortars and in particular, it depends on the type of the aggregate rather than the size of the specimen. In fact  $\overline{G_F}$  of FS and CS specimens is similar and the values are close to that of concrete, while EP specimens showed the lowest  $\overline{G_F}$ , which is comparable to the value obtained for tuff. Values of  $\overline{G_F}$  for the two matrices differed from each other, Matrix 2 is comparable with the values obtained for concrete, while for Matrix 1 values of the fracture energy are on average closer to that obtained from fired-clay bricks.

Table 17 Comparison of  $G_F$  values of quasi-brittle materials

| Material                    | $\bar{G}_F$ [N/m]<br>(CoV) |
|-----------------------------|----------------------------|
| Concrete                    | 63.4-128.1                 |
| Alkali-activated mortars FS | 52.1<br>(0.079)            |
| Alkali-activated mortars CS | 56.4<br>(0.204)            |
| Alkali-activated mortars EP | 14.1<br>(0.503)            |
| <i>Tharros</i> sandstone    | 23.6<br>(0.26)             |
| Vivo brick                  | 29.5<br>(0.272)            |
| Asti brick                  | 26.6<br>(0.234)            |
| Modena brick                | 57.1<br>(0.236)            |
| Pesaro brick                | 32.5<br>(0.476)            |
| Naples tuff                 | 17.7<br>(0.238)            |
| Rome tuff                   | 24.6<br>(0.117)            |
| Lime-based mortar           | 30.3<br>(0.219)            |
| Cement-based mortar         | 101.0<br>(0.220)           |

### 3.3.7 Evaluation of the Elastic modulus from DIC

The elastic modulus reported in Table 5 is compared with the values of the modulus obtained indirectly from the  $P - \delta$  response employing the linear elastic fracture mechanics (LEFM) formulas. The initial portion of the linear response was considered (between 20% and 50% of  $P_{\max}$ ). The elastic solution of an edge-cracked beam is used to express the elastic modulus as a function of the applied load and displacement. Equation 13 provides the load point deflection in LEFM of a notched beam loaded in a TPB configuration [18]:

$$\delta = \frac{P}{BE'} \hat{v}(\alpha) \quad (13)$$

where  $E' = E/(1-\nu^2)$  for plane strain,  $\nu$  is the Poisson ratio assumed equal to 0.2 (measurements of  $\nu$  were not attempted in this work as the calculations of this Section were only meant to be used to check the direct measurements of the elastic modulus),  $\alpha = a_0 / D$  is the relative crack depth, and:

$$\hat{v}(\alpha) = \hat{v}_0 + \hat{v}_c(\alpha) \quad (14)$$

$$\hat{v}_0 = \delta_0 \frac{BE}{P} \quad (15)$$

$$\hat{v}_c(\alpha) = 3 \int_0^\alpha \hat{k}^2(\alpha') d\alpha' \quad (16)$$

$\delta_0$  is the elastic displacement of the uncracked structure and:

$$\hat{k}(\alpha) = \sigma_N \sqrt{Dk(\alpha)} \quad (17)$$

$$\sigma_N = \frac{3PS}{2BD^2} \quad (18)$$

$k(\alpha)$  is the shape factor and its expression for  $S/D = 4$  and  $\infty$  (pure bending) can be found in [18].

For this study, in which  $S/D = 3$ ,  $k(\alpha)$  is evaluated with the superposition method [18].

The calculation of elastic modulus using Equation 13 can be carried out for both the LVDT and DIC  $P - \delta$  responses. The corresponding elastic moduli are termed  $E_{LVDT}^{(13)}$  and  $E_{DIC}^{(13)}$ . Superscript (13) is used to recall that the elastic modulus has been obtained employing Equation 13. LEFM formulas for TPB notched beams that have an  $S/L$  ratio equal to 4 are considered as well. For this case, both the expression of the CMOD and  $\delta$  are considered [169]. The expression of the CMOD is reported in Equation 19, while the expression of  $\delta$  is reported in Equation 21 as  $\delta_{tot}$ . The corresponding values of the elastic moduli obtained by means of Equations 19 and 21 and using the linear part (between 20% and 50% of  $P_{max}$ ) of the load response are termed  $E_{CMOD}^{(19)}$ ,  $E_{LVDT}^{(21)}$ , and  $E_{DIC}^{(21)}$ . To determine  $E_{CMOD}^{(19)}$  the  $P - CMOD$  curves were employed. When Equation 21 was used, both the LVDT and DIC  $P - \delta$  responses were employed.

$$CMOD = \frac{a_0 6PS}{EBD^2} V_1(\alpha) \quad (19)$$

where

$$V_1(\alpha) = 0.76 - 2.28\alpha + 3.87\alpha^2 - 2.04\alpha^3 + \frac{0.66}{(1-\alpha)^2} \quad (20)$$

and

$$\delta_{tot} = \delta_{crack} + \delta_{nocrack} \quad (21)$$

where

$$\delta_{crack} = \sigma_N S V_2(\alpha) \quad (22)$$

$$\delta_{nocrack} = \frac{PS^3}{48E'I} \quad (23)$$

$$V_2(\alpha) = \left( \frac{\alpha}{1-\alpha} \right)^2 [5.58 - 19.57\alpha + 36.82\alpha^2 - 34.94\alpha^3 + 12.77\alpha^4] \quad (24)$$

The values of the elastic moduli obtained from the inverse procedure described above and their averages for each mortar are reported in Table 18. It can be observed that the values of the elastic modulus are lower than the average value obtained from the direct measurement (Table 5).

However, among the values of the elastic modulus reported in Table 18, the closest to the experimental results of Table 5 are the elastic moduli obtained from equation 19 and the second closest are the ones from equation 21 using the DIC  $P$ - $\delta$  response. It should be observed that the scope of this Section was twofold. While the elastic modulus has been determined directly from compression test and compared with the dynamic modulus, it was important to verify if the order of magnitude could be captured from an inverse procedure to validate the test setup. Secondly, the results of this Section show that measurements of the deformation of the specimen that are based on external transducers (see difference between  $E_{LVDT}^{(21)}$ , and  $E_{DIC}^{(21)}$ ) should be critically considered as the transducer could read additional deformation related to the way it is mounted on the specimen. The LVDT might experience some small rotation as the point where it is fixed to the bar is far from the tip, which would lead to additional displacement. The clip-on gauge on the other hand is firmly fixed to the knives and therefore its measurements should be accurate (as confirmed by the values of  $E_{CMOD}^{(19)}$ ).

The same procedure was used to evaluate the elastic modulus of concrete specimens.

The elastic modulus was equal to 19.4 GPa, therefore the elastic modulus evaluated with Equation 19 gives values that are closer to the actual one.

Table 18 Indirect determination of the elastic modulus from the  $P - \delta$  and  $P - CMOD$  responses

| Specimen                | $E_{LVDT}^{(13)}$<br>[GPa] | $\bar{E}_{LVDT}^{(13)}$<br>[GPa] | $E_{DIC}^{(13)}$<br>[GPa] | $\bar{E}_{DIC}^{(13)}$<br>[GPa] | $E_{CMOD}^{(19)}$<br>[GPa] | $\bar{E}_{CMOD}^{(19)}$<br>[GPa] | $E_{LVDT}^{(21)}$<br>[GPa] | $\bar{E}_{LVDT}^{(21)}$<br>[GPa] | $E_{DIC}^{(21)}$<br>[GPa] | $\bar{E}_{DIC}^{(21)}$<br>[GPa] |
|-------------------------|----------------------------|----------------------------------|---------------------------|---------------------------------|----------------------------|----------------------------------|----------------------------|----------------------------------|---------------------------|---------------------------------|
| FM_70×70×300_CS_1       | 4.2                        |                                  | 9.8                       |                                 | 15.4                       |                                  | 4.1                        |                                  | 9.6                       |                                 |
| FM_70×70×300_CS_2       | 3.5                        | 4.3                              | 27.4                      | 18.6                            | 15.4                       | 15.6                             | 3.4                        | 4.2                              | 26.9                      | 18.3                            |
| FM_70×70×300_CS_3       | 4.3                        |                                  | /                         |                                 | 14.5                       |                                  | 4.2                        |                                  | /                         |                                 |
| FM_70×70×300_CS_4       | 5.1                        |                                  | /                         |                                 | 16.9                       |                                  | 5.0                        |                                  | /                         |                                 |
| FM_70×70×300_EP_1       | 1.2                        |                                  | /                         |                                 | 3.1                        |                                  | 1.2                        |                                  | /                         |                                 |
| FM_70×70×300_EP_2       | 1.7                        | 1.5                              | 2.7                       | 4.6                             | 3.3                        | 3.6                              | 1.6                        | 1.5                              | 2.6                       | 4.5                             |
| FM_70×70×300_EP_3       | 1.7                        |                                  | 6.5                       |                                 | 3.3                        |                                  | 1.7                        |                                  | 6.4                       |                                 |
| FM_70×70×300_EP_4       | 1.5                        |                                  | /                         |                                 | 4.7                        |                                  | 1.5                        |                                  | /                         |                                 |
| FM_70×70×300_FS_1       | 5.3                        |                                  | /                         |                                 | 7.5                        |                                  | 19.6                       |                                  | 5.2                       |                                 |
| FM_70×70×300_FS_2       | 5.2                        | 4.8                              | 30.5                      | 19.0                            | 17.8                       | 18.4                             | 5.2                        | 4.7                              | 29.1                      | 18.7                            |
| FM_70×70×300_FS_3       | 4.2                        |                                  | /                         |                                 | 17.2                       |                                  | 4.1                        |                                  | /                         |                                 |
| FM_70×70×300_FS_4       | 4.3                        |                                  | /                         |                                 | 19.0                       |                                  | 4.2                        |                                  | /                         |                                 |
| FM_35_70_300_G7_1       | 5.1                        |                                  | /                         |                                 | 9.8                        |                                  | 20.8                       |                                  | 5.1                       |                                 |
| FM_35_70_300_G4_2       | 3.4                        | 5.3                              | 16.3                      | 14.3                            | 22.7                       |                                  | 3.3                        | 5.2                              | 16.0                      | 14.1                            |
| FM_35_70_300_G7_3       | 7.7                        |                                  | 16.9                      |                                 | 23.5                       |                                  | 7.6                        |                                  | 16.7                      |                                 |
| FM_35_70_300_G7_4       | 6.3                        |                                  | /                         |                                 | 22.8                       |                                  | 6.2                        |                                  | /                         |                                 |
| FM_35_70_300_G7_5       | 3.9                        |                                  | /                         |                                 | 22.7                       |                                  | 3.8                        |                                  | /                         |                                 |
| FM_35_70_300_G4_W-DRY_1 | 2.8                        |                                  | 2.8                       |                                 | /                          |                                  | /                          |                                  | 22.2                      |                                 |
| FM_70_70_300_G8_1       | 4.9                        | 4.3                              | 7.3                       | 10.3                            | 22.3                       |                                  | 4.8                        | 4.2                              | 7.2                       | 10.2                            |
| FM_70_70_300_G8_2       | 5.2                        |                                  | 5.7                       |                                 | 21.4                       |                                  | 5.1                        |                                  | 5.6                       |                                 |
| FM_70_70_300_G6_3       | 3.5                        |                                  | 17.9                      |                                 | 18.2                       |                                  | 3.4                        |                                  | 17.7                      |                                 |

|                          |      |     |      |      |      |      |      |     |      |      |
|--------------------------|------|-----|------|------|------|------|------|-----|------|------|
| FM_70_70_300_G6_4        | 5.0  |     | /    |      | 18.7 |      | 4.9  |     | /    |      |
| FM_70_70_300_G8_5        | 3.0  |     | /    |      | 19.5 |      | 3.0  |     | /    |      |
| FM_70_70_300_G6_W-DRY_1  | 4.7  | 4.7 | /    | /    | 20.9 |      | 4.6  | 4.6 | /    | /    |
| FM_150_70_300_G6_1       | 9.6  |     | 8.6  |      | 17.2 |      | 9.5  |     | 8.5  |      |
| FM_150_70_300_G6_2       | 10.7 |     | 25.8 | 14.3 | 21.2 |      | 10.6 |     | 25.4 |      |
| FM_150_70_300_G7_3       | 4.2  | 6.7 | 8.5  |      | 19.3 |      | 4.1  | 6.6 | 8.4  | 14.1 |
| FM_150_70_300_G6_4       | 4.4  |     | /    |      | 19.3 |      | 4.3  |     | /    |      |
| FM_150_70_300_G7_5       | 4.4  |     | /    |      | 21.4 |      | 4.3  |     | /    |      |
| FM_150_70_300_G7_W-DRY_1 | 4.8  | 4.8 | /    | /    | 21.2 |      | 4.8  | 4.8 | /    | /    |
| FM_35_150_600_G6_1       | 4.0  |     | 5.8  |      | 19.9 |      | 3.9  |     | 5.7  |      |
| FM_35_150_600_G7_2       | 7.1  |     | 26.7 | 19.3 | 19.6 |      | 7.0  |     | 26.3 |      |
| FM_35_150_600_G6_3       | 4.0  | 5.8 | 25.4 |      | 21.7 | 21.1 | 3.9  | 5.7 | 25.0 | 19.0 |
| FM_35_150_600_G6_4       | 8.1  |     | /    |      | 21.4 |      | 7.9  |     | /    |      |
| FM_35_150_600_G7_5       | 5.8  |     | /    |      | 22.9 |      | 5.7  |     | /    |      |
| FM_70_150_600_G8_1       | 4.3  |     | /    |      | 22.8 |      | 4.2  |     |      |      |
| FM_70_150_600_G4_2       | 3.6  |     | 17.3 |      | 21.9 |      | 3.6  |     | 17.1 |      |
| FM_70_150_600_G4_3       | 4.5  | 4.6 | 10.3 | 13.8 | 21.6 | 22.7 | 4.4  | 4.5 | 10.1 | 13.6 |
| FM_70_150_600_G8_4       | 4.5  |     | /    |      | 21.5 |      | 4.4  |     | /    |      |
| FM_70_150_600_G8_5       | 6.0  |     | /    |      | 25.9 |      | 5.9  |     | /    |      |
| FM_70_150_600_G4_W-DRY_1 | 4.0  | 4.0 | /    | /    | 22.5 | 22.5 | 4.0  | 4.0 | /    | /    |
| FM_150_150_600_G4_1      | 4.9  |     | 13.4 |      | 22.4 |      | 4.8  |     | 13.2 |      |
| FM_150_150_600_G4_2      | 5.1  | 4.9 | 16.9 | 15.3 | 22.7 | 22.6 | 5.0  | 4.8 | 16.6 | 15.1 |
| FM_150_150_600_G4_3      | 5.8  |     | 15.7 |      | 23.5 |      | 5.7  |     | 15.4 |      |
| FM_150_150_600_G7_4      | 3.8  |     | /    |      | 21.0 |      | 3.7  |     | /    |      |

|                           |     |     |   |   |      |      |     |     |   |   |
|---------------------------|-----|-----|---|---|------|------|-----|-----|---|---|
| FM_150_150_600_G7_5       | 4.7 |     | / |   | 23.1 |      | 4.7 |     | / |   |
| FM_150_150_600_G6_DRY_1   | 4.7 |     | / | / | 17.2 |      | 4.6 |     | / |   |
| FM_150_150_600_G6_DRY_2   | 5.5 | 4.9 | / | / | 17.0 | 17.1 | 5.4 | 4.8 | / | / |
| FM_150_150_600_G6_DRY_3   | 4.4 |     | / | / | 17.2 |      | 4.4 |     | / |   |
| FM_150_150_600_G7_W-DRY_1 | 6.6 | 6.6 | / | / | 21.0 | 21.0 | 6.5 | 6.5 | / | / |

### 3.3.8 Strain profiles, contour plots and crack opening from DIC analysis

#### 3.3.8.1 Alkali-activated mortars

DIC analysis was employed to evaluate the horizontal strain component  $\epsilon_{xx}$  on the side surface of the specimens.

The profile of the horizontal strain component  $\epsilon_{xx}$  was plotted along the ligament for all specimens for which DIC analysis was available. The coordinate system for the strain and displacement fields is reported in Figure 52. The origin of the system coincides with the notch tip and the  $y$ -axis is along the ligament. The values of  $\epsilon_{xx}$  for each value of  $y$  correspond to the average of the values of  $\epsilon_{xx}$  across an interval of  $x$  centered with respect to the  $y$ -axis. Two intervals of  $x$  were chosen, which correspond to two widths ( $d$ ) of the strip shown in Figure 52, i.e.  $d = 5$  mm and  $d = 10$  mm.  $\xi$  is the distance between the centroids of the rectangles. The reason behind averaging across the  $x$  interval is to take into account the inhomogeneity of the mortars due to the presence of the aggregates. A similar expedient has been used to evaluate the strain profiles in [57] [119]. Furthermore, the reason to choose two different widths of the interval, i.e.  $d = 5$  mm and  $d = 10$  mm, is to determine the influence of the width of the interval itself and therefore the size of the inhomogeneity. The  $\epsilon_{xx}$  versus  $y/(D-a_0)$  plot for specimen FM\_70\_70\_300\_CS\_2 is reported in Figure 53a and b for two combinations of subset and step (i.e. 31-10 and 41-10) and  $d=10$  mm. Figure 53 shows the  $\epsilon_{xx}$  profiles for seven points of the load response of specimen FM\_70\_70\_300\_CS\_2 that correspond to different percentages of the peak load and the peak load itself (Figure 44b). The points selected are marked in the load response of Figure 44b. It can be noted that there is no significant difference between the profiles of Figure 53a and b.

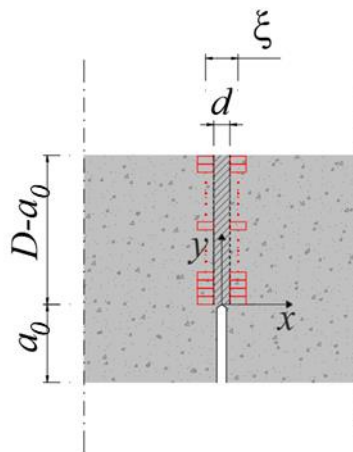


Figure 52 Definition of the interval of  $x$  and rectangular areas used to average the strain and displacement values.

In addition, the same plots of Figure 53 a and b were considered for  $d=5$  mm and it was observed that there was no effect of choice of the interval of  $x$  on the plot of  $\epsilon_{xx}$ .

Three values of the strain corresponding to the tensile strength of the mortar were considered. The first value was computed using  $R_f$  and the  $E$  at 300 days (Table 5), which is approximately the same age of the specimens when they were tested:

$$\varepsilon_{t,fl} = \frac{R_f}{E} \quad (25)$$

The second and third values were computed from the splitting strength ( $f_{ct,sp}$ ) and axial tensile strength ( $f_{ct,ax}$ ), which are obtained as a fraction of  $R_f$  [73] (Equations 26 and 27). From Equations 26 and 27  $f_{ct,sp}$  was evaluated.

$$f_{ct,ax} = 0.5R_f \quad (26)$$

$$f_{ct,ax} = 0.9f_{ct,sp} \quad (27)$$

$$\varepsilon_{t,sp} = \frac{f_{ct,sp}}{E} \quad (28)$$

$$\varepsilon_{t,ax} = \frac{f_{ct,ax}}{E} \quad (29)$$

The value of  $E$  for CS specimens, reported in Table 5, was used and the three values of the strain corresponding to Equations 25, 28 and 29 were equal to 0.00059, 0.00033, and 0.00030, respectively. These values are marked in Figure 53a and b with a vertical dashed line. In the remainder of this Section the value of  $\varepsilon_{t,sp}$  will be used. It can be pointed out that at the peak load (point C in Figure 53), almost all the ligament experienced values of  $\varepsilon_{xx}$  lower than  $\varepsilon_{t,sp}$  (Figure 53) except for a portion of the ligament whose length is approximately equal to 6.5 mm (i.e.  $y/(D-a_0)=0.14$ ). This is the portion of the ligament where the FPZ has partially developed. This observation confirms the quasibrittle nature of the AAMs investigated. A circle was used to mark where the dashed line corresponding to  $\varepsilon_{t,sp}$  intersects the strain profile of point C. The circle is roughly 6.5 mm away from the notch tip. At point D (Figure 53), almost half of the ligament is characterized by values of  $\varepsilon_{xx}$  greater than  $\varepsilon_{t,sp}$ . A diamond-shaped marker was used to indicate the intersection between the dashed line corresponding to  $\varepsilon_{t,sp}$  and the strain profile of Point D. The distance of the diamond-shaped marker from the notch tip is approximately 16.5 mm (i.e.  $y/(D-a_0)=0.36$ ). Interestingly, for Points A, B, and C (Figure 53) the neutral axis appears to be at a fixed location, while for point D (but also Points E, F, and G) the location of the neutral axis shifts towards to top surface, which suggests that the FPZ is developing and the crack is about to propagate. As mentioned earlier, crack formation occurs before Point C, as the strain profile

intersect the dashed line corresponding to  $\varepsilon_{t,sp}$ . For Point E, 2/3 of the ligament experiences strain values greater than  $\varepsilon_{t,sp}$ . A square-shaped marker indicates the intersection of the  $\varepsilon_{t,sp}$  line and the strain profile of Point E. It should be mentioned that values of the strain greater than  $\varepsilon_{t,sp}$  are meaningless and they are shown with a dashed line for  $\varepsilon_{xx} > \varepsilon_{t,sp}$  only for the purpose of determining the size of the fracture process zone (FPZ) [18]. The FPZ for Points C, D, and E is bounded by the crack tip and the intersection between the dashed line and the strain profile, i.e. where the markers are located in Figure 53a and b.

The main question that is still open is related to the size of the FPZ. In other words, as the test reached Point E, was the FPZ fully established or its size was too large compared with the size of the ligament to be fully exploited? In order to gain an insight on this topic, which is source of debate among the community of fracture mechanics of quasi-brittle materials, the displacement field will be considered later.

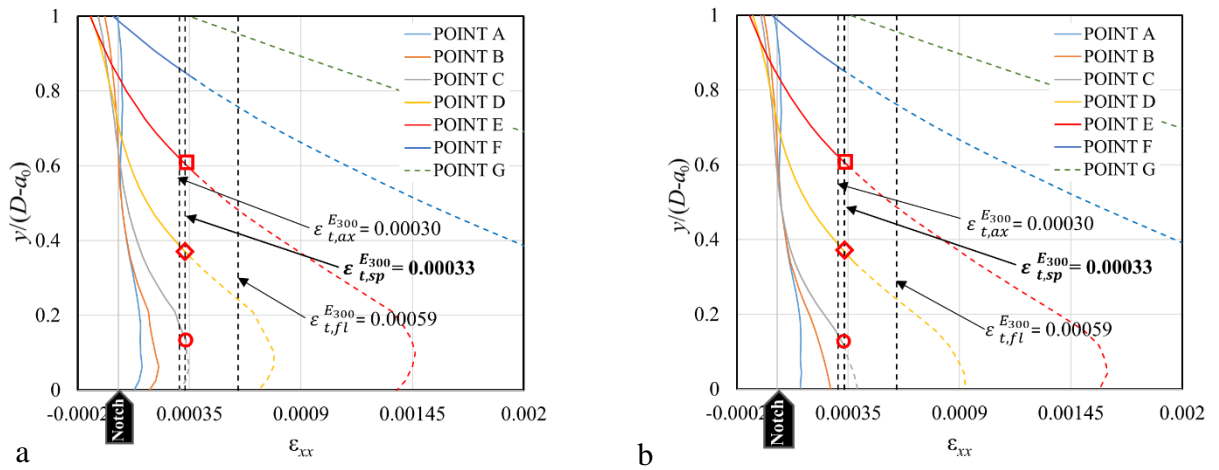


Figure 53  $\varepsilon_{xx}$  versus  $y/(D-a_0)$  of FM\_70\_70\_300\_CS\_2 specimen for  $d=10$  mm: (a) subset=31 and step=10; and (b) subset=41 and step=10.

The same strain analysis is reported for specimen FM\_70\_70\_300\_EP\_2. Figure 54b shows the  $\varepsilon_{xx}$  profile for seven points that correspond to different percentages of the peak load and the peak load itself (Figure 54a). The three values of the strain corresponding to Equations 25,28 and 29 are equal to 0.00089, 0.00050, and 0.00045, respectively, and are marked in Figure 54b with a dashed line. The curves of Figure 54b refer to  $d = 10$  mm, subset=41, and step=10. Similar plots were obtained by varying subset, step and  $d$  as noted for specimens CS\_2.

At point C, at approximately 0.7 mm (i.e.  $y/(D-a_0)=0.01$ ) from the tip the value of  $\varepsilon_{xx}$  is equal to  $\varepsilon_{t,sp}$ . The intersection of the strain profile of Point C with the dashed line corresponding to  $\varepsilon_{t,sp}$  is marked with a circle in Figure 54b. For points A, B and, C the neutral axis is fixed at the same location, while for point D the location of the neutral axis shifts towards the top surface, due to the development of the FPZ. At point D, the intersection between  $\varepsilon_{xx}$  and  $\varepsilon_{t,sp}$  is marked with a diamond-shaped marker, which is located 7.6 mm (i.e.  $y/(D-a_0)=0.16$ ) away from the tip. For point E, a

square marker indicates the intersection between  $\varepsilon_{xx}$  and  $\varepsilon_{t,sp}$  and is approximately 21 mm (i.e.  $y/(D-a_0)=0.44$ ) away from the tip. It should be noted that for the same percentage of the peak load, the extension of the FPZ is larger for specimen CS\_2 with respect to specimen EP\_2. Following the work of [133], the plot of  $\varepsilon_{xx}$  suggested that for EP specimens the FPZ might be small enough to fully developed within the size of the ligament.

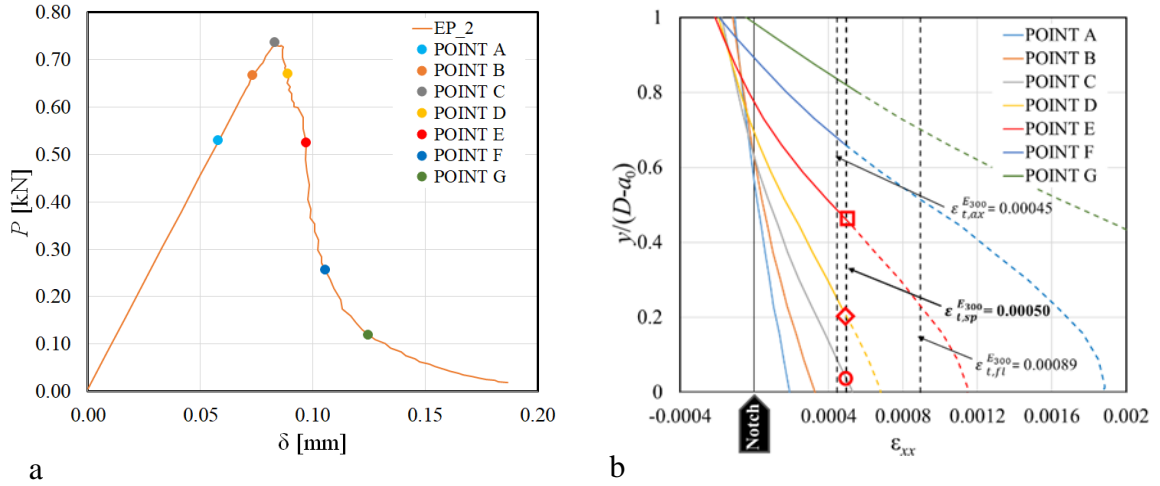


Figure 54 Specimen FM\_70\_70\_300\_EP\_2: (a)  $P - \delta$  response; (b)  $\varepsilon_{xx}$  versus  $y/(D-a_0)$  for  $d=10$  mm, subset=41, and step=10.

In order to determine the crack opening  $w$  that characterizes the softening curve and defines the FPZ [18] [119], the difference of the displacements  $\Delta u$  in the horizontal direction along the ligament were computed. Two sets of rectangular areas, each of dimensions 5 mm (length)  $\times$  2.5 mm (height), were considered, as shown in Figure 52. For each pair of rectangular areas, the average of the horizontal displacements obtained from DIC were computed and subtracted to obtain  $\Delta u$ . To be consistent with the strain profiles, the two rectangular areas were placed apart one another by a distance  $d=5$  mm or  $d=10$  mm, along the  $x$  direction (Figure 52).  $\Delta u$  was computed for pairs of rectangular areas in order to cover the entire length of the ligament. Thus, two consecutive and adjacent rectangles in the  $y$ -direction shared one 5 mm side.

$\Delta u$  versus  $y/(D-a_0)$  for the points of the load response of specimen CS\_2 shown in Figure 44b, is plotted in Figure 55a for  $d=10$  mm (no significant difference was observed between the  $d=5$ mm and  $d=10$  mm plots). The maximum elastic elongation  $\Delta u_{x,e}$  before the formation of the FPZ is computed as:

$$\Delta u_{x,e} = \varepsilon_{t,sp} \xi \quad (30)$$

where  $\xi$  is the distance between the centroids of the two rectangular areas (Figure 52), and  $\varepsilon_{t,sp}$  is provided above for specimen CS\_2. In a tensile test (which was the original test studied in [13]), when the load response is expressed in terms of stress versus elongation, the elongation is typically

measured with a gauge length that spans over at least half of the specimen. Thus, in the descending part of the response, when softening occurs because of the quasi-brittle nature of the material, the elongation would comprise a reduction due to the release of the strain energy in the bulk of the specimen and an increase due to the crack opening [170]. Equation 32 does not consider the release in the bulk as  $\Delta u$  is computed where the crack line is. A similar scenario would be observed by considering a very small gauge length across the crack line in a tensile test. It should be also pointed out that in a tensile test there is uniform energy release throughout the bulk of the specimen, while in a TPB test the energy release has a more complex redistribution. Thus, Equation 32 represents a simplified approach. An improvement of Equation 32 would require to consider the actual redistribution of the energy release along the ligament and the effect of averaging the displacement over the rectangles shown in Figure 52.

The value of  $\Delta u_{x,e}$  is equal to 0.0049 mm for specimen CS\_2 and is marked in Figure 55a with a vertical dashed line. The FPZ is bounded by the crack tip and the intersection of the  $\Delta u_{x,e}$  dashed line with the  $\Delta u$  profile. For example, for point C the FPZ extends for approximately 9 mm (i.e.  $y/(D-a_0)=0.21$ ). In fact, the distance between the circular marker, which defines the intersection of the vertical dashed line in Figure 55a with the  $\Delta u$  profile of point C, and the crack tip is roughly 9 mm. For Point D of specimen CS\_2, the extension of the FPZ is approximately 20 mm (i.e.  $y/(D-a_0)=0.43$ ) from the tip, while for Points E and F the extension of the FPZ is 30 (i.e.  $y/(D-a_0)=0.65$ ) and 42 mm (i.e.  $y/(D-a_0)=0.92$ ) respectively. These measurements of the FPZ are consistent with what observed about Figure 53a and b.

Figure 55b shows the  $\Delta u$  versus  $y/(D-a_0)$  plot for specimen EP\_2 with subset=41, step=10, and  $d = 10$  mm. The maximum elastic elongation  $\Delta u_{x,e}$  is equal to 0.0074 mm and it is marked with a dashed line in Figure 55b. For Points C, D and E, the FPZ extends for approximately 10 mm (i.e.  $y/(D-a_0)=0.21$ ), 14 mm (i.e.  $y/(D-a_0)=0.31$ ) and 27 mm (i.e.  $y/(D-a_0)=0.57$ ), respectively.

The crack opening  $w$  is obtained from  $\Delta u$  by subtracting  $\Delta u_{x,e}$  for the portion of the ligament where the FPZ has formed, i.e. when  $\Delta u \geq \Delta u_{x,e}$ . The magnitude of the crack opening  $w_f$ , associated with the physical separation of the crack surfaces and therefore the end of the FPZ, can be determined using the following formula [170]:

$$w_f = \frac{5.6G_F}{f'_t} \quad (31)$$

where  $G_F$  is the average fracture energy and  $f'_t$  is the splitting strength (which is assumed equal to  $f_{ct,sp}$  [73]). It should be noted that the value provided in Equation 31 is associated with a bilinear softening curve in which the change of slope occurs at  $0.25 f'_t$ . It should be pointed out that the critical opening  $w_f$  used in this work is not necessarily correct for AAMs, and it will be discussed later. The value adopted is widely used in the concrete community and its role in this work was to

establish a comparison among the AAMs investigated to monitor the development of the FPZ. For CS\_2, the value of  $w_f$  resulted equal to 0.050 mm when the average of  $G_F$  is considered and it is computed from the LVDT  $P - \delta$  curve, and 0.047 mm from DIC curve. The magnitude of  $w_f$  computed through Equation 31 for specimen EP\_2 resulted equal to 0.045 and 0.027, using the values of the average  $G_F$  reported in Table 16 from the DIC and LVDT response, respectively. It should be observed that for specimen EP\_2 the sizes of the FPZ measured from the strain and displacement profiles at different points of the load response are not as consistent as they are for CS\_2 specimen. This is particularly true in the first part of the test. There are two key points that should be considered: 1) for EP specimens the perlite was mainly present on the opposite side of the surface where DIC was employed; 2) the expression of  $w_f$  might not be applicable when coarse aggregate is not present as the formula has been derived for concrete [170].

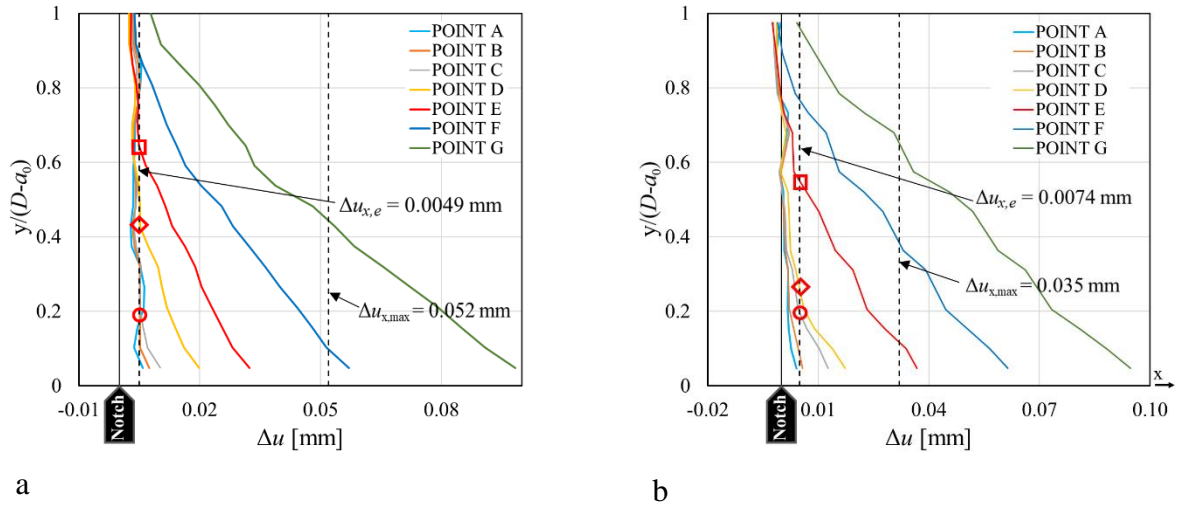


Figure 55.  $\Delta u$  versus  $y/(D-a_0)$  for subset=41, step=10 and  $d = 10$  mm: (a) FM\_70\_70\_300\_CS\_2 specimen; and (b) FM\_70\_70\_300\_EP\_2 specimen

Should the value of  $w_f$  computed through Equation 31 be considered correct, the quantity:

$$\Delta u_{\max} = \Delta u_{x,e} + w_f \quad (32)$$

defines the value of  $\Delta u$  at the crack tip that corresponds to the physical separation of the crack surfaces. Figure 55a would suggest that at Point F of specimen CS\_2  $\Delta u > \Delta u_{\max}$  at the crack tip. This would mean that the FPZ has reached the maximum development before Point F. It is possible that Equation 31 overestimates  $w_f$ , therefore the exact extension of the FPZ cannot be captured. The size of the maximum extension of the FPZ can be estimated for each specimen based on the intersection of the  $\Delta u$  profile with the dashed line of  $\Delta u_{\max}$  (reported in Figure 55) at the crack tip. After the FPZ reaches the maximum extension, it is forced to shrink and change due to the propagation of the crack and the limit imposed by the length of the ligament and the presence of the compression zone on top. A rough estimate of the maximum extension of the FPZ is between

34 mm and 42 mm (i.e.  $y/(D-a_0)$  between 0.72 and 0.92) for CS specimens (employing DIC analysis for two CS specimens). Since the maximum aggregate size  $d_{\max}$  is 6 mm for the CS mortar, the FPZ would have a size between  $5d_{\max}$  and  $7d_{\max}$ , which is smaller than what observed for concrete [156]. A similar procedure was carried out for EP and FS specimens. For EP specimens, the size of FPZ can be estimated to be between 27 and 29 mm (i.e.  $y/(D-a_0)$  between 0.57 and 0.62), i.e. between  $9d_{\max}$  and  $11d_{\max}$ . FS specimens exhibit the most interesting results. As observed above, their fracture energy does not differ significantly from the fracture energy of CS specimens. In addition, the extension of the FPZ from the DIC analysis is between 35 and 40 mm. Because of the smaller aggregate size, the FPZ size is in between  $18d_{\max}$  and  $20d_{\max}$ . This result calls for additional research on the FPZ of AAMs. It could be observed that the FPZ should be a function of the aggregate size and the ratio between the length of the FPZ and  $d_{\max}$  should be similar for different concrete mixes that differ by the maximum aggregate size. This seems to be contradicted by the results of CS and FS specimens. While more research is needed, there are two factors that should be taken into account. The fracture process involved the fracture of the aggregates as it can be seen in Figure 47b. When large aggregates are used, fracture occurs in the paste and a tortuous crack path around the aggregate is observed. In this work, the size of the aggregate might have been small enough to create some tortuosity in the crack path while still fracturing the aggregates. This could be a first reason why the ratio between the length of the FPZ and  $d_{\max}$  varied. The second factor to be taken into account is that the use of DIC herein presented allows to determine the maximum extension of the FPZ during the TPB test but this might not be the actual full extension of the FPZ since the compression zone might limit its extension. This aspect was discussed in [161] and requires further investigation.

Figure 56 shows the  $\epsilon_{xx}$  contour plots for points C, D, E, and F of the load response of specimen CS\_2 (Figure 44b). In this work the entire surface of the specimen was considered for DIC analysis. Having a large area of interest for DIC might imply that the resolution is reduced. However, as pointed out in [57] [161], increasing the resolution might not always be the right choice. For non-homogenous materials like concrete and mortar, high resolution would allow to investigate the interaction between the mortar and the aggregate, which is outside the scope of this work. Since macro-scale engineering quantities are used herein, the resolution used was sufficient to obtain values of the strain that were representative of the AAMs considered as homogenous materials. In addition, having the full view of the specimen was important to consider any damage near the supports. Because of the LVDT, on the left side of the notch (Figure 56) the correlation of the DIC images and therefore the displacement field was not evaluated. Consequently, this area was covered with a black patch. The width  $b$  and the depth  $h$  of the FPZ is measured for each contour plot corresponding to different Points of the load response as shown in Figure 56. The values of  $b$  and  $h$  are determined considering the area of the contour plot where  $\epsilon_{xx} \geq \epsilon_{t,sp}$ . The values of  $\epsilon_{xx}$  are capped at  $\epsilon_{t,sp}$ . For Point C,  $b = 12$  mm and  $h = 7$  mm. For points D, E, and F,  $b$  is equal to 17 mm,

19, and 20 mm, while  $h$  is equal to 15 mm, 27 mm, and 35, respectively, which suggests that the FPZ has an increasing width as it reaches the full extension approximately at Point F. An interesting point that should be raised is whether the work of fracture could be used to determine the fracture energy. As it can be seen from Figure 56, at Point F the FPZ is most likely fully established and when the crack will propagate it will be forced to shrink due to the limited extension of the ligament and the presence of the compression zone. This means that the remaining part of the load response from Point F until failure does not correspond to a self-similar crack propagation as it should be to use correctly the concept of work of fracture. It should be noted that the contour plots were cropped below the tip of the notch because of the bar used to mount the LVDTs. However, contour plots of companion AAM specimens reported in [171] show that the FPZ does not extend below the tip of the notch.

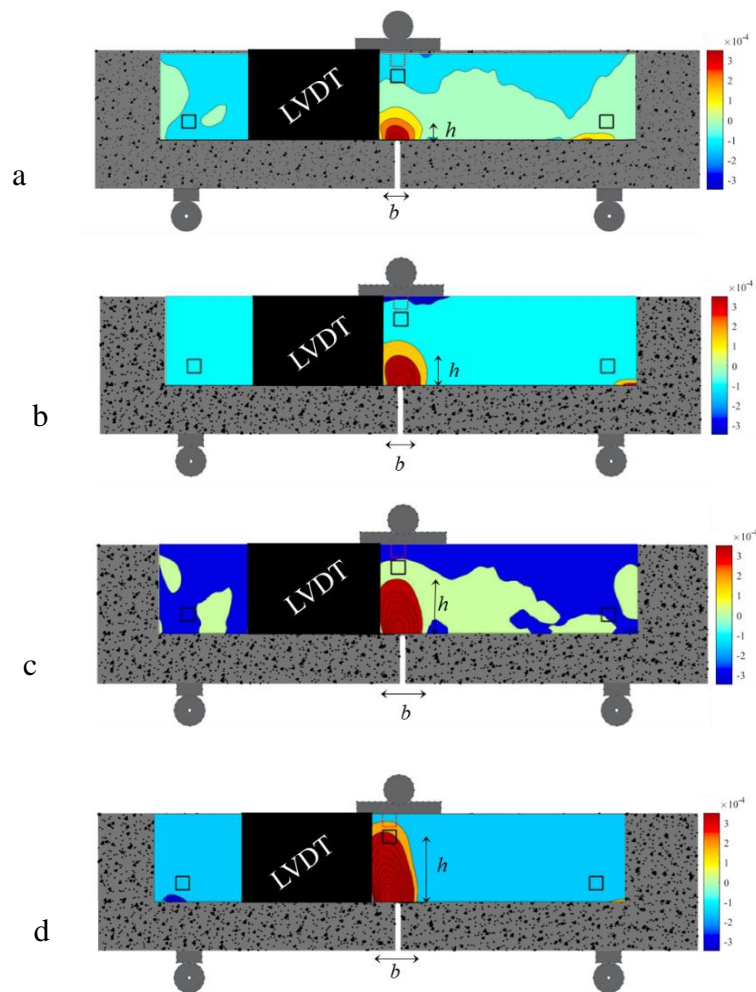


Figure 56 Contour plots of strain component  $\varepsilon_{xx}$  for specimen FM\_70\_70\_300\_CS\_2, points: (a) C; (b) D; (c) E; and (d) F

The same comments can be made for 35×35×200 specimens. As an example, the strain and  $\Delta u$  profiles were plotted in Figure 57 for specimen FM\_35\_35\_200\_CS\_2. The value of  $w_f$  for the FM\_35\_35\_200\_CS family was equal to 0.051 mm and  $\Delta u_f = 0.056$  mm, which means that the FPZ was not fully established at point E.

The values of  $w_f$  for the 35×35×200\_FS and 35×35×200\_EP families were equal to 0.051 mm and 0.034 mm, respectively, which provide  $\Delta u_f = 0.056$  mm and  $\Delta u_f = 0.041$  mm. The plots of  $\epsilon_{xx}$  and  $\Delta u$  for these two families of specimens confirm that for the smaller specimens the FPZ was not fully developed.

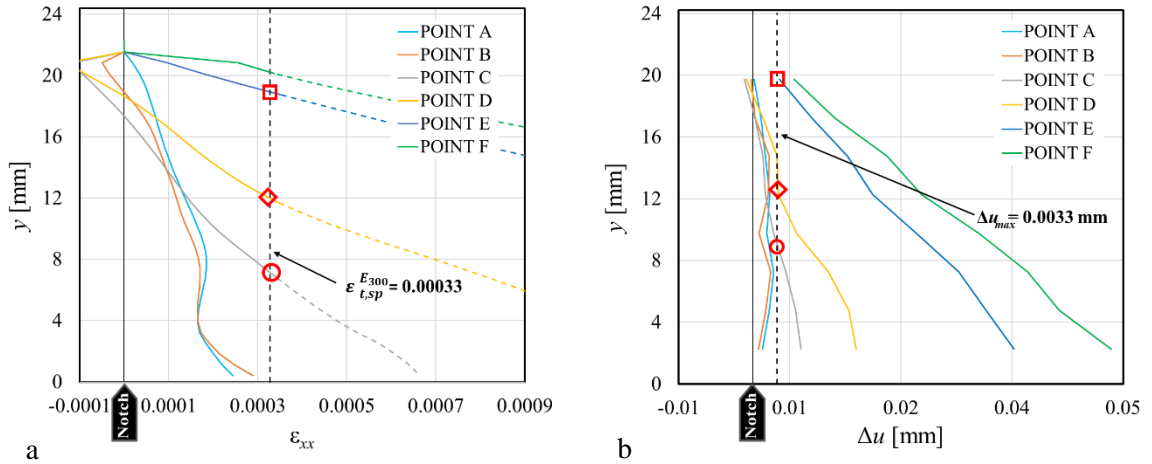


Figure 57 Strain (a) and  $\Delta u$  (b) profiles along the crack ligament for specimen FM\_35\_35\_200\_CS\_2 for different points of the load response

Contour plots of the horizontal strain component  $\epsilon_{xx}$  for 4 points (B, C, D, and E) of the load response of Figure 45 (specimen FM\_35\_35\_200\_CS\_2) are shown in Figure 58. The points selected correspond to 90% of  $P_{max}$  in the ascending branch of the curve,  $P_{max}$ , and 90% and 50% of  $P_{max}$  in the descending branch. The color scale was chosen so that the maximum tensile strain was approximately equal to  $\epsilon_{t,sp}^{E_{300}}$  in order to be consistent with the dashed line reported in Figure 57a. This expedient allowed to identify the region in red as the region where the strain was higher than  $\epsilon_{t,sp}^{E_{300}}$  and therefore corresponded to the FPZ. It is interesting to note that the FPZ expands in the post peak region both in length and width. It appears to be almost of the same width between points D and E. At point E, as observed earlier, the FPZ extends for almost the entire height of the specimen and therefore since at this point the value of  $\Delta u_f$  is still not reached the FPZ does not have room to fully develop.

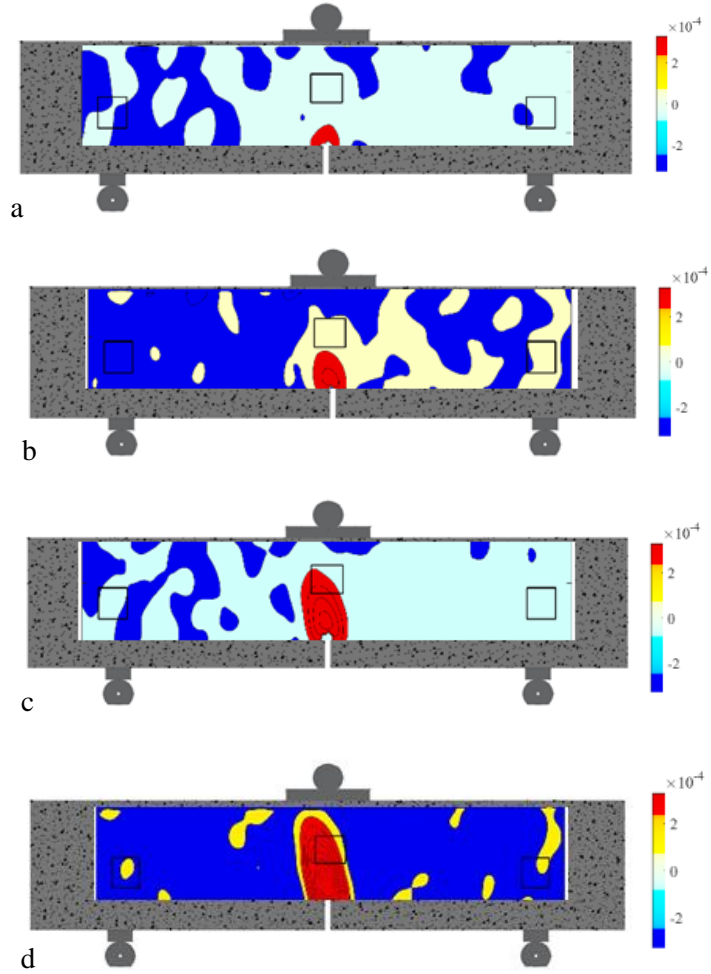


Figure 58 Contour plots of strain component  $\varepsilon_{xx}$  for specimen FM\_35\_35\_200\_CS\_2, for points B (a), C (b), D (c) and E (d) of the load response

### 3.3.8.2 Concrete specimens

In this Section, the study of horizontal strain component  $\varepsilon_{xx}$  obtained from the DIC analysis on the front face of specimen FM\_150\_150\_600\_G4\_2 is presented. The coordinates reported in this section refer to the Cartesian System shown in Figure 52. Before discussing the strain behavior of specimen FM\_150\_150\_600\_G4\_2, it is worth evaluating the tensile strain,  $\varepsilon_t$ , which corresponds to the tensile strength of concrete. Two elastic moduli were considered for the evaluation of  $\varepsilon_t$ , i.e. the elastic modulus,  $E_c$ , evaluated in Section 2.1 according to [172] and the elastic modulus  $E_c^{f_{cm}}$  evaluated according to [173] using the following equation:

$$E_c^{f_{cm}} = 4730\sqrt{f_{cm}} \quad (33)$$

$E_c^{f_{cm}}$  resulted equal to 21.0 GPa. The ultimate tensile strain,  $\varepsilon_t$ , can be then evaluated as:

$$\varepsilon_t^{E_c} = \frac{f_{t,232days}}{E_c} \quad (34)$$

$$\varepsilon_t^{E_{fc}^{cm}} = \frac{f_{t,232days}}{E_c^{f_{cm}}} \quad (35)$$

where  $f_{t,232days}$  is the tensile strength obtained from splitting tests at 232 days, i.e. approximately the same age when fracture mechanics tests were performed,  $\varepsilon_t^{E_c}$  is the tensile strain evaluated considering  $E_c$ , while  $\varepsilon_t^{E_{fc}^{cm}}$  is the tensile strain evaluated considering  $E_c^{f_{cm}}$ .  $\varepsilon_t^{E_c}$  resulted equal to 98  $\mu\varepsilon$ , while  $\varepsilon_t^{E_{fc}^{cm}}$  resulted equal to 91  $\mu\varepsilon$ . Since  $\varepsilon_t^{E_c}$  and  $\varepsilon_t^{E_{fc}^{cm}}$  are consistent, only the tensile strain evaluated considering  $E_c$ , will be considered in the remainder of this section. It should be pointed out that the elastic modulus could be computed from the linear portion of the load responses using Equation 9. The elastic modulus computed from the load response is in agreement with the elastic modulus from the compression tests although lower. However, as pointed out earlier, the LVDT readings might not be accurate in the first part of the tests. This fact was observed while comparing the LVDT and the DIC readings in Figure 43. It can be observed that the slope of the initial branch might be different and consequently the modulus of elasticity would be affected by the choice of the plot (i.e. LVDT vs DIC).

Figure 59 shows the  $\varepsilon_{xx}$  contour for different points of the load response of specimen FM\_150\_150\_600\_G4\_2 shown in Figure 60b. It can be observed that at the peak load (point C in Figure 60b) almost all the cross-section at midspan is characterized by  $\varepsilon_{xx}$  lower than  $\varepsilon_t^{E_c}$  except for a region close to the crack tip (with a length approximately equal to 20-25 mm) where the ultimate tensile strain has already been reached.  $\varepsilon_t^{E_c}$  is characterized by a light blue color in Figure 59. In Figure 59b-c it can be observed that, at points D and E in the descending branch of the load response shown in Figure 60b, the region characterized by  $\varepsilon_{xx}$  exceeding  $\varepsilon_t^{E_c}$  enlarged, moving gradually towards the point where the load is applied. Figure 59 shows also the square areas (represented with red squares) that have been used to evaluate the vertical displacements through DIC and to plot the load versus displacement responses in Section 3.3.3. The contour plots are in good agreement with the work by Cedolin et al. [2].

The  $\varepsilon_{xx}$  profile along the crack ligament for different values of the load is reported in Figure 60a. It can be observed that at the peak load (point C) part of the fracture process zone (FPZ) has formed, and near the crack tip  $\varepsilon_{xx}$  has exceeded  $\varepsilon_t^{E_c}$  (black dotted line in Figure 60a).

It is interesting to note, as pointed out in [170], that as the depth of the specimen decreases the portion of the FPZ corresponding to the peak load changes with the size.

Values plotted in Figure 60a were obtained by averaging the strain over a 7.5 mm wide strip of concrete centered with respect to the crack tip. The width of the strip was chosen equal to half of the maximum aggregate size  $d_a$ . Figure 60e-f-g shows the  $\varepsilon_{xx}$  for different values of  $y$  at point C, D, and E, respectively (Figure 60b). It can be observed that the width of the FPZ can be roughly estimated to be in the range of 25-30 mm [2].

From the DIC analysis it was also possible to evaluate the crack opening,  $w$ , close to the crack tip at any location of the load-displacement response. The crack opening was evaluated by calculating the difference between the average horizontal displacements of two  $4\text{ mm} \times 4\text{ mm}$  square areas located, respectively, on the left and on the right of the crack tip [174].

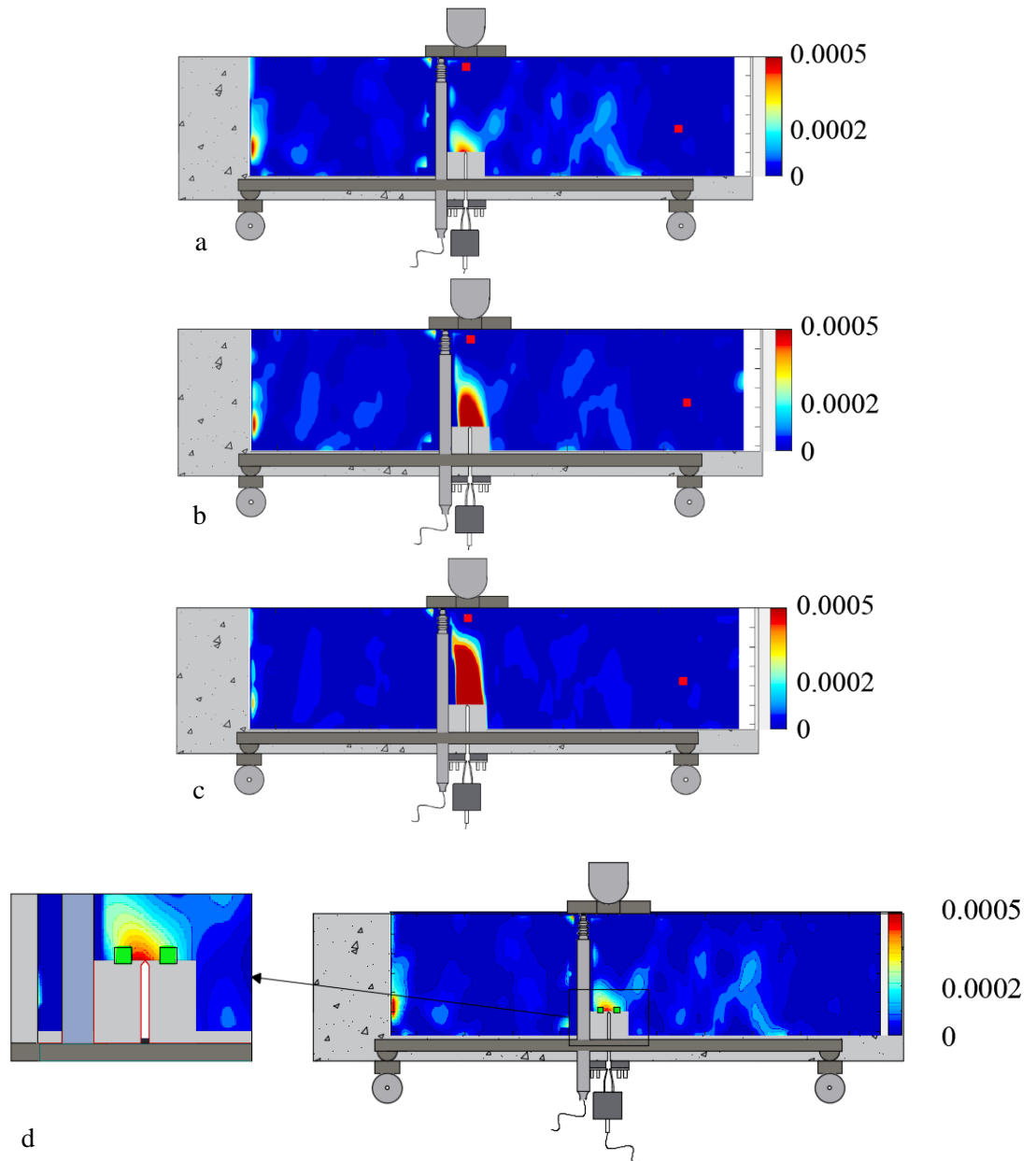
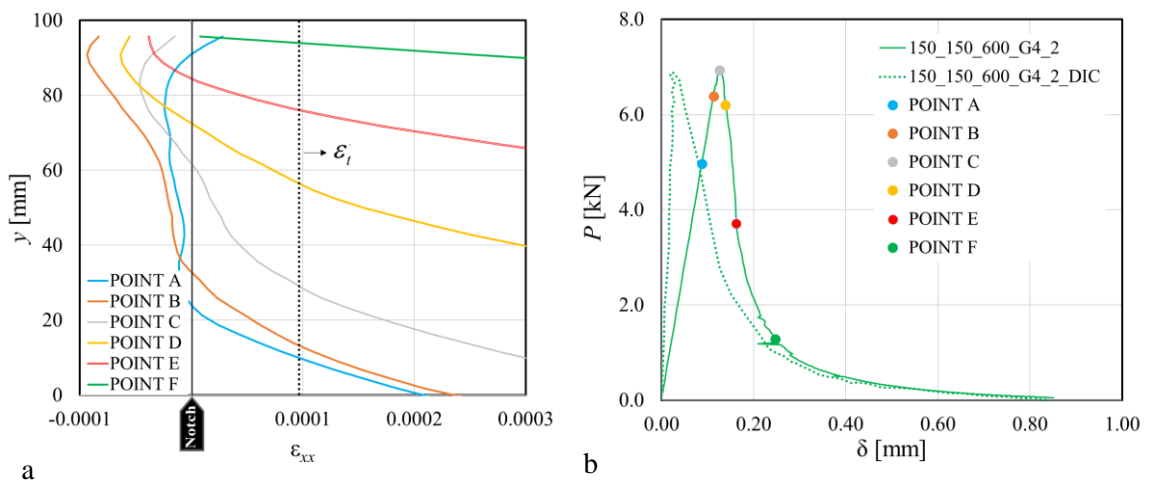


Figure 59. Contour plot of  $\varepsilon_{xx}$  at different points of the load response (Figure 60b) for specimen FM\_150\_150\_600\_G4\_2: Point C (a), Point D (b), Point E (c). Square areas for the evaluation of  $w$  (d).

The two square areas were placed 7.5 mm apart. The crack opening,  $w$ , was evaluated for specimen FM\_150\_150\_600\_G4\_2 and specimen FM\_70\_70\_300\_G8\_1 at point F of the load-displacement response, and compared with the ultimate crack opening,  $w_f$ , i.e. the crack opening beyond which no stress transfer is possible. The value of  $w_f$  was evaluated using the Equation 31 [170].

The value of  $w_f$  for specimen FM\_150\_150\_600\_G4\_2 resulted equal to 0.24 mm, while for specimen FM\_70\_70\_300\_G8\_1 resulted equal to 0.16 mm. In the evaluation of  $w_f$ , the fracture energy  $G_F$  computed from the load response of the LVDTs and obtained for the same specimen was employed. It is worth noting that, as already mentioned, the fracture energy of specimens with a large weight could be affected by friction. Therefore, in order to overcome the influence of the friction, the evaluation of  $w_f$  could be performed by considering the average fracture energy  $G_F$  obtained from all specimens with the same depth, that will be referred as  $\overline{G_{F,150}}$  and  $\overline{G_{F,70}}$  for 150 mm-depth specimens and 70 mm-depth specimens, respectively. Using the average values of the fracture energy, the value of  $w_f$  for specimen FM\_150\_150\_600\_G4\_2 resulted equal to 0.26 mm ( $\overline{G_{F,150}} = 86.6$  N/m), while for specimen FM\_70\_70\_300\_G8\_1 resulted equal to 0.20 mm ( $\overline{G_{F,70}} = 66.8$  N/m). The value of  $w$  obtained from DIC at point F for specimen FM\_150\_150\_600\_G4\_2 and FM\_70\_70\_300\_G8\_1 resulted equal to 0.14 mm and 0.10 mm, respectively. Although these results should be carefully considered, it appears that at point F of the load responses, which correspond to a specific percentage of the peak value (15%), the FPZ is not fully established and the portion of the FPZ that develops is related to the depth of the specimen. When the FPZ is still not fully formed, the portion of concrete near the outermost fibers at the top of the specimen experience a quite complex stress distribution due to the load concentration from the Z-shaped plate. This aspect is highlighted by the strain profile in Figure 60, which shows that tensions in the horizontal direction arise near the plate (some of the plots were cropped). This observation made the authors question the calculation of the fracture energy from the area under the curve. In fact, most of the tail of the response is associated with a stagnating FPZ near the top of the cracked cross-section where a complex stress distribution occurs.



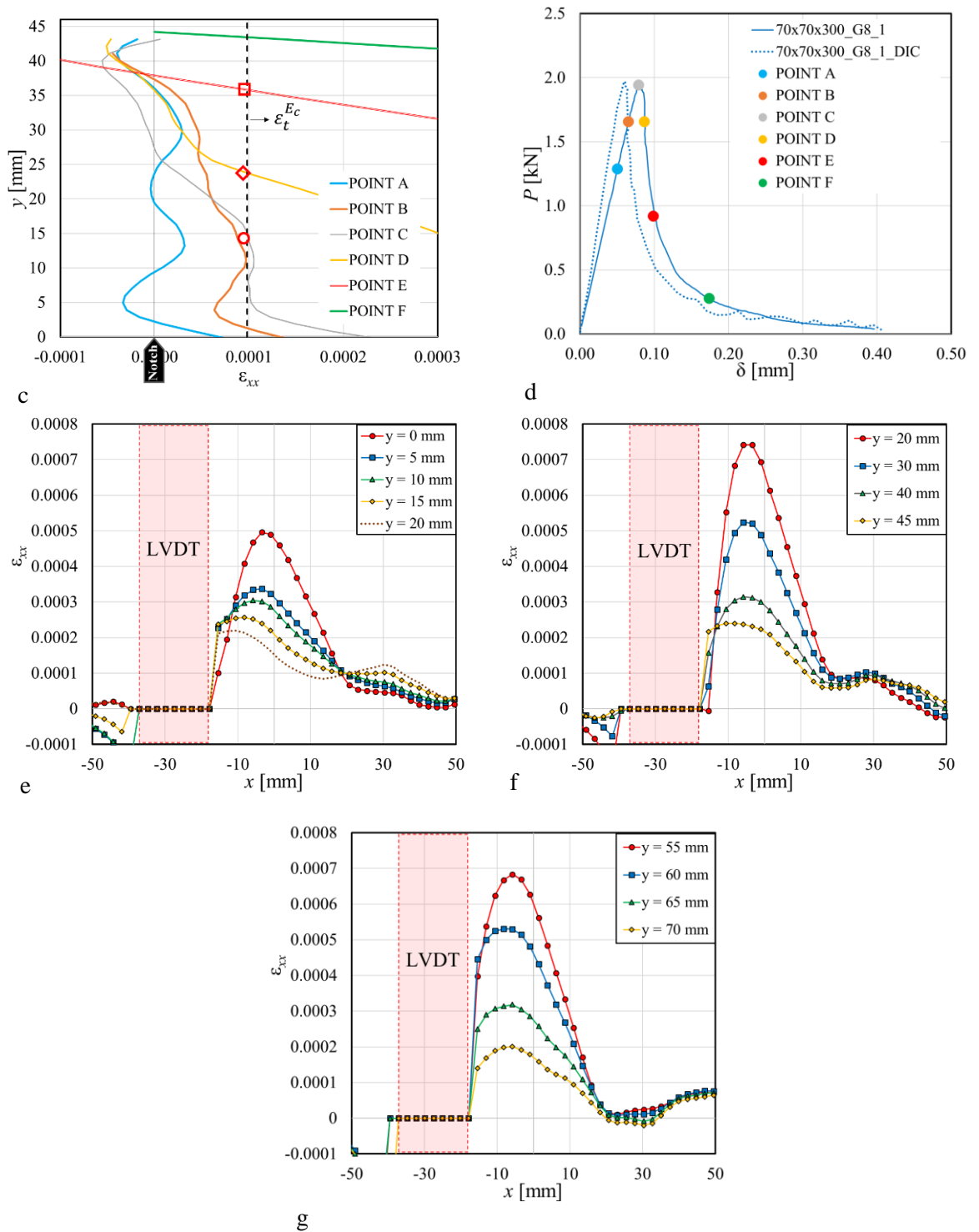


Figure 60.  $\epsilon_{xx}$  profile along the crack ligament for different values of the load for specimen FM\_150\_150\_600\_G4\_2 (a). Load-displacement response obtained from LVDT readings for specimen FM\_150\_150\_600\_G4\_2 (b).  $\epsilon_{xx}$  profile along the crack ligament for different values of the load for specimen FM\_70\_70\_300\_G8\_1 (c). Load-displacement response obtained from LVDT readings for specimen FM\_70\_70\_300\_G8\_1 (d).  $\epsilon_{xx} - x$  plot for specimen FM\_150\_150\_600\_G4\_2 at point C (e), point D (f), and point E (g).

In addition, the results herein presented suggest that in the tail of the response friction might play an important role for wider specimens that are heavier.

### 3.3.9 Size and width effect

#### 3.3.9.1 Concrete specimens

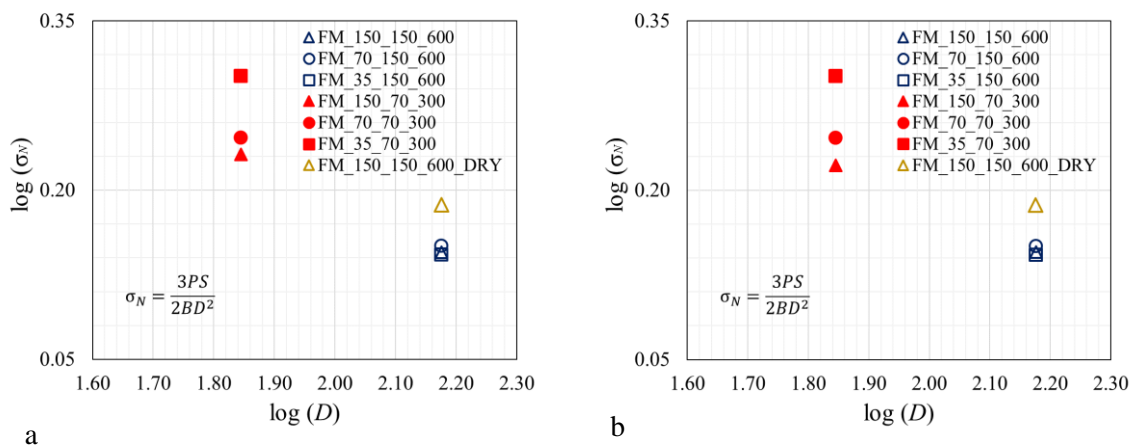
The size effect is shown through the plot  $\log(\sigma_N)$  versus  $\log(D)$ . The nominal stress  $\sigma_N$  has been computed using the flexural formula considering the unnotched cross-section (Equation 3).

The expression of the nominal stress is not unique and the length of the ligament  $D-a_0$  could have been used instead of  $D$ . In this regard, it should be noted that the CoV for the measurements of  $a_0$  varies from 0.28 to 6.06 %; whereas, the CoV of the measurements of  $D$  ranges between 0.09 and 1.26% (Table 13). For a single specimen, the measurements of  $D$  are less scattered than the measurements of  $a_0$ . The average value of  $D$  can be considered more representative of the dimension of the specimen than the average value of  $D-a_0$ . Therefore,  $D$  was considered a better choice than  $D-a_0$  in order to minimize the variability due to the geometry in the calculation of  $\sigma_N$ .

In Figure 61a, the average of the log values for each width and depth are reported, for specimens cured in lime saturated bath and DRY specimens. In Figure 61b, the same plot is reported considering only four specimens out of the five with cross-section equal to 150 mm × 70 mm; in fact, specimen FM\_150\_70\_300\_G6\_4 is not considered in the plot. Figure 61c shows the load per unit width,  $P/B$ , versus the point load displacement,  $\delta$ , for specimens with a cross-section equal to 150 mm × 70 mm. The peak load of specimen FM\_150\_70\_300\_G6\_4 is higher than the other specimens with the same cross-section. Thus, if one would have not tested or considered specimen FM\_150\_70\_300\_G6\_4 the trend of Figure 61a would have changed to the one in Figure 61b with an even-more pronounced difference between specimens with smaller size and different widths.

It can be observed that results of specimens with  $B=35$  mm are more scattered than the others. These results should be used carefully since  $B < 4d_a$ .

Figure 61a-b suggests that, while for the deeper beams a width effect is negligible, the smaller depth beams reveal a quite substantial width effect. However, even though these are preliminary results, a careful interpretation of the size effect fitting curve [170] should be made when the width of the specimens is kept constant. Additional comments are provided with reference to Figure 62.



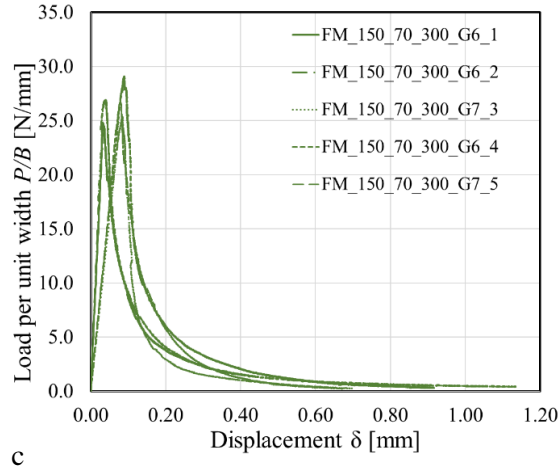


Figure 61 Logarithmic plots of  $\sigma_N$  versus  $D$  to investigate size and width effects: average  $\sigma_N$  for each width and depth (a); average of  $\sigma_N$  for each width and depth without specimen FM\_150\_70\_300\_4 (b); and  $P/B$  versus  $\delta$  response for specimens with a cross-section equal to  $150 \text{ mm} \times 70 \text{ mm}$  (c).

Figure 62 shows the plot of  $\sigma_N$  versus CMOD. The plots were intentionally cropped to focus on the first part of the response and in particular on the peak load. In each graph, three families are compared to investigate whether the size effect could be potentially coupled with a width effect. In Figure 62a, when families with the same geometries are compared (i.e.  $70 \times 70 \times 300$  and  $150 \times 150 \times 600$ ), it can be observed that as the size increases the average peak stress decreases by 21.08%, which implies a size effect. In this case, the size effect is observed between two sets of beams that have a square cross-section. On the other hand, when families of the same size ( $D=150 \text{ mm}$ ) but different widths are compared, i.e.  $70 \times 150 \times 600$  and  $150 \times 150 \times 600$ , there is only a slight difference since the average peak stress decreases by 1.32%. In Figure 62b, the size effect is investigated between beams that have either two different depths but same proportion between width and depth (i.e.  $35 \times 70$  and  $70 \times 150$ ) or the same width but different depth (i.e.  $70 \times 70$  and  $70 \times 150$ ). First, it is observed that if  $D$  is constant and equal to  $70 \text{ mm}$ , the average peak stress decreases by 11.56% if two different widths are considered. In fact, the average peak stress for  $35 \times 70$  is  $2.00 \text{ MPa}$ , while the average peak stress for  $70 \times 70$  is  $1.77 \text{ MPa}$ . This suggests that an increase of the width entails for a decrease of the stress. In Figure 62a, it was observed that no width effect existed when  $D=150 \text{ mm}$ . Further, if two sizes of the beam are considered, the average peak stress decreases by 29.27% and 20.02% when the same cross-section proportion ( $35 \times 70$  vs.  $70 \times 150$ ) or the same width ( $70 \times 70$  vs.  $70 \times 150$ ) are considered, respectively. This suggests that the set of specimens with  $D=70 \text{ mm}$  exhibit a width effect combined with a size effect. In other words, a decrease in the nominal stress is expected with size. However, by considering two sizes and specimens that have proportional cross-sections (i.e. the width changes accordingly with the depth) the decrease with the depth is 29.27%. On the other hand, if the width is kept constant, the decrease is 20.02%.

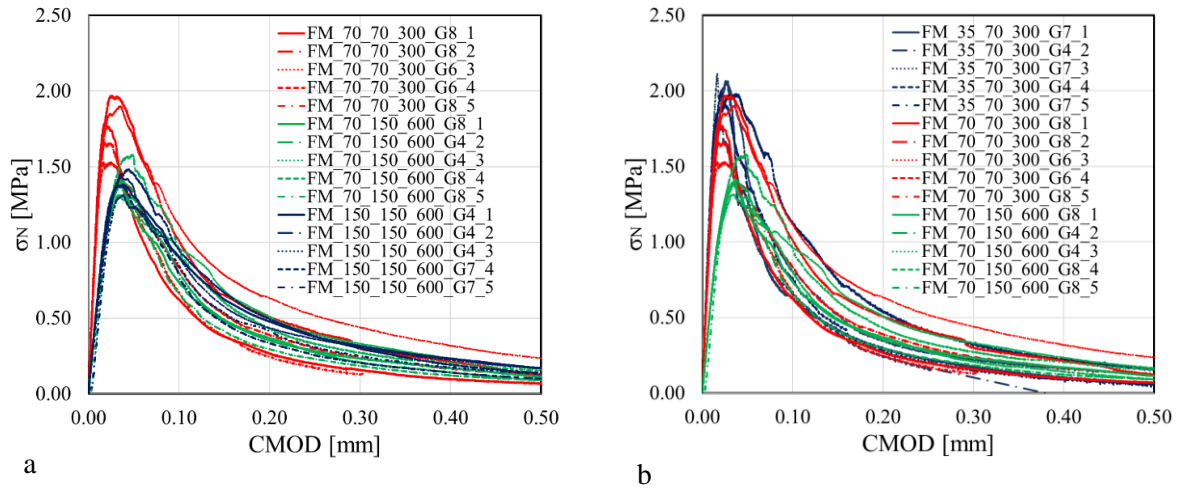
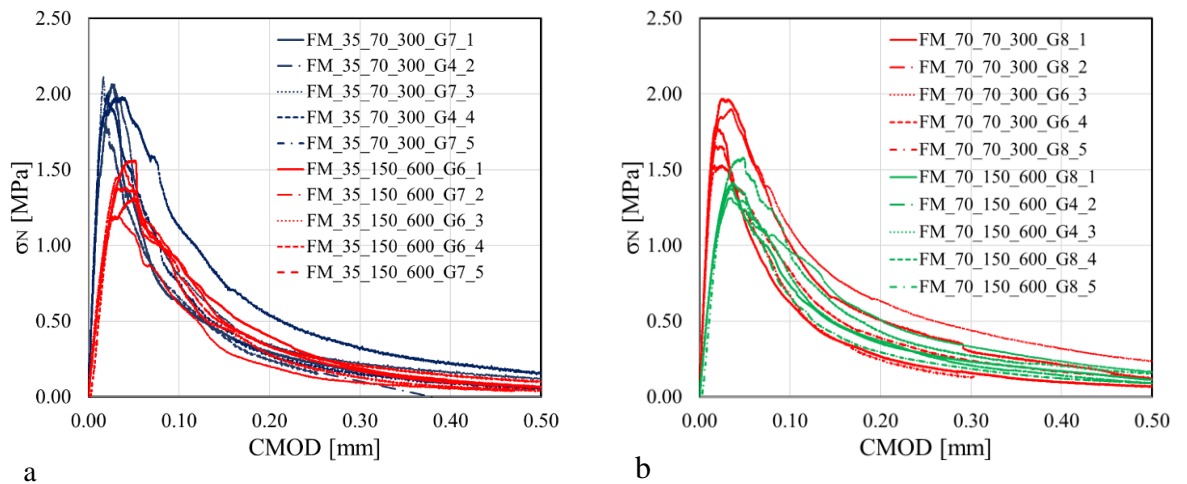


Figure 62 Comparison of the nominal stress vs. CMOD for families with the same geometries (i.e.  $70 \times 70 \times 300$  and  $150 \times 150 \times 600$ ) or the same depth ( $D=150$  mm) and two widths ( $B=70$  mm,  $B=150$  mm) (a) and specimens with rectangular cross-section (i.e.  $35 \times 70 \times 300$  and  $70 \times 150 \times 600$ ) or the same width ( $B=70$  mm) and two depths ( $D=70$  mm and  $D=150$  mm) (b)

To further investigate what it was observed about Figure 62b, different combinations of width and size are considered in Figure 63. As expected, increasing the depth of the specimen implies that the peak stress decreases. For 35 mm wide specimens, as the depth increases, the average peak stress decreases by 30.32%. For specimens 70 mm and 150 mm wide, the average peak stress decreases by 20.02% and 20.44%, respectively. It can be concluded that as the width of the specimen increases, the difference in terms of peak stress between families of the same width but different depth is smaller.

The plots of Figure 62 and Figure 63 make the authors question whether the width should be constant when specimens of different sizes are tested, which is common practice when size effect tests are performed on notched beams.



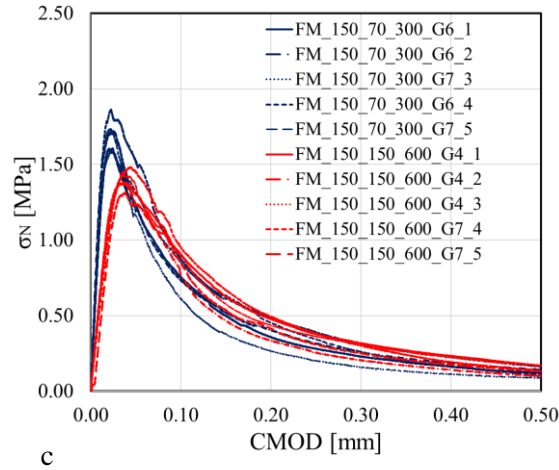


Figure 63 Size effect study in terms of nominal stress vs. CMOD for 35 mm wide specimens (a), 70 mm wide specimens (b), and 150 mm wide specimens (c)

The experimental program herein presented covers specimens with only two depths and three widths for each depth. Nevertheless, the results herein presented indicate that size effect and width effect are possibly coupled.

### 3.3.9.2 Alkali-activated mortars

The same comments can be made for alkali-activated mortars. In fact, the average peak load  $\bar{P}_{\max}$  of each family of specimens can be used, in terms of nominal stress  $\sigma_N$ , to build the double log plot to study the size effect [14] [18] [130] [131]. The plot is shown in Figure 64. It is interesting to note how the slope of the line connecting the points corresponding to two sizes of the same AAM is very similar.

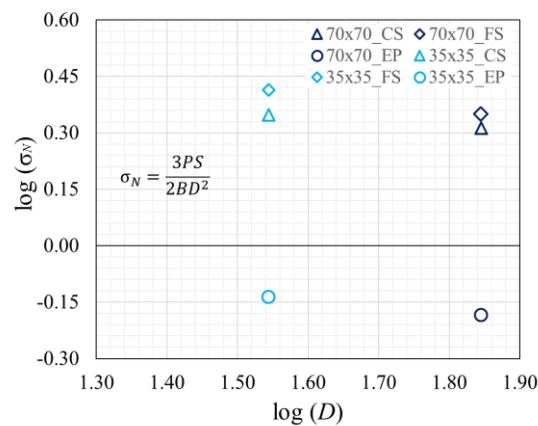


Figure 64 Logarithmic plot of  $\sigma_N$  versus  $D$  for the three AAMs

This is expected for specimens FS and CS because they have a similar size of the FPZ and even the larger size of the specimens for these two mortars can barely accommodate the fully developed FPZ. On the other hand, the FPZ of EP specimens is estimated to be relatively smaller than the

height of the larger specimens. Nevertheless, the slope of the lines connecting the points relative to EP specimens is similar to the other AAMs. A possible justification can be found in the results of Table 13.

The CoV of  $\bar{P}_{\max}$  for both sizes of the EP specimens is relatively high compared to the others. Thus, the plot of  $\sigma_N$  should be critically considered for these specimens. It should be pointed out that after the failure of the specimens, the fracture surfaces of the EP specimens revealed that the distribution of the perlite was not uniform across the width, which could be potentially a cause of the large variability of the results of the EP specimens.

### **3.3.10 A new method to determine the critical crack opening**

#### **3.3.10.1 Concrete specimens**

Further considerations were made using the DIC available data. When a notched beam is tested under TPB, it would be interesting to know when the crack opens. Thus, the variation of the horizontal strain  $\varepsilon_{xx}$ , in the region close to the notch tip, over the time is evaluated. Therefore, the output data of all DIC images of each specimen were analyzed with the software Matlab. The strain was determined as the average of the values of strain evaluated in a rectangle area, close to the notch tip and centered in the tip itself. Two dimensions of the rectangle were considered, 5 mm (depth  $d$ )  $\times$  10 mm (length  $l$ ) and 5 mm (depth  $d$ )  $\times$  15 mm (length  $l$ ), to understand if the variation of the rectangular area considered influences the calculation of the average strain. For sake of brevity, only two concrete specimens are shown (FM\_70\_70\_300\_G8\_1 and FM\_70\_70\_300\_G8\_2).

Strain versus time is plotted in Figure 65 and the variation of the strain over time ( $\Delta\varepsilon_{xx}/\Delta t$ ) versus time is shown in Figure 66. By analyzing the curves of Figure 65, three parts are identified: at the beginning of the test, when  $\varepsilon_{xx} < \varepsilon_{t,sp}$  the horizontal strain increases almost linearly. When  $\varepsilon_{xx}$  reaches  $\varepsilon_{t,sp}$  the trend becomes nonlinear, and finally, when the crack opens, the trend becomes again linear until the end of the test. In Figure 65b and d the graph is cropped to visualize when the plot becomes linear, identifying therefore the time that corresponds to the opening of the crack, highlighted in the plot with red dashed line, and equal to 270s for FM\_70\_70\_300\_G8\_1, and 350s for FM\_70\_70\_300\_G8\_2.

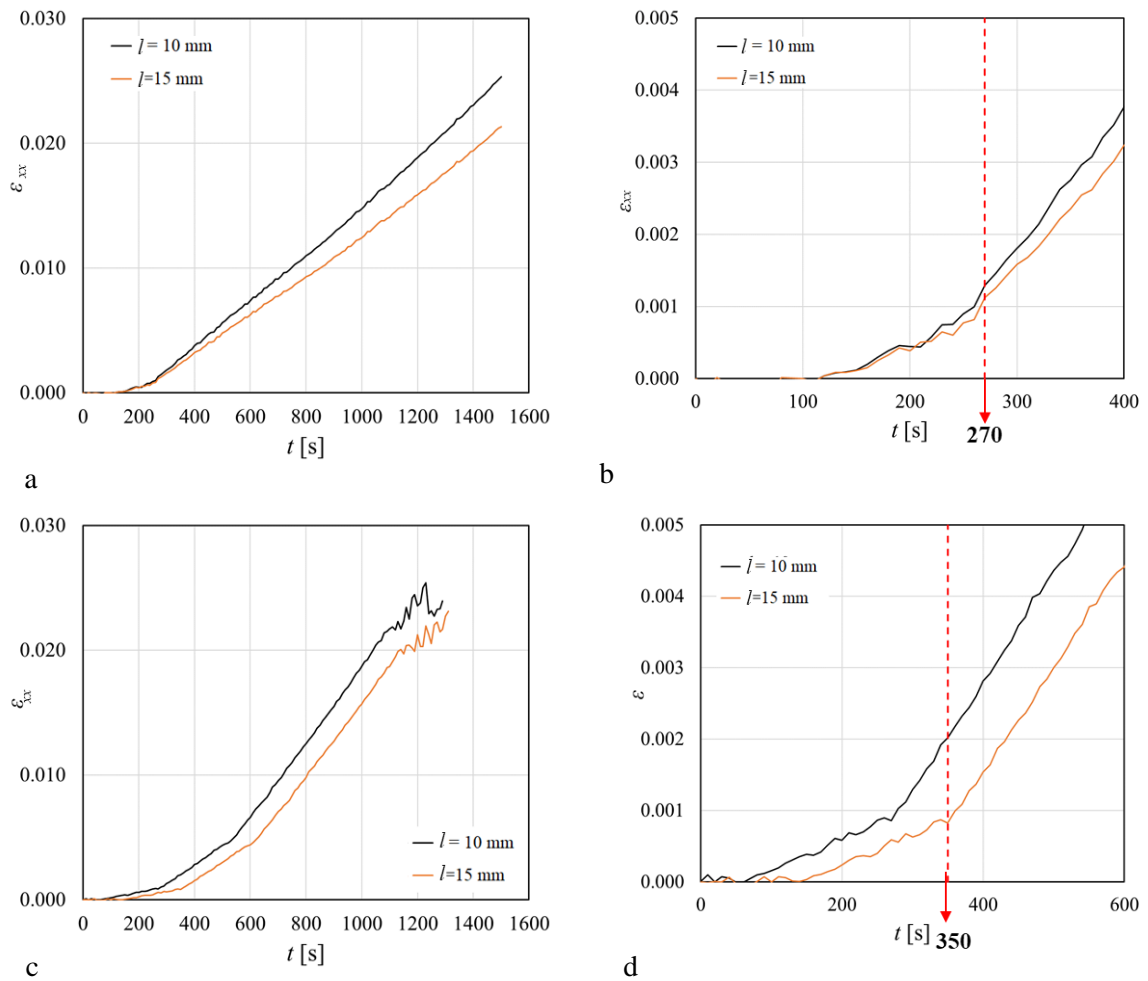


Figure 65 Time versus strain for specimen (a) FM\_70\_70\_300\_G8\_1; (c) FM\_70\_70\_300\_G8\_2; Cropped graph for (b) 70\_70\_300\_G8\_1 and (d) 70\_70\_300\_G8\_2 specimen

In Figure 66 the variation of strain over the time ( $\Delta\epsilon_{xx}/\Delta t$ ) versus time is shown. By plotting the variation of strain versus time, it was noted that all the curves were scattered, and therefore the expedient of the moving average function was adopted to plot  $\Delta\epsilon_{xx}/\Delta t$  (Figure 66). The moving average function gives as a result a set of values obtained from partial averages, based on the interval chosen. Three intervals were used, 5, 10 and 20 to understand which interval is the most suitable for the analysis. When the interval chosen was equal to 5, the corresponding curve, which is the black solid line in Figure 66, showed a lot of peaks and drops, and the trend of the variation of the strain versus time was clearly defined. Conversely, when the other two intervals were chosen (i.e. 10 and 20), it was not easy to capture the information needed for the analysis. In the same plot, different curves were plotted changing the length of the rectangle (i.e. 10 and 15 mm). Two concrete specimens of the same dimensions are herein compared. It should be pointed out that for FM\_70\_70\_300\_G8\_1 specimen, only one change in the velocity occurred during the three-point bending test, while for FM\_70\_70\_300\_G8\_2 the velocity was changed three times. This is an important aspect to consider for the analysis. In fact, the change in the velocity is clearly identified

with the plateau. Knowing the time at which the crack opened, which is approximately 270s (70% of  $P_{max}$  in the descending branch of the response) for FM\_70\_70\_300\_G8\_1 and 350s for FM\_70\_70\_300\_G8\_2 (80% of  $P_{max}$  in the descending branch of the response).

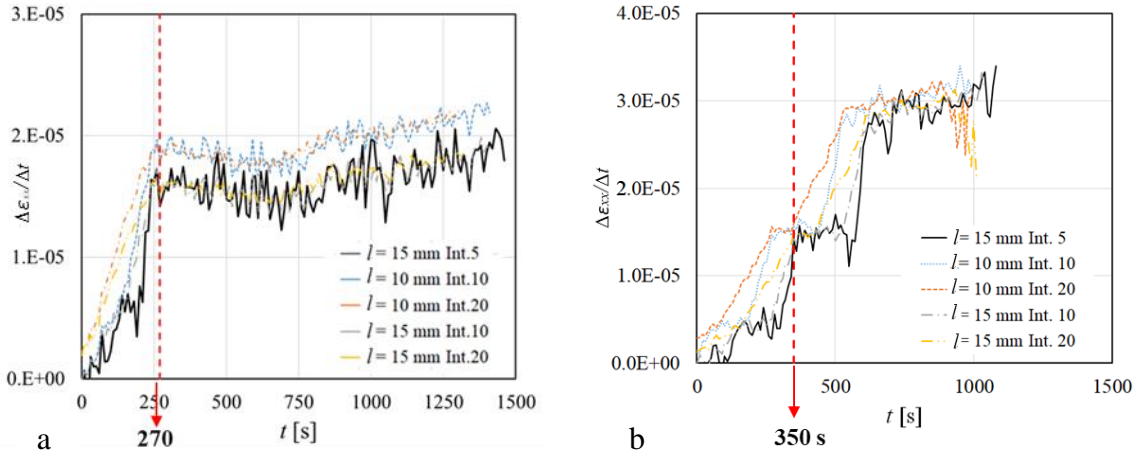


Figure 66  $\Delta\varepsilon_{xv}/\Delta t$  versus time for (a) FM\_70\_70\_300\_G8\_1; (b) FM\_70\_70\_300\_G8\_2

Once the time at which the crack opened is known, with a “back analysis”, it is possible to find the value of the load that corresponds to the opening of the crack, which is the POINT G in Figure 67, the displacement profile associated to this point is plotted, and  $\Delta u_{max}$  at the notch tip is evaluated.

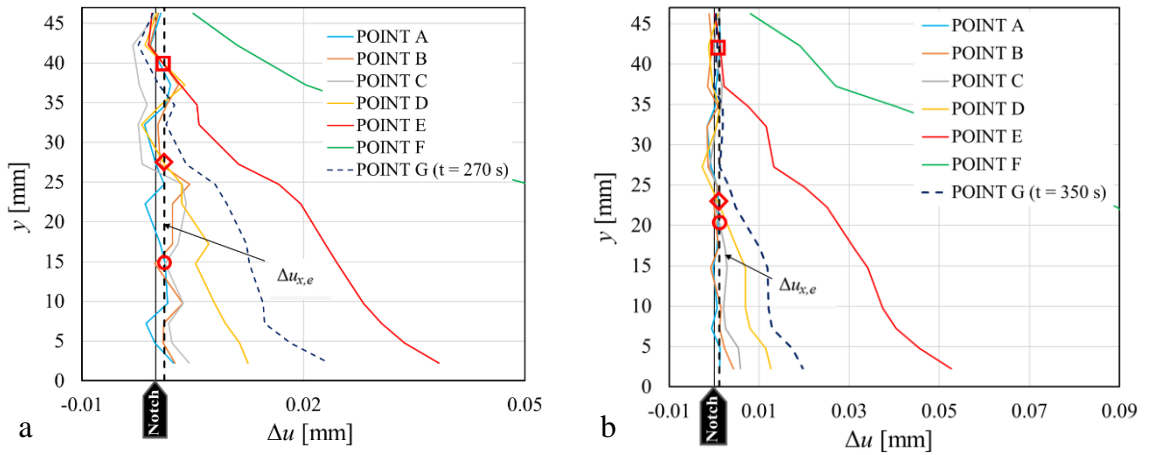


Figure 67  $\Delta u$  plot for (a) FM\_70\_70\_300\_G8\_1; (b) FM\_70\_70\_300\_G8\_2

By subtracting  $\Delta u_{x,e}$  from  $\Delta u_{max}$ ,  $w_f$  is evaluated. Knowing  $G_F$  and  $f'_t$  it is possible to understand if the values of the coefficients (which will be named  $\beta$  in the rest of the paragraph) experimentally evaluated and proposed in literature, equal to 5.6 (Equation 31 [170]) and 3.6 ([7] [175]), are acceptable for this type of specimens.

To determine the value of  $\beta$ , four cases were considered based on the value of fracture energy used to evaluate the coefficient itself:  $G_F$  and  $\overline{G_F}$  obtained from the LVDTs ( $\beta_{G_F(LVDT)}$  and  $\beta_{\overline{G_F}(LVDT)}$ ) and  $G_F$  and of  $\overline{G_F}$  from DIC ( $\beta_{G_F(DIC)}$  and  $\beta_{\overline{G_F}(DIC)}$ ).

Values of  $\beta$  determined with the method described above, are lower than the coefficients proposed in literature [7] [170].

*Table 19 Evaluation of  $\beta$  coefficients*

| Specimen          | $\beta_{G_F(LVDT)}$ | $\beta_{\overline{G_F}(LVDT)}$ | $\beta_{G_F(DIC)}$ | $\beta_{\overline{G_F}(DIC)}$ |
|-------------------|---------------------|--------------------------------|--------------------|-------------------------------|
| FM_70_70_300_G8_1 | 0.78                | 0.63                           | 0.95               | 0.68                          |
| FM_70_70_300_G8_2 | 0.54                | 0.52                           | 0.61               | 0.56                          |
| FM_70_70_300_CS_2 | 1.57                | 1.73                           | 2.16               | 1.85                          |
| FM_70_70_300_FS_2 | 1.23                | 1.18                           | 1.34               | 1.27                          |
| FM_70_70_300_EP_2 | 2.59                | 2.13                           | 2.94               | 3.48                          |

Some factors that may influence the result is the low values of  $G_F$  and the uncertainties on the evaluation of  $\Delta u$  plot. For concrete specimens, since the size of the FPZ is very large, to understand if the values of  $\beta$  coefficients are realistic, the same procedure would be applied to specimens of larger sizes. However, for AAMs, results are more similar to that proposed in literature [7].

## 4 Chapter 4 – Bond behavior between SRG composites and quasi-brittle substrate

This chapter describes the bond behavior between concrete and masonry and composite materials. In this section, results of single-lap direct shear test for concrete and masonry specimens reinforced with SRG composites are presented and discussed. Several parameters are considered, including matrix width, matrix type, test rate, type of substrate and presence of anchorage. The first part describes the preparation of masonry and concrete blocks and the application of composite material on the substrate. In the second part, single-lap direct shear test is described and then the results in terms of failure mode and load-slip response are presented. The last part explains the indirect method used to find the relationship between shear stresses and the relative displacement between the two faces of the interfacial crack.

### 4.1 Preparation of masonry specimens

#### 4.1.1 Masonry blocks without anchorage

Twenty-seven masonry blocks were constructed with solid fired-clay bricks and a nominally low strength mortar for the joints. The mortar joint was chosen to reproduce the quality and the mechanical behavior of weak mortars that typically connect the bricks in the existing masonry structures. The mortar used for the majority of masonry joints is a certified natural plaster of pure lime (NHL3.5), ecofriendly, that contains only natural raw materials and recycled minerals [176]. For five masonry blocks, the mortar used for the joints was cement-based mortar. All masonry blocks were constructed with six layers of half-bricks and five 10 mm-thick mortar joints. Nominal dimensions of blocks were 120 mm (length)  $\times$  120 mm (width)  $\times$  380 mm (height).

Before applying the composite, all the masonry blocks were left to soak in a bucket filled with water for at least 20 minutes (Figure 68a). This procedure was necessary to avoid water absorption by the masonry surfaces during the application of the SRG composite.

All composite strips were applied using a wet layup process, with a bonded width ( $b_f$ ) equal to 50 mm and a bonded length ( $\ell$ ) equal to 315 mm. The bonded area started approximately 35 mm from the top edge (loaded end of the fibers) of the masonry block to avoid spalling of the first brick of the specimen.

It should be noted that the mortar was used to embed the fibers only in the bonded area. The fibers were left bare outside the bonded area. The width of the mortar matrix was varied: specimens used as reference [162] had a matrix width equal to the width of the steel fiber sheet, i.e., 50 mm.

For the remaining blocks, the width of the mortar was increased to 70 mm and 90 mm, while keeping the width of the fiber sheet constant and equal to 50 mm.



*Figure 68 Preparation of specimen prior to the application of the SRG composite: (a) masonry blocks left soak in the water (b) wet specimen removed from the bucket*

The procedure used to bond the SRG composite strip to the masonry substrate can be described as:

- 1) delimitation of the bonded area using cardboard (Figure 69a);
- 2) application of the first 4 mm-thick layer of mortar matrix, leveled with a trowel (Figure 69b);
- 3) application of steel fibers, gently pressed into the mortar using a trowel (Figure 69c);
- 4) application of the second 4 mm-thick layer of mortar matrix to fully cover the steel fibers (Figure 69d).

The cardboard was then removed and a wet cloth was placed on the SRG composite strip to maintain the composite under moisture and all the specimens were left to cure in the laboratory environment under wet cloths for 28 days.

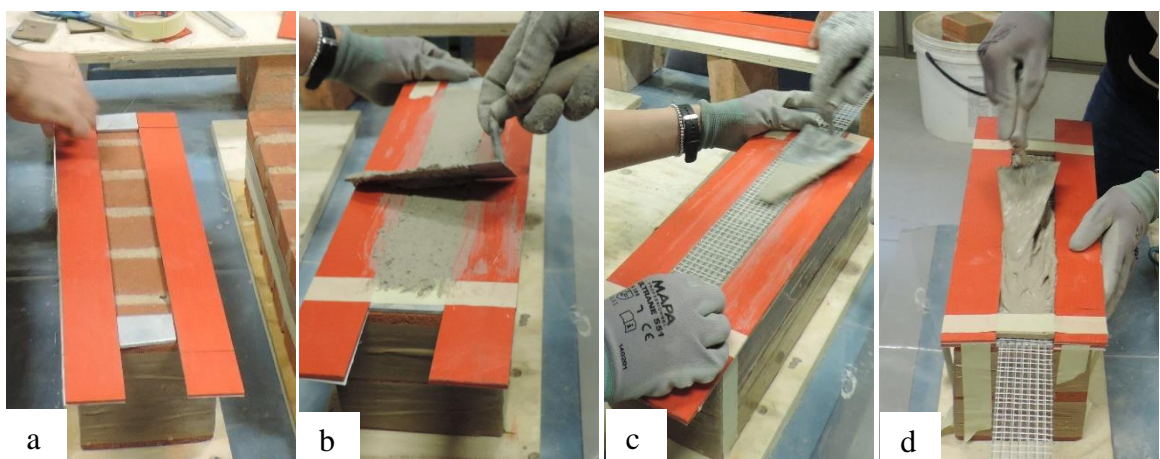


*Figure 69 Phases of application of SRG reinforcement (a) delimitation of the bonded area; (b) application of the first layer of mortar matrix; (c) application of steel fiber sheet; (d) application of the second layer of mortar matrix*

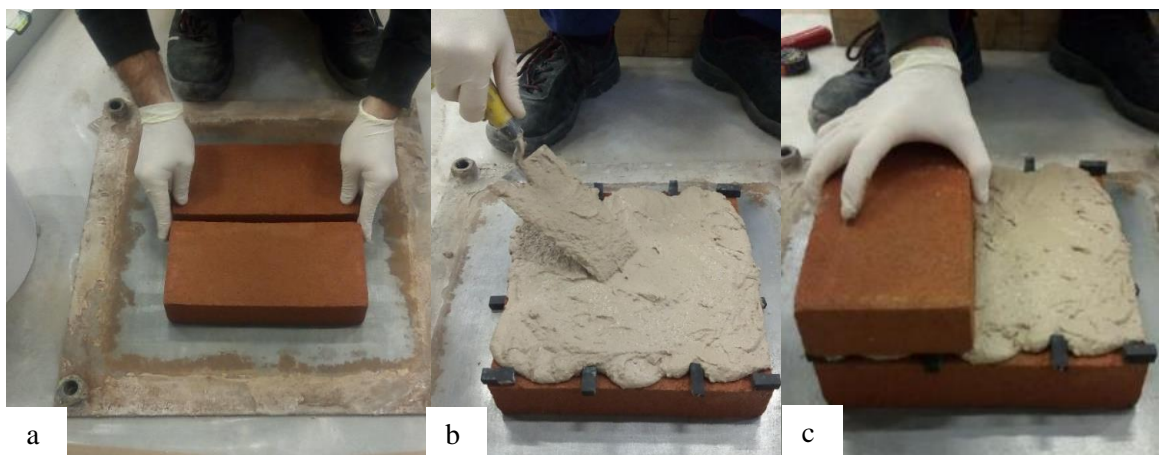
Specimens were named following the notation DS\_A\_B\_C\_D\_E\_F\_Z where A indicates the bonded length, B refers to the matrix width, C indicates the density of steel fiber ( $LD = 670 \text{ g/m}^2$ ), D is the matrix mortar employed (LM = lime-based mortar, CM = cement-based mortar matrix), E when present refers to the test rate, F is present only for specimens that have the anchorage system, (A1 = masonry blocks with bonded strip with extension of the fibers into the hole, A2 = masonry blocks with separate spike in the second top layer of bricks, A3 = masonry blocks with separate spike in the second bottom layer of bricks, and A4=concrete specimens with anchorage at  $45^\circ$ ), and Z is the number of the specimen.

#### 4.1.2 Masonry blocks with anchorage

Twelve masonry blocks were constructed using solid clay bricks. Before constructing the masonry blocks, bricks were left to soak in a bucket filled with water for at least 30 minutes. Each block consisted of six layers of bricks arranged in a stretcher and header configuration, with five 10 mm-thick mortar joints. The same mortar employed above (section 4.1.1) was used for mortar joints. Each block had the same nominal dimensions of 250 mm (width)  $\times$  250 mm (depth)  $\times$  380 mm (height). All the masonry blocks were left curing under wet cloths for 28 days at laboratory conditions (Figure 70).

After the curing time, the wet cloths were removed and the blocks were placed on a stable support for the realization of the hole.

The effectiveness of the anchorages was studied by conducting single-lap shear tests on SRG strips bonded to a masonry block with the presence of an anchorage either at the loaded end of the strip or at the free end. The longitudinal fibers of the SRG strip bonded to the masonry substrate were left bare outside the bonded area.



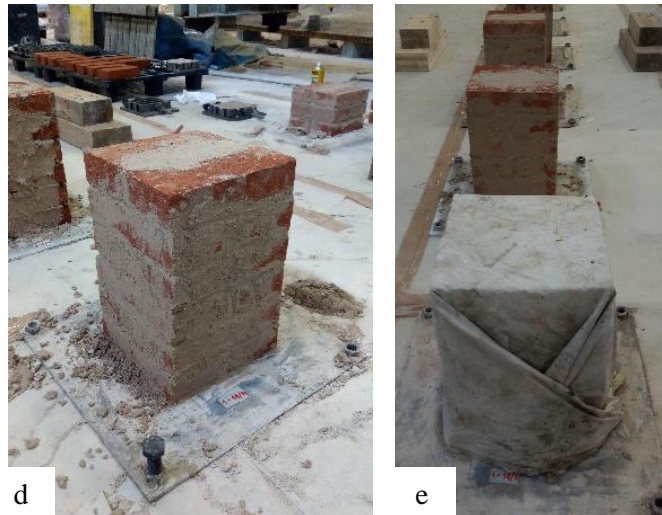


Figure 70 Construction phases of masonry block: (a) first layer of bricks; (b) mortar joints; (c) second layer of brick; (d) finished specimen and (d) masonry block covered with wet cloths

Two types of anchorage were considered: an extension of the fibers of the SRG strip was inserted into the masonry block (Figure 71a). The fibers were pre-bent and inserted into a drilled through-thickness hole filled with the injectable mortar after the placement of the fibers.

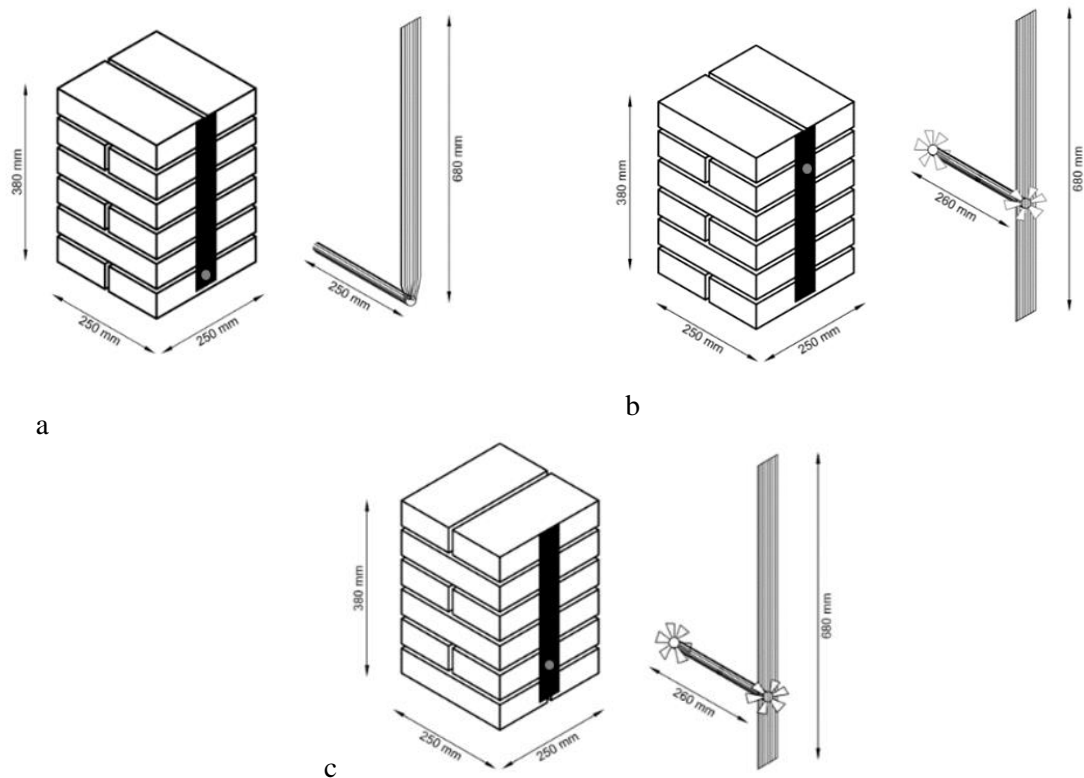


Figure 71 Types of anchorage: (a) extension of the fibers of the SRG strip inserted into the masonry block at the free end; (b) separate spike at the loaded end (second top layer of bricks); and (c) separate spike at the free end (second bottom layer of bricks)

The second type of anchorage was a separate spike that interacted with the bonded strip (Figure 71b and c).

The fibers were placed into the drilled through-thickness hole, which was then filled with the injectable mortar. The fiber strip of the spike was longer than the hole. The fibers were pre-bent at two locations corresponding to the end of the hole in order to create a double umbrella-like spike that, on the side where the SRG strip was applied, was interweaved with the longitudinal fibers of the SRG, and on the opposite side were covered with mortar. For all masonry blocks, the hole was drilled in the center of the brick, although the location varied based on the anchorage configuration. The hole, whose dimensions were 18 mm (diameter)  $\times$  250 mm (length), was performed orthogonally to the height of the block.

Dimensions of bonded area of the SRG strip was the same for all specimens and it was equal to 50 mm (width)  $\times$  310 mm (length), and it started 35 mm away from the top edge of the masonry block to avoid shear failure, i.e. spalling of the brick.

The first group of specimens, named A1, was comprised of four masonry blocks. For this group the hole was drilled in the bottom layer of bricks. Steel fiber sheets were cut into the desired length, with dimensions of 50 mm (width)  $\times$  930 mm (length). Fiber sheet strip was bent at a distance of 250 mm from the end of the fiber strip opposite to the loaded end, and then bundled in order to be inserted into the hole. After the insertion of fibers (Figure 72), the hole was filled with mortar and then the masonry blocks were left at room temperature for 24 hours before the application of the mortar to realize the SRG strip. The bonded area was previously marked (Figure 72) and then the first layer of 4 mm thick mortar was applied.

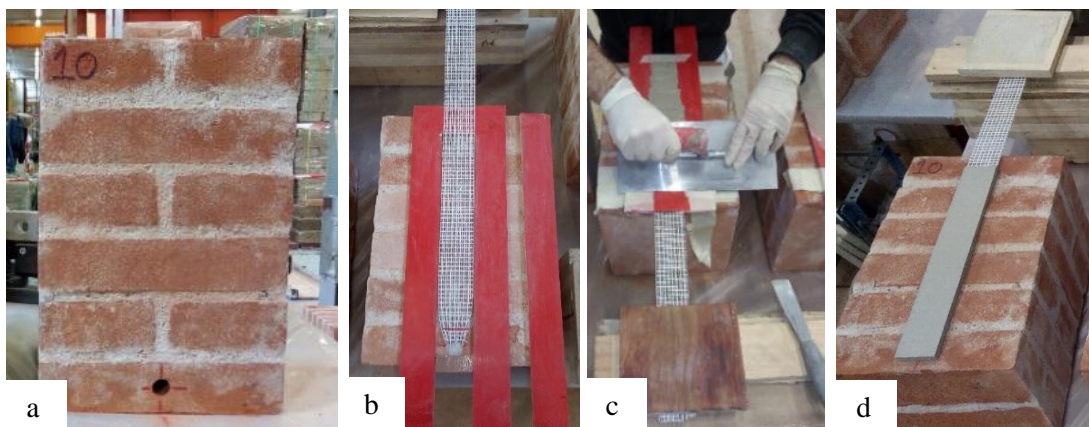


*Figure 72 Preparation of A1 specimens: (a) masonry block with of the hole; (b) Insertion of steel fibers into the hole; (c) application of the first layer of mortar (d) finished masonry block with SRG strip*

Steel fibers were lifted up as the mortar was applied and then laid over while exerting a small pressure with a trowel. As the fibers strip was embedded into the mortar, the second layer of mortar

was applied to fully cover the fibers (Figure 72). All the A1 SRG-masonry joints were cured at room temperature under wet cloths for 28 days.

For the second and third groups of specimens, named A2 and A3, eight masonry blocks were employed, four per each group. For four masonry blocks, the hole was drilled in the second top layer of bricks, while for the remaining blocks, the hole was in the second bottom layer.

A separate fiber strip, with dimensions of 100 mm (width)  $\times$  460 mm (length), was used for the spike to be inserted into the hole. The fiber strip was pre-bent at two locations corresponding to the end of the hole in order to create a double umbrella-like spike (Figure 73).

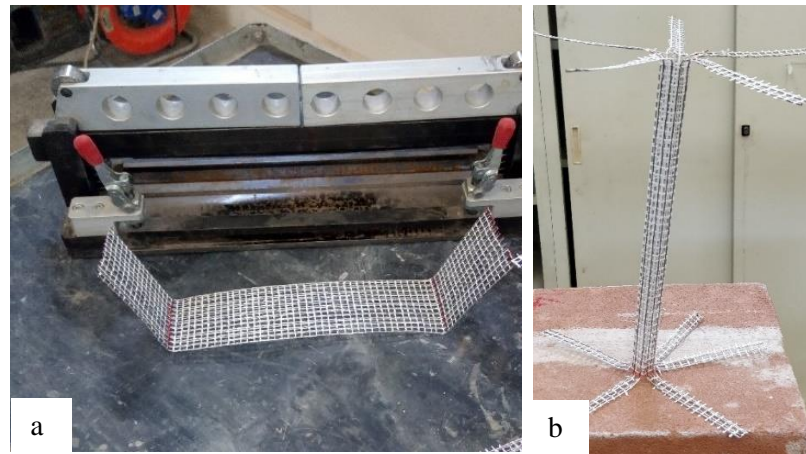


Figure 73 Preparation of the spike: (a) bending fibers; (b) bundled anchor spike

After the insertion of the fibers into the hole, the spike strands were opened radially in the back face of the masonry block at the pre-bent location.

The fibers were covered with mortar on the back face (Figure 74b).

The spike strands on the front face were also opened. The hole was then filled with fluid mortar, and all the masonry blocks were left to cure for 24 hours at room temperature before the application of the SRG strip. Steel fiber sheets with a density of 1200 g/m<sup>2</sup> were used for the bond strip, with dimensions of 50 mm (width)  $\times$  680 mm (length).



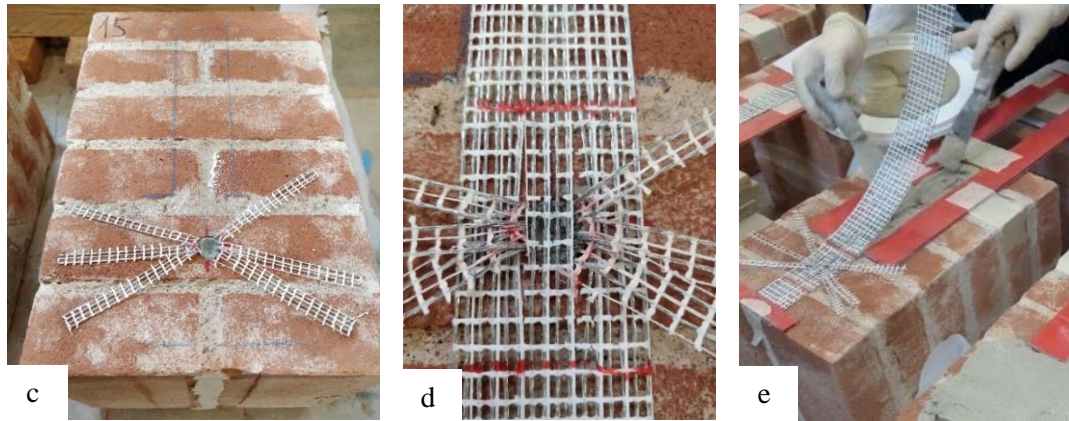


*Figure 74 Preparation of A3 specimens: (a) realization of the hole; (b) fibers covered with mortar; (c) anchor spike open radially in the front face; (d) spike fibers interweaved with the longitudinal fibers of the SRG strip (e) application of first layer of mortar*

Prior to applying the first layer of the mortar of the SRG strip, the spike fibers were interweaved with the longitudinal fibers of the SRG strip (Figure 74d). The fiber of the strip were then lifted to apply the first 4 mm-thick layer of mortar (Figure 74e). Subsequently, the steel fibers were delicately pressed onto the layer of mortar by means of a trowel and fully covered with the second layer of the mortar matrix. All the SRG-masonry joints were cured at room temperature under wet cloths for 28 days.

#### **4.1.3 Concrete prisms with anchorage**

In total, three concrete prisms were cast with nominal dimensions of 150 mm (width)  $\times$  150 mm (depth)  $\times$  600 mm (length). All concrete prisms can be classified as Concrete type 2 (see section 2.1). Four prisms were taken from another experimental campaign [162] and used as reference, since they were reinforced without the presence of the anchorage system. Prisms used as reference had  $b_f$  equal to 50 mm and  $\ell$  equal to 450 mm.

Three prisms were prepared with the presence of an anchorage system (A4 group). Before the application of the SRG composite, 18 mm (diameter)  $\times$  210 mm (length) hole was realized with an electrical drill at the height of 258 mm from the bottom of the beam with an inclination of 45° (Figure 75).

Steel fibers with a density of 1200 g/m<sup>2</sup> were used. Dimensions of the SRG strip were 50 mm (width)  $\times$  880 mm (length): one end of the fiber strip, 210 mm long, was bent of 45° and cut along the principal direction to have separate wires and finally bundled. The bundle of fibers was inserted into the hole, and then the hole was filled with fluid mortar. All the concrete prisms were left curing for 24 hours under wet clothes at laboratory conditions. After the curing time, the SRG strip was applied to the concrete substrate following the four phases described above.

The first layer of cement-based mortar was applied on the surface inside the bonded area previously defined, then the steel fiber strip was gently pressed into the mortar, and finally the second layer of mortar was applied to fully cover the fibers (Figure 76).

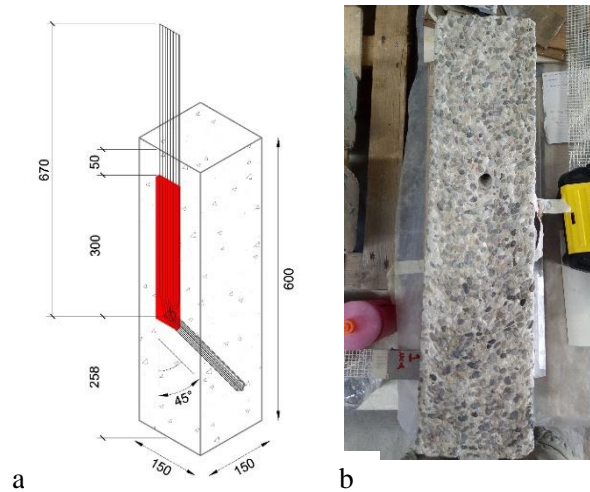


Figure 75 (a) Concrete prisms configuration; (b) prims with the hole

All the prisms has a constant bonded width  $b_f$  equal to 50 mm and bonded length  $\ell$  of 300 mm. The reinforced concrete prisms were left in a room under controlled temperature and humidity for 28 days.

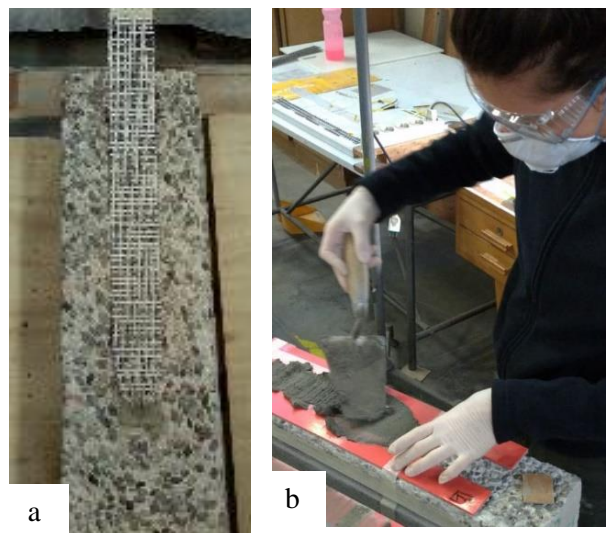


Figure 76 (a) Steel fibers inserted into the hole filled with fluid mortar; (c) application of the second layer of SRG mortar matrix

## 4.2 Test set-up and procedure

Direct single-lap shear tests were conducted under displacement control using a closed-loop servohydraulic universal testing machine with a capacity of 100 kN. The classical push-pull configuration, described in section 1.2.2, was adopted for both concrete prisms and masonry blocks.

Thin neoprene sheets were placed at the top and at the bottom, in between the structural element and the steel plates, in order to avoid stress concentrations. The steel fibers were pulled, while the specimen was restrained by a steel fixture (Figure 77). Fibers were placed carefully inside the two wedges of the testing machine to guarantee a perfect vertical alignment of the fibers within the grips. In order to avoid the premature rupture of fibers in the gripping area, an epoxy tab of approximately 7 cm was built at free end of fibers.

Specimens are restrained against movements by two steel plates: the bottom square plate is bolted to a cylindrical element gripped to the testing machine [177]. The top steel plate, which was either square or c-shaped, depending on the specimen, is connected through the bottom plate through four steel bars.

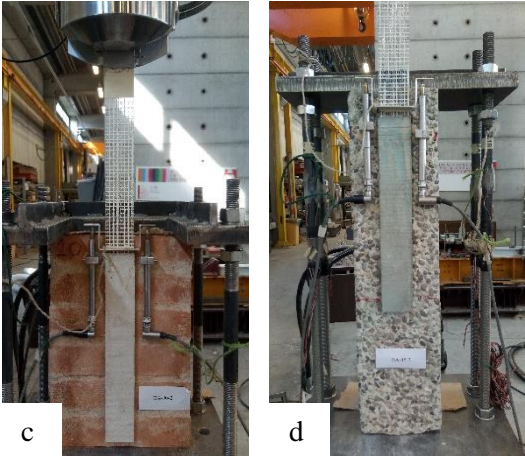
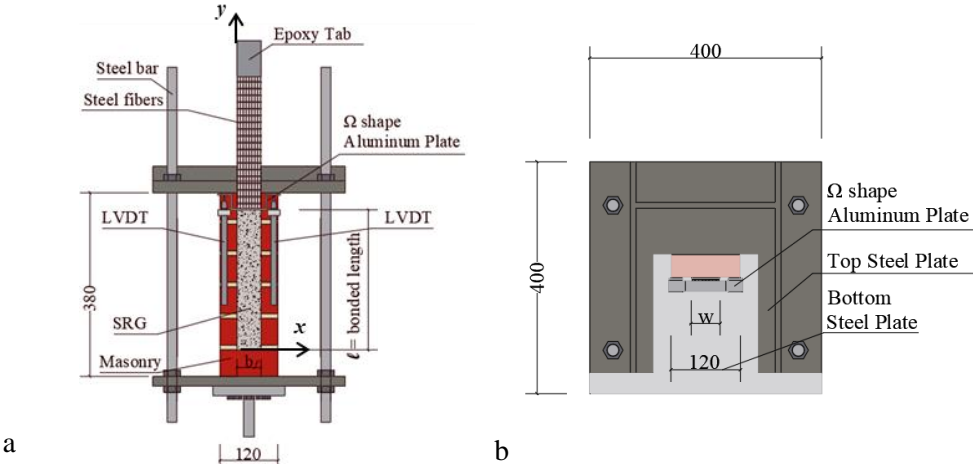
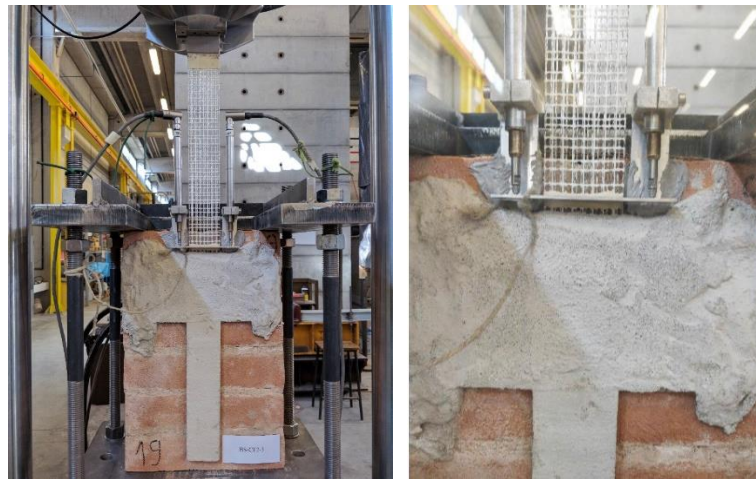


Figure 77 Single-lap direct shear test set-up: (a) sketch of the test set-up, front view and (b) top view; photo of (c) masonry and (d) concrete set-up

For all the specimens, a 7 mm epoxy tab was constructed to allow the clamping by the machine top grip. Two linear variable displacements transformers (LVDT) were mounted on the masonry surface close to the beginning of the bonded area (LVDTa and b in Figure 77). The LVDTs reacted off of a thin aluminum  $\Omega$ -shaped plate that was attached to the bare fiber surface adjacent to the

top edge of the bonded area. The average of the two LVDT measurements is named global slip  $g$ , which is the relative displacement at the beginning of the bonded area. SRG specimens were tested increasing the value of the global slip  $g$  at a constant rate equal to 0.00084 mm/s.

The two LVDTs were mounted on the first layer of bricks of each masonry block, through two holders that were glued to the brick itself, except for one group of specimens. In fact, for all the masonry blocks that have the separate anchor spike in the second top layer, it was not possible to place the LVDTs on the first layer of brick, since it was covered by mortar. Therefore, the two LVDTs reacted off of a rectangular steel plate glued on the bare fibers, at the beginning of the bonded area. The two holders employed to sustain the LVDTs were attached to two steel plates that were glued vertically on the first layer of brick. Therefore, the LVDTs were mounted upside down, as shown in Figure 78, and therefore the test rate was controlled by the stroke of the machine and equal to 0.2 mm/min.



*Figure 78 Test set-up for A2 specimens*

## **4.3 Discussion of results**

### **4.3.1 Failure modes**

For masonry blocks without any anchorage system, three failure modes were observed:

1. Interlaminar failure with debonding at the interface between the internal layer of mortar and steel fibers (MF);
2. Rupture of steel fibers (FR);
3. Detachment of the SRG strip from the substrate with a thin layer of substrate attached to a limited portion (SF).

In general, the most frequent failure mode was interlaminar failure: twenty-five specimens out of thirty-two failed due to the debonding between the internal (i.e., attached to the substrate) layer of mortar and steel fibers (Figure 79a). For masonry blocks with a matrix width greater than that of the steel fibers, when interlaminar failure occurred, it involved only the central part of the SRG

composite strip. This means that two lateral portions of mortar remained attached to the masonry substrate (Figure 79b). It should be noted that when the width of the matrix was larger than the width of the fiber sheet, interlaminar failure did not occur for the entire length of the SRG strip (Figure 79b). Three masonry blocks out of five with a matrix width of 70 mm and only two out of five with a matrix width of 90 mm, failed due to the rupture of steel fibers (Figure 79 c). Therefore, for these specimens, the value of  $P^*$  was higher than that of other specimens that did not exhibit fiber rupture. The third failure mode was observed only in one specimen, DS\_315\_50\_LD\_CM\_1, strengthened with a cement-based mortar matrix (Figure 79d). All the blocks tested with a test rate ten times higher than the standard rate [177], [178] failed due to the interlaminar failure between the internal layer of matrix and fibers.

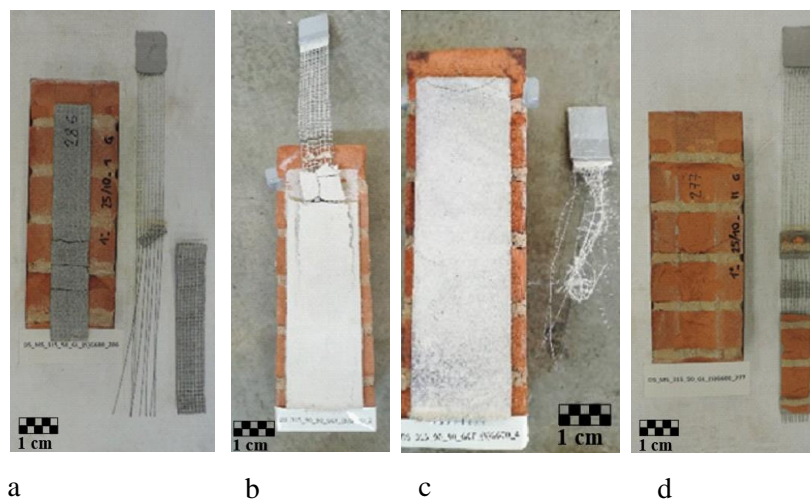


*Figure 79 Failure modes of representative specimens: (a) interlaminar failure with debonding at the interface between the internal layer of mortar and steel fibers (MF); (b) partial interlaminar failure at the interface between the internal layer of mortar and steel fibers (MF\*); (c) rupture of fibers (FR); (d) detachment of the SRG strip from the substrate with a thin layer of masonry attached to it (SF).*

On the other hand, masonry blocks with the presence of the anchorage system exhibited two failure modes:

1. Interlaminar failure at the matrix-fiber interface (MF);
2. Mixed failure mode (Figure 30a), which consists of interlaminar failure at the matrix-fiber interface and debonding of part of the SRG strip with a thin layer of brick attached to the matrix (SF/MF).

Specimens of A1 experienced both types of failure modes (Figure 80a). It should be noted that after the fibers in the hole were engaged and the SRG strip was fully debonded, the test was stopped because of the significant backward rotation of the masonry block.

All the specimens of A2 and A3 showed the interlaminar failure with delamination at the matrix-fiber interface (Figure 80b and c). However, for both groups, it was not possible to see the complete detachment of the SRG strip due to the presence of the anchor spike system.

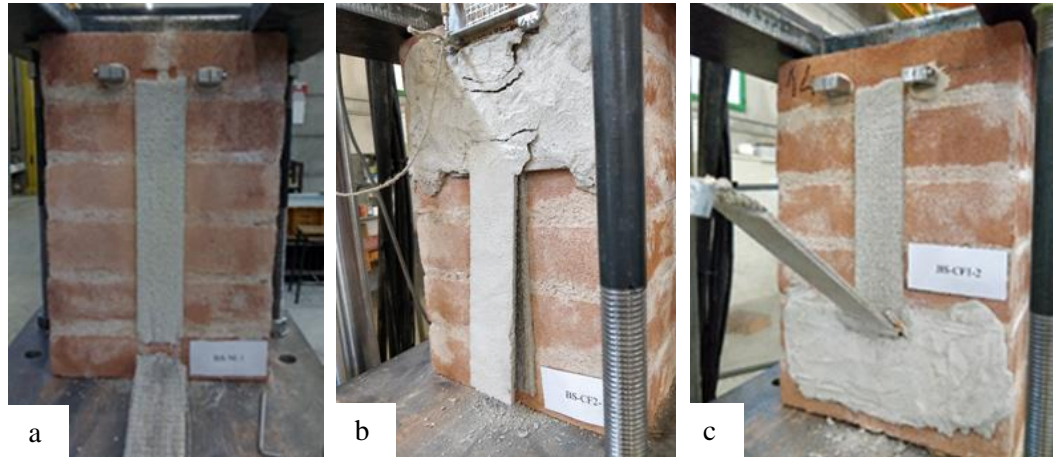


Figure 80 Example of failure modes for a) A1 b) A2 and c) A3 specimens

Also for these specimens, the test was stopped after the engagement of the spike because of the magnitude of the rotation of the block.

#### 4.3.2 Load responses

Bond behavior between SRG composite and masonry or concrete substrate is analyzed in terms of applied load  $P$  versus global slip  $g$ . Four aspects are considered:

- The change in the width of the SRG mortar matrix while keeping the width of the fiber sheet fixed;
- The type of mortar used for the SRG;
- The influence of the test rate;
- The type of substrate (i.e. concrete and masonry);
- The presence of an anchorage system.

Results of single-lap direct shear tests for all the masonry blocks that were tested are reported in Table 20.

Table 20 Experimental results in terms of  $g_1$  and  $g_2$ ,  $P_{crit}$ ,  $P^*$ , and failure mode

| Specimen          | $g_1$ | $g_2$ | $P_{crit}$<br>[kN] | $\overline{P}_{crit}$<br>(CoV)<br>[kN] | $P^*$<br>[kN] | $\overline{P}^*$<br>(CoV)<br>[kN] | Failure mode |
|-------------------|-------|-------|--------------------|--|---------------|-----------------------------------|--------------|
| DS_315_50_LD_LM_1 | 1.33  | 2.18  | 5.8                |  | 6.1           |                                   | MF           |
| DS_315_50_LD_LM_2 | \     | \     | \                  |  | 11.4          |                                   | MF           |
| DS_315_50_LD_LM_3 | 1.15  | 2.26  | 6.7                | 5.8                                    | 8.1           | 7.6                               | MF           |
| DS_315_50_LD_LM_4 | 0.73  | 1.30  | 5.3                | (0.178)                                | 7.5           | (0.278)                           | MF           |
| DS_315_50_LD_LM_5 | \     | \     | \                  |  | 12.7          |                                   | FR           |
| DS_315_50_LD_LM_6 | \     | \     | \                  |  | 6.2           |                                   | MF           |

|                        |      |      |      |         |       |         |       |
|------------------------|------|------|------|---------|-------|---------|-------|
| DS_315_50_LD_LM_7      | 1.00 | 2.30 | 6.3  |         | 6.8   |         | MF    |
| DS_315_50_LD_LM_8      | 1.03 | 2.70 | 3.3  |         | 5.1   |         | MF    |
| DS_315_50_LD_LM_9      | 1.03 | 2.49 | 6.9  |         | 7.8   |         | MF    |
| DS_315_50_LD_LM_10     | 1.54 | 2.35 | 6.7  |         | 7.8   |         | MF    |
| DS_315_50_LD_LM_11     | 1.12 | 2.22 | 5.8  |         | 7.5   |         | MF    |
| DS_315_50_LD_LM_12     | \    | \    | \    |         | 6.5   |         | MF    |
| DS_315_50_LD_LM_13     | 0.58 | 1.92 | 5.5  |         | 5.9   |         | MF    |
| DS_315_50_LD_LM_14     | 1.18 | 2.29 | 5.8  |         | 6.4   |         | MF    |
| DS_315_70_LD_LM_1      | \    | \    | \    |         | 12.7  |         | FR    |
| DS_315_70_LD_LM_2      | 1.08 | 1.58 | 6.8  | 8.8     | 7.0   | 11.2    | MF    |
| DS_315_70_LD_LM_3      | \    | \    | \    | (0.321) | 12.7  | (0.219) | FR    |
| DS_315_70_LD_LM_4      | 3.68 | 5.52 | 10.8 |         | 11.0  |         | MF*   |
| DS_315_70_LD_LM_5      | \    | \    | \    |         | 12.6  |         | FR    |
| DS_315_90_LD_LM_1      | 1.17 | 2.22 | 9.9  |         | 10.3  |         | MF*   |
| DS_315_90_LD_LM_2      | 1.45 | 2.13 | 10.9 | 9.8     | 11.4  | 11.4    | MF*   |
| DS_315_90_LD_LM_3      | 1.11 | 1.53 | 8.6  | (0.118) | 9.0   | (0.155) | MF*   |
| DS_315_90_LD_LM_4      | \    | \    | \    |         | 13.0  |         | FR    |
| DS_315_90_LD_LM_5      | \    | \    | \    |         | 13.1  |         | FR    |
| DS_315_50_LD_LM_10TR_1 | \    | \    | \    |         | 8.46  |         | MF    |
| DS_315_50_LD_LM_10TR_2 | \    | \    | \    | \       | 10.31 | 10.4    | MF    |
| DS_315_50_LD_LM_10TR_3 | \    | \    | \    |         | 12.46 | (0.192) | MF    |
| DS_315_50_LD_CM_1      | 0.65 | 1.10 | 6.2  |         | 10.9  |         | SF    |
| DS_315_50_LD_CM_2      | 0.98 | 2.55 | 7.9  |         | 8.7   |         | MF    |
| DS_315_50_LD_CM_3      | 1.20 | 2.60 | 7.9  | 7.7     | 8.6   | 9.1     | MF    |
| DS_315_50_LD_CM_4      | 0.90 | 2.30 | 8.0  | (0.109) | 8.7   | (0.111) | MF    |
| DS_315_50_LD_CM_5      | 0.98 | 2.20 | 8.3  |         | 8.6   |         | MF    |
| DS_315_50_LD_LM_A1_1   | 0.49 | 1.22 | 4.29 |         | 15.44 |         | SF/MF |
| DS_315_50_LD_LM_A1_2   | /    | /    | /    |         | 10.99 |         | MF    |
| DS_315_50_LD_LM_A1_3   | 0.74 | 0.84 | 4.40 |         | 6.14  |         | SF/MF |
| DS_315_50_LD_LM_A1_4   | 0.58 | 1.32 | 4.83 |         | 8.91  |         | SF/MF |
| DS_315_50_LD_LM_A2_1   | /    | /    | /    |         | 12.07 |         | MF    |
| DS_315_50_LD_LM_A2_2   | /    | /    | /    |         | 13.44 |         | MF    |
| DS_315_50_LD_LM_A2_3   | /    | /    | /    |         | 14.09 |         | MF    |
| DS_315_50_LD_LM_A2_4   | /    | /    | /    |         | 14.20 |         | MF    |
| DS_315_50_LD_LM_A3_1   | 0.35 | 0.74 | 4.80 |         | 9.41  |         | MF    |
| DS_315_50_LD_LM_A3_2   | 0.28 | 0.75 | 4.62 |         | 8.97  |         | MF    |
| DS_315_50_LD_LM_A3_3   | 0.27 | 0.65 | 4.63 |         | 10.04 |         | MF    |
| DS_315_50_LD_LM_A3_4   | 0.38 | 0.73 | 4.53 |         | 9.25  |         | MF    |

\*Interlaminar failure did not occur along the entire length of the SRG bonded strip (see Figure 80b)

#### 4.3.2.1 Influence of SRG matrix width

For fourteen SRG-masonry joints, the width of the SRG matrix was equal to the width of steel fiber sheet, i.e. 50 mm, and their behavior in terms of  $P$  versus  $g$  is shown in Figure 82a. The SRG matrix of the remaining blocks had two different widths: Figure 82b shows the results of SRG-masonry joints with matrix width equal to 70 mm, while Figure 82c shows the load response of specimens with the matrix width equal to 90 mm. The load responses are quite scattered even among specimens that belong to the same group, due to the variability of the mortar employed for the SRG matrix [177].

For low values of the load, the  $P$ - $g$  curves are approximately linear. As the load increases, a series of load drops occurs, which are associated with the onset of the interfacial crack. For some

specimens, after the initial drops, the global slip continues to increase at an almost constant value of the load (plateau). The value of  $g$  at the first substantial drop, which corresponds to the beginning of the plateau, is called  $g_1$ . While the value of  $g$  at the end of the plateau is  $g_2$ , which nominally corresponds to the end of the test.  $P_{crit}$  is defined as the average of the load in the interval  $g_1 - g_2$ , while  $P^*$  denoted the maximum load. To better visualize these quantities, an example of a load responses is represented in Figure 81.

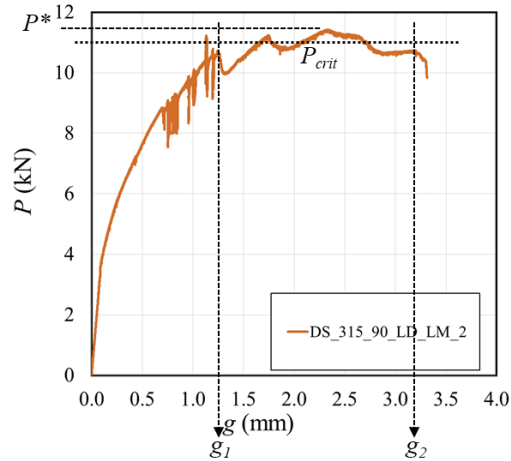


Figure 81 Definition of  $g_1$  and  $g_2$ ,  $P_{crit}$  and  $P^*$

The distinction between  $P^*$  and  $P_{crit}$  was first introduced to distinguish between the load at the onset of the interfacial crack and the average load-carrying capacity of the joint during the propagation of the crack, respectively, in the case of steel-reinforced polymer (SRP) composites [177]. Since the energy required to create a unit-length crack is higher than that required for a unit-length self-similar increase of the crack,  $P^*$  was generally higher than the corresponding  $P_{crit}$  for the SRG-masonry joints that showed a plateau in the response.

For twelve SRG-masonry joints, it was not possible to evaluate the  $P_{crit}$  since after the first drop of the load, the response continued to increase until failure. Interestingly, for specimens with a matrix width equal to 70 mm and 90 mm, the always-increasing load response (i.e. the lack of a plateau) was associated with fiber rupture. On the other hand, when the matrix width was 50 mm, only one specimen out of four that exhibited an always-increasing response failed due to fiber rupture. This behavior was observed in [177]. The matrix-fiber bond is initially capable to sustain loads almost close to the fiber rupture and then a weakness at the matrix-fiber interface triggers the sudden interlaminar debonding. Most likely, the increase in the matrix width is capable of compensate for the presence of weaknesses at the matrix-fiber interface and fiber rupture is often reached.

The average of  $P_{crit}$  ( $\overline{P_{crit}}$ ) for specimens with SRG matrix width equal to 70 mm (8.8 kN) increased by 52% with respect to the specimens with a matrix width of 50 mm (5.8 kN). Increasing the matrix width from 50 mm to 90 mm,  $\overline{P_{crit}}$  increased by 69% (9.8 kN). Therefore, increasing the matrix

width for a constant fiber width entailed for an increase in the load-carrying capacity of the SRG-masonry joint, due to a higher amount of energy required for the crack to initiate and propagate.

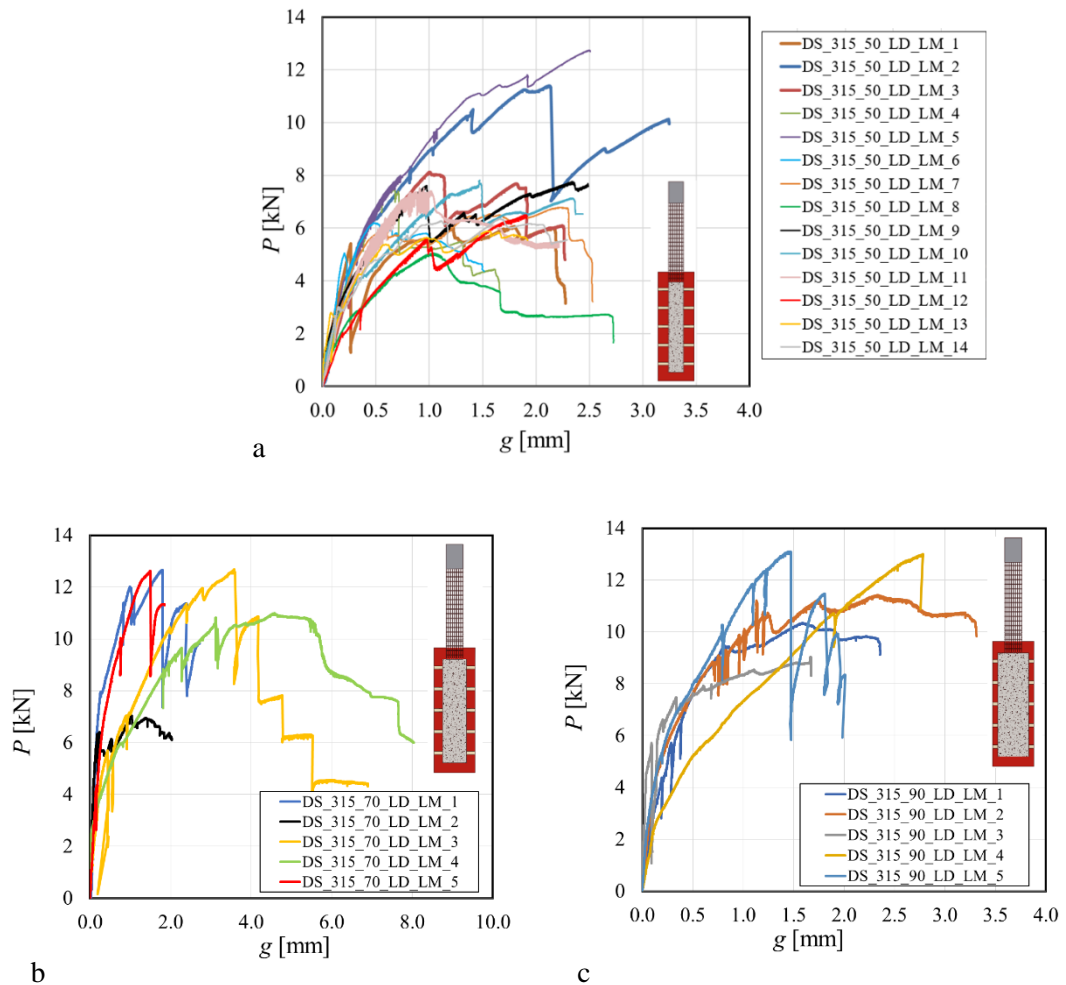


Figure 82 Load responses of SRG-masonry joints with matrix width equal to (a) 50 mm [162]; (b) 70 mm; and (c) 90 mm

The average peak load  $\overline{P^*}$  is greater for specimens with a matrix width equal to 70 mm ( $\overline{P^*} = 11.2$  kN) and 90 mm ( $\overline{P^*} = 11.4$  kN) mm, when compared to 50 mm ( $\overline{P^*} = 7.6$  kN), but there was no significant difference between the 70 mm and 90 mm specimens.

#### 4.3.2.2 Influence of the type of matrix

In this Section, load responses of five masonry blocks strengthened with cement-based matrix SRG are shown and compared with those of masonry blocks strengthened with lime-based matrix SRG (Figure 83). The matrix width for all the specimens compared in this section was equal to 50 mm, i.e. it was the same as the width of the fiber sheet. The light green curves represent the masonry blocks strengthened with lime-based matrix SRG (herein called all together as DS\_315\_50\_LD\_LM\_ALL).

For masonry blocks strengthened with cement-based matrix SRG, the initial branch is linear followed by a non-linear branch with some drops of the load. The first substantial drop of the load corresponds to the onset of the interfacial crack. When the interfacial crack propagates, the load remains almost constant while the global slip increases. The load-carrying capacity was quite consistent among specimens strengthened with cement-based matrix SRG, and the average values of the peak load and load-carrying capacity were  $\overline{P^*} = 9.1$  kN and  $\overline{P_{crit}} = 7.7$  kN, respectively. Compared with specimens with the same matrix width but strengthened with lime-based matrix SRG,  $\overline{P_{crit}}$  of cement-based matrix specimens increased by 33% (7.7 kN versus 5.8 kN), and the average peak load  $\overline{P^*}$  by 20% (9.1 kN versus 7.6 kN). This result was expected as the cement-based matrix has higher mechanical properties (including fracture energy, see Table 17). Indeed, as the matrix between fibers fractures in the interlaminar failure, the load-carrying capacity of the SRG-masonry joint depends on the properties of the matrix itself.

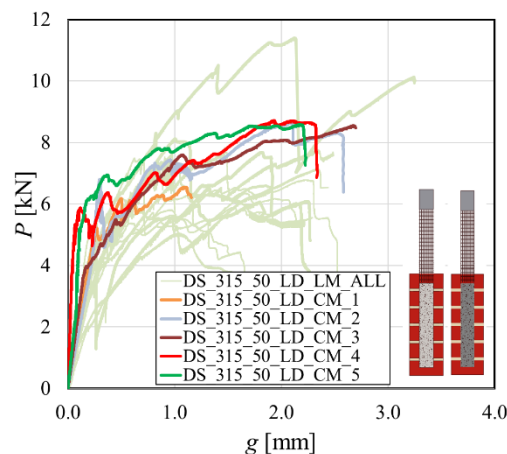


Figure 83 Comparison of load responses of SRG-masonry joints strengthened with two types of matrix

#### 4.3.2.3 Influence of the test rate

Three SRG-masonry joints with lime-based mortar were tested using a test rate (0.0084 mm/s) that was ten times the standard rate (0.00084 mm/s). The load responses obtained were similar to those of specimens tested with the standard test rate (Figure 84). However, when specimens tested with different test rates are compared, it can be observed that increasing the test rate implies an increase of the average peak load by 37% (from 7.6 kN to 10.4 kN).

Therefore, even if only three SRG-masonry joints were tested at a higher rate, it appears that a rate effect, which was also observed for para-phenylene benzobisoxazole PBO FRCM-concrete joints [178], is present for the type of composite investigated. However, further work will be needed to understand how the test rate affects the load response, failure mode, and peak load. Figure 84 shows the comparison between specimens tested with the standard rate and specimens tested with a higher

test rate. It was decided not to include specimens that presented failure modes other than interlaminar failure. Therefore, the light green curves in Figure 84 are associated with the load responses of all masonry blocks with matrix width of 50 mm, except for DS\_315\_50\_LD\_LM\_5, since the failure mode (i.e. fiber rupture, see Table 20) was different from all the other specimens. It should be noted that for the three specimens with higher rate the plateau load  $P_{crit}$  could not be computed, as the load response was resembling the always-increasing response observed for other specimens.

As mentioned above, this type of load response was observed for other specimens with the same characteristics and standard test rate and it is possible that the high rate has induced this type of response.

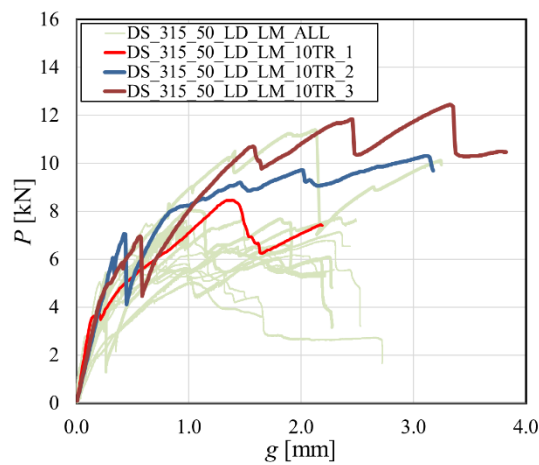


Figure 84 Comparison of load response of SRG-masonry joints tested with two test rates

#### 4.3.2.4 Influence of the substrate

In addition to SRG-masonry joints, three concrete prisms strengthened with the SRG composite were tested using the same single-lap direct test set-up, for comparison. These tests were part of another experimental campaign [162].

The main results of these tests are reported in Table 21, whereas the corresponding load responses are depicted in Figure 85b. It should be noted that the bonded length  $\ell$  for these three specimens was 200 mm.

Comparison was made with masonry blocks strengthened with the same type of matrix used for concrete prisms, i.e. cement-based mortar matrix, of the same width (50 mm) and the same type of steel fibers. It was noted that, instead of interlaminar failure typically observed for the companion masonry specimens, the failure of all concrete prisms was due to the rupture of fibers (Figure 85a). This is particularly important as the bonded length of the SRG-concrete joints was even less than the bonded length of the masonry counterparts. It should be observed that while the masonry surface was not roughened prior to the application of the SRG, the concrete surface was sandblasted to reach a 4 mm roughness.

Thus, the different behavior between masonry and concrete could be linked to the fact that there was a good adhesion between the internal layer of matrix and concrete substrate, due to the roughness of the substrate itself.

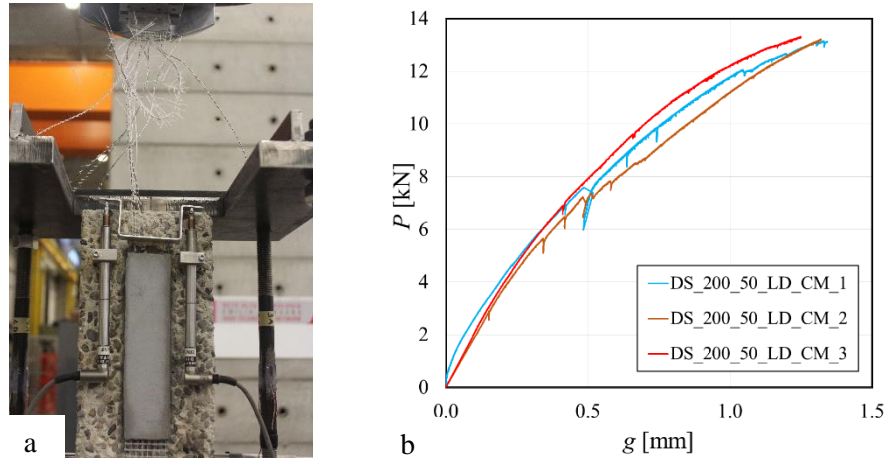


Figure 85 (a) Photo of failure mode due to the rupture of steel fibers and (b) Load response of SRG-concrete joints [162]

The different matrix-substrate bond behavior and the stress field influenced by the roughness may have affected the matrix-fiber interface stress distribution, thus changing the behavior of the specimen. In addition, masonry blocks absorb more water than concrete prisms, therefore it is possible (although the blocks were soaked prior to the application of the SRG [162]) that water absorption by the masonry had weakened the matrix and consequently the bond between the composite and the substrate.

Table 21 Test results of SRG-concrete joints [162]

| Specimen          | $g_1$ | $g_2$ | $P_{crit}$<br>[kN] | $\overline{P}_{crit}$<br>(CoV)<br>[kN] | $P^*$<br>[kN] | $\overline{P}^*$<br>(CoV)<br>[kN] | Failure mode |
|-------------------|-------|-------|--------------------|--|---------------|-----------------------------------|--------------|
| DS_200_50_LD_CM_1 | \     | \     | \                  | \                                      | 13.15         | 13.2<br>(0.006)                   | FR           |
| DS_200_50_LD_CM_2 | \     | \     | \                  | \                                      | 13.23         |                                   | FR           |
| DS_200_50_LD_CM_3 | \     | \     | \                  | \                                      | 13.31         |                                   | FR           |

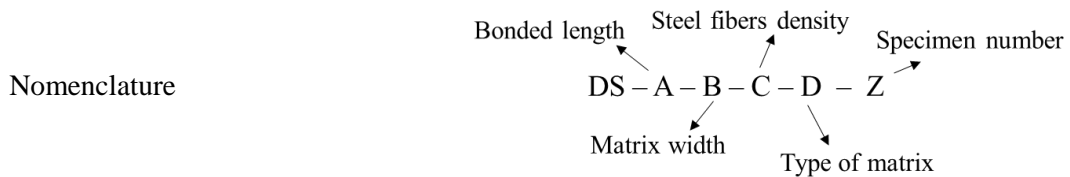


Figure 85b shows a low dispersion of the experimental curves compared to that of specimens with lime-based mortar and a masonry substrate (Figure 85) or a different bond behavior when compared

to cement-based SRG applied to masonry (Figure 83). FRCMs and SRGs based on hydraulic lime mortar exhibit some inherent variability and results of bond tests are usually quite scattered [177]. For cement-based inorganic-matrix composites the variability is almost non-existent, therefore testing a large number of specimens is pointless. Specifically, for the SRG herein investigated when a cement-based mortar is used and it is applied to concrete the tensile strength of the fibers can be reached and therefore the results are very consistent.

#### 4.3.2.5 Influence of the anchorage

The applied load versus global slip responses are plotted in Figure 86. All specimens exhibited an initial linear branch. For A1 specimens, except for DS\_315\_50\_LD\_LM\_A1\_3, the end of the linear branch is characterized by a drop of the load that indicates the beginning of the debonding process of the strip.

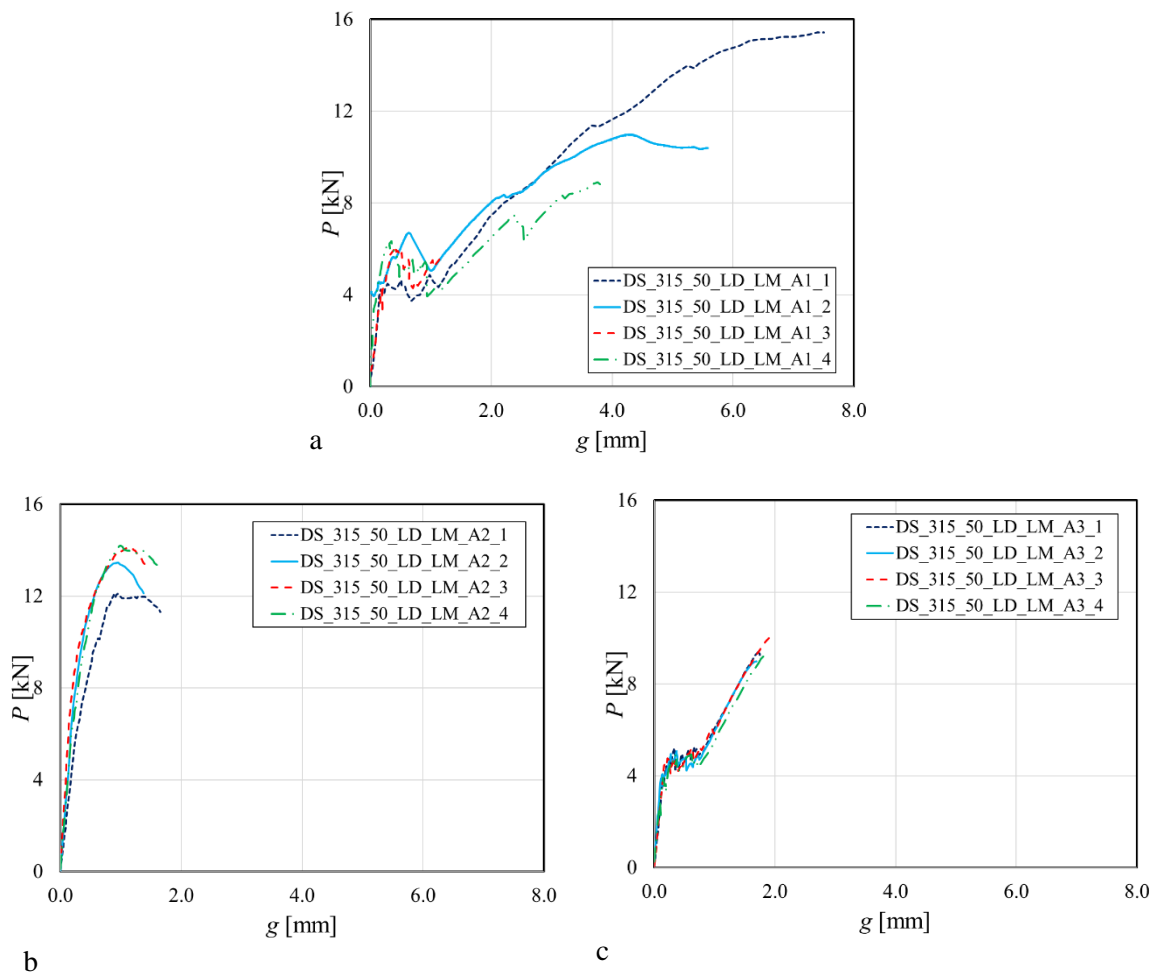


Figure 86 Load responses of (a) A1 (b) A2 and (c) A3 specimens

If no anchorage was present, the load drop would be followed by a constant branch (or plateau) that is associated with the progressive debonding of the strip towards the free end.

With the addition of an anchorage at the free end, as the stress transfer between the strip and the masonry block reaches the free end, the force is partially transferred within the anchorage, which entails for an increase of the load. A second major load drop is observed when the strip fully debonds. Once the strip is fully debonded, the only stress transfer mechanism occurs within the anchorage and the load increases again.

For DS\_315\_50\_LD\_LM\_A1\_3, the test was prematurely stopped because of a control issue in the loading rate. Load responses of A3 specimens are similar to those of specimens of A1. The linear branch is followed by a constant branch (plateau) marked by a load drop.

The load started to increase again when the complete detachment of the composite occurred and the spike was engaged. For A3 specimens, the plateau branch was more evident than A1 specimens because the engagement of the spike was associated with the splice obtained by interweaving the fibers of the strip and the spike and therefore more gradual.

For A2 specimens, no load drop was observed. A non-linear branch followed directly the linear branch because the spike was engaged from the beginning of the test. The load increases until the peak is reached, which is probably associated with large slips between the strip and the spike. As the load level is too high for the bonded strip, a sudden debonding occurs for it, which is associated with a decrease of the load.

For each specimen  $g_1$  was determined as the global slip that corresponds to the first drop of the load, while  $g_2$  was determined as the global slip at the end of the plateau, i.e. the second load drop for A1 specimens. The critical load  $P_{crit}$  is the average of the load values evaluated within the range  $g_1$  and  $g_2$ .

$P^*$  is the absolute peak of the load response. All values for the specimens herein presented are reported in Table 20.

The activation of the anchor system started at different points of the load response for each type of anchorage. For A1 and A3 specimens, the activation of the anchorage can be associated with the value  $g_2$  of the global slip  $g$ . The values of  $g_2$  for A1 specimens are slightly larger than the values for A3 specimens because the hole was placed further away from the loaded end in A1 specimens. For A3 specimens, the activation of the anchorage occurred from the very beginning of the test since the end of the linear response is associated with values of  $g$  smaller than the values of  $g_1$  for A1 and A3 specimens.

#### 4.3.2.6 Concrete prisms with anchorage

As for masonry blocks, single-lap direct shear test results are presented in terms of global slip  $g$  versus applied load  $P$  (Figure 87b). Three concrete prisms with the presence of the anchorage were tested under single-lap direct shear test. In the first part of the response, the load increases while the global slip increases gradually. Then a drop in the load occurred, which corresponds to the onset of the interfacial crack, followed by a plateau, in which the crack is propagating. The following

branch corresponds to an increment of the load, which is when the interfacial crack reaches the anchorage. The increment of the load can be associated to the activation of the anchorage. The increment of the load is then followed by a sudden drop, which could be associated to an adjustment and consequently a movement of the anchorage inside the concrete hole. After that, the load increases again and then the test was stopped to avoid any possible rotations of the concrete block at higher value of the load, and the deformation of the steel bars of the set-up. Results of another experimental campaign are herein reported for comparison [162].

Table 22 Single-lap direct shear test results for concrete prisms

| Specimen             | $g_1$<br>[mm] | $g_2$<br>[mm] | $P_{crit}$<br>[kN] | $\overline{P}_{crit}$<br>(CoV)<br>[kN] | $P^*$<br>[kN] | $\overline{P}^*$<br>(CoV)<br>[kN] | Failure mode |
|----------------------|---------------|---------------|--------------------|--|---------------|-----------------------------------|--------------|
| DS_450_50_MD_CM_1    | 0.33          | 0.65          | 7.67               |  | 7.90          |                                   | MF           |
| DS_450_50_MD_CM_2    | 0.40          | 0.89          | 7.37               | 7.72                                   | 7.58          | 8.10                              | MF           |
| DS_450_50_MD_CM_3    | 0.38          | 1.31          | 8.11               | (0.039)                                | 8.69          | (0.059)                           | MF           |
| DS_450_50_MD_CM_4    | 0.44          | 1.22          | 7.72               |  | 8.24          |                                   | MF           |
| DS_300_50_MD_CM_A4_1 | 0.26          | 0.57          | 6.76               | 6.07                                   | 7.10          | 6.56                              | MF           |
| DS_300_50_MD_CM_A4_2 | 0.22          | 0.46          | 6.63               | (0.160)                                | 6.92          | (0.120)                           | MF           |
| DS_300_50_MD_CM_A4_3 | 0.30          | 0.60          | 4.83               |  | 5.65          |                                   | MF           |

Load responses and failure modes of the same concrete prisms but without the presence of the anchorage [162] and herein reported for comparison (Figure 88b).

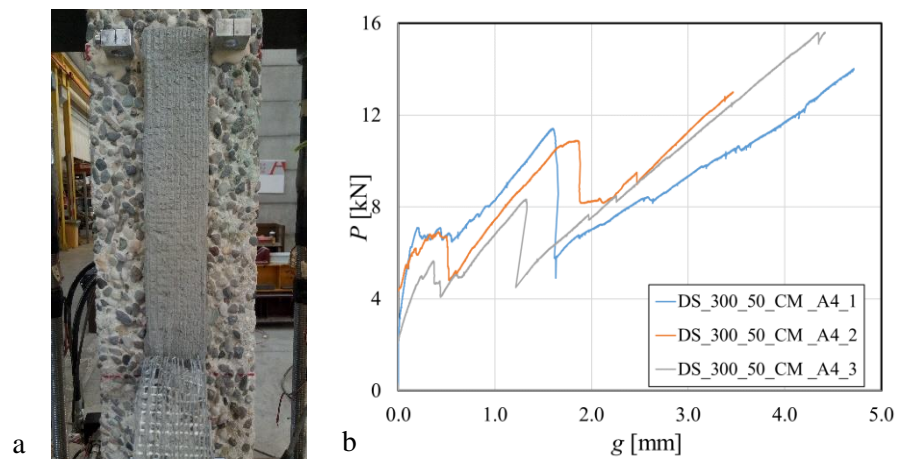


Figure 87 Concrete prism with anchorage: (a) failure mode and (b) load-slip responses

It can be noted that differently from concrete prisms with the anchorage, for these specimens, after the plateau, there is a drop in the load, which corresponds to the debonding of the SRG strip.

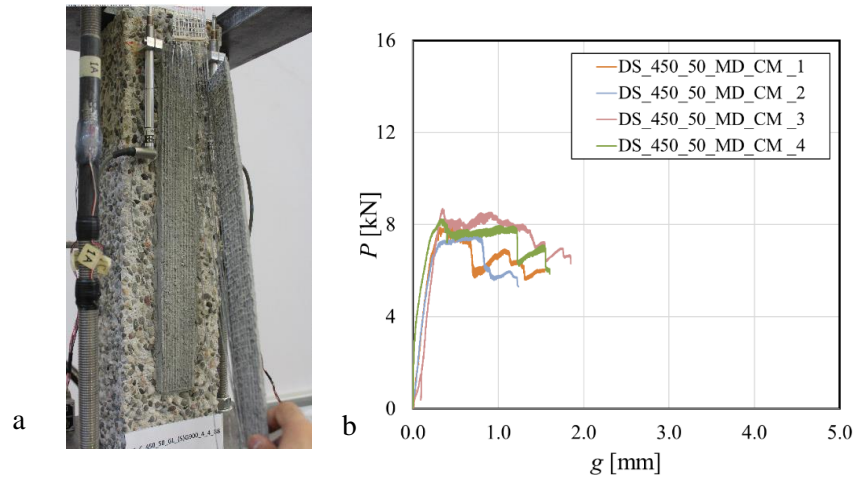


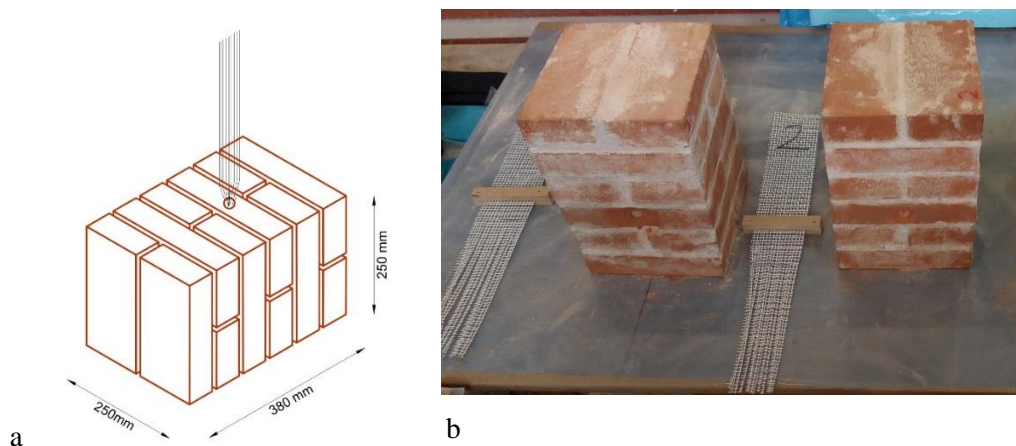
Figure 88 Concrete prism without anchorage: (a) failure mode and (b) load-slip responses [162]

## 4.4 Pull-out test

In the following paragraph, results of pull-out test of masonry blocks strengthen with SRGs are presented. The aim of the test is to evaluate the pull-out strength of SRGs anchor to masonry substrate. In fact, the possibility to anchor the SRGs inside the structural element that needs to be reinforced, is expected to improve the anchorage strength of the reinforcement.

### 4.4.1 Preparation of specimens

Eight masonry blocks were prepared for pull-out test. The hole was realized in the fourth layer of bricks from the top (Figure 89a). Fiber sheets ( $1200 \text{ g/m}^2$ ) were cut into the desired dimensions of  $100 \text{ mm}$  (width)  $\times$   $650 \text{ mm}$  (length). The free end of fibers,  $250 \text{ mm}$  long, was cut along the principal direction (Figure 89b) to have separate steel wires and then they were bundled to be inserted into the hole. The hole was then filled with fluid mortar until its complete saturation, and the blocks were left curing until testing. Seven mm long epoxy tab was constructed at the fibers loaded end (Figure 89c) to facilitate the gripping of the fibers by the jaws of the machine.



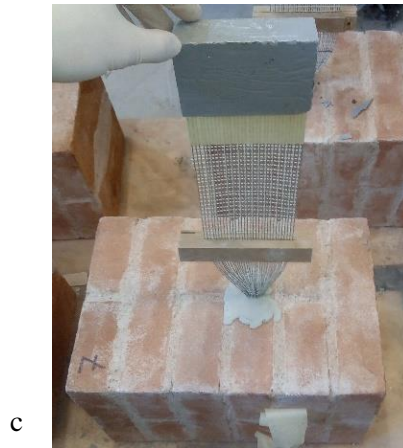


Figure 89 (a) Sketch of pull-out specimen; (b) masonry blocks with fiber sheets cut along the principal direction; (c) 7-mm epoxy tab

#### 4.4.2 Test set-up

Eight masonry blocks were tested using the classic pull-out set-up (Figure 90a). Tests were performed according to [179] with some deviations. Tests were conducted using a closed-loop servo hydraulic universal testing machine with a maximum capacity of 500 kN.

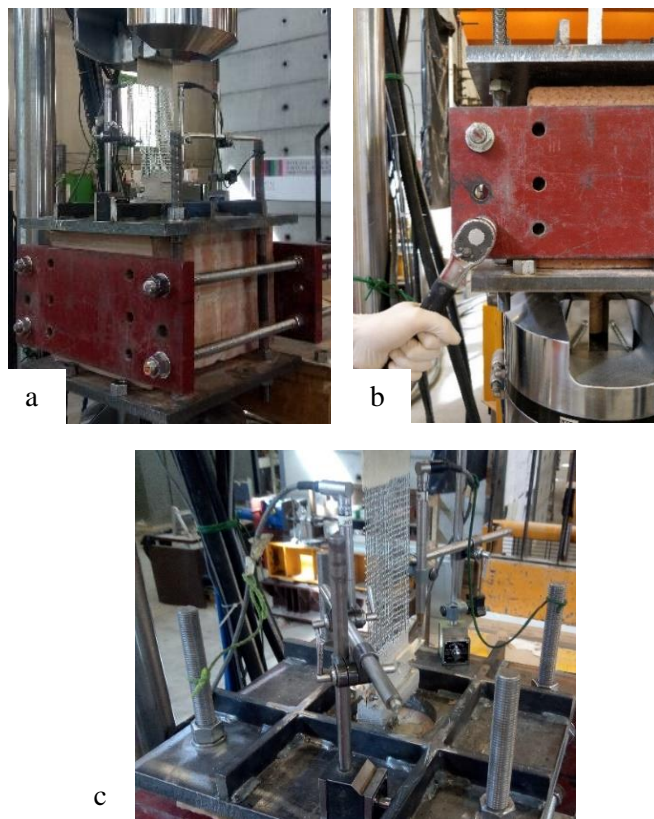


Figure 90 (a) Pull-out test set-up; (b) application of torque and (c) position of LVDTs

To avoid vertical movements, masonry blocks were restrained by two 400 mm × 400 mm steel plates, placed on the top and on the bottom of the specimen, connected with four steel bars through bolts, while fibers were pulled-out.

The top steel plate was designed with a central 75 mm diameter hole to guarantee the passage of the steel fibers. In addition to the top and bottom plate, two rectangular steel plates were used to restrain the masonry blocks from horizontal movements. A torque wrench was used (Figure 90b) to tighten the bolts, applying a defined torque to give a pre-compression equal to 0.20 MPa and 0.75 MPa.

Tests were performed at a constant rate of 1 mm/min and it was controlled by the stroke of the machine. For PO\_MD\_FLM\_0.75\_1 block, the test rate was equal to 0.2 mm/sec.

Two LVDTs were used to measure the displacement ( $\delta$ ) and they were mounted on an aluminum plate attached to two wooden boards that were connected with the bare fibers (Figure 90c).

#### 4.4.3 Discussion of results and failure modes

The value of the maximum load ( $P^*$ ), the corresponding displacement ( $\delta_{pull-out}$ ) and the pull-out strength ( $\sigma_{pull-out}$ ) [180] are reported in Table 23.

Table 23 Pull-out test results

| Specimen      | $P^*$<br>[kN] | $\overline{P^*}$<br>(CoV)<br>[kN] | $\delta_{pull-out}$<br>[mm] | $\sigma_{pull-out}$<br>[MPa] | $\overline{\sigma_{pull-out}}$<br>[MPa] | Failure<br>mode |
|---------------|---------------|-----------------------------------|-----------------------------|------------------------------|---|-----------------|
| PO_FLM_0.75_1 | 23.5          |                                   | 5.0                         | 1365                         |   | FE              |
| PO_FLM_0.75_2 | 38.1          |                                   | 7.8                         | 2215                         |   | PR              |
| PO_FLM_0.75_3 | 40.1          |                                   | 10.3                        | 2330                         | 2185                                    | PR              |
| PO_FLM_0.75_4 | 45.2          |                                   | 9.8                         | 2620                         |   | FR              |
| PO_FLM_0.75_5 | 41.3          |                                   | 9.0                         | 2400                         |   | FE              |
| PO_FLM_0.20_6 | 35.1          |                                   | 8.9                         | 2040                         |   | FE              |
| PO_FLM_0.20_7 | 27.9          |                                   | 7.8                         | 1620                         | 1940                                    | FE              |
| PO_FLM_0.20_8 | 37.4          |                                   | 9.1                         | 2170                         |   | FE              |

The pull-out strength is defined as the ratio between  $P^*$  and  $A_{f,tot}$ , which is the fabric cross sectional area evaluated as the number of yarns (32) multiplied by the single yarn cross sectional area of the fibers (0.538 mm<sup>2</sup>).

Three failure modes were observed:

- 1) rupture of steel fiber sheet (FR);
- 2) partial rapture of steel fibers (PR);
- 3) fibers extraction from the masonry block (FE).

For the masonry blocks that experienced fibers extraction, the  $P$ - $\delta$  response presents a plateau, after the peak load was reached (Figure 91b). For the remaining masonry blocks, that experienced total or partial fibers rupture, the test stopped once the peak load was reached. It should be noted that when the pre-compression given to the masonry block was 0.75 MPa (curves represented with solid line in Figure 91a), all the failure modes were observed, while when the pre-compression given to the block was lower (dashed line), the failure was associated to the extraction of the fibers.

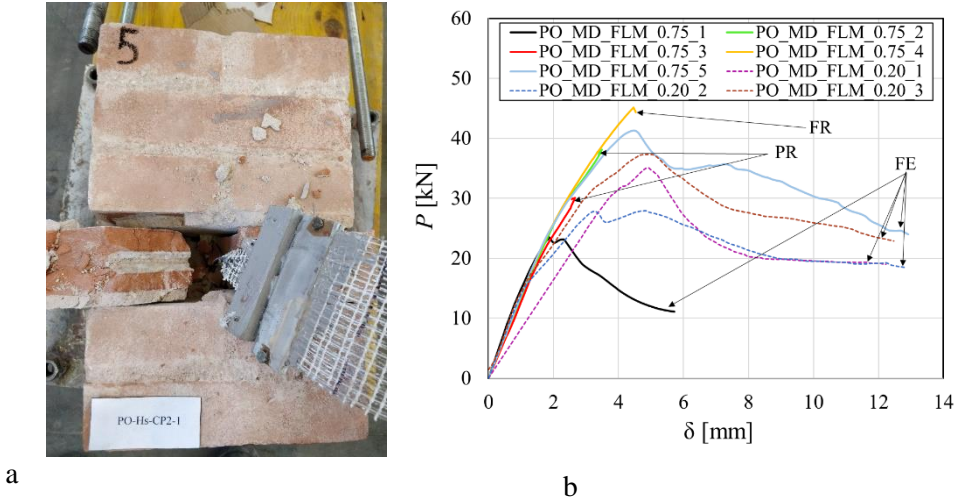


Figure 91 (a) Failure mode; (b) load responses

## 5 Chapter 5 – Indirect calibration of the cohesive material law

Bond properties of SRG-masonry and concrete joints were investigated by testing the specimens under single lap direct shear test set-up. A fracture mechanics approach was used to study the phenomenon, assuming a Mode-II conditions [181]. The Mode II condition implies the detachment of the SRG composite along the interfaces between matrix and fibers, due to the presence of shear stresses ( $\tau$ ) associated with the relative slip ( $s$ ) of the two faces of the interfacial crack. One way to determine the strain along the fibers is to apply strain gauges on the bare fibers. However, fibers are embedded into the matrix, and therefore these measurements are sometimes complex and not reliable. In addition, since the shear stresses and the relative displacement are at the interface matrix-fibers, it is not possible to obtain useful information from digital image analysis. Thus, the indirect method based on the global response of single-lap direct shear tests is proposed to analyze the interfacial properties. The indirect calibration method is employed to find the relationship between shear stresses and the relative displacement between the two faces of the interfacial crack. The proposed method has several advantages: it does not require any complex equipment to measure the strain along the bonded area, and only the experimental  $P(g)$  response is needed for the calibration. In addition, this method can be applied to other failure modes where it is difficult to measure the strain [182], and the method can be employed to obtain the  $P(g)$  for any bonded length.

Debonding mechanisms of FRPs bonded to masonry substrates were largely investigated by several researchers [22] [48] [50] [183] [184]. It was noted that when FRPs were bonded to masonry elements, failure occurred in the substrate, with a cohesive crack that propagates in bricks and masonry joints. Differently from FRP-masonry joints, in which the main failure mode is associated with the debonding of the FRP strip from the substrate, for SRGs typically failure occurs at the matrix-fibers interface. The shear stress is the shear at the matrix-fiber interface, while the slip is the relative displacement of the steel fibers with respect to the matrix, considered perfectly bonded to the masonry substrate. The  $\tau$ - $s$  relationship is described by a cohesive material law (CML). One way to determine the CML is to employ the indirect method, which is based on several experimental parameters.

The shape of the CML is not known a priori and therefore, as a first attempt, several CML shapes can be considered to investigate the robustness and accuracy of the proposed method. With a wide set of CML functions, it is possible to investigate the ability of these functions to reproduce the experimental data. In [182], five CML functions were considered, whose expressions were proposed by [185] [186] [187]. Each function has several unknown parameters that are evaluated through the calibration method.

### 5.1.1 Definition of the analytical expression of the CML

The indirect method requires the definition of an analytical expression of the CML with the parameters that are determined by fitting the experimental data. As mentioned above, different functions can be considered for the indirect calibration [182]. In this work, two analytical expressions were considered and compared with the results obtained in [177].

The first CML adopted was derived from the expression proposed by Dai et al. [186]:

$$\tau(s) = A(e^{-\alpha s} - e^{-2\alpha s}) \quad (36)$$

Where the two unknown parameters are  $A$  and  $\alpha$ . Equation 36 implies that when  $s = 0$ , the shear stress is equal to zero. It implies an infinite effective bond length [188] [189].

The second CML adopted was proposed by Focacci and Carloni [188], in which  $\tau(s)$  is a trilinear function and it is expressed as:

$$\tau(s) = \begin{cases} \tau_0 + \frac{\tau_m - \tau_0}{s_m} s & \text{if } 0 \leq s \leq s_m \\ \tau_{01} - \frac{\tau_{01}}{s_{01}} s & \text{if } s_m \leq s \leq s_c \\ \tau_{02} - \frac{\tau_{02}}{s_f} s & \text{if } s_c \leq s \leq s_f \end{cases} \quad (37)$$

Where the set of six unknown parameters is  $\tau_0$ ,  $\tau_{01}$ ,  $\tau_{02}$ ,  $s_{01}$ ,  $s_f$  and  $s_m$ . Equation 37 implies a finite effective bond length [177] [188] [189].

Therefore, from Equation 37, the CML is characterized by a shear stress equal to  $\tau_0$  when the relative displacement  $s$  is equal to zero.

### 5.1.2 Construction of the analytical load-global slip response

The method herein adopted for the calibration of the CML employs the load-global slip response. There are two ways to determine the unknown parameters of the cohesive material law by fitting the experimental data. The first way is to consider the  $P$ - $g$  response for each single specimen. The second way, which is the one employed in this work, consists of plotting the average curve for each family of specimen, and fitting this curve to find the unknown parameters.

Once the CML is chosen, the analytical load-slip response associated to that CML is determined by solving the fundamental equation that describes the Mode II debonding for a homogeneous substrate [188] [189]:

$$\frac{d^2 s}{dy^2} = \frac{P_f}{E_f A_f} \tau(s) \quad (38)$$

Where  $p_f$  is the perimeter of the fibers cross-section,  $E_f$  is the elastic modulus of fibers and  $A_f$  is the area of the fibers cross-section, and  $s = s(y)$  is the slip corresponding to the coordinate  $y$  (Figure 77).

The same procedure explained in [182] was adopted herein to define the analytical  $P$ - $g$  response. Two branches  $P_1(g)$  and  $P_2(g)$  can be adopted to define the global  $P$ - $g$  response:

- $P_1(g)$  is characterized by null slips  $s_f$  at the free end;
- $P_2(g)$  corresponds to a nonzero slip at the free end.

Figure 92a shows an example of the typical CML for FRCC material and the associated  $P$ - $g$  response [182].

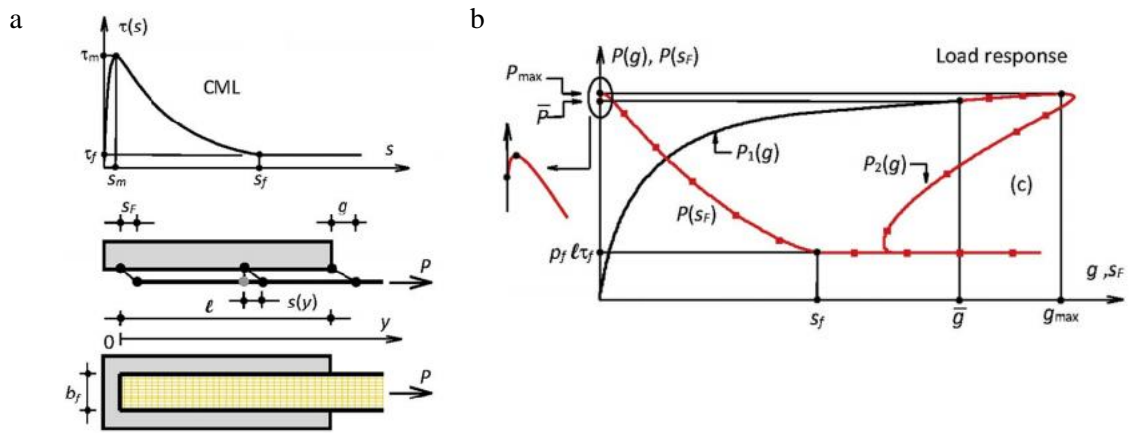


Figure 92 (a) Example of a typical CML for FRCC composites; (b) load-slip response associated to the typical CML [182]

The procedure consists of four steps.

In the first step, the applied force  $\bar{P}$  and the corresponding loaded end slip  $\bar{g}$  at the onset of nonzero slip at the free end are determined by solving the fundamental equation (Equation 38), imposing the boundary conditions at the free end (without the anchorage):

$$\begin{cases} s(0) = 0 \\ \varepsilon(0) = \frac{ds}{dy} \Big|_{y=0} = 0 \end{cases} \quad (39)$$

Therefore,  $\bar{P}$  and  $\bar{g}$  are determined as:

$$\begin{aligned} \bar{g} &= \bar{s}(l) \\ \bar{P} &= E_f A_f \frac{ds}{dy} \Big|_{y=l} \end{aligned} \quad (40)$$

With  $\bar{s}(y)$  solution of the fundamental equation (Equation 38) with the boundary conditions defined above.

The second step of the procedure consists in determining the first branch of the  $P$ - $g$  response.  $P_1(g)$  can be determined using the following equation

$$g = s(l)$$

$$P_1(g) = \sqrt{2\rho E_f A_f \int_0^g \tau(s) ds} \quad (41)$$

The third step consists on determining the second branch of the response.  $P_2(g)$  is determined by considering an array of value of the free end slip and solving Equation 38, imposing the boundary conditions:

$$\begin{cases} s(0) = s_f \\ \varepsilon(0) = \left. \frac{ds}{dy} \right|_{y=0} = 0 \end{cases} \quad (42)$$

The solution  $s(y) = s_{sF}(y)$  of the fundamental equation with the boundary conditions (Equation 42) allows correlating the load and the slip with each value of  $s_F$ :

$$g(s_F) = s_{sF}(l)$$

$$P(s_F) = E_f A_f \left. \frac{ds_{sF}}{dy} \right|_{y=l} \quad (43)$$

The meaning of the subscript  $s_F$  is that the corresponding slip profile  $s_{sF}(y)$  is associated with a certain  $s_F$ , and therefore for each value of  $s_F$  it is possible to determine the slip profile. This allows to determine the value of the loaded end slip  $g(s_F)$  and the corresponding load  $P(s_F)$  for each value of  $s_F$ .

With the last step, the load-slip response is determined. As mentioned above, the  $P$ - $g$  response consists of two branches that were determined in the second and third step of the procedure adopted. Once  $P_1(g)$  and  $P_2(g)$  are determined it is possible to evaluate the global response. It is important to observe that if the CML is characterized by  $\tau(0) = 0$ , then the first branch does not exist. This expedient allows to understand that the existence of the two branches used to describe the  $P$ - $g$  response depends on the CML adopted.

The criterion adopted to minimize the distance between the analytical and the experimental response to define the parameters of the CML is the least square method.

### 5.1.3 Implementation of the indirect method and modelling of the anchorage

The cohesive material law (CML) characterizes the bond behavior of SRG applied to concrete and masonry elements and it was calibrated through the indirect method. Two analytical expressions were adopted, the first one proposed by Dai et al. [186] and the second one proposed by Focacci and Carloni [188]. The parameters of the CML were obtained by fitting the experimental data. The average load-global slip response (black dashed line in Figure 93a, b and c) of specimens of group A1, A3 and A4, defined in section 4.1.2, characterized by the same mode of failure (i.e. interlaminar failure at the matrix-fiber interface), was considered. To compute the average  $P$ - $g$  curve, the average of the loads of the  $P$ - $g$  responses of the specimens was evaluated for each value of  $g$ . The calibration criterion is applied by minimizing the distance between the analytical load response, determined as described above, and the average experimental one.. Once the CML is chosen, the analytical expression associated to a  $\tau(s)$  was evaluated based on Equation 38.

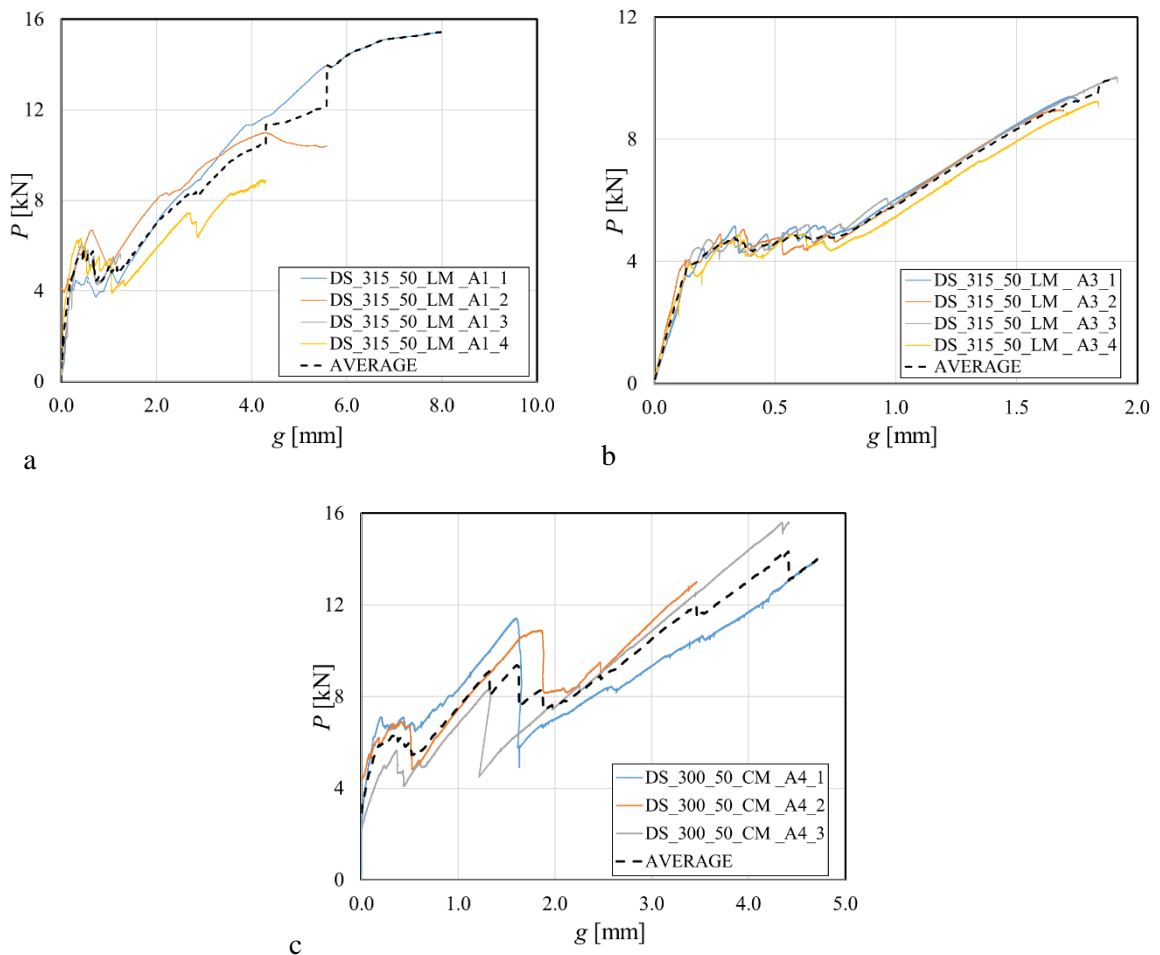


Figure 93 Experimental  $P$ - $g$  responses with the average  $P$ - $g$  curve for (a) A1 masonry blocks; (b) A3 masonry blocks and (c) A4 concrete prisms

At this stage, the calibration method was applied only to the portion of the experimental load-global slip response corresponding to plateau, which means that the effect of the anchorage was not

considered yet. The parameters of the CML obtained from the trilinear function and Dai et al. are reported in Table 24, and the  $\tau(s)$  relationship is plotted in Figure 94a. Once the CML was defined, the associated  $P$ - $g$  response was evaluated (Figure 94b).

Comparing the maximum stresses ( $\tau_{max}$ ) obtained from the two analytical expressions, for group A1 and A3 values are consistent, also when compared with the values found in [177]. For group A4 the value of  $\tau_{max}$  appeared to be higher when the trilinear function is adopted. It should be noted that for concrete specimens (group A4) some problems during the fitting process could arise since the first branch of the experimental load response is almost vertical, as shown in Figure 93c, and therefore the calibration may not be accurate.

Table 24 Fracture parameters obtained from the indirect calibration method

| Calibration                 | Trilin. Eq. 37 [188]  |                   |                 | Dai et al. Eq. 36 [186] |                   |                 |
|-----------------------------|-----------------------|-------------------|-----------------|-------------------------|-------------------|-----------------|
|                             | $\tau_{max}$<br>[MPa] | $s_{max}$<br>[mm] | $G_F$<br>[N/mm] | $\tau_{max}$<br>[MPa]   | $s_{max}$<br>[mm] | $G_F$<br>[N/mm] |
| CAL. $\overline{P(g)}_{A1}$ | 1.38                  | 0.19              | 0.19            | 1.36                    | 1.01              | 0.31            |
| CAL. $\overline{P(g)}_{A3}$ | 1.11                  | 0.09              | 0.10            | 0.75                    | 0.60              | 0.17            |
| CAL. $\overline{P(g)}_{A4}$ | 2.80                  | 0.01              | 1.33            | 0.93                    | 0.29              | 0.29            |

The fracture energy, reported in Table 24, is calculated as the area under  $\tau(s)$  curve. Figure 94b compares the average experimental  $P$ - $g$  response of A3 specimens ( $\overline{P(g)}_{A3}$ ) and the analytical response obtained from the calibration method (dotted red line in Figure 94). The  $P$ - $g$  curve is cropped because as stated above, only the  $P$ - $g$  curve until the end of the plateau is considered.

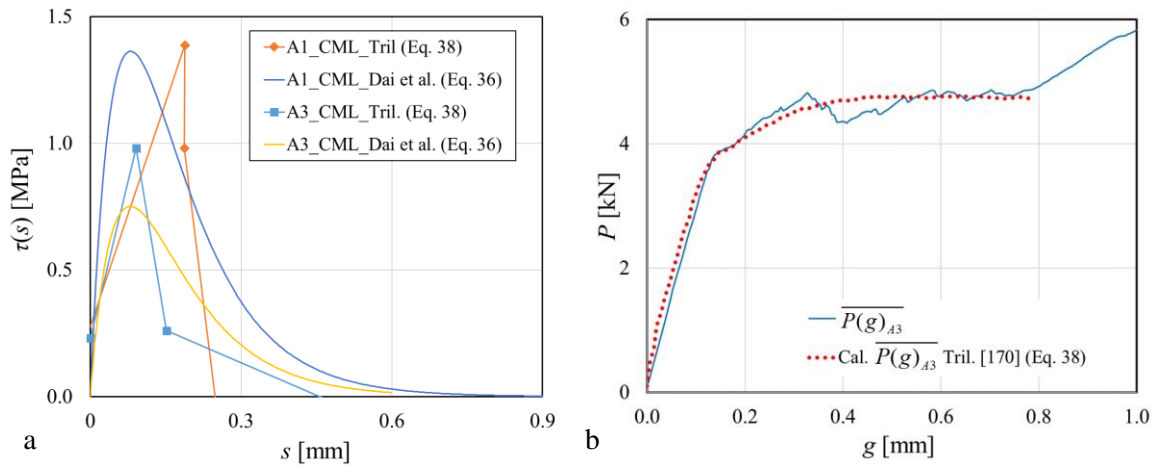


Figure 94 (a) Comparison between CMLs obtained from the calibration method of load-responses of A1 and A3 masonry blocks; (b) comparison between experimental and analytical  $P$ - $g$  response

In section 3.3.6, Mode I fracture energy of quasi-brittle materials are compared (Table 17). Values of  $G_F$  evaluated using the concept of the work of fracture of Matrix 1 and 2 can be compared with values of  $G_F$  obtained from the indirect method, thus evaluating the area under the  $\tau(s)$  curve. For Matrix 1, when the trilinear function [188] is adopted,  $G_F$  of Mode II is between 3 (CAL.  $\overline{P(g)}_{A3}$ ) and 6 (CAL.  $\overline{P(g)}_{A1}$ ) times  $G_F$  of Mode I (30.3 N/m), while for Matrix 2,  $G_F$  of Mode II is 10 times  $G_F$  of Mode I.

Once the CML was obtained, the effect of the anchorage was modeled. For masonry blocks with the extension of the fibers of the SRG strip inserted into the block (group A1), the differential equation was solved as above but the boundary condition imposed at the free end was derived from the  $P$ - $\delta$  of the pull out test. The average  $P$ - $\delta$  curve of the pull out test (black dotted line in Figure 95a) was used together with the CML. At the free end, when  $s_F$  was not zero, instead of being associated with zero strain was associated with the strain derived from the load in the  $P$ - $\delta$  curve associated with the value of  $s_F$ . The associated analytical  $P$ - $g$  is compared with experimental responses (Figure 95b).

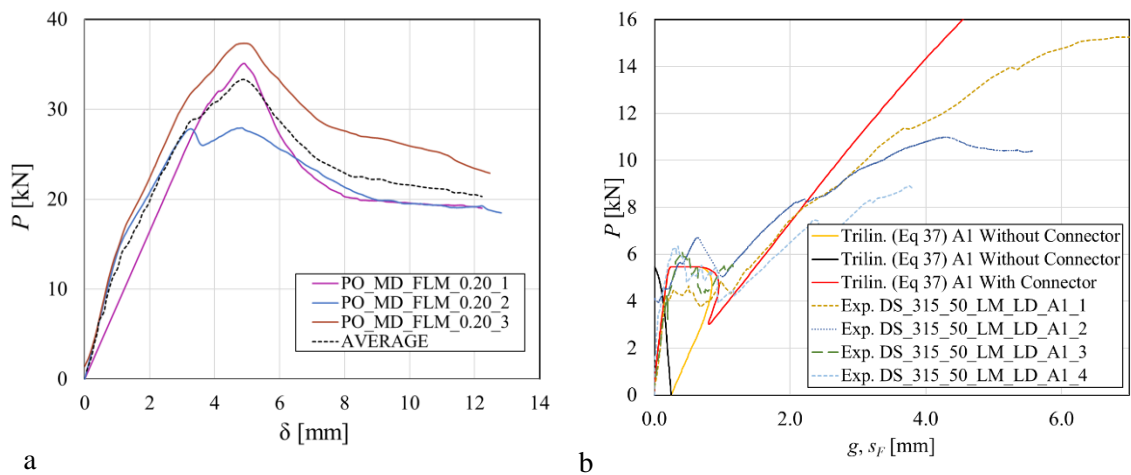


Figure 95 (a) average curve of pull out tes; (b) comparison between experimental and analytical curves

When the experimental and the analytical curves are overlapped, a good match between the two responses is observed. It should be pointed out that, as mentioned above, single-lap direct shear tests on specimens with the anchorage system were stopped before the end of the test due to the rotation of the masonry block (see section 4.3.1). Therefore, the value of the maximum load associated to the analytical response appeared to be higher than the value obtained experimentally.

## Conclusions

The whole research aimed to evaluate Mode I fracture parameters of quasi-brittle materials. Digital image correlation (DIC) was employed to get an insight into the extension of the fracture process zone (FPZ). First, the displacement field and the strain profiles from DIC were evaluated and then the size of the FPZ was measured. For this purpose, digital image analysis was employed during three-point bending tests performed on notched concrete beams and alkali-activated mortars (AAMs).

Load-displacement responses obtained from DIC were compared to the load-displacement responses obtained from the average of the two LVDTs readings. Generally, a good agreement between the DIC-based load response and the LVDT-based load response was observed. However, for some specimens the initial slope of the  $P$ - $\delta$  response obtained from the DIC analysis appeared to be greater than the  $P$ - $\delta$  response obtained from the LVDTs. This difference can be related to small adjustments or rotations of the LVDTs holders that could affect the measure of the vertical displacement, thus obtaining values of  $\delta$  larger than the values obtained from DIC.

To evaluate the vertical displacement from DIC, two locations of the top squares under the application of the load were considered. It was observed that there was no difference between the two  $P$ - $\delta$  curves from DIC when the top square is moved vertically, which means that no damage of concrete occurred due to stress concentrations.

In addition, one aspect that it is not usually discussed is the importance of choosing a suitable combination of subset and step, while analyzing DIC data. In fact, finding a suitable combination of subset and step, translates into obtaining reliable fracture parameters.

Digital image analysis was also employed to evaluate the variation of the horizontal strain ( $\epsilon_{xx}$ ), as the average value of  $\epsilon_{xx}$  across an interval  $x$ , close to the notch tip, to understand which value of the load corresponded to the opening of the crack. Two intervals of  $x$  were chosen, 5 and 10 mm, to determine the influence of the width of the interval itself and to take into account the inhomogeneity of the mortars due to the presence of the aggregates. The same expedient was adopted to evaluate the crack opening profile computed as the difference of the displacements ( $\Delta u$ ) in the horizontal direction along the ligament. In fact, to be consistent with the strain profiles, displacement were averaged in two sets of rectangular areas and then subtract to obtain  $\Delta u$  that were placed apart one another by two distances, 5 and 10 mm. When different intervals of  $x$  were considered, the difference between the two strain profiles was not substantial, and the same was noted for the crack opening profile. On the other hand, choosing a non-suitable dimension of the rectangular area in which the displacements were averaged might results in a wrong interpretation of the value of the crack opening ( $w$ ). The importance of choosing a suitable dimensions of the rectangular areas, in which the quantity considered was averaged, was confirmed when the variation of the horizontal

strain versus time was plotted for concrete specimens. A correct dimension of the rectangle area coupled with a suitable interval of the moving average, permitted to evaluate the coefficients  $\beta$  to understand if the values proposed in literature are correct for these types of specimens.

The value of fracture energy ( $G_F$ ) was evaluated using the method of work of fracture. Several parameters may influence the value of  $G_F$  as the width and the size of the specimens, curing method and type of aggregate. In fact, for larger width specimens with certain depths, the friction could compromise the evaluation of the fracture energy. For concrete specimens, it was noted that a different curing protocol was associated with a different value of the fracture energy for specimens that had the same cross-section. It should be pointed out that concrete specimens were left in the water bath until testing to avoid humidity gradients that could have entailed for shrinkage strains that do not scale with the width of the specimen. Therefore, the curing conditions must be the same for all specimens. For AAMs, the fracture energy is highly dependent on the type of aggregate used and within the same type a variation of the maximum aggregate size between 2 and 6 mm does not strongly influence the value of the fracture energy. Values of  $G_F$  available in the literature are quite scattered as they are associated with geopolymers obtained with different curing conditions and compositions. It was observed that the fracture energy appears also to be influenced by geopolymer microstructure and in particular by unreacted FA particles and expanded perlite aggregates.

Other quasi-brittle materials, which included sandstone specimens, tuff and fired-clay bricks were tested using the same three-point bending set-up, the fracture energy was evaluated and all the values were compared. Natural stones, which comprised tuff from Rome and Naples, and sandstone from the archeological site of *Tharros* (Sardinia), showed the lowest values of the fracture energy. A low value of fracture energy could be associated to the origin of the stone itself. In fact, due to its volcanic origin, both Naples and Roman tuff presented lot of inclusions and clasts, while *Tharros* stone showed a high percentage of voids, which could decrease the fracture energy. On the other hand, fired-clay bricks collected from demolished structures showed, on average, values of  $G_F$  higher than those of tuff and *Tharros* stone. However, results appeared to be quite scattered among each family of brick: Modena bricks showed the highest value of  $G_F$ , which could be associated to the different manufacturing process of the brick itself.

The fracture process zone for concrete and AAMs specimens was measured using DIC. The extension of the FPZ at different points of the load response was evaluated and it was observed that a complex stress distribution arose at the top of the concrete beam while the FPZ stagnated during the development of the long tail of the response. For AAMs the experimental results suggested that the size of the FPZ and the fracture energy depended on the type of aggregate used in the mixture rather than its size. Thus, the size of the FPZ was related to the size of the aggregate but the relationship is not unique for the three AAMs. The full development of the FPZ occurred in the descending branch of the load response. As the length of the ligament did not allow for a shifting of the full FPZ after it was formed, the remaining portion of the load response did not correspond

to a self-similar propagation of the crack, which would be required to use correctly the concept of the work of fracture.

Although digital image analysis was employed to evaluate the critical value of the crack opening ( $w_c$ ) of Mode I fracture, DIC was not used to study the fracture process of steel reinforced grout (SRG) composites bonded to masonry and concrete elements, since the slip occurred at the interface between matrix and fibers.

Therefore, two alternative methods were proposed. A Mode II condition is assumed to determine the interfacial parameters of SRG composites bonded to quasi-brittle materials. Therefore, single-lap direct shear tests were performed on SRG composite externally bonded to masonry and concrete substrate. The slip at the interface between matrix and fibers was evaluated from the load-global slip response and indirectly through the calibration method.

Five parameters were analyzed to determine their influence: width of the SRG matrix, type of SRG matrix, test rate, role of the substrate and effectiveness of the anchorage system. Test results suggested that increasing the width of the SRG matrix (without increasing the width of the fibers), from 50 mm to 70 and 90 mm, the average load-carrying capacity ( $P_{crit}$ ) increased by 52% and 69%, respectively, due to a higher amount of energy required for the crack to initiate and propagate. Results of masonry blocks strengthened with cement-based mortar SRG were less scattered with respect to blocks strengthened with lime-based mortar SRG. Compared to specimens with the same matrix width but strengthened with lime-based matrix SRG, the average load-carrying capacity and peak load ( $P^*$ ) of specimens strengthened with cement-based matrix SRG increased by 33% and 20%, respectively. The average peak load of SRG-masonry joints tested at a rate ten times the standard rate increased by 37%. Therefore, it appeared that for this type of composite a rate effect might have been present. Comparing masonry and concrete substrate strengthened with the same SRG system, the mode of failure changed: failure of SRG-concrete joints (with low density steel fibers) was due to rupture of steel fibers, while SRG-masonry joints exhibited predominantly interlaminar failure. Therefore, for concrete specimens, it was not possible to evaluate  $P_{crit}$ . When the averages of peak load were compared, the highest average value was observed in concrete specimens since rupture of the fibers occurred.

One of the most observed failure mode when SRGs were bonded to masonry elements is premature debonding, and the same failure mode was observed when SRGs (with medium density steel fibers), were bonded to concrete specimens. Therefore, to prevent or delay this type of failure, a new study of a possible solution with an anchorage system was proposed. The anchorage system could be required to improve the bond capacity and therefore the maximum force transferable between the composite and the substrate. When SRGs were bonded to masonry blocks, two types of anchorage were considered: an extension of the SRG fibers into the masonry block obtained by bending the fibers and inserting them into a hole filled with a mortar, and a separate anchor spike that interacts with the bonded strip. In addition to masonry blocks, concrete prisms strengthened with the same

SRG system with 45° anchor spike inserted into the prisms were tested for comparison, using the same test set-up. Effectiveness of the SRG strip was positively affected by the anchorage systems. The anchorages were able to carry additional load with respect to the load-carrying capacity of the SRG–masonry and concrete interface. In general, depending on the use of the anchorage systems, it would be more appropriate to choose one system over the other. One advantage of the bonded strip with extension of the SRG fibers into the masonry block and concrete prisms is the ease of realization. In fact, a separate spike requires more work, in particular when spike fibers have to be interweaved with the longitudinal fibers of the SRG. However, in some applications, such as repairing of continuous masonry wall, a separate spike will be required.

Further studies will be needed to understand if the type of SRG mortar matrix influences the responses when the anchorage is applied, and how the change in the interaction between fibers used for the SRG bonded strip and fibers used for the anchorage influences the results. Moreover, it would be interesting to know if the behavior of specimens changes when the same types of fibers are used for the bonded strip and for the anchor spike.

As stated above, the second method to evaluate the slip at the interface between the matrix and the fibers was the indirect method, which was also employed to model the effect of the anchorage. Once the cohesive material law (CML) was defined by fitting the experimental data, then the associated analytical  $P$ - $g$  response was plotted. It was observed a good match between the analytical and the experimental response.

The area under the  $\tau(s)$  curve was computed to evaluate the fracture energy of Mode II, and then compared with Mode I fracture energy evaluated from the work of fracture. For Matrix 1, when the trilinear function is adopted,  $G_F$  of Mode II is between 3 and 6 times  $G_F$  of Mode-I (30.3 N/m), while for Matrix 2,  $G_F$  of Mode II is approximately 10 times  $G_F$  of Mode-I.

When the effect of the anchorage was modeled, for masonry blocks with the extension of the bonded strip into the masonry block (A1), the differential equation was solved and the boundary condition imposed at the free end derived from the  $P$ - $g$  response of the pull out test. The slip at the free end was not equal to zero and therefore associated with the strain derived from the  $P$ - $\delta$  curve associated with the value of  $s_F$ . The obtained analytical  $P$ - $g$  response was compared to the experimental responses of masonry blocks with the anchorage system. A good match between the two curves was observed, which means that with the calibration method it was possible to model the effect of the anchorage properly. Further studies will be carried out on masonry blocks with the separate spike in the second bottom layer of bricks (group A3) using the same procedure. For this group of specimens, instead of using the boundary condition derived from the pull out test, the differential equation will be solved by using the boundary condition derived from the  $P$ - $g$  response of masonry blocks with the separate spike in the second top layer of bricks (group A2). This expedient will be used to have the same fibers density for the SRG bonded strip and for the anchor spike.

## References

- [1] S. Y. Alam, J. Saliba, and A. Loukili, “Fracture examination in concrete through combined digital image correlation and acoustic emission techniques,” *Construction and Building Materials*, vol. 69, pp. 232–242, 2014, doi: 10.1016/j.conbuildmat.2014.07.044.
- [2] Cedolin L., Dei Poli S., Iori I., “Tensile Behavior of Concrete,” *Journal of Engineering Mechanics*, vol. 113, no. 3, 1987.
- [3] A. Hillerborg, “The theoretical basis of a method to determine the fracture energy  $G_F$  of concrete,” *Matériaux et Construction*, vol. 18, no. 106, p. 6.
- [4] G. L. Golewski, “Measurement of fracture mechanics parameters of concrete containing fly ash thanks to use of Digital Image Correlation (DIC) method,” *Measurement: Journal of the International Measurement Confederation*, vol. 135, pp. 96–105, 2019, doi: 10.1016/j.measurement.2018.11.032.
- [5] S. G. Shah and J. M. C. Kishen, “Fracture Properties of Concrete-Concrete Interfaces Using Digital Image Correlation,” *Experimental Mechanics*, vol. 51, no. 3, pp. 303–313, 2011, doi: 10.1007/s11340-010-9358-y.
- [6] Z. Wu, H. Rong, J. Zheng, F. Xu, and W. Dong, “An experimental investigation on the FPZ properties in concrete using digital image correlation technique,” *Engineering Fracture Mechanics*, vol. 78, no. 17, pp. 2978–2990, 2011, doi: 10.1016/j.engfracmech.2011.08.016.
- [7] P.-E. Petersson, “Crack growth and development of fracture zones in plain concrete and similar materials,” Doctoral Thesis, Lund Institute of Technology, Lund, Sweden, 1981.
- [8] L. Graziani, M. Kneć, T. Sadowski, M. D’Orazio, and S. Lenci, “Measurement of R-curve in clay brick blocks using optical measuring technique,” *Engineering Fracture Mechanics*, vol. 121–122, pp. 1–10, May 2014, doi: 10.1016/j.engfracmech.2014.04.007.
- [9] A. A. Griffith, *The Phenomena of Rupture and Flow in Solids*, vol. 221. 2020.
- [10] Z. P. Bazant, *Fracture Mechanics of Concrete Structures: Proceedings of the First International Conference on Fracture Mechanics of Concrete Structures (FraMCoS1), held at Beaver Run Resort, Breckenridge, Colorado, USA, 1-5 June 1992.*, 1st ed. CRC Press, 2014.
- [11] C. Carloni, “Analyzing bond characteristics between composites and quasi-brittle substrates in the repair of bridges and other concrete structures,” in *Advanced Composites in Bridge Construction and Repair*, Elsevier, 2014, pp. 61–93.
- [12] G. I. Barenblatt, “The Mathematical Theory of Equilibrium Cracks in Brittle Fracture,” in *Advances in Applied Mechanics*, vol. 7, Elsevier, 1962, pp. 55–129.
- [13] A. Hillerborg, M. Modéer, and P.-E. Petersson, “Analysis of crack formation and crack growth in concrete by means of fracture mechanics and finite elements,” *Cement and Concrete Research*, vol. 6, no. 6, pp. 773–781, Nov. 1976, doi: 10.1016/0008-8846(76)90007-7.
- [14] Z. P. Bažant, *Fracture in concrete and reinforced concrete*. 1985.

- [15] G. V. Guinea, J. Planas, and M. Elices, “Measurement of the fracture energy using three-point bend tests: Part 1—Influence of experimental procedures,” *Materials and Structures*, vol. 25, no. 4, pp. 212–218, May 1992, doi: 10.1007/BF02473065.
- [16] C. Carloni, M. Santandrea, and G. Baietti, “Influence of the width of the specimen on the fracture response of concrete notched beams,” *Engineering Fracture Mechanics*, vol. 216, p. 106465, Jul. 2019, doi: 10.1016/j.engfracmech.2019.04.039.
- [17] J. Planas, M. Elices, and G. V. Guinea, “Measurement of the fracture energy using three-point bend tests: Part 2—Influence of bulk energy dissipation,” *Materials and Structures*, vol. 25, no. 5, pp. 305–312, Jun. 1992, doi: 10.1007/BF02472671.
- [18] Z. P. Bažant and J. Planas, *Fracture and size effect in concrete and other quasibrittle materials*. Boca Raton: CRC Press, 1998.
- [19] O. Gunes, O. Buyukozturk, and E. Karaca, “A fracture-based model for FRP debonding in strengthened beams,” *Engineering Fracture Mechanics*, p. 13, 2009.
- [20] C. E. Bakis *et al.*, “Fiber-Reinforced Polymer Composites for Construction—State-of-the-Art Review,” *J. Compos. Constr.*, vol. 6, no. 2, pp. 73–87, May 2002, doi: 10.1061/(ASCE)1090-0268(2002)6:2(73).
- [21] A. Bilotta, F. Ceroni, E. Nigro, and M. Pecce, “Efficiency of CFRP NSM strips and EBR plates for flexural strengthening of RC beams and loading pattern influence,” *Composite Structures*, vol. 124, pp. 163–175, Jun. 2015, doi: 10.1016/j.compstruct.2014.12.046.
- [22] P. Carrara, D. Ferretti, and F. Freddi, “Debonding behavior of ancient masonry elements strengthened with CFRP sheets,” *Composites Part B: Engineering*, vol. 45, no. 1, pp. 800–810, Feb. 2013, doi: 10.1016/j.compositesb.2012.04.029.
- [23] A. Nanni *et al.*, “Guide to Design and Construction of Externally Bonded Fabric-Reinforced Cementitious Matrix (FRCM) and Steel-Reinforced Grout (SRG) Systems for Repair and Strengthening Masonry Structures.” Unpublished, 2020, doi: 10.13140/RG.2.2.17929.26721.
- [24] Wiberg A., “Strengthening of Concrete Beams Using Cementitious Carbon Fibre Composites,” Doctoral Thesis, Royal Institute of Technology SE-100 44 Stockholm, Sweden.
- [25] A. Napoli and R. Realfonzo, “Reinforced concrete beams strengthened with SRP/SRG systems: Experimental investigation,” *Construction and Building Materials*, vol. 93, pp. 654–677, Sep. 2015, doi: 10.1016/j.conbuildmat.2015.06.027.
- [26] Bisby L.A., Stratford T., Ward R.M., “Fibre Reinforced Cementitious Matrix Systems for Fire-Safe flexural Strengthening of Concrete: Pilot Testing at Ambient Temperatures.”
- [27] Ombres L., Verre S., “Shear Performance of FRCM Strengthened RC Beams.”
- [28] D’Antino T., Focacci F., Sneed L.H. and Pellegrino C., “Shear Strength Model for RC Beams with U-Wrapped FRCM Composites.”

- [29] A. Younis, U. Ebead, and K. C. Shrestha, "Different FRCM systems for shear-strengthening of reinforced concrete beams," *Construction and Building Materials*, vol. 153, pp. 514–526, Oct. 2017, doi: 10.1016/j.conbuildmat.2017.07.132.
- [30] S. Babaeidarabad, F. De Caso, and A. Nanni, "URM Walls Strengthened with Fabric-Reinforced Cementitious Matrix Composite Subjected to Diagonal Compression," *J. Compos. Constr.*, vol. 18, no. 2, p. 04013045, Apr. 2014, doi: 10.1061/(ASCE)CC.1943-5614.0000441.
- [31] A. Borri, G. Castori, and M. Corradi, "Shear behavior of masonry panels strengthened by high strength steel cords," *Construction and Building Materials*, vol. 25, no. 2, pp. 494–503, Feb. 2011, doi: 10.1016/j.conbuildmat.2010.05.014.
- [32] Z. Dong, M. Deng, Y. Zhang, C. Zhang, and P. Ma, "Out-of-plane strengthening of unreinforced masonry walls using textile reinforced mortar added short polyvinyl alcohol fibers," *Construction and Building Materials*, vol. 260, p. 119910, Nov. 2020, doi: 10.1016/j.conbuildmat.2020.119910.
- [33] L. H. Sneed, G. Baietti, G. Fraioli, and C. Carloni, "Compressive Behavior of Brick Masonry Columns Confined with Steel-Reinforced Grout Jackets," *J. Compos. Constr.*, vol. 23, no. 5, p. 04019037, Oct. 2019, doi: 10.1061/(ASCE)CC.1943-5614.0000963.
- [34] T. D. Krevaikas, "Experimental study on carbon fiber textile reinforced mortar system as a means for confinement of masonry columns," *Construction and Building Materials*, vol. 208, pp. 723–733, May 2019, doi: 10.1016/j.conbuildmat.2019.03.033.
- [35] G. Ramaglia, G. P. Lignola, A. Balsamo, A. Prota, and G. Manfredi, "Seismic Strengthening of Masonry Vaults with Abutments Using Textile-Reinforced Mortar," *J. Compos. Constr.*, vol. 21, no. 2, p. 04016079, Apr. 2017, doi: 10.1061/(ASCE)CC.1943-5614.0000733.
- [36] V. Alecci, F. Focacci, L. Rovero, G. Stipo, and M. De Stefano, "Intrados strengthening of brick masonry arches with different FRCM composites: Experimental and analytical investigations," *Composite Structures*, vol. 176, pp. 898–909, Sep. 2017, doi: 10.1016/j.compstruct.2017.06.023.
- [37] A. Razavizadeh, B. Ghiassi, and D. V. Oliveira, "Bond behavior of SRG-strengthened masonry units: Testing and numerical modeling," *Construction and Building Materials*, vol. 64, pp. 387–397, Aug. 2014, doi: 10.1016/j.conbuildmat.2014.04.070.
- [38] *Guide for the design and construction of externally bonded FRP systems for strengthening existing structures.* ] CNR-DT200, Guide for the design and construction of externally bonded frp systems for strengthening existing structures-materials, RC and PC structur.
- [39] W. M. Sebastian, "Significance of Midspan Debonding Failure in FRP-Plated Concrete Beams," *J. Struct. Eng.*, vol. 127, no. 7, pp. 792–798, Jul. 2001, doi: 10.1061/(ASCE)0733-9445(2001)127:7(792).

- [40]O. Rosenboom and S. Rizkalla, “Modeling of IC Debonding of FRP-Strengthened Concrete Flexural Members,” *J Compos Constr*, vol. 12, no. 2, pp. 168–179, Apr. 2008, doi: 10.1061/(ASCE)1090-0268(2008)12:2(168).
- [41]T. H.-K. Kang, J. Howell, S. Kim, and D. J. Lee, “A State-of-the-Art Review on Debonding Failures of FRP Laminates Externally Adhered to Concrete,” *Int J Concr Struct Mater*, vol. 6, no. 2, pp. 123–134, Jun. 2012, doi: 10.1007/s40069-012-0012-1.
- [42]J. F. Chen and J. G. Teng, “Anchorage Strength Models for FRP and Steel Plates Bonded to Concrete,” *J. Struct. Eng.*, vol. 127, no. 7, pp. 784–791, Jul. 2001, doi: 10.1061/(ASCE)0733-9445(2001)127:7(784).
- [43]Tiljsten B., “Defining anchor lengths of steel and CFRP plates bonded to concrete,” *Int. J. Adhesion and Adhesives*, vol. 17, pp. 319–327, 1997.
- [44]Bizindavyi, L. and Neal, K.W., “Transfer Lengths and Bond Strengths for Composites Bonded to Concrete,” *Journal of Composites for Construction*, vol. 3, no. 4, pp. 153–159, 1990.
- [45]Michael J. Chajes, William W. Finch, Jr., Ted F. Januszka, and Theodore A. Thomson, Jr., “Bond and Force Transfer of Composite-Material Plates Bonded to Concrete,” *Structural Journal*, vol. 93, no. 2, pp. 209–217.
- [46]S. De Santis, F. G. Carozzi, G. de Felice, and C. Poggi, “Test methods for Textile Reinforced Mortar systems,” *Composites Part B: Engineering*, vol. 127, pp. 121–132, Oct. 2017, doi: 10.1016/j.compositesb.2017.03.016.
- [47]S. De Santis *et al.*, “Round Robin Test on tensile and bond behaviour of Steel Reinforced Grout systems,” *Composites Part B: Engineering*, vol. 127, pp. 100–120, Oct. 2017, doi: 10.1016/j.compositesb.2017.03.052.
- [48]C. Mazzotti, B. Ferracuti, and A. Bellini, “Experimental bond tests on masonry panels strengthened by FRP,” *Composites Part B: Engineering*, vol. 80, pp. 223–237, Oct. 2015, doi: 10.1016/j.compositesb.2015.05.019.
- [49]E. Sassoni, V. Sarti, A. Bellini, C. Mazzotti, and E. Franzoni, “The role of mortar joints in FRP debonding from masonry,” *Composites Part B: Engineering*, vol. 135, pp. 166–174, Feb. 2018, doi: 10.1016/j.compositesb.2017.10.021.
- [50]F. Ceroni, M. Leone, V. Rizzo, A. Bellini, and C. Mazzotti, “Influence of mortar joints on the behaviour of FRP materials bonded to different masonry substrates,” *Engineering Structures*, vol. 153, pp. 550–568, Dec. 2017, doi: 10.1016/j.engstruct.2017.10.030.
- [51]F. G. Carozzi, P. Colombi, G. Fava, and C. Poggi, “A cohesive interface crack model for the matrix–textile debonding in FRCM composites,” *Composite Structures*, vol. 143, pp. 230–241, May 2016, doi: 10.1016/j.compstruct.2016.02.019.
- [52]A. Bellini, M. Bovo, and C. Mazzotti, “Experimental and numerical evaluation of fiber-matrix interface behaviour of different FRCM systems,” *Composites Part B: Engineering*, vol. 161, pp. 411–426, Mar. 2019, doi: 10.1016/j.compositesb.2018.12.115.

- [53] J. Salsavilca, J. Yacila, N. Tarque, and G. Camata, "Experimental and analytical bond behaviour of masonry strengthened with steel reinforced grout (SRG)," *Construction and Building Materials*, vol. 238, p. 117635, Mar. 2020, doi: 10.1016/j.conbuildmat.2019.117635.
- [54] B. Ghiassi, D. V. Oliveira, V. Marques, E. Soares, and H. Maljaee, "Multi-level characterization of steel reinforced mortars for strengthening of masonry structures," *Materials & Design*, vol. 110, pp. 903–913, Nov. 2016, doi: 10.1016/j.matdes.2016.08.034.
- [55] Nakaba K, Kanakubo T, Furuta T, Yoshizawa H, "Bond Behavior between Fiber-Reinforced Polymer Laminates and Concrete," *SJ*, vol. 98, no. 3, 2001, doi: 10.14359/10224.
- [56] Chajes, M J, Finch Jr, W W, Januszka, T F, and Chajes, M J; Finch Jr, W W; Januszka, T F; Thomson Jr, T A, "Bond and force transfer of composite material plates bonded to concrete," *ACI Structural Journal*, vol. 93, no. 2, pp. 208–217, 1966.
- [57] C. Carloni, M. Santandrea, and I. A. O. Imohamed, "Determination of the interfacial properties of SRP strips bonded to concrete and comparison between single-lap and notched beam tests," *Engineering Fracture Mechanics*, vol. 186, pp. 80–104, Dec. 2017, doi: 10.1016/j.engfracmech.2017.09.020.
- [58] S. V. Grelle and L. H. Sneed, "Review of Anchorage Systems for Externally Bonded FRP Laminates," *Int J Concr Struct Mater*, vol. 7, no. 1, pp. 17–33, Mar. 2013, doi: 10.1007/s40069-013-0029-0.
- [59] F. Ceroni, M. Pecce, S. Matthys, and L. Taerwe, "Debonding strength and anchorage devices for reinforced concrete elements strengthened with FRP sheets," *Composites Part B: Engineering*, vol. 39, no. 3, pp. 429–441, Apr. 2008, doi: 10.1016/j.compositesb.2007.05.002.
- [60] S. V. Grelle, "Categorization and experimental evaluation of anchorage systems for fiber-reinforced polymer laminates bonded to reinforced concrete structures," p. 174.
- [61] Q. Jin and C. K. Y. Leung, "Fiber Reinforced Cementitious Composites (FRCC) Plate for the Anchoring of FRP Sheet on Concrete Member," in *Advances in FRP Composites in Civil Engineering*, L. Ye, P. Feng, and Q. Yue, Eds. Berlin, Heidelberg: Springer Berlin Heidelberg, 2011, pp. 53–56.
- [62] R. Kalfat, R. Al-Mahaidi, and S. T. Smith, "Anchorage Devices Used to Improve the Performance of Reinforced Concrete Beams Retrofitted with FRP Composites: State-of-the-Art Review," *J. Compos. Constr.*, vol. 17, no. 1, pp. 14–33, Feb. 2013, doi: 10.1061/(ASCE)CC.1943-5614.0000276.
- [63] Teng, J. G., Chen, J. F., Smith, S. T., & Lam, L, *FRP strengthened RC structures*. 2002.
- [64] S. J. Kim and S. T. Smith, "Pullout Strength Models for FRP Anchors in Uncracked Concrete," *J. Compos. Constr.*, vol. 14, no. 4, pp. 406–414, Aug. 2010, doi: 10.1061/(ASCE)CC.1943-5614.0000097.

- [65]H. W. Zhang and S. T. Smith, “FRP-to-concrete joint assemblages anchored with multiple FRP anchors,” *Composite Structures*, vol. 94, no. 2, pp. 403–414, Jan. 2012, doi: 10.1016/j.compstruct.2011.07.025.
- [66]M. A. Aiello, L. Valente, and A. Rizzo, “Moment redistribution in continuous reinforced concrete beams strengthened with carbon-fiber-reinforced polymer laminates,” *Mech Compos Mater*, vol. 43, no. 5, pp. 453–466, Sep. 2007, doi: 10.1007/s11029-007-0043-x.
- [67]H. W. Zhang, S. T. Smith, and S. J. Kim, “Optimisation of carbon and glass FRP anchor design,” *Construction and Building Materials*, vol. 32, pp. 1–12, Jul. 2012, doi: 10.1016/j.conbuildmat.2010.11.100.
- [68]R. Sadone, M. Quiertant, S. Chataigner, J. Mercier, and E. Ferrier, “Behavior of an Innovative End-Anchored Externally Bonded CFRP Strengthening System under Low Cycle Fatigue,” in *Advances in FRP Composites in Civil Engineering*, L. Ye, P. Feng, and Q. Yue, Eds. Berlin, Heidelberg: Springer Berlin Heidelberg, 2011, pp. 537–540.
- [69]ACI Committee 440, *Guide for the design and construction of externally bonded FRP systems for strengthening concrete structures (ACI 440.2R-08)*, Farmington Hills, MI: American Concrete Institute. 2008.
- [70]British Standards Institution and European Committee for Standardization, *Testing hardened concrete. Part 3, Part 3*,. 2011.
- [71]“Testing concrete: Method for determination of static modulus of elasticity in compression,” BSI British Standards. doi: 10.3403/00049274U.
- [72]British Standards Institution (BSI), *BS EN 12390-6:2009. Testing hardened concrete. Part 6: tensile splitting strength of test specimens*. BSI, 2009.
- [73]British Standards Institution and European Committee for Standardization, *Eurocode 2: design of concrete structures - part 1-1 :general rules and rules for buildings*. 2015.
- [74]British Standards Institution, *Methods of testing cement. Part 1, Part 1*,. 2016.
- [75]*BS EN 12504-4:2004 Testing concrete. Determination of ultrasonic pulse velocity*. 2004.
- [76]“<https://sanmarco.it/>.”
- [77]“Metodi di prova per elementi per muratura - Parte 1: Determinazione della resistenza a compressione.”
- [78]G. Baietti, E. Franzoni, G. Quartarone, A. Fregni, and C. Carloni, “Bond Behavior between Tuff and Fired-Clay Brick Masonry Blocks and SRG Composites,” *KEM*, vol. 817, pp. 118–125, Aug. 2019, doi: 10.4028/www.scientific.net/KEM.817.118.
- [79]Casadei, M., “Application of FRCM composites to masonry blocks manufactured with historical bricks: bond behaviour with and without salt contamination,” University of Bologna.
- [80]“Methods of test for masonry units. Determination of compressive strength,” May 2011.

- [81] Semprini, Simone, “Mechanical and chemical-physical characterization of sandstone from the Phoenician-Punic necropolis of Tharros (Sardinia, Italy) with the aim of its conservation and strengthening,” Master thesis, University of Bologna.
- [82] “Standard Test Method for Compressive Strength of Dimension Stone.”
- [83] “Suggested Methods for Determining Tensile Strength of Rock Materials.”
- [84] “Natural stone test methods. Determination of static elastic modulus.”
- [85] S. Pessiki, K. A. Harries, J. T. Kestner, R. Sause, and J. M. Ricles, “Axial Behavior of Reinforced Concrete Columns Confined with FRP Jackets,” *J. Compos. Constr.*, vol. 5, no. 4, pp. 237–245, Nov. 2001, doi: 10.1061/(ASCE)1090-0268(2001)5:4(237).
- [86] K. Abdelrahman and R. El-Hacha, “Behavior of Large-Scale Concrete Columns Wrapped with CFRP and SFRP Sheets,” *J. Compos. Constr.*, vol. 16, no. 4, pp. 430–439, Aug. 2012, doi: 10.1061/(ASCE)CC.1943-5614.0000278.
- [87] R. Abbasnia, R. Ahmadi, and H. Ziaadiny, “Effect of confinement level, aspect ratio and concrete strength on the cyclic stress–strain behavior of FRP-confined concrete prisms,” *Composites Part B: Engineering*, vol. 43, no. 2, pp. 825–831, Mar. 2012, doi: 10.1016/j.compositesb.2011.11.008.
- [88] G. Campione and N. Miraglia, “Strength and strain capacities of concrete compression members reinforced with FRP,” *Cement and Concrete Composites*, vol. 25, no. 1, pp. 31–41, Jan. 2003, doi: 10.1016/S0958-9465(01)00048-8.
- [89] T. Triantafillou and C. C. G. Papanicolaou, “Innovative Applications of Textile-Based Composites in Strengthening and Seismic Retrofitting as Well as in the Prefabrication of New Structures,” *AMR*, vol. 639–640, pp. 26–41, Jan. 2013, doi: 10.4028/www.scientific.net/AMR.639-640.26.
- [90] T. C. Triantafillou, “Composites: a new possibility for the shear strengthening of concrete, masonry and wood,” *Composites Science and Technology*, vol. 58, no. 8, pp. 1285–1295, Aug. 1998, doi: 10.1016/S0266-3538(98)00017-7.
- [91] T. Trapko, “Behaviour of fibre reinforced cementitious matrix strengthened concrete columns under eccentric compression loading,” *Materials & Design (1980-2015)*, vol. 54, pp. 947–954, Feb. 2014, doi: 10.1016/j.matdes.2013.09.008.
- [92] P. Colajanni, F. De Domenico, A. Recupero, and N. Spinella, “Concrete columns confined with fibre reinforced cementitious mortars: Experimentation and modelling,” *Construction and Building Materials*, vol. 52, pp. 375–384, Feb. 2014, doi: 10.1016/j.conbuildmat.2013.11.048.
- [93] Shahreza S. K., Baietti, G., Quartarone, G., Santandrea, M., Carloni C., “Effect of Steel-Reinforced Grout Confinement on Concrete Square and Cylindrical Columns,” *SJ*, vol. 117, no. 5, Sep. 2020, doi: 10.14359/51725842.
- [94] L. H. Sneed, C. Carloni, G. Fraioli, and G. Baietti, “Confinement of Brick Masonry Columns with SRG Jackets,” p. 10.

- [95] L. H. Sneed, C. Carloni, G. Baietti, and G. Fraioli, “Confinement of Clay Masonry Columns with SRG,” *KEM*, vol. 747, pp. 350–357, Jul. 2017, doi: 10.4028/www.scientific.net/KEM.747.350.
- [96] Nanni A., “A New Tool for Concrete and Masonry Repair. Strengthening with fiber-reinforced cementitious matrix composites,” 2012.
- [97] B. Barton *et al.*, “Characterization of reinforced concrete beams strengthened by steel reinforced polymer and grout (SRP and SRG) composites,” *Materials Science and Engineering: A*, vol. 412, no. 1–2, pp. 129–136, Dec. 2005, doi: 10.1016/j.msea.2005.08.151.
- [98] L. H. Sneed, S. Verre, C. Carloni, and L. Ombres, “Flexural behavior of RC beams strengthened with steel-FRCM composite,” *Engineering Structures*, vol. 127, pp. 686–699, Nov. 2016, doi: 10.1016/j.engstruct.2016.09.006.
- [99] C. G. Papanicolaou, T. C. Triantafillou, M. Papathanasiou, and K. Karlos, “Textile reinforced mortar (TRM) versus FRP as strengthening material of URM walls: out-of-plane cyclic loading,” *Mater Struct*, vol. 41, no. 1, pp. 143–157, Nov. 2007, doi: 10.1617/s11527-007-9226-0.
- [100] M. Corradi, A. Borri, G. Castori, and R. Sisti, “Shear strengthening of wall panels through jacketing with cement mortar reinforced by GFRP grids,” *Composites Part B: Engineering*, vol. 64, pp. 33–42, Aug. 2014, doi: 10.1016/j.compositesb.2014.03.022.
- [101] V. Giamundo, G. P. Lignola, G. Maddaloni, A. Balsamo, A. Prota, and G. Manfredi, “Experimental investigation of the seismic performances of IMG reinforcement on curved masonry elements,” *Composites Part B: Engineering*, vol. 70, pp. 53–63, Mar. 2015, doi: 10.1016/j.compositesb.2014.10.039.
- [102] V. Alecci, F. Focacci, L. Rovero, G. Stipo, and M. De Stefano, “Extrados strengthening of brick masonry arches with PBO–FRCM composites: Experimental and analytical investigations,” *Composite Structures*, vol. 149, pp. 184–196, Aug. 2016, doi: 10.1016/j.compstruct.2016.04.030.
- [103] V. Giamundo, G. P. Lignola, G. Maddaloni, F. da Porto, A. Prota, and G. Manfredi, “Shaking table tests on a full-scale unreinforced and IMG-retrofitted clay brick masonry barrel vault,” *Bull Earthquake Eng*, vol. 14, no. 6, pp. 1663–1693, Jun. 2016, doi: 10.1007/s10518-016-9886-7.
- [104] Ł. Bednarz, A. Górski, J. Jasieńko, and E. Rusiński, “Simulations and analyses of arched brick structures,” *Automation in Construction*, vol. 20, no. 7, pp. 741–754, Nov. 2011, doi: 10.1016/j.autcon.2011.01.005.
- [105] Ł. Hojdys and P. Krajewski, “Laboratory Tests on Masonry Vaults with Backfill Strengthened at the Extrados,” *KEM*, vol. 624, pp. 510–517, Sep. 2014, doi: 10.4028/www.scientific.net/KEM.624.510.
- [106] “<https://www.kerakoll.com/>.”

- [107] British Standards Institution, “Methods of test for mortar for masonry. Part 11. Part 11.,” 1999.
- [108] Kesler, C E, Kesler, C E, C E, Naus, D J, and Lott, J L, “Fracture mechanics - its applicability to concrete,” 1972, pp. 113–124.
- [109] M.F. Kaplan, “Crack Propagation and the Fracture of Concrete,” *Journal Proceedings*, vol. 58, no. 11, pp. 591–610, Jan. 11, 1961.
- [110] G. I. Barenblatt, “The formation of equilibrium cracks during brittle fracture. General ideas and hypotheses. Axially-symmetric cracks,” *Journal of Applied Mathematics and Mechanics*, vol. 23, no. 3, pp. 622–636, Jan. 1959, doi: 10.1016/0021-8928(59)90157-1.
- [111] D. S. Dugdale, “Yielding of steel sheets containing slits,” *Journal of the Mechanics and Physics of Solids*, vol. 8, no. 2, pp. 100–104, May 1960, doi: 10.1016/0022-5096(60)90013-2.
- [112] C. G. Hoover and Z. P. Bažant, “Comprehensive concrete fracture tests: Size effects of Types 1 & 2, crack length effect and postpeak,” *Engineering Fracture Mechanics*, vol. 110, pp. 281–289, Sep. 2013, doi: 10.1016/j.engfracmech.2013.08.008.
- [113] J. R. Rice, “Mathematical Analysis in the Mechanics of Fracture,” in *Fracture: An Advanced Treatise*, vol. 2, Academic Press, 1968, pp. 191–311.
- [114] Bažant Z.P., *Crack Band Model for Fracture of Geomaterials*, vol. 3. 1982.
- [115] Belletti B, Cerioni R, Iori I, Ferretti D., “L’energia di frattura del laterizio: due metodi per la sua determinazione. Costruire in Laterizio,” vol. 68, pp. 66–71, 1999.
- [116] M. Salviato, K. Kirane, S. Esna Ashari, Z. P. Bažant, and G. Cusatis, “Experimental and numerical investigation of intra-laminar energy dissipation and size effect in two-dimensional textile composites,” *Composites Science and Technology*, vol. 135, pp. 67–75, Oct. 2016, doi: 10.1016/j.compscitech.2016.08.021.
- [117] A. Needleman, “A Continuum Model for Void Nucleation by Inclusion Debonding,” *Journal of Applied Mechanics*, vol. 54, no. 3, pp. 525–531, Sep. 1987, doi: 10.1115/1.3173064.
- [118] A. Needleman, “An analysis of tensile decohesion along an interface,” *Journal of the Mechanics and Physics of Solids*, vol. 38, no. 3, pp. 289–324, Jan. 1990, doi: 10.1016/0022-5096(90)90001-K.
- [119] A. Hillerborg, “Results of three comparative test series for determining the fracture energy  $G_F$  of concrete,” *Materials and Structures*, vol. 18, no. 5, pp. 407–413, Sep. 1985, doi: 10.1007/BF02472416.
- [120] M. Elices and J. Planas, “Fracture mechanics parameters of concrete,” *Advanced Cement Based Materials*, vol. 4, no. 3–4, pp. 116–127, Oct. 1996, doi: 10.1016/S1065-7355(96)90080-2.
- [121] G. V. Guinea, J. Planas, and M. Elices, “A general bilinear fit for the softening curve of concrete,” *Materials and Structures*, vol. 27, no. 2, pp. 99–105, Mar. 1994, doi: 10.1007/BF02472827.

- [122] Guinea G, Elices M, Planas J., “On the initial shape of the softening function of cohesive materials,” *Int. J Fracture*, no. 87, pp. 139–49, 1997.
- [123] Elices M., Planas J., *Size effect and experimental validation of fracture mechanics*, 1st Edition. 1990.
- [124] Planas J., Elices M., “Conceptual and experimental problems in the determination of the fracture energy of concrete,” in *International workshop on fracture toughness and fracture energy (1988-10-12)*, 1989, pp. 165–181.
- [125] Planas J, Elices M., “Cracking and damage,” *Elsevier*, pp. 462–76, 1989.
- [126] Guinea G.V., “Correlation between the softening and the size effect curves,” *Size effect in concrete structures. London; 1994. p. 233–44.*, pp. 233–44, 1994.
- [127] J. Planas, M. Elices, and G. V. Guinea, “Cohesive cracks versus nonlocal models: Closing the gap,” *Int J Fract*, vol. 63, no. 2, pp. 173–187, Sep. 1993, doi: 10.1007/BF00017284.
- [128] Planas J, Guinea GV, Elices M., “Determination of the fracture parameters of Bažant and Jenq-Shah based on simple tests.,” *ACI-SEM Joint Task Group Fract Test Concr*, 1994.
- [129] P. F. Walsh, “Linear fracture mechanics in orthotropic materials,” *Engineering Fracture Mechanics*, vol. 4, no. 3, pp. 533–541, Sep. 1972, doi: 10.1016/0013-7944(72)90064-1.
- [130] Bažant Z.P., “Instability, Ductility, and Size Effect in Strain-Softening Concrete,” *Journal of Engineering Mechanics-asce*, 1976.
- [131] Z. P. Bažant, “Size Effect in Blunt Fracture: Concrete, Rock, Metal,” *Journal of Engineering Mechanics*, vol. 110, no. 4, pp. 518–535, Apr. 1984, doi: 10.1061/(ASCE)0733-9399(1984)110:4(518).
- [132] J. Planas, M. Elices, G. V. Guinea, “Measurement of the fracture energy using three-point bend tests: Part 2—Influence of bulk energy dissipation,” vol. 25, pp. 305–312, 1992.
- [133] L. Cedolin and G. Cusatis, “Identification of concrete fracture parameters through size effect experiments,” *Cement and Concrete Composites*, vol. 30, no. 9, pp. 788–797, Oct. 2008, doi: 10.1016/j.cemconcomp.2008.05.007.
- [134] C. Carloni, M. Santandrea, and R. Wendner, “An investigation on the ‘width and size effect’ in the evaluation of the fracture energy of concrete,” *Procedia Structural Integrity*, vol. 3, pp. 450–458, 2017, doi: 10.1016/j.prostr.2017.04.065.
- [135] C. G. Hoover, Z. P. Bažant, J. Vorel, R. Wendner, and M. H. Hubler, “Comprehensive concrete fracture tests: Description and results,” *Engineering Fracture Mechanics*, vol. 114, pp. 92–103, Dec. 2013, doi: 10.1016/j.engfracmech.2013.08.007.
- [136] C. G. Hoover and Z. P. Bažant, “Cohesive crack, size effect, crack band and work-of-fracture models compared to comprehensive concrete fracture tests,” *Int J Fract*, vol. 187, no. 1, pp. 133–143, May 2014, doi: 10.1007/s10704-013-9926-0.

- [137] M. S. Imbabi, C. Carrigan, and S. McKenna, "Trends and developments in green cement and concrete technology," *International Journal of Sustainable Built Environment*, vol. 1, no. 2, pp. 194–216, Dec. 2012, doi: 10.1016/j.ijse.2013.05.001.
- [138] K. L. Scrivener, V. M. John, and E. M. Gartner, "Eco-efficient cements: Potential economically viable solutions for a low-CO<sub>2</sub> cement-based materials industry," *Cement and Concrete Research*, vol. 114, pp. 2–26, Dec. 2018, doi: 10.1016/j.cemconres.2018.03.015.
- [139] J. L. Provis, "Alkali-activated materials," *Cement and Concrete Research*, vol. 114, pp. 40–48, Dec. 2018, doi: 10.1016/j.cemconres.2017.02.009.
- [140] B. Singh, G. Ishwarya, M. Gupta, and S. K. Bhattacharyya, "Geopolymer concrete: A review of some recent developments," *Construction and Building Materials*, vol. 85, pp. 78–90, Jun. 2015, doi: 10.1016/j.conbuildmat.2015.03.036.
- [141] C. Monticelli *et al.*, "Corrosion behavior of steel in alkali-activated fly ash mortars in the light of their microstructural, mechanical and chemical characterization," *Cement and Concrete Research*, vol. 80, pp. 60–68, Feb. 2016, doi: 10.1016/j.cemconres.2015.11.001.
- [142] L. Carabba, M. Santandrea, C. Carloni, S. Manzi, and M. C. Bignozzi, "Steel fiber reinforced geopolymer matrix (S-FRGM) composites applied to reinforced concrete structures for strengthening applications: A preliminary study," *Composites Part B: Engineering*, vol. 128, pp. 83–90, Nov. 2017, doi: 10.1016/j.compositesb.2017.07.007.
- [143] S. A. Bernal and J. L. Provis, "Durability of Alkali-Activated Materials: Progress and Perspectives," *J. Am. Ceram. Soc.*, vol. 97, no. 4, pp. 997–1008, Apr. 2014, doi: 10.1111/jace.12831.
- [144] P. Duxson, J. L. Provis, G. C. Lukey, and J. S. J. van Deventer, "The role of inorganic polymer technology in the development of 'green concrete,'" *Cement and Concrete Research*, vol. 37, no. 12, pp. 1590–1597, Dec. 2007, doi: 10.1016/j.cemconres.2007.08.018.
- [145] P. Sturm, G. J. G. Gluth, C. Jäger, H. J. H. Brouwers, and H.-C. Kühne, "Sulfuric acid resistance of one-part alkali-activated mortars," *Cement and Concrete Research*, vol. 109, pp. 54–63, Jul. 2018, doi: 10.1016/j.cemconres.2018.04.009.
- [146] V. F. F. Barbosa and K. J. D. MacKenzie, "Thermal behaviour of inorganic geopolymers and composites derived from sodium polysialate," *Materials Research Bulletin*, vol. 38, no. 2, pp. 319–331, Jan. 2003, doi: 10.1016/S0025-5408(02)01022-X.
- [147] J. Davidovits, "Geopolymers: Inorganic polymeric new materials," *Journal of Thermal Analysis*, vol. 37, no. 8, pp. 1633–1656, Aug. 1991, doi: 10.1007/BF01912193.
- [148] L. Carabba, R. Moricone, G. E. Scarponi, A. Tugnoli, and M. C. Bignozzi, "Alkali activated lightweight mortars for passive fire protection: A preliminary study," *Construction and Building Materials*, vol. 195, pp. 75–84, Jan. 2019, doi: 10.1016/j.conbuildmat.2018.11.005.

- [149] M.C. Bignozzi, “High-Temperature Behaviour of Alkali-Activated Composites based on Fly Ash and Recycled Refractory Particles,” *J. Ceram. Sci. Technol.*, no. 03, 2017, doi: 10.4416/JCST2017-00047.
- [150] W. D. A. Rickard, G. J. G. Gluth, and K. Pistol, “In-situ thermo-mechanical testing of fly ash geopolymer concretes made with quartz and expanded clay aggregates,” *Cement and Concrete Research*, vol. 80, pp. 33–43, Feb. 2016, doi: 10.1016/j.cemconres.2015.11.006.
- [151] R. Zhao and J. G. Sanjayan, “Geopolymer and Portland cement concretes in simulated fire,” *Magazine of Concrete Research*, vol. 63, no. 3, pp. 163–173, Mar. 2011, doi: 10.1680/mac9.00110.
- [152] Y. Ding, C.-J. Shi, and N. Li, “Fracture properties of slag/fly ash-based geopolymer concrete cured in ambient temperature,” *Construction and Building Materials*, vol. 190, pp. 787–795, Nov. 2018, doi: 10.1016/j.conbuildmat.2018.09.138.
- [153] P. Nath and P. K. Sarker, “Fracture properties of GGBFS-blended fly ash geopolymer concrete cured in ambient temperature,” *Mater Struct*, vol. 50, no. 1, p. 32, Feb. 2017, doi: 10.1617/s11527-016-0893-6.
- [154] Z. L. Xie, H. F. Zhou, L. J. Lu, and Z. A. Chen, “An investigation into fracture behavior of geopolymer concrete with digital image correlation technique,” *Construction and Building Materials*, vol. 155, pp. 371–380, Nov. 2017, doi: 10.1016/j.conbuildmat.2017.08.041.
- [155] Z. Pan, J. G. Sanjayan, and B. V. Rangan, “Fracture properties of geopolymer paste and concrete,” *Magazine of Concrete Research*, vol. 63, no. 10, pp. 763–771, Oct. 2011, doi: 10.1680/mac9.2011.63.10.763.
- [156] P. K. Sarker, R. Haque, and K. V. Ramgolam, “Fracture behaviour of heat cured fly ash based geopolymer concrete,” *Materials & Design*, vol. 44, pp. 580–586, Feb. 2013, doi: 10.1016/j.matdes.2012.08.005.
- [157] Cedolin L., Dei Poli S., Lori I., “Simplified Parametric (Phenomenological) Model of Creep of Concrete in Direct Tension,” *Journal of Engineering Mechanics*, vol. 113, no. 3, 1987.
- [158] ACI Committee 446, “Draft ASTM Test Procedure.”
- [159] G. Baietti, G. Quartarone, L. Carabba, S. Manzi, C. Carloni, and M. C. Bignozzi, “Use of digital image analysis to determine fracture properties of alkali-activated mortars,” *Engineering Fracture Mechanics*, vol. 240, p. 107313, Dec. 2020, doi: 10.1016/j.engfracmech.2020.107313.
- [160] Daissè G., “Interfacial bond behavior of steel reinforced grout composites applied to a masonry substrate,” Mater Thesis, University of Bologna.
- [161] T. D’Antino, M. Santandrea, and C. Carloni, “Advances in Knowledge of the Fracture Properties of Cohesive Materials: Fired-Clay and Tuff Bricks,” *J. Eng. Mech.*, vol. 146, no. 8, p. 04020079, Aug. 2020, doi: 10.1061/(ASCE)EM.1943-7889.0001815.

- [162] M. Santandrea, “Bond behavior between fiber reinforced composites and quasi-brittle material interfaces.”
- [163] L.-M. Czernuschka, R. Wan-Wendner, and J. Vorel, “Investigation of fracture based on sequentially linear analysis,” *Engineering Fracture Mechanics*, vol. 202, pp. 75–86, Oct. 2018, doi: 10.1016/j.engfracmech.2018.08.008.
- [164] D. Darwin, S. Barham, R. Kozul, and S. Luan, “Fracture Energy of High-Strength Concrete,” *ACI Materials Journal*, p. 8, 2001.
- [165] W. Gerstle, “Progress in Developing a Standard Fracture Toughness Test for Concrete,” *Structures Congress*, p. 12, 2010.
- [166] M. Elices, “On the measurement of concrete fracture energy using three-point bend tests,” p. 2.
- [167] S. P. Shah, “Fracture toughness of cement-based materials,” *Materials and Structures*, p. 6.
- [168] Elices M, Guinea VG, Planas J., “Measurement of the fracture energy using three-point bend tests: Part 3—influence of cutting the P- $\delta$  tail,” *Mater Struct*, vol. 25, no. 6, pp. 327–34., 1992.
- [169] Tada H, Paris P, Irwin G. T, *The stress analysis of cracks handbook*. 1976.
- [170] Z. P. Bažant, “Concrete fracture models: testing and practice,” *Engineering Fracture Mechanics*, vol. 69, no. 2, pp. 165–205, Jan. 2002, doi: 10.1016/S0013-7944(01)00084-4.
- [171] G. Baietti, L. Carabba, G. Quartarone, C. Carloni, S. Manzi, and M. C. Bigozzi, “Fracture properties of alkali activated mortars,” presented at the 10th International Conference on Fracture Mechanics of Concrete and Concrete Structures, Jun. 2019, doi: 10.21012/FC10.238496.
- [172] “BS 1881-121: testing concrete. Method for determination of static modulus of elasticity in compression,” British Standards, 1983.
- [173] *Building code requirements for reinforced concrete*. 1989.
- [174] D. Ferretti, M. Rossi, and G. Royer-Carfagni, “An ESPI experimental study on the phenomenon of fracture in glass. Is it brittle or plastic?,” *Journal of the Mechanics and Physics of Solids*, vol. 59, no. 7, pp. 1338–1354, Jul. 2011, doi: 10.1016/j.jmps.2011.04.008.
- [175] Petersson, P-E., “Comments on the method of determining the fracture energy of concrete by means of three-point bend tests on notched beams,” *Division of Building Materials, Lund University.*, vol. 3011, 1982.
- [176] “Building lime - Part 1: Definitions, specifications and conformity criteria,” European Standard.
- [177] M. Santandrea, F. Focacci, C. Mazzotti, F. Ubertini, and C. Carloni, “Determination of the interfacial cohesive material law for SRG composites bonded to a masonry substrate,”

- Engineering Failure Analysis*, vol. 111, p. 104322, Apr. 2020, doi: 10.1016/j.engfailanal.2019.104322.
- [178] C. Carloni, S. Verre, L. H. Sneed, and L. Ombres, “Loading rate effect on the debonding phenomenon in fiber reinforced cementitious matrix-concrete joints,” *Compos Part B*, vol. 108, pp. 301–314, Jan. 2017, doi: 10.1016/j.compositesb.2016.09.087.
- [179] *BS EN 1881 2006: Products and systems for the protection and repair of concrete structures. Test methods. Testing of anchoring products by the pull-out method.* .
- [180] *UNI EN 1542:2000: Prodotti e sistemi per la protezione e la riparazione delle strutture di calcestruzzo - Metodi di prova - Misurazione dell’aderenza per trazione diretta.* .
- [181] T. D’Antino, C. Carloni, L. H. Sneed, and C. Pellegrino, “Matrix–fiber bond behavior in PBO FRCM composites: A fracture mechanics approach,” *Engineering Fracture Mechanics*, vol. 117, pp. 94–111, Feb. 2014, doi: 10.1016/j.engfracmech.2014.01.011.
- [182] F. Focacci, T. D’Antino, C. Carloni, L. H. Sneed, and C. Pellegrino, “An indirect method to calibrate the interfacial cohesive material law for FRCM-concrete joints,” *Materials & Design*, vol. 128, pp. 206–217, Aug. 2017, doi: 10.1016/j.matdes.2017.04.038.
- [183] C. Carloni and K. V. Subramaniam, “Direct determination of cohesive stress transfer during debonding of FRP from concrete,” *Composite Structures*, vol. 93, no. 1, pp. 184–192, Dec. 2010, doi: 10.1016/j.compstruct.2010.05.024.
- [184] Carloni C., Subramaniam K.V., “Application of fracture mechanics to debonding of FRP from RC members,” in *ACI Special Publication*, 2012, vol. 286, pp. 1–16.
- [185] A. D’Ambrisi, L. Feo, and F. Focacci, “Bond-slip relations for PBO-FRCM materials externally bonded to concrete,” *Composites Part B: Engineering*, vol. 43, no. 8, pp. 2938–2949, Dec. 2012, doi: 10.1016/j.compositesb.2012.06.002.
- [186] J. Dai, T. Ueda, and Y. Sato, “Unified Analytical Approaches for Determining Shear Bond Characteristics of FRP-Concrete Interfaces through Pullout Tests,” *ACT*, vol. 4, no. 1, pp. 133–145, 2006, doi: 10.3151/jact.4.133.
- [187] J. Dai, T. Ueda, and Y. Sato, “Development of the Nonlinear Bond Stress–Slip Model of Fiber Reinforced Plastics Sheet–Concrete Interfaces with a Simple Method,” *J. Compos. Constr.*, vol. 9, no. 1, pp. 52–62, Feb. 2005, doi: 10.1061/(ASCE)1090-0268(2005)9:1(52).
- [188] F. Focacci and C. Carloni, “Periodic variation of the transferable load at the FRP-masonry interface,” *Composite Structures*, vol. 129, pp. 90–100, Oct. 2015, doi: 10.1016/j.compstruct.2015.03.008.
- [189] C. Carloni and F. Focacci, “FRP-masonry interfacial debonding: An energy balance approach to determine the influence of the mortar joints,” *European Journal of Mechanics - A/Solids*, vol. 55, pp. 122–133, Jan. 2016, doi: 10.1016/j.euromechsol.2015.08.003.